



**HAL**  
open science

# Dustiness and mechanical properties of cohesive and non-cohesive bulk solids

Somik Chakravarty

► **To cite this version:**

Somik Chakravarty. Dustiness and mechanical properties of cohesive and non-cohesive bulk solids. Chemical and Process Engineering. Université de Technologie de Compiègne, 2018. English. NNT : 2018COMP2423 . tel-03357886

**HAL Id: tel-03357886**

**<https://theses.hal.science/tel-03357886v1>**

Submitted on 29 Sep 2021

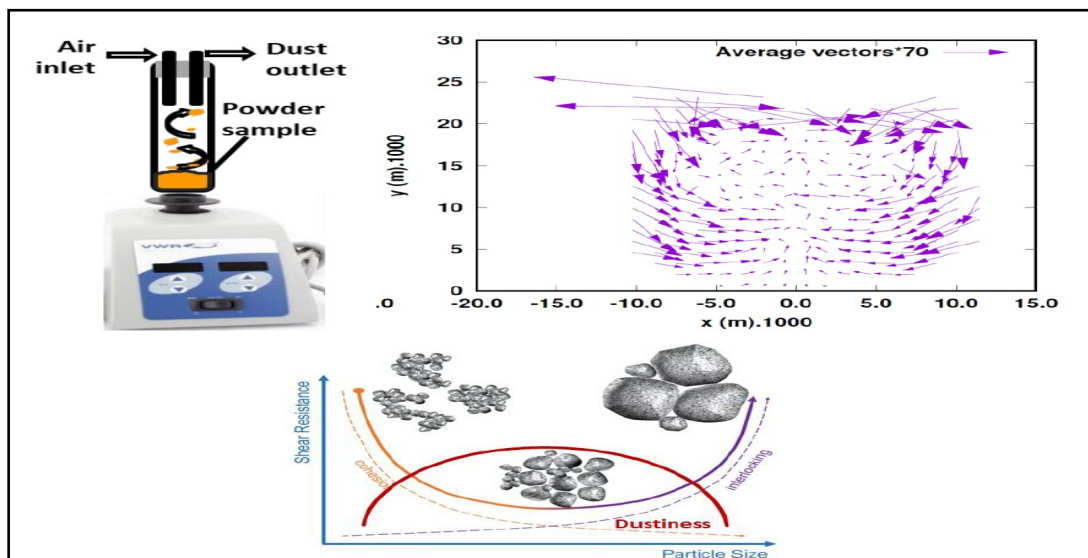
**HAL** is a multi-disciplinary open access archive for the deposit and dissemination of scientific research documents, whether they are published or not. The documents may come from teaching and research institutions in France or abroad, or from public or private research centers.

L'archive ouverte pluridisciplinaire **HAL**, est destinée au dépôt et à la diffusion de documents scientifiques de niveau recherche, publiés ou non, émanant des établissements d'enseignement et de recherche français ou étrangers, des laboratoires publics ou privés.

Par **Somik CHAKRAVARTY**

*Dustiness and mechanical properties of cohesive  
and non-cohesive bulk solids*

Thèse présentée  
pour l'obtention du grade  
de Docteur de l'UTC



Soutenu le 25 mai 2018

**Spécialité :** Génie des Procédés Industriels et développement durable : Transformations intégrées de la matière renouvelable (EA-4297)

D2423



**THESE POUR L'OBTENTION DU GRADE DE DOCTEUR DE L'UNIVERSITE DE  
TECHNOLOGIE DE COMPIEGNE**

---

**Dustiness and mechanical properties of cohesive  
and non-cohesive bulk solids**

---

Présentée par :

**Somik CHAKRAVARTY**

Champ disciplinaire :

**Génie des Procédés Industriels et développement durable**

Soutenue le **25 mai 2018** devant le jury composé de :

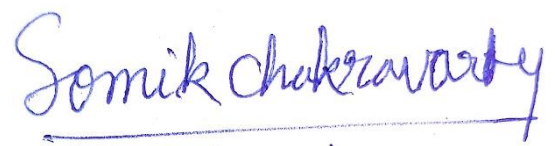
<b>Mme Laurence LE COQ</b>	Professeur, IMT Atlantique	Rapporteur
<b>M. François-Xavier OUF</b>	Dr. HDR, IRSN France	Rapporteur
<b>M. Eberhard SCHMIDT</b>	Professeur, Bergische Universität Wuppertal	Examineur
<b>M. Eugene VOROBIEV</b>	Professeur, UTC Compiègne	Examineur
<b>M. Olivier WITSCHGER</b>	Chercheur, INRS France	Examineur
<b>M. Martin MORGENEYER</b>	Dr. Ing. HDR, UTC Compiègne	Directeur de thèse
<b>M. Olivier LE BIHAN</b>	Dr. HDR, INERIS France	Encadrant de thèse



*Dedicated to my family, friends and mentors without whom  
this milestone would never have been reached !!*

# DECLARATION

To the best of my knowledge, this thesis contains no material previously published by any other person except where due acknowledgment has been made. This thesis contains no material which has been accepted for the award of any other degree or diploma in any university.



**Somik CHAKRAVARTY**

## ACKNOWLEDGEMENT

I would like to thank the Director and Co-director of my thesis, Dr. Ing. HDR. Martin MORGENEYER and Dr. HDR. Olivier LE BIHAN respectively, for their invaluable supervision, guidance, and inspiring me to finish my thesis during these three and half years. I would always be grateful to them for providing me with this opportunity. They motivated me to work in the field powder characterization and dust generation, which is only poetic justice for a person who suffered from dust allergies in his childhood. Their expertise, patience and guidance, which I experienced during the complete course of this PhD, combined with their continuous and stimulating participation, always kept me motivated and enthusiastic. I would also like to thank former post-doc and dear friend, Marc FISCHER for his invaluable scientific knowledge and extensive discussions essential towards finishing this thesis.

I thank the honorary jury members who have taken time from their busy schedule and accepted to bring their expertise for assessing the present PhD work.

My gratitude goes to the people at INERIS, NOVA team head Dr. Olivier AGUERRE CHARIOL, the research engineers Dr. Christophe BRESSOT, Dr. Christophe DUTOUQUET, and the technicians Morgane DALLE and Laurent MEUNIER. Thank you all for your help and support during my time at INERIS. I would also like to thank my friend Dr. Alexis VIGNES, for always cheering me up every time we met.

The IMID group in Lab- T.I.M.R - Génie des procédés has been instrumental in providing me with the necessary scientific, technical and logistical tools and services to finish my thesis. I would like to thank the technician and lab-staff at UTC including Michaël Lefebvre, Bruno Dauzat and Dr. Hervé Leclerc.

To Prof. Arno KWADE, Prof. Stefan LUDING and Miguel A. Romero VALLE, I will be grateful to you for welcoming me to TU Braunschweig, University of Twente and BASF SE, respectively for my three secondments. The knowledge and skills gained from interacting with you made me a better researcher. Thank you to Ramon CABISCOL at TU Braunschweig, Hao SHI and Dr Thomas WEINHART at the University of Twente, and Thorsten MOHR at the BASF labs for all your help and encouragement regarding the experimental and simulation work. Miguel, I appreciate your feedback, supervision, corrections, candidness and choice of German and Mexican beer during the secondment. I profited a lot from your insights and ingenuity and I will remember the skills gained while working in industry.



T-MAPPP ITN consortium has been the highlight of my doctoral studies. I would like to thank the professors, advisors, industrial partners, lecturers and colleagues for their valuable feedback on my research and your constant encouragement through the various T-MAPPP events and at international conferences. A shout out to Kianoosh TAGHIZADEH, Alexander PODLOZHNYUK, Behzad SOLTANBEIGI and Rohit SHRIVASTAVA who started as my colleagues but have become very close friends during our time in T-MAPPP. Thank you for all the harmless banter, the long discussions and the words of encouragement.

I would like to thank Dr. Pablo GARCIA TRINANES, Dr. Thomas LEEDBEATER and Prof. David PARKER for their invaluable help while performing PEPT experiments at the University of Birmingham.

Compiègne is a beautiful city and it has provided me much more than just good food, wine and cheese. The friends and relationships which I made during my time there would always be special to me. I would like to thank my dear friend and flatmate Qi LIU who taught me how to cook Chinese food and at times, had to push me out of my bed as my morning alarm would wake him instead of me. Thank you to Kate CORSYN, Maia A. RAMIREZ, Theophile GAUDIN, Chunmei LIU, Lorine LE PRIOL for helping me realize there is fun to be had outside work.

Most importantly, I would like to thank my mom and dad for their Sunday Skype calls helping me connect with all things happening at home and making me miss home cooked meal so much. Thank you for believing in me and supporting me at every crucial step of my life. I hope to make you proud.

Thank you to Aru for her love and support. I am thankful to you for making these last three and half years of Ph.D. seem like an adventure. With all the ups and some downs, thank you for being there for me. The memories I shared during this time with you will always be close to my heart.

# ABSTRACT

Handling and processing of granular material release fine solid dust particles, which in an occupational setting, can severely affect worker health & safety and the overall plant operation. Dustiness or the ability of a material to release dust particles depends on several material and process parameters and is usually measured by lab-scale dustiness testers. Dustiness tests remain mostly experimental studies and lack reliable predictive ability due to limited understanding of the dust generation mechanisms and the complex interactions between the particles, wall and fluid, occurring simultaneously during dust generation.

In the framework of EU ITN project T-MAPPP, this thesis uses an experimental approach to understand the dust generation mechanisms by studying: a) the effects of key bulk and particle properties on powder dustiness; b) the nature and magnitude of inter-particle, particle-wall and particle-fluid interactions; c) the evolution of dustiness and generation mechanisms for long duration powder applications.

The results indicate that the dust generation mechanisms differ based on particle size and size distribution of the powder. For the given test samples and experimental conditions, the differences in powder dustiness and dust emission patterns can be characterized by three different groups of powders; powders containing fine cohesive particles, bi-modal (consisting of fine and large particles) powders and lastly, powders consisting of only large particles. While bulk cohesion, especially that stemming from van der Waals forces (measured using shear testers) determines the level of dustiness for the fine powders (in such a way that higher bulk cohesion leads to lower dustiness), both the fraction of fine particles and cohesion determine the dustiness of bi-modal powders. The large particles can emit dust only through attrition of the primary particles into smaller aerosolizable fine particles.

Analysis of a traced particle motion inside a cylindrical tube agitated by a vortex shaker dustiness tester shows the cyclic nature of the particle motion. The motion (position and velocity) is symmetric and isotropic in the horizontal plane with lowest radial velocities close to the tube centre and highest at the boundary wall of the test tube. The particles tend to rise up slowly in the middle of the tube while descending rapidly close to the wall. The highest values of the velocity are found at the highest heights and close to the wall of the test tube, where the population densities are lowest. Increasing particle size and vortex rotation speeds tends to increase particle velocity whereas increase in powder mass leads to a decrease in particle velocity for rotation speeds up to 1500 rpm.

For the given samples (silicon carbide, alumina and acetylene coke) and the experimental conditions, the initial dustiness is determined by the fraction of fine respirable particles present in the powder but the long-term dust generation patterns and levels are influenced by the material attrition behaviour. Dust is generated by the fragmentation and/or abrasion of primary particles, which may lead to the production and emission of fine daughter particles as dust. The samples with large irregularly shaped particles are likely to show high dustiness by shedding angular corners through inter-particle and particle-wall collisions, thus becoming more spherical in shape. On the contrary, the smaller particles are more resistant to abrasion and generate relatively less dust. While the vortex shaker dustiness tests show similar trends as an attrition tester, our study using alumina and acetylene coke indicate that the results are not interchangeable.

Results from this thesis help understand the influence of powder and process parameters which may be manipulated to reduce dust generation. Furthermore, experimental results can be used to develop and validate numerical models to predict dustiness.

**Keywords:** Powder characterization, Dustiness, Vortex shaker, PEPT, Long-term applications

## RESUME (en français)

La manutention et la mise en œuvre des matériaux granulaires libèrent de fines particules de poussière qui, dans un contexte professionnel, peuvent gravement affecter la santé et la sécurité des travailleurs, ainsi que le fonctionnement global de l'installation. L'émission de poussières et la capacité d'un matériau à libérer des particules de poussière, dépendent de plusieurs paramètres relatifs au matériau mais aussi au procédé. Ces émissions sont généralement mesurées par des tests d'empoussièrement à l'échelle du laboratoire. Ces tests reposent principalement sur des études expérimentales et manquent de capacité prédictive fiable en raison d'une compréhension limitée des mécanismes mis en jeu et des interactions complexes entre particules, paroi et fluide, survenant simultanément pendant la génération de poussières.

Dans le cadre du projet EU ITN T-MAPPP, cette thèse utilise des approches expérimentales et statistiques pour comprendre les mécanismes de génération de poussières en étudiant: a) les effets des caractéristiques des particules et poudres en vrac sur l'émission de poussières; b) la nature et l'ampleur des interactions entre particules, entre particules et parois, et entre particules et fluides; c) l'évolution de l'empoussièrement et des mécanismes de génération pour des applications de poudre de longue durée.

Les résultats indiquent que les mécanismes de génération de poussière diffèrent en fonction de la taille des particules et de la distribution de taille de la poudre. Pour les échantillons d'essai et les conditions expérimentales donnés, les différences dans les modèles initiaux de libération de poussière peuvent être caractérisées par trois groupes différents de poudres : - des poudres contenant des particules cohésives fines, - des poudres bimodales (constituées de fines et de grosses particules), - et enfin des poudres constituées de grosses particules.

Tandis que la cohésion globale, surtout celle due aux forces de van der Waals (mesurée à l'aide de testeurs de cisaillement) détermine le niveau de poussières pour les poudres fines, de telle sorte qu'une cohésion globale plus élevée conduit à moins de poussière, la fraction de particules fines et la cohésion déterminent toutes deux l'empoussièrement provenant des poudres bi-modales. Les grosses particules peuvent émettre de la poussière uniquement par usure des particules primaires en particules fines aérosolisables plus petites.

L'analyse d'un mouvement de particules tracées à l'intérieur d'un tube cylindrique agité par un testeur d'empoussièrement à vortex montre une nature cyclique du mouvement des particules. Le mouvement des particules (position et vitesse) est symétrique et isotrope dans le plan horizontal, les vitesses radiales les plus basses et les plus élevées étant proches du centre du tube et de la paroi, respectivement. Les particules ont tendance à s'élever lentement au milieu du tube tout en descendant rapidement près de la paroi. Les valeurs les plus élevées de la vitesse se trouvent aux hauteurs les plus élevées et près de la paroi interne du tube à essai, où les densités de population sont les plus faibles. Les valeurs plus élevées de la vitesse pourraient provenir d'une diminution du nombre de chocs due à des densités de population plus faibles. L'augmentation de la taille des particules et des vitesses de rotation des tourbillons tend à augmenter la vitesse des particules tandis que l'augmentation de la masse de poudre conduit à une diminution de la vitesse des particules pour des vitesses de rotation allant jusqu'à 1500 tr / min.

Pour les échantillons donnés (carbure de silicium, alumine et coke d'acétylène) et les conditions expérimentales, l'empoussièrement initial est déterminé par la fraction de fines particules respirables présentes dans la poudre, mais les modèles et les niveaux de génération de poussière à long terme sont influencés par le comportement d'attrition matérielle. La poussière est générée par la fragmentation et/ou l'abrasion des particules primaires, ce qui conduit à la production et à l'émission de fines particules-filles sous forme de poussière. Les échantillons ayant de grandes particules de forme irrégulière sont susceptibles de montrer une grande quantité de poussière en détruisant des coins angulaires par des collisions entre particules et les particules et la paroi, devenant ainsi de forme plus sphérique. Au contraire, les particules plus petites sont plus résistantes à l'abrasion et génèrent relativement moins de poussière. Alors que les essais de dépoussièrement par vortex montrent des tendances similaires à celles d'un testeur d'attrition, notre étude utilisant de l'alumine et du coke d'acétylène indique que les résultats ne sont pas interchangeables.

Les résultats de cette thèse aident à comprendre l'influence des paramètres de la poudre et du procédé qui peuvent être manipulés pour réduire la production de poussière. De plus, des résultats expérimentaux peuvent être utilisés pour développer et valider des modèles numériques afin de prédire l'empoussièrement.

**Mots clés:** Caractérisation des poudres, Poussières, Vortex shaker, PEPT, Applications à long terme

## LIST OF PUBLICATIONS (in the order of their appearance)

1. **Chakravarty, Somik**, Marc Fischer, Olivier Le Bihan, and Martin Morgeneyer. "A review of dust generation studies from powder" *Granular Matter T-MAPPP special issue* (submitted: April 2018). **Pages 20 - 60**
2. Shi, Hao, Rahul Mohanty, **Somik Chakravarty**, Ramon Cabiscol, Martin Morgeneyer, Harald Zetzener, Jin Y. Ooi, Arno Kwade, Stefan Luding, and Vanessa Magnanimo. "Effect of Particle Size and Cohesion on Powder Yielding and Flow." *KONA Powder and Particle Journal* (2017): 2018014. Doi: <https://doi.org/10.14356/kona.2018014>. **Pages 63 - 101**
3. **Chakravarty, Somik**, Olivier Le Bihan, Marc Fischer, and Martin Morgeneyer. "Dust generation in powders: Effect of particle size distribution." In *EPJ Web of Conferences*, vol. 140, p. 13018. EDP Sciences, 2017. Doi: <https://doi.org/10.1051/epjconf/201714013018>. **Pages 103 - 112**
4. **Chakravarty, Somik**, Marc Fischer, Pablo García-Triñanes, David Parker, Olivier Le Bihan, and Martin Morgeneyer. "Study of the particle motion induced by a vortex shaker." *Powder Technology* 322 (2017): 54-64. Doi: <https://doi.org/10.1016/j.powtec.2017.08.026>. **Pages 116 - 137**
5. Fischer, Marc, **Somik Chakravarty**, Olivier Le Bihan, and Martin Morgeneyer. "Parametric study of the particle motion induced by a vortex shaker." *Powder Technology* (submitted: December 2017). **Pages 140 - 159**
6. **Chakravarty, Somik**, Marc Fischer, Pablo García-Triñanes, Morgane Dalle, Laurent Meunier, Olivier Aguerre-Chariol, Olivier Le Bihan, and Martin Morgeneyer. "Long-term dust generation from silicon carbide powders." *Process Safety and Environmental Protection* 116 (2018). Doi: <https://doi.org/10.1016/j.psep.2018.01.021>. **Pages 164 - 188**
7. **Chakravarty, Somik**, Marc Fischer, Miguel A. Romero Valle, Olivier Le Bihan, and Martin Morgeneyer. "Dust generation behaviour of alumina and coke powders using a vortex shaker and a fluid-jet attrition tester." *Powder Technology* (submitted: June 2018). **Pages 192 - 216**

# INDEX (with embedded publications)

1	INTRODUCTION.....	13
2	STATE OF THE ART	
	<b>Research article:</b> A review of dust generation studies from powder.....	20
3	CHARACTERISATION OF POWDER BULK PROPERTIES INFLUENCING DUSTINESS	
	<b>Research article:</b> Effect of Particle Size and Cohesion on Powder Yielding and Flow.....	63
	<b>Research article:</b> Dust generation in powders: Effect of particle size distribution.....	103
4	EXPERIMENTAL DUSTINESS TESTER: PARTICLE MOTION AND PARAMETRIC STUDY OF THE VORTEX SHAKER DUSTINESS TESTER	
	<b>Research article:</b> Study of the particle motion induced by a vortex shaker.....	116
	<b>Research article:</b> Parametric study of the particle motion induced by a vortex shaker.....	140
5	VORTEX SHAKER TESTER APPLICATIONS BASED ON LONG-TERM POWDER TESTING	
	<b>Research article:</b> Long-term dust generation from silicon carbide powders.....	164
	<b>Research article:</b> Dust generation behaviour of alumina and coke powders using a vortex shaker and a fluid-jet attrition tester.....	192
6	CONCLUSION.....	219
7	PERSPECTIVES.....	226
8	APPENDICES.....	231

# Table of Contents

ACKNOWLEDGEMENT.....	iv
ABSTRACT .....	vi
RESUME (en français).....	vii
LIST OF PUBLICATIONS (in the order of their appearance).....	viii
INDEX (with embedded publications).....	ix
1 Introduction.....	13
1.1 Research background and challenges .....	13
1.2 Objectives of the thesis .....	15
1.3 Outline of the thesis .....	16
1.4 References.....	17
2 State of the Art .....	18
2.0 Overview.....	18
2.1 Article (submitted to Granular Matter T-MAPPP special issue, March 2018) .....	20
2.1.1 Abstract .....	20
2.1.2 Introduction .....	21
2.1.3 Dustiness tests .....	24
2.1.4 Mechanisms of dust generation .....	27
2.1.5 Parametric studies on powder dustiness .....	31
2.1.6 Modelling approaches .....	40
2.1.7 Conclusion and outlook.....	50
2.1.8 References .....	53
3 Characterization of bulk properties influencing powder flow and dustiness.....	62
3.0 Overview.....	62
3.1 Article (published in KONA Powder and Particle journal, 2017):.....	63
3.1.1 Abstract .....	63
3.1.2 Introduction .....	64
3.1.3 Material description and characterization .....	66
3.1.4 Experimental setup .....	69
3.1.5 Test procedures.....	76
3.1.6 Comparison of shear devices.....	79
3.1.7 Effects of varying particle size.....	88
3.1.8 Conclusion and outlook.....	97
3.1.9 Nomenclature.....	99
3.1.10 References .....	100

3.2	Article (published in peer-reviewed EPJ Web of Conferences, EDP Sciences, 2017) .....	103
3.2.1	Abstract .....	103
3.2.2	Introduction .....	103
3.2.3	Material and experimental methods .....	105
3.2.4	Results and discussion .....	108
3.2.5	Conclusion .....	113
3.2.6	References .....	113
4	Experimental dustiness tester: particle motion and parametric study of the vortex shaker dustiness tester .....	115
4.0	Overview .....	115
4.1	Article (published in Powder Technology, 2017) .....	116
4.1.1	Abstract .....	116
4.1.2	Introduction .....	117
4.1.3	Experimental foundations .....	119
4.1.4	Presentation of the statistical methodology .....	123
4.1.5	Analysis of the particle's behaviour under standard conditions .....	129
4.1.6	Conclusions and outlook .....	135
4.1.7	References .....	137
4.2	Article (submitted to Powder Technology, December 2017): .....	140
4.2.1	Abstract .....	140
4.2.2	Introduction .....	141
4.2.3	Experimental foundation and prior results .....	142
4.2.4	Results and discussion .....	144
4.2.5	Conclusion and outlook .....	159
4.2.6	References .....	160
5	Application of the vortex shaker: Dust generation from long-term industrial operations and comparison with a pilot-scale fluidized bed attrition tester .....	162
5.0	Overview .....	162
5.1	Article (published in Process Safety and Environmental Protection, 2018) .....	164
5.1.1	Abstract .....	164
5.1.2	Introduction .....	165
1.1.1	Materials and Methods .....	168
1.1.2	Results .....	175
5.1.5	Discussion .....	184
5.1.6	Conclusion and Perspective .....	187

5.1.7	References .....	189
5.2	Article (submitted to Powder Technology, March 2017):.....	192
5.2.1	Abstract .....	192
5.2.2	Introduction .....	193
5.2.3	Experimental method and test samples .....	195
5.2.4	Results and discussion.....	204
5.2.4	Summary and outlook .....	214
5.2.5	References .....	215
6	Conclusion .....	219
6.3	Key parameters influencing dust generation from bulk: identification and characterization..	220
6.4	Selection of experimental setup: vortex shaker dustiness tester.....	221
6.3	Physical mechanisms of dust generation process: role of inter-particle and particle-wall interactions.....	222
6.4	Time-evolution of dust generation processes: mechanisms and applications .....	224
7	Perspectives.....	226
7.1	Other parameters which influence dust generation from bulk.....	226
7.2	Dustiness tests and testers.....	227
7.3	Characterization of powder.....	228
7.4	Approaches towards development of predictive models for material dustiness.....	229
8	Appendices.....	231
8.1	Appendix A: Supplementary data for section 3.1.....	231
8.1.1	Test details on yield locus and steady state locus .....	231
8.1.2	Test results of all the powders and devices shown in this paper .....	232
8.2	Appendix B: Supplementary data for section 3.2.....	233
8.3	Appendix C: Supplementary data for section 4.1 .....	238



# 1 Introduction

## 1.1 Research background and challenges

Bulk solids or granular materials are omnipresent and its expansive reach is demonstrated from the first cup of coffee to the last meal of the day. Bulk solids, as the name suggests, is defined as any material consisting of many individual solid particles. Handling of granular material is an essential part of almost every major industry including the chemical, pharmaceutical, cosmetic and agricultural among others. It is estimated that granular material constitutes over 50% of the products and over 75% of the raw material feedstock, based on their mass in the chemical industry (Nedderman, 2005). Bulk solids are classified based on particle size and often referred as powders or particulates, sub-groups of granular material with fine grain sizes. The science and technology of handling and processing granular matter is often referred to particle or powder technology and deals with a variety of particles with sizes between sub-micrometre to large grains often in multi-phase mixtures.

Handling and processing of bulk solids can span through their entire life-cycle, from their initial production till its end-use application. The processes range across different industries and can include transportation, feeding, bagging, mixing, and storage, crushing and grinding among others. Such mechanical or man-made processes leads to generation of dust particles or dust cloud in industrial workplace and can be detrimental to efficient industrial operation. Worker exposure to airborne dust can significantly affect their health. Moreover, dust generation in industries can lead to material loss, contamination of products and equipment resulting in significant increases in the cost of smooth plant operations with low downtimes (Levy and Kalman, 2001). In addition to that, any airborne flammable dust laden atmospheres, with sufficient concentration can lead to dangerous explosions (Eckhoff, 2005).

The airborne fine solid particles (also referred to 'dust' and 'aerosol dust') are defined as small airborne solid particles, usually of sizes inferior to 75  $\mu\text{m}$  in diameter which settle under their own weight but may remain suspended for some time (ISO 4225, International Organization for Standardization, 1994). Similar to the ISO definition, (IUPAC, 1990) defines dust particle within the size ranges of 1 and 100  $\mu\text{m}$ , projected into the air by natural forces or mechanical/anthropogenic processes.

Airborne dust particles are of particular concern in a working environment primarily because the exposure to such particles has been associated with occupational diseases such as byssinosis (caused by the inhalation of asbestos, silica and cotton dust), silicosis, the bakers flour aversion, and pneumoconiosis (commonly related to the inhalation of asbestos fibres, coal

mine dust, or crystalline silica dust) (Maizlish, 2000; Iossifova et al., 2010). There are also concerns regarding systematic intoxications, such as lead poisoning, usually at higher dust concentrations. Furthermore, diseases such as cancer, asthma, allergic alveolitis and irritation can take place at much lower dust concentrations (Bickis, 1998).

The materials ability to generate dust upon handling is known as its dustiness. Dustiness of a material is not physical property and depends on several parameters including the physico-chemical properties of the material, the type and magnitude of the stresses applied during handling and processing of the material and also the external environmental conditions, such as the relative humidity and ventilation. Thus, the study of powder dustiness requires the study of factors that affect inter-particle forces and the physical mechanisms involved from the powder at rest to the bulk response due to a mechanical agitation which leads to separation of dust particles from the bulk.

The inter-particle forces such as van der Waals and capillary forces are related to various powder parameters such as the size and shape of the particles, moisture content among others. Since the effect of such parameters on the inter-particle forces can be extremely complex, dustiness cannot yet be reliably predicted using theory and is usually measured (Boundy et al., 2006). Testing for dustiness of a material involves measuring dust particles aerosolized from a specific amount of bulk material, subjected to a precise amount and type of energy for a defined period of time (Plinke et al., 1992). The dustiness testers are lab-scale (bench-top) experimental tests which simulate diverse industrial processes (Hamelmann and Schmidt, 2003).

While several methods exist to measure dustiness, there has been limited efforts in fundamental understanding of the dust generation mechanisms, the physics behind factors affecting the inter-particle binding forces, or the forces acting on the particles due to the mechanical agitation from the testers. Furthermore, no single tester is suitable for measuring dustiness for all scenarios, thus each powder sample may need to be tested several times, often using several test methods to determine its dustiness which can be expensive and time consuming, especially for industries which rely on production and use of small batches of new material, such as the pharmaceutical industry. While new test methods, such as the vortex shaker dustiness tester offers the ability to test fine-scale powders using a fraction of the material used by the traditional test methods, there exist few studies which delves into the theoretical foundations and the overall dust generation process starting from the onset of mechanical stimuli to the bulk material leading to separation and movement of airborne particles.

The time of suspension of a dust particle is directly related to its size, shape and density (Green, 2007; Klippel et al., 2013). Thus, it is important to not only test and report dustiness of

material in their original pristine state but also at their used or *tested* form in order to assess the risks of handling such material throughout their operation cycle. Dust generation from *tested* or *aged* powders are especially important for powder applications which prolong over long durations (weeks to months). Furthermore, the effect of powder and particle properties after such long-term tests are of importance as the effects of dustiness might influence their physical properties, and consequently their mechanical behaviour for the purpose which they were intended to be used in the first place.

In terms of research, the ultimate goal would be the ability to predict dustiness of a hypothetical powder based on its physical characteristics, thus having the ability to engineer a less dusty powder at the inception of the powder lifecycle. But without the understanding of the physical processes and mechanisms involved in dust generation from a bulk sample, this goal may not be realized. Thus, this thesis is aimed at identifying the mechanisms involved in dust generation process, evaluation of key parameters affecting dust generation, and addressing the risks associated with powder applications which prolong over long durations.

This thesis is a synthesis of a doctoral program carried out under the European Union FP7 Marie Curie Actions T-MAPPP Initial Training Network. The network constitutes a consortium of leading academic and industrial partners with an extensive background in the field of granular materials. They provide an important industrial link in the field of granular material used in agriculture, food processing, chemicals, pharmaceuticals and equipment manufacturers. The training network enabled collaborative work with leading powder technology groups across Europe. The research study benefits from the multi-disciplinary expertise of the members in the network, thus adding value to the overall objectives of the thesis and a scope beyond the scientific communities/regimes.

## **1.2 Objectives of the thesis**

The present thesis is motivated from the lack of understanding of the key dust generation mechanisms and theoretical knowledge regarding the effects of bulk and particle parameters influencing the inter-particle forces in bulk, thus their dust generation and emission behaviour. The objectives of the thesis are to:

- Use an extensive literature review, to identify the underlying mechanisms and key material properties affecting dust generation in existing dustiness testers.
- Select and evaluate key material properties using a range of state-of-the art characterization methods.
- Develop a methodology to study the physical mechanisms and interparticle and particle-wall movement in the dust generation process by tracking and analysing a

single particle in the bulk using particle tracking technique (Positron Emission Particle Tracking, PEPT). Furthermore, investigate the effect of bulk and tester parameters on the motion of a dust particle.

- Measure and analyse the differences in generation mechanisms involved over initial (short-term) and long-term dustiness of powders. Additionally, characterize the changes in material properties due to long-term dust generation.
- Compare and evaluate the similarities and differences between dustiness and attrition tests using common industrial-grade catalysts.

As is often the case in particle technology, the topics covered in this thesis are of multi-disciplinary nature and delve into the fields of powder characterization, bulk handling and processing, powder yielding and flow, aerosol physics and occupational hygiene. Ignorance of the symbiotic nature of the problems may lead to increase in risk to worker's health and safety, loss of valuable resources and ultimately, inefficient industrial operations.

### 1.3 Outline of the thesis

The thesis is presented as an anthology of published and submitted articles in peer-reviewed scientific journals and conference proceedings. It follows the basic structure as mentioned above in Section 1.2.

**Chapter 2** introduces the state of the art in the field of dustiness of powders in industrial settings. We review the impact of relevant studies contributing towards understanding of the dust generation mechanism, role of powder parameters and the attempted empirical and numerical modelling techniques used to predict dustiness.

**Chapter 3** evaluates the influence of particle size and distribution on powder properties such as bulk cohesion and flowability (Section 3.1) and dustiness (Section 3.2) using calcium carbonate powders.

**Chapter 4** introduces and validates the statistical methodology developed to study the behaviour of a single traced particle in a bulk agitated by a vortex shaker (Section 4.1 Article (published in Powder Technology, 2017)). Furthermore, the methodology is used to study the influence of powder and tester parameters on the motion of a traced particle in the bulk (Section 4.2).

**Chapter 5** discusses the role of long-term dustiness tests to analyse the dust generation from powder processes prolonging over long durations using two case studies.

One using common abrasive particles such as the silicon carbide powders used in continuous circulation in solar thermal application (Section 5.1) while the other using catalysts used in automotive, petroleum and iron & steel industry (Section 5.2). It also explores the mechanism of dust generation through attrition of particles and compares the similarities and differences between a lab-scale dustiness test and a pilot-scale attrition test.

**Chapter 6** summarizes the key results and conclusions drawn from the previous section focussing on the meeting the objectives of the thesis (as mentioned in Section 1.2).

**Chapter 7** recommends possible improvements in powder characterization tests, dustiness testing and proposes approach towards developing analytical and numerical models to predict dustiness of powders.

## 1.4 References

- Bickis, Ugis. "Hazard prevention and control in the work environment: airborne dust." *World Health* 13 (1998): 16.
- Boundy, Maryanne, David Leith, and Thomas Polton. "Method to evaluate the dustiness of pharmaceutical powders." *The Annals of occupational hygiene* 50.5 (2006): 453-458.
- Eckhoff, R. K. "Current status and expected future trends in dust explosion research." *Journal of loss prevention in the process industries* 18.4-6 (2005): 225-237.
- Green, Don W. "Perry's chemical engineering handbook." *McGrawHill Professional* (2007): 2-83.
- Hamelmann, Frank, and Eberhard Schmidt. "Methods of estimating the dustiness of industrial powders—a review." *KONA Powder and Particle Journal* 21 (2003): 7-18.
- International Organization for Standardization. ISO 4225: Air quality - General aspects - Vocabulary 1994.
- Iossifova Y, Bailey R, Wood J, Kreiss K. "Concurrent silicosis and pulmonary mycosis at death." *Emerging infectious diseases* 16.2 (2010): 318.
- IUPAC, 1990, "Glossary of atmospheric chemistry terms. International Union of Pure and Applied Chemistry, Applied Chemistry Division, Commission on Atmospheric Chemistry." *Pure and Applied Chemistry* 62.11 (1990): 2167–2219.
- Klippel, Alexander, Marc Scheid, and Ulrich Krause. "Investigations into the influence of dustiness on dust explosions." *Journal of Loss Prevention in the Process Industries* 26.6 (2013): 1616-1626.
- Levy, Avi, and Christopher J. Kalman, eds. *Handbook of conveying and handling of particulate solids*. Vol. 10. Elsevier, 2001.
- Maizlish, Neil A., ed. *Workplace health surveillance: an action-oriented approach*. Oxford University Press, 2000.
- Nedderman, Ronald Midgley. *Statics and kinematics of granular materials*. Cambridge University Press, 2005.
- Plinke, Marc AE, Ralf Maus, and David Leith. "Experimental examination of factors that affect dust generation by using Heubach and MRI testers." *American Industrial Hygiene Association Journal* 53.5 (1992): 325-330.
- Richard, P., Nicodemi, M., Delannay, R., Ribiere, P., & Bideau, D. (2005). Slow relaxation and compaction of granular systems. *Nature materials*, 4(2), 121.
- Terentjev, Eugene Michael, and David A. Weitz, eds. *The Oxford handbook of soft condensed matter*. Oxford Handbooks, 2015.

## 2 State of the Art

### 2.0 Overview

The chapter aims at summarizing the most fundamental knowledge with respect to the measurement and prediction of dust generation from the handling of powders in an occupational setting. The shortcomings of not fully understanding the physical mechanisms of dust generation and the parameters that affect inter-particle forces limit the theoretical understanding and the ability to predict dustiness of powders. Thus, dustiness studies are characterised by a very large number of experimental articles in comparison to the limited amount of theoretical and modelling work.

Section 2.1 consists of the article titled “Towards a theoretical understanding of dustiness”, which reviews and summarizes literature related to the dust generation mechanisms (Section 2.1.4), and the powder parameters which affect the inter-particle interactions and dustiness (Section 2.1.5). Furthermore, a review of empirical and numerical models to predict powder dustiness is presented (Section 2.1.6).

While experimental and numerical studies have progressed significantly in the field of powder handling and processing, tackling challenges such as bridging, caking, segregation etc., there has been relatively fewer advances made in the field of dust generation due to the handling of powders in industries. While dust measurement techniques have evolved over the years, the generation mechanisms and the underlying physics involved in dust release is not fully understood inhibiting the development of predictive techniques based on material and process parameters.

The major challenges related to studying powder dustiness from the handling of bulk solids are identified in this chapter, which includes:

- Lack of understanding of the underlying physical mechanisms and complex interplay of inter-particle forces limiting the theoretical understanding of the dust generation from bulk solids.
- Overemphasis on comparing dustiness levels of different testers, but relatively limited studies understanding the physical behaviour of powders in testers at the bulk and particle (micro-) scales.

- Very few studies analysing the influence of powder properties (such as the PSD, shape, cohesion/flowability etc.) on dustiness whereas, that might aid in comparing the key parameters influencing dust generation powders and understanding generation mechanisms.
- The time-scale of dustiness test studies traditionally spans over few seconds to minutes, which may not be representative of dust generation from powders over long durations such as weeks or months. Furthermore, there are few studies related to the role of attrition mechanism in dust generation and its effect on bulk properties and eventually, further dust emissions.
- There is a lack of detailed studies related to relatively new dustiness testers (such as the vortex shaker) which can potentially reduce the cost and risks involved with powder testing compared to the standardized testers.
- With no fundamental understanding of the particle motion (trajectory) inside the testers, the conventional methods of dustiness testing are inadequate to analyse inter-particle interactions within the testers and their effect on dust generation.

Following the state of the art (Chapter 2), certain key parameters were identified and their role in powder dustiness are studied in detail in Chapters 3 to 5.

- Chapter 3: Characterization of bulk cohesion and flowability, Effect of particle size and size distribution
- Chapter 4: Effect of particle size, tester speed, sample mass and air flow on the particle motion (trajectory).
- Chapter 5: Effect of particle material, shape, size and attrition behaviour on dustiness.

## 2.1 Article (submitted to Granular Matter T-MAPPP special issue, March 2018)

### Towards a theoretical understanding of dustiness

Somik Chakravarty<sup>1</sup>, Marc Fischer<sup>1,2</sup>, Olivier Le Bihan<sup>2</sup> and Martin Morgeneyer<sup>1</sup>

<sup>1</sup> *Laboratoire Transformations Intégrées de la Matière Renouvelable (TIMR), Université de Technologie de Compiègne (UTC) Sorbonne Universités, France*

<sup>2</sup> *Institut National de l'Environnement Industriel et des Risques (INERIS), NOVA/CARA/DRC/INERIS, Parc Technologique Alata, BP2, F-60550 Verneuil-En-Halatte, France*

#### 2.1.1 Abstract

While there are plenty of experimental studies pertaining to the dust generation from and dustiness of powders, few of them aim at reaching a theoretical understanding of the phenomena. In the present article, the literature on dustiness has been systematically reviewed with respect to its contribution to a better comprehension of the processes involved. The majority of industrial raw materials exist in the form of dry powders. Due to the complex interplay of multiple parameters, a theoretical understanding of dust generation processes is not trivial and presently relies on experimental studies using bench-top testers called dustiness testers. Given the existence of several reviews about dustiness testers, we limited ourselves to the presentation of the drop test and the rotating drum and a relatively new tester, the vortex shaker. We reviewed parametric studies related to sample mass, particle size and particle size distribution, moisture content, bulk density, particle shape, temporal evolution, attrition strength, flowability, and cohesion. Approaches to modelling dustiness have been systematically reviewed. The simplest and most straightforward one consists of defining the dust emission as a result of empirical terms describing the ratio between the cohesion and separation forces. Good results could be reached through that approach but its simplistic assumptions may limit its validity to narrow ranges of conditions the parameters must be adapted to. To reach a more systematic understanding, numerical modelling methods such as CFD (Computational Fluid Dynamics) and DEM (Discrete Element Method) must be considered. Their combination is currently the most complete approach but it is computationally very demanding. In order to make progress in theoretical dustiness studies, both the simplified and the numerical modelling approaches should be followed.



## 2.1.2 Introduction

Dusts are solid particles, which are either already airborne or may become airborne, depending on their origin, physical characteristics and ambient conditions [1]. The maximum size of such dust particles is arbitrarily defined, usually based on the material and the industrial application. While the World Health Organisation defines its size as close to 100  $\mu\text{m}$  [1], it is close to 75  $\mu\text{m}$  according to the International Organization for Standardization (ISO 4225, 2016) [2]. Klippel et al. mentioned the elastic nature of the particle sizes usually classified as dust [3]. About 90% of dust emissions in an industrial environment are a consequence of the storage and handling of bulk solids [4]. The nature and magnitude of dust generation depends on the specific process and the material [1, 5]. These processes include some of the most common industrial operations, ranging from mining and quarrying to mixing and coating and practically any process which involves the handling of bulk solids [1].

Airborne dust particles are of particular concern in a working environment primarily because the exposure to such particles has been associated with occupational diseases such as byssinosis (caused by the inhalation of asbestos, silica and cotton dust), silicosis, the bakers flour aversion, and pneumoconiosis (commonly related to the inhalation of asbestos fibres, coal mine dust, or crystalline silica dust) [6, 7]. There are also concerns regarding systematic intoxications, such as lead poisoning, usually at higher dust concentrations. Furthermore, diseases such as cancer, asthma, allergic alveolitis and irritation can take place at much lower dust concentrations [1]. Moreover, dust generation in industries can lead to material loss, contamination of products and equipment resulting in significant increases in the cost of smooth plant operations with low downtimes [8]. In addition to that, dust laden atmospheres can lead to dangerous explosions [3]. The study of dust generation in occupational settings is thus indispensable to control and possibly reduce dust concentrations stemming from different industrial processes. The size of a dust particle is directly related to its ability to penetrate and stay in lungs. The usually irregularly shaped dust particles are expressed in terms of an idealised spherical particle with a density of 1000  $\text{kg}/\text{m}^3$  with the same settling velocity as the particle of interest, known as the aerodynamic diameter. The smaller the aerodynamic diameter is, the greater the probability of its penetrating deep into the lungs is. For these reasons, the emitted dust needs to be sampled according to biologically relevant aerosol sampling conventions [9]. The three dust size fractions include the inhalable fraction (mouth/nose), the thoracic fraction

(respiratory tract below the larynx) and the respirable fraction (the alveolar region in the lung) [10, 11]. The size fractions depend on the aerodynamic diameters of the dust particles and are classified based on the dust median particle size with 100  $\mu\text{m}$  for inhalable, 10  $\mu\text{m}$  for thoracic, and 4  $\mu\text{m}$  for respirable fractions, for a sampling efficiency of 50%.

Ultra-fine and nano-scale particles with sizes less than 100 nm show a wide array of favourable properties such as a large surface area relative to their size and the quantum effects due to the concentrations of atoms at their surfaces [15]. These unique properties give rise to their high surface reactivity and enhanced mechanical, chemical, optical, and electrical properties when compared to materials made up of larger particles [16]. Thus, they are increasingly being manufactured and used in a wide array of applications such as pigment particles in paints, micro-carriers in biotechnology [12], or the production of improved catalysts [13, 14].

Even though the production and processing of fine and nano-scale particles are rapidly increasing, challenges associated with their unpredictable flow behaviour pose major risks in an industrial environment such as failure of silos or worker exposure to fine particles during powder handling or even dust explosion, which can lead to significant losses of human life and resources [15]. With the ever higher contribution of nanomaterials to industry, there is a critical need for risk assessments of ultra-fine nanopowders in industrial workplaces. According to a survey conducted by Plitzko et al. in Germany in 2007, 21% of the chemical companies involved used nanoscale materials in their production cycle [17]. It was also reported that the industrial production and use of nanomaterials pose a exposure risk, especially for workers dealing with the manual handling, bagging and transfer of these materials [18, 19]. Although exposure in the form of inhalation is acknowledged to be the major source, dermal, ocular and ingestion routes can also be probable routes of exposure [20]. Due to the novelty of such materials and the rapid rate of their development, testing them using conventional techniques may be inadvisable due to differences in their material properties, safety concerns regarding their exposure and explosivity and the low availability of test samples owing to their cost when compared to larger-scale powders.

The ability of a material to generate airborne dust particles or dust clouds due to a mechanical stimulus is known as its dustiness [3, 21]. The dustiness of a material is always a function of the mechanical stresses that are conventionally chosen so as to mimic typical industrial conditions. A higher dustiness number for a given bulk material indicates higher chances of being exposed to the suspended particles when handling the material [22-25]. Dustiness has been found to be important for dust explosion protection as flammable dust particles in sufficient concentrations can be explosive [1]. Thus results from dustiness studies

can aid in analysing and optimising risk-prone zones and designing and adapting venting or confinement systems. While there are some dustiness test studies which showed positive correlations with exposure levels ([26] using a rotating drum with insulation materials, [27, 28] using biofuels), the majority of studies do not show a clear relationship between dustiness and workplace exposure levels [24, 25, 29-32]. The differences may stem from work practices, equipment maintenance, process leakage, or dust emission from external sources [9] or the gentle nature of the used tests and the variability of the external parameters [33].

The dustiness of a material is traditionally quantified by using a gravimetric measure of the dust emitted from a unit mass of sample for the test duration [21]. While the method allows one to obtain a non-dimensional value of the dust level that can be drawn upon for comparisons, it is also strongly interesting to know the *dust concentration by number* in fields such as clean room monitoring or nanomaterial exposure protection, where the nanoscaled dust may not weigh too much but can be potentially more harmful if inhaled due to the small particle sizes.

Dustiness prevention by means of dustiness estimation even before a new method is installed or a material is changed is the objective of process engineers [34-36]. Without any other influences, airborne particles deposit due to gravity but the duration of total deposition and the easiness of re-suspension depend a lot on the specific dust sample and the boundary conditions. In this review, dustiness is always related to the measured inhalable fraction and the associated health risks.

Dustiness is not a physical property of a material and it depends on several parameters including material properties (such as particle size distribution, density and the adhesive forces binding the particles) [3, 37] and process-specific parameters and operational time-scales [5]. Because of such a complexity, the dustiness of a bulk material cannot yet be reliably predicted theoretically and needs to be measured using lab-scale dustiness testers [21]. Thus, most of the experimental studies using lab-scale dustiness testers aim to generate, emit and sample the dust produced by a known quantity of a material. Quantitative information regarding the dust concentration and particle size distribution of the released dust aids in determining the risks of exposure whilst handling different powders.

Dust generation, on a fundamental level, is all about the separation of particles which are adhered to the bulk due to some attractive forces, which may be gravitational or surface forces (operating across contact surfaces between the particles, such as van der Waals forces) [9, 37]. Plinke et al. suggested that in order to predict and minimise dust generation, it is necessary to determine the binding forces which hold the particles together [38]. Dustiness is related to the interplay of the binding forces and the method used to separate the particles in the form of dust. While assessing the dust liberation mechanisms of limestone during quarry operations

Petavratzi et. al. [39] suggested that dustiness is a two-stage process, starting with dust generation and followed by dust emission. The mechanisms involved in dust generation from minerals include impaction, abrasion or attrition forces which may either act independently or in combination with one another. Plinke et al. stated that although there exists several methods for estimating the dustiness of a material, there is a lack of theoretical investigations into the interparticle forces and the processes that act as separation forces [38]. Indeed, even in 2018, there appears to be much more articles entirely devoted to dustiness experiments than to dustiness theories and modelling. This stands in stark contrast to fields such as combustion research [40], atmospheric dispersion [41] or hydrology [42] where the industry and regulatory agencies can draw on reliable predictions from models largely based on theory. The purpose of this article is to improve that situation by providing researchers and practitioners alike with an easily accessible overview of dustiness studies contributing to a better theoretical understanding of the phenomenon of dustiness.

It is organised as follows. In Section 2, dustiness tests are presented. We do not go into the details of the traditional testers, as this has already been abundantly done elsewhere. In Section 3, mechanisms of dust generation are presented and section 4 reviews the parametric studies on powder dustiness. Section 5 describes the modelling efforts made in the field of powder dustiness. In Section 6, the conclusion and the outlook are given.

### **2.1.3 Dustiness tests**

A dustiness tester provides a mechanical stimulus of a certain kind and magnitude to a known amount of test sample for a definite amount of time. The amount of energy is selected in such a way that it is sufficient to overcome the adhesive forces between the particles of the bulk solids, which, in turn, emit dust particles that can be quantified in the air [9, 43, 44]. Powders usually consist of individual primary particles which are aggregated (sintered or tightly bonded) and then further agglomerated [20]. While the agglomerates dissociate easily when subjected to some force, it takes a significant amount of mechanical energy to disintegrate aggregates into primary particles. Whilst conducting a dustiness test, care should be taken not to provide an unnecessarily high amount of mechanical energy so that the primary particles are not fractured too much. The dustiness test of a bulk solid should aim at releasing and quantifying only the loosely bound primary particles and agglomerates. It is important to make sure that the characteristics of a typical bulk solid process such as mixing, coating, pneumatic drying, bagging, etc. are well represented as the amounts and types of energy imposed on the bulk [45]. However, the test should be conducted in a controlled environment with few disturbances stemming from external factors.

There are a wide range of dustiness testers including the air jet dispersion [33, 46] and gas fluidisation systems [47, 48], the drop test [29, 49], and the rotating drum [26, 50, 51]. Among them, the latter two are the standard testers for measuring the dustiness of bulk materials according to EN 15051 [52]. However these testers need large amounts of powders (35 cm<sup>3</sup> or 500 g) [53, 54] and can give disparate results for different materials [21, 23]. Reviews by [3, 21, 34] trace the development of dustiness testers over time and the efforts towards a standardisation of test

### ***2.1.1 Standardized testers: Rotating drum and Powder drop test***

Efforts to standardise the testing protocol gave birth to the norm EN 15051: "*Workplace atmospheres: measurement of the dustiness of bulk materials*" where the dustiness of the bulk solids is measured using the rotating drum experiment and the particle drop test [52]. In the rotating drum method, a bulk sample is rotated in a drum with internal baffles, so that the substrate angle periodically increases, which results in the powder exceeding its angle of repose and then in an avalanche of particles [51, 68]. The particle drop method involves a granular material being dropped from a given height. The aerosolisation of bulk solids occurs during the interaction of the solid with the air while it is falling and also through the force generated by its impact at the bottom of the falling device [29, 59, 69].

These methods are designed to simulate various industrial processes and are characterised by the conveying of a fairly gentle mechanical agitation to the powder material. As they require large quantities of sample material (higher than 10 g) [20], they can be very expensive for the nanomaterial and pharmaceutical industry. There are also limitations regarding the comparability of the results obtained with these test methods, as pointed out by Pensis et al. [23] and Bach et al. [70].

### ***2.1.2 Vortex shaker***

In addition to the rotating drum and the particle drop test, the vortex shaker (VS) has been gaining prominence as an apparatus for determining the dustiness of bulk solids including nanopowders [53, 57, 71]. The setup of a vortex shaker experiment can be seen in Figure 2.1. Such shakers or mixers are commonly utilised in laboratories all around the world to mix small quantities of liquids or as small reactors [72]. It is made of an electric motor with a drive shaft oriented vertically, which is connected to a rubber cup mounted slightly off-centre. Dust is generated from a small amount (around 2 g) of bulk solid sample contained in a cylindrical glass

tube. As the motor runs, the rubber cup oscillates rapidly in a circular motion which is transmitted to the solid sample within the cylindrical tube. The shaker is able to generate a uniform vortex field with rotational velocities ranging from 500 rpm to 2,500 rpm along the vertical axis. Owing to the centrifugal forces spawned in the vortex shaker setup, the particles in the bulk sample are subjected to the outward centrifugal force acting as a separation force, the vertical gravitational force and attractive surface forces between the particles acting as binding forces. Airborne aerosol particles from the test-tube are carried to the respirable-fraction cyclone (50 % cut point of 4  $\mu\text{m}$ ) by an inlet flow ( $Q_V$ ) of 4.2 L/min. While the cyclone keeps the larger particles from going any further, the respirable aerosol particles pass it and are further diluted through a flow ( $Q_D$ ) of 7.4 L/min of filtered air (HEPA) and split into 3 channels before the measurements and characterisation of the aerosol [73]. The aerosol number concentration  $N_{\text{CPC}}$  over the 4 nm to 3  $\mu\text{m}$  size range is measured through the use of a condensation particle counter (CPC TSI 3775, TSI Inc.). Simultaneously, the aerosol number concentration  $N_{\text{APS}}$  and mass  $M_{\text{APS}}$  over a size range of 0.54  $\mu\text{m}$  to 20  $\mu\text{m}$  are measured through the use of an aerodynamic particle sizer (APS TSI 3321, TSI Inc.). The APS records the particle numbers by their aerodynamic size which is based on the times of flight of individual aerosol particles [45].

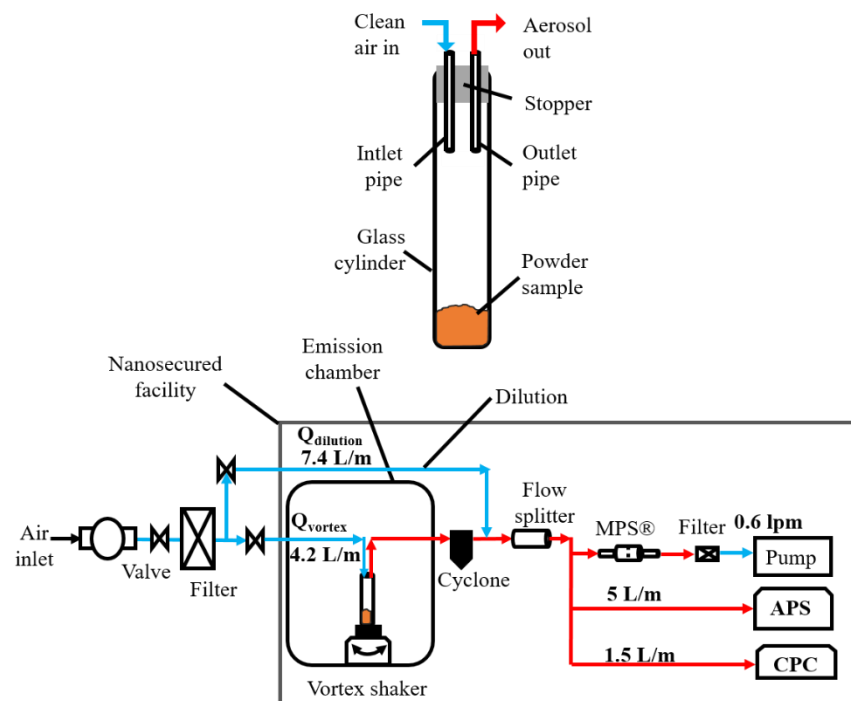


**Figure 2.1:** The vortex shaker experimental setup [109]

Some of the advantages of using a vortex shaker over the other methods include the possibility of conducting the experiment with a reasonably small quantity of material, which can

have a significant effect on the overall cost of the test. They can be used with quantities of sample material as low as 0.197 mg [45], which enables the prudent testing of expensive nano-materials and potent pharmaceutical powders. Ogura et al. [74] reported a correlation between the results of VS dustiness tests and dust exposition values measured at workplaces, thereby emphasising the ability of the vortex shaker to incorporate some of the process features which lead to the aerosolisation of bulk solids in industries. Morgeneyer et al. [53] and Le Bihan et al. [45] used the VS method to study the dust generation of micron-sized alumina particles and nanoscale carbon nano-tubes (CNTs) for one hour with sample masses as small as 0.5 g, respectively. Morgeneyer et al. [53] studied the minimum levels of bulk masses and the optimum vortex speeds (between 1000 rpm and 2500 rpm) necessary to aerosolise micron-sized alumina particles. They reported a sample mass of 2 g and a vortex speed of 1,500 rpm 1,800 rpm as suitable parameters for attaining a stable aerosolisation of alumina particles without impacting the particle size distribution (PSD) of the powder. The experimental setup of the vortex shaker is optimised to test potentially toxic nanopowders and pharmacologically active samples, without the user being exposed to such hazardous materials.

#### **2.1.4 Mechanisms of dust generation**

During the handling and conveying of bulk solids, dust is generated primarily through three mechanisms [8], namely free fall forced elevation and attrition (See Figure 2.2). Free fall consists of the dropping of powders from one height to a lower one. One common example in the industry is the powder fall at the transfer points of mechanical conveyors [75]. The stresses applied to the bulk at the transfer points can release its native bulk powder and remains suspended in the air. Forced elevation is commonly utilised for the pneumatic conveying or the re-suspension of settled dust particles [76]. During free fall, the aerodynamic stresses generated through the high relative velocity of the fluid and the pressure gradient can lead to the separation and suspension of dust particles from the bulk [77]. Lastly, dust generation from attrition takes place when the individual particles in the bulk material interact (grind and collide) with each other to produce fine-scale particles which can be aerosolized as dust [47, 78, 79]. In addition to the material properties and kinetic energy of the system, the time-scale of the operation also influences the production and generation of dust through attrition [39].

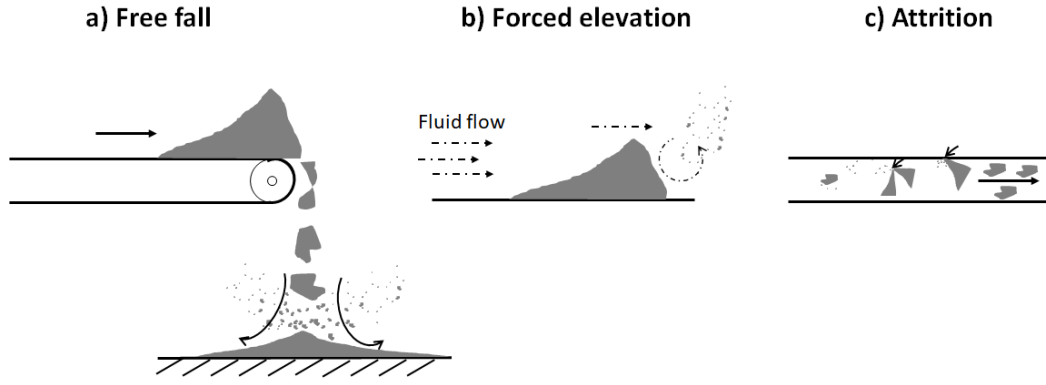


**Figure 2.2:** Dust generation mechanisms: a) Free fall; b) Forced elevation; c) Attrition.

Dust generation, on a fundamental level, is all about the interplay between separation forces and some attractive binding forces which bind the individual particles together in the bulk. The separation forces stem from the mechanical agitation of the bulk, which is usually applied during handling and conveying operations, whereas the binding forces mainly consist of the van der Waals forces, electrostatic forces, capillary forces (under wet conditions) and solid bridges (after drying) [38]. For dry materials, van der Waals and electrostatic forces are the two most important binding forces. While electrostatic effects are often significant for powder handling operations, the van der Waals forces often dominate them [80]. Van der Waals forces are the collective forces resulting from the Keesom interaction (permanent-permanent dipoles), Debye force (permanent-induced dipole) and London dispersion force (induced-induced dipole interaction) [81]. Intermolecular vdW forces decay with the molecular separation  $a$ , but when the pair potentials are integrated over macroscopic objects such as 2 spherical particles, the resulting force decays with  $a^{-2}$  [82] according to Equation 2.1.

$$F_{vdw} = \frac{AR}{12a^2} \quad (\text{Eq. 2.1})$$

$R$  is the radius of the sphere and  $A$  is the Hamaker constant (based on material properties). Surface roughness also plays an important role in the van der Waals interaction between non-ideal bodies. A smoother surface is usually associated with a larger contact area whereas the asperities in the bodies/particles can act as an obstruction between atoms and molecules on the surface of the particles. The vdW forces between 2 spherical particles (of diameter  $R$ ) with asperities of size ( $r_{asp}$ ) is given by Castellanos [83] as shown in Eq. 2.2:

$$F_{vdw} = \frac{AR^3}{12(a+r_{asp})^2 \cdot (a+R_{asp}+R)^2} \quad (\text{Eq. 2.2})$$



The maximum range of the vdW interactions is in the order of 100 nm, which is much larger than the short range of the chemical bonds which are generally smaller than 3 nm [84]. The vdW forces, are in turn, more short-ranged than the Coulombic or electrostatic forces.

Electrostatic forces involve the transfer of electrons or ions between the surfaces of two or more bodies [81]. In bulk solids, the particles can be electrostatically charged due to frictional contacts depending on their conduction/insulation properties. This phenomenon is known as tribo-charging [85]. Since electrostatic forces are related to material resistivity, the effects are more prominent under dry and cold ambient conditions [8]. They are given by Eq. 2.3.

$$F_E = \frac{-Q_A Q_B}{4\pi\epsilon_r\epsilon_0 a^2} \quad (\text{Eq. 2.3})$$

$Q_A$  and  $Q_B$  are the total charges on two particles (A and B),  $a$  is the distance between their centres.  $\epsilon_0$  and  $\epsilon_r$  are the permittivity of free space and the relative permittivity, respectively. For dry fine neutral particles, it is generally assumed that electrostatic force is negligible compared to the van der Waals forces [86-88].

Capillary forces are attractive forces due to the surface tension and bonding between a liquid film and a solid particle surface [89]. The layer of liquid forms a liquid bridge between solid particles. The magnitude of the force depends on the amount of free liquid and its properties, particularly surface tension and viscosity [82]. Compared to the vdW and electrostatic forces, the capillary forces are negligible for dry powders but may be very important in humid environments [83, 90]. The total capillary force  $F_c$  for 2 identical spherical particles is given by Eq. 2.4 [91].

$$F_c = 2\pi R\gamma \left[ \frac{2t^2 - t + 1}{(1 + t^2)^2} \right] \quad (\text{Eq. 2.4})$$

$R$  is particle radius,  $\gamma$  is the liquid surface tension and  $t = \tan(\beta/2)$  and  $\beta$  is the half-angle of the liquid bridge.

The variation in the magnitude of the three interparticle forces including the van der Waal, electrostatic, capillary forces and the gravitational force based on theoretical calculations for particle diameters comprised between 1  $\mu\text{m}$  and 1000  $\mu\text{m}$  is shown in Figure 2.3.

The interplay of these binding forces and of separation forces can be seen in parametric dust emission studies (treated in the next section) and in modelling works (reviewed in Section 2.5).

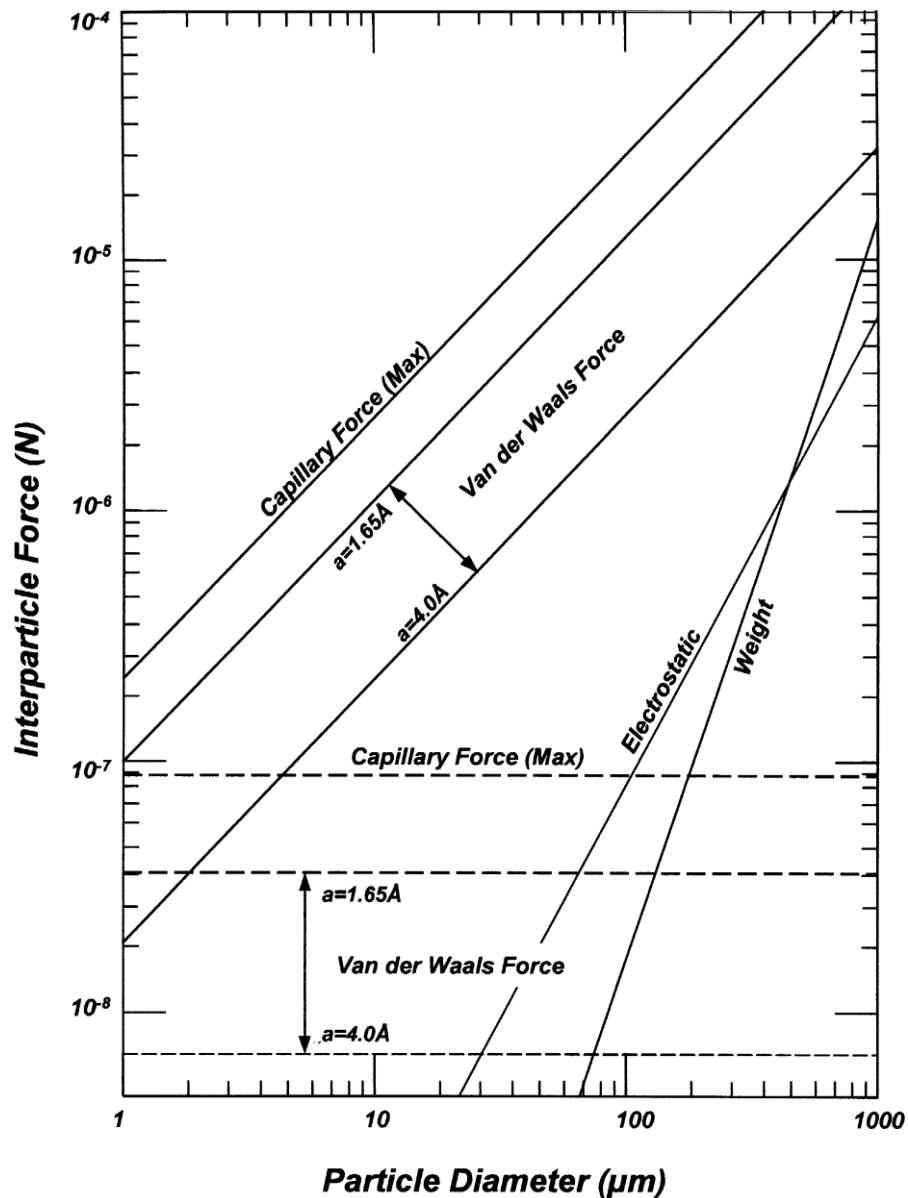


**Figure 2.3:** Comparison of the magnitude of interparticle forces (dashed lines indicate asperity-to-plane contact). Theoretical interparticle forces for single-point contact between equal spheres (in air), with particle weight plotted for comparison. [91]. Van der Waals:  $A = 6.5 \times 10^{-20}\text{J}$  (quartz), values presented for interparticle separations of  $1.65 \text{\AA}$  and  $4.0 \text{\AA}$ . The dashed lines assume asperity-to-plane contact with asperity radius  $0.1 \text{ mm}$ . Capillary:  $\gamma = 72.8 \times 10^{-2} \text{ Nm}^{-1}$  (water). Values are maximum ( $\beta \rightarrow 0$ ). Dashed lines indicate asperity contact as above. Electrostatic: maximum force (opposite sign).  $\epsilon_r = 1$ ;  $\epsilon_0 = 8.9 \times 10^{-12} \text{ C}^2 \text{ N}^{-1} \text{ m}^{-2}$ . Charge density =  $10 \mu\text{C m}^{-2}$ . Weight:  $\rho_p = 3 \times 10^3 \text{ kg m}^{-3}$ . Image taken from Seville et al. [91].

### 2.1.5 Parametric studies on powder dustiness

Since powder dustiness is not a physical property of a material, it depends on several variables including the measurement method and the material properties [3]. Section 2 dealt with the former, and in this section we discuss the studies aimed at evaluating the effects of material properties on powder dustiness. Predicting the dustiness level of a bulk solid by simply knowing its physical properties and the forces acting on it is of great importance to the control of dust emissions in the industrial world. Although most of the literature in dustiness studies mentions the importance of knowing the fundamental processes which take place before the bulk solid emits dust, there is only a very limited knowledge on how and why certain particles are separated and aerosolised from their bulk state under the influence of an external force [92]. There exists a plethora of dustiness testers currently available in academic and industrial research centres. They are based on different handling processes and measurement techniques, thus resulting in scattered results. As a consequence, analysing the influence of parameters on dust emissions is necessary to understand the underlying physics behind the aerosolisation of particles out of their bulk state. Relatively few studies aimed at assessing the influence of potential powder parameters or physical properties on dustiness were undertaken. Some of these physical characteristics and their effects on powder dustiness are discussed in this section.

Since dustiness depends on powder parameters and boundary (tester and ambient) conditions, studying the effect of each of these parameters without the influence from other variables may not be possible. Thus in our review of material parameters affecting dust generation we classify the parameters based on the testers used. We also limit ourselves to the two standardised methods and a relatively new tester in the form of the vortex shaker method. To the best of our knowledge, the review by [34] has been the only comprehensive review of dustiness studies evaluating the effects of powder physical properties such as particle size distribution (PSD), particle shape, powder mass, bulk and particle true density, flowability, cohesion, and moisture content on powder dustiness.

#### 2.1.5.1 *Sample mass*

The sample mass may have an effect on the dust generation levels for both the drop tests and the rotating drum as an increase in sample mass can be interpreted as an increased fraction of aerosolisable fine particles.

In the case of the drop test, Davies et al. [93] studied the dust generation behaviour of chalk powders (volume median diameter = 13  $\mu\text{m}$ ) for a 1-meter drop height which showed an

initial increase in dustiness as the sample mass increased, followed by a sharp decline with an increasing sample mass. Using a rotating drum tester, Lyons & Mark [94] and Breum [68] showed that for most of the tested powders, dustiness is positively correlated with the sample mass, however results by Heitbrink [25] and Pujara [95] found that increasing the sample mass leads to an increase in dust release up to a certain mass, beyond which there is a decrease in the dust generated. Lyons and Mark [94] found that there is a slight increase in absolute dust generation and dust index from alumina powders, with an increase in sample mass between 25 and 200 g. Furthermore, they found the dustiness levels to increase significantly beyond 200 g. On the other hand, Heitbrink [25] found an increase in dustiness index for limestone powders using 10g to 80g, but a decrease in dustiness index for an increase in sample mass from 80 g to 160 g.

The initial increase in dustiness with the sample mass could be explained through the higher number of fines present in the bulk while the final decrease in dustiness could stem from a stronger cohesive bonds between the particles present in bulk.

In the case of the vortex shaker tester, Morgeneyer et. al. [53] showed that the dustiness of alumina particles measured (in  $\text{mg}/\text{cm}^3$ ) is characterised by a quadratic relationship with the sample bulk mass (0.5 g to 4 g) for vortex speeds of 1500 and 1250 rpm, while there was barely any dust generated at 1000 rpm for masses between 0.5 g and 4 g.

#### ***2.1.5.2 Particle size and Particle size distribution***

The particle size and size distribution have a great impact on powder dustiness as they are the governing factor influencing the motion of particles in the fluid [34]. The works of Cowherd et al. [29], Plinke et al. [37, 38, 59], Pensis et al. [23] showed a high correlation between the quantity of dust generated and the PSD of the dust emitted.

Plinke et al. [59] conducted tests with a rotating drum and a MRI tester (bench scale gravity dispersion) with silicon carbide and alumina powders. They showed a decrease in the total dust generation rate with an increase in the median particle size of the bulk from 3  $\mu\text{m}$  to 25  $\mu\text{m}$ . Blending a small portion of fines into the coarse bulk led to as much dust emission as for materials comprised entirely of small fines. On the other hand, the *size-specific* dust generation rate increased with increasing particle diameters. Plinke et al. suggested that the separation forces such as the impaction increase with the particle size by an order of 3, whereas the binding forces such as the van der Waal and capillary forces increase linearly with the particle size [59]. Thus, the separation forces increase more rapidly with the particle size than the binding forces, thereby resulting in higher dustiness.

Plinke et al. [37, 38] studied the effects of particle size (distribution) during his parametric study of dust generated from 4 different powders (titanium dioxide, limestone, glass beads and lactose) using a drop test. They suggested that for dry powders, interparticle binding forces responsible for cohesion decrease linearly with particle diameters and that materials with high cohesion show lower dust emissions. Furthermore, based on their results, reducing the amount of the respirable particles with sizes inferior to 5  $\mu\text{m}$  by 50% resulted in a decrease of 35% in the mass concentration of the particles emitted as dust with the same particle size. Thus, he suggested that decreasing the fraction of respirable particles in the original bulk material is not a particularly effective method for reducing dustiness.

Pensis et al. [23] compared the dustiness of 9 industrial minerals using the EN 15051 testers; the continuous drop method and the rotating drum method. They found that both the inhalable and respirable dust fractions measured by the two testers show a strong correlation with  $\log(d_{90}/d_{10})$ , representing the width of the powder PSD. The dustiness mass fraction shows an increase with  $\log(d_{90}/d_{10})$  for powders characterised by  $d_{50} > 100 \mu\text{m}$ , however the dustiness of finer materials characterised by  $d_{50}$  (in  $\mu\text{m}$ ) shows no variation with  $\log(d_{90}/d_{10})$ .

Chakravarty et al. [71] used a vortex shaker setup to study the influence of the grain size distribution on respirable dustiness for 8 calcium carbonate powders whose median diameters ranged from 2 to 136  $\mu\text{m}$ . They found that the dustiness of the cohesive powders ( $d_{50}$  smaller than 10  $\mu\text{m}$ ) shows a correlation with the median particle size ( $d_{50}$ ). The smaller the primary particles are, the more cohesive the powder and the smallest the dust emissions are, as can be seen in Figure 2.4. Bi-modal powders with similar flowability but different  $d_{50}$  are characterised by similar dustiness levels that depend on the fraction of particles present in the first mode (in the respirable fraction). They had only one sample where  $d_{50}$  is greater than 100  $\mu\text{m}$ , which was found to be the least dusty powder.

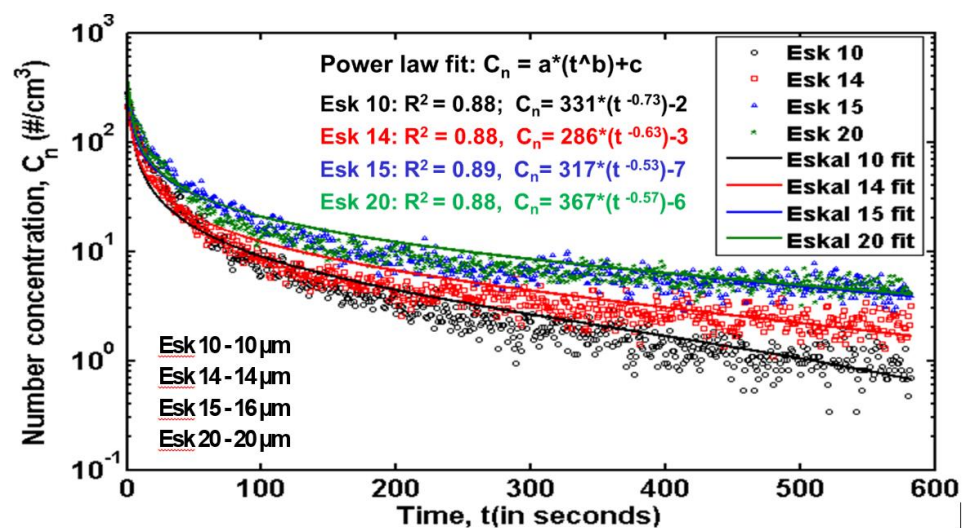


Figure 2.4: Effects of the median size on dustiness [71]

### **2.1.5.3 Moisture content**

The effect of the moisture content on powder dustiness has been studied using different powders and dustiness testers such as the fluidised bed [48, 96], the drop test by [29, 37, 59], and the rotating drum [59, 95, 97-100]. For most of the studies, an increase in the moisture content increases particle cohesion, resulting in lower dust generation while there are some studies where moisture content in the powders did not reduce dustiness [97].

An increase in moisture leads to the formation of liquid films on the surface of the particles [101] which do not react with water. The liquid bridges formed at the particle contact points are stronger than the van der Waals and electrostatic binding forces and they can considerably reduce dustiness. Plinke et al. [59] test with alumina powders showed no change in particle size distribution corresponding to a slight increase in moisture content, whereas Farrugia et al. [99] saw a decrease in small particle sizes for carbon particles. Plinke et al. [37] tested the influence of moisture on dustiness from limestone, titanium dioxide, glass beads, and lactose powders using a continuous drop method. They increased the moisture content of the powders between 1% and 10% of the initial sample mass and reduced it to a certain level by drying the powders in an oven for 24 hours. For water-insoluble materials including limestone, titanium dioxide and glass beads, the dustiness levels increased with decreasing moisture, but lactose was found to generate less dust upon drying whilst the others did not. Plinke et al. [37] suggested that the drying of moisture-exposed powders make the liquid bridges evaporate, thereby reducing the binding forces between the particles, but for water-soluble materials such as lactose the evaporation of liquid bridges due to drying leads to the formation of solid bridges (as seen under the SEM micrographs), thereby significantly increasing the bonding forces. The influence of PSD coupled with humidity on powder dustiness has not been studied yet and may have an influence on the cumulative cohesive forces spawning from van der Waals and capillary forces.

### **2.1.5.4 Bulk density**

Jensen et al. [102] tested loose and compacted samples of bentonite and organoclay powder to show the influence of the compaction of powders (increase in bulk density) on dustiness kinetics (the evolution of dust generation) and the dustiness levels. They used a combined single drop - rotating drum tester to evaluate the dustiness of the loose and compacted powders based on mass dustiness, dust particle number concentrations, the temporal evolution of dust generation and dust size distributions. The dustiness tests showed intermediate dustiness

indices (1,077-2,077 mg/kg of powder) for the bentonite (loose and compacted samples) and the organoclay (loose sample), whereas the compacted organoclay sample shows a high-level dustiness index (3,487 mg/kg). The tri-modal size distributions by particle number of the dust were not too different for the loose and compacted samples. Regarding the dustiness kinetics, Jensen et al. [102] observed 4 different particle volume generation rate profiles as a function of time: a brief initial burst followed by a rapid decrease (as observed by them in most of their previous studies), an initial increase followed by a slow decrease (for the loose nano-clay and bentonite), a constant generation rate (for the compacted nano-clay), and a slowly rising generation rate (for the compacted bentonite). The former three were also observed by Schneider & Jensen [50]. The different profiles and their levels of dustiness can be important indicators of the mechanisms involved in powder dustiness and may be useful in accurate dust exposure assessment in specific processes [102]. Thus, depending on the specific use of the powders, it may change the risk of exposure.

#### ***2.1.5.5 Particle shape***

Particle shape and surface morphology are known to have an effect on powder bulk properties [103]. This may be partly caused by the fact that the particle-fluid interactions are different for spherical and non-spherical particles [104]. Consequently, the effects of particle shape and morphology on powder dustiness need to be addressed.

Janhunen et al. [97] studied the dustiness of 39 chemical products using a rotating drum. They found that spherical particles are the least dusty followed by rectangular particles with no irregularities which had low dustiness. Samples with irregular and angular particles had the highest level of dust emission. Authier-Martin [105] studied the dustiness of alumina powders stemming from 13 different sources and concluded that there is no clear correlation between the powder bulk properties and their dustiness. A visual study of the micrographs obtained from scanning electronic microscopy (SEM) analyses indicated that less dusty alumina powders generate coarser "mosaic type structure" dust particles, whereas the dusty alumina powders generate finer "single crystal shaped" dust particles. There were no SEM analysis for the actual powder samples and no quantitative analysis were performed to establish the hypothesis presented by the authors, i.e., the shape of the dust particle is the critical factor in powder dustiness.

Hjemsted and Schneider [106] used a rotating drum tester to compare the dustiness of 2 copper powders to suggest that particle size, shape and tendency to agglomerate affect their dustiness. The powder sample (consisting of "flaky" particles) showed a dustiness index of

about 2 orders of magnitude higher than the "spherical" particles. The authors suggested that the differences in dustiness may result from higher particle-particle interactions for the "flaky" sample compared to weaker interaction due to lower surface contact for the "spherical" shaped sample.

There were no quantitative shape parameters measured and it is unclear why higher particle-particle interaction would lead to less dustiness.

Olsen et al. [107] studied the effect of morphology on alumina strength and dustiness. They used a Perra dustiness tester and the Malvern PharmaVision equipment to determine the sample dustiness and morphological characteristics, respectively. They found a relatively good correlation ( $R = 0.84$ ) between the number based roundness parameter from the PharmaVision data and the dustiness index from the Perra tester. The results showed that the irregular shape of the larger particles contributes to dustiness whereas the irregularity of the smallest particles contributes to a reduction in dustiness. To explain these contradictory findings, they speculated that the deviation from roundness in the small particles may increase the probability of finding a relatively large surface they can attach to thanks to interparticle interactions. Another possibility is that the small particles may stick to crevices or corners of the much larger particles, thereby resulting in an increase in the physical friction of the particles.

Pujara [108] used an image analysis system to characterise shape factors including aspect ratio, circularity and elongation ratio, roundness, and sphericity for 18 different powder samples. The shape factors, by themselves and also when multiplied by the mean particle sizes, were found not to correlate well with dustiness indices for the powder samples. An empirical shape coefficient,  $K_p$  multiplied by the particle size (in  $\mu\text{m}$ ) showed a negative linear correlation ( $R = 0.91$ ) with dustiness index.

$K_p$  is defined as the product of specific surface area ( $\text{m}^2/\text{g}$ ), true density ( $\text{kg}/\text{m}^3$ ), surface-volume mean diameter (in  $\mu\text{m}$ ) and elongation ratio (ratio of the maximum and minimum diameter of a particle) of the sample.

Chakravarty et al. [109] used the vortex shaker method to test the long-term (6 hours) dust generation from 2 silicon carbide (SiC) powder samples. They characterised particle shape factors by particle number using a microscopic image analysis (Malvern Morphologi G3s). The measured shape factors were the high-sensitivity circularity (roundness parameter), aspect ratio and convexity of individual particles. The dusty SiC samples were characterised by smaller values of both the circularity and aspect ratio than those of the less dusty SiC sample. Furthermore, the particle circularity and aspect ratio were found to increase after the dustiness



test for the dusty sample whereas barely any change was observed for the less dusty powder sample.

#### **2.1.5.6 Flowability**

The flowability of a bulk solid is typically defined as its ability to flow with ease but that definition has been criticised as lacking the depth necessary to capture the essence of the observed phenomena [110]. Instead, it should be thought of as the interaction of physical properties of the powder that affect its flow and the equipment utilised for treating, storing, or processing the material [110]. A bulk solid with higher flowability is usually associated with a friendly handling and flow behaviour whereas a cohesive powder (characterised by a low flowability) goes hand in hand with difficulties related to its handling owing to the higher resistance of the flow. There are various flow properties which play an important role in determining the flowability of bulk solids including:

1. Cohesive Strength [111]
2. Wall Friction [112]
3. Internal Friction [1121, 113]
4. Flow function [110, 112]

There are also relevant flow indicators useful for describing the flow behaviour of bulk solids. They include the permeability, angle of repose (AOR) [114], compressibility (or Carr-index), [115] and bulk density. The AOR is the angle formed between the edges of a cone-shaped pile of granular matter with the horizontal base when it is dispensed of a funnel with specified dimensions under specified test conditions while avoiding pile-slumping. The pile is formed because of the internal friction between the particles.

Results from the angle of repose method correlated poorly with the dustiness index measured using a modified Perra pulverimeter [105,116]. Cowherd et al. [29] used a bench-scale impact-type tester to determine the dustiness of 14 materials only to find poor correlations between the material dustiness and the angle of repose. They speculated that the greater the angle of repose of a material is, the lower its dustiness is since a higher AOR is associated with low flowability. AOR measurements are seldom repeatable and reproducible as they crucially depend on the test setup and the operator's skills [117]. Furthermore, the measurement of AOR for fine cohesive powders can be difficult as they agglomerate easily. Authier-Martin [105] also used a Perra pulverimeter to determine the dustiness index of alumina powders and found them to be "fairly" correlated with the angle of repose ( $R = 0.58$  and  $0.72$  for the minimum and maximum densities, respectively) [105] .

### ***2.1.5.7 Cohesion***

The cohesivity or cohesion of a powder lie in its ability to hold the particles together through interparticle interactions (Van der Waals forces, electrostatic forces, liquid bridges, solid bonds) [92, 118].

Plinke et al. [38] used a rotational shear tester (Peschl) to measure the cohesion or the interparticle binding forces between the particles and found a negative correlation between the cohesion values and dustiness [37]. Plinke et al. [38] found the measured cohesion to be related to the moisture content of the material, its mass, its median diameter and its melting temperature. During a shear test, the bulk sample is subjected to shear forces as the shear cell rotates relatively to the lid and it goes through the stages of pre-shear, shear and failure, thus enabling the evaluation of the yield locus. The shear stress is calculated from the torque required to prevent the lid from rotating. The yield locus for zero normal stress (or the stress necessary to shear the material with no normal stress) is used as the value of cohesion. Since the cohesion values cannot be measured without preconsolidating the bulk sample, the measured values of the consolidated powders may not be representative of the real state of the powders since consolidation can change the interparticle arrangements within the bulk. Furthermore, the cohesion values are extrapolated from the yield loci, which may not be accurate and may depend on the used shear tester as discovered during the comparison of cohesion values measured with 4 different shear testers and a FT4 powder rheometer [119].

### ***2.1.5.8 Temporal evolution***

Dustiness tests are usually performed for few seconds and minutes as most of the handling operations are between those time scales. For most cases, it is assumed that the powder dust generation shows an initial increase whereby the loose aerosolisable particles are carried out by the air flow, after which dust generation decreases with time. However, depending on the material and the operation dust generation patterns may be different. Jensen et al. [102] suggested that different dust particle generation patterns and their relative levels are important descriptors of the mechanism of dust generation during powder handling and can potentially be used for more accurate dustiness exposure assessments for specific processes. More accurate exposure assessment and dust containment strategies can be achieved depending on whether the dust is generated during the initial few moments of operation or whether it is continuously released [120]

Heitbrink [120] found an increase in dust emission with time, which soon attains a plateau. Furthermore, they found that time durations greater than 10 min have a negligible effect on the powder dust generation.

Hjemsted and Schneider used a rotating drum dustiness tester and found that the dustiness index increases with time (from 3 min to 10 min) [56]. Interestingly, the dustiness index and the rate of increase were greater for 50 g of sample mass than for 200 g of sample mass. They also observed large differences in the time dependent dust concentration profiles measured using a TEOM for drum rotation speeds from 40 rpm to 60 rpm (with 200 g of sample and a flow rate of 80 L/min). The 40 rpm experiment was characterised by an initial peak of the dust concentration which is quickly followed by a decrease in dust concentration. This generation profile is representative of most of the materials tested with a drum tester [56]. On the other hand, the 60 rpm experiment showed a continuous dust release for the whole test duration. They concluded that the initial decrease in dust mass concentration (at 40 rpm) is caused by the finite time constant of the drum whereas the atypical dust evolution at 60 rpm, was tentatively attributed to material wear and the adhesive nature of the alumina particles. The high adhesive and cohesive nature of alumina particles can make them stick to walls they reach through the strong centrifugal forces inside the drum, thus reducing the amount of powders actually dropping and generating dust.

Chakravarty [109] used a vortex shaker to determine the dustiness of two samples of silicon carbide powders with different particle size distributions for six hours instead of a few minutes. They found that both powders differ in their dust generation behaviour whereby the powder with bigger particle sizes is characterised by a higher dustiness index and an increase in dust emission after 2-3 hours of testing, not seen with the other sample. The bigger and dustier sample showed changes in its particle size distribution and increases in mean particle circularity and aspect ratio, whereas no such changes were observed for the less dusty powder. The authors suggested that their results indicate that abrasion is the dominant source of attrition due to interparticle and particle-wall impaction which are more prominent for powders consisting of bigger and irregularly shaped particles.

#### ***2.1.5.9 Attrition strength of granular materials***

Attrition in the form of the wearing, fracturing or chipping of particles may occur when applied stresses (impact, compression or shear) overcomes the material's resistance to such causes of failure or when the stress loads are repeated and the material fails below the critical

stress levels due to fatigue. The process results in undesirable production of fine particle in the bulk material which may contribute to dust generation during handling of the material.

Friability or fragility of powders are usually tested using attrition tests, which measures the resistance of a granular material to wear.

Authier-Martin [105] used different alumina powders to compare attrition index (measured using the Forsythe-Hertwig attrition test [121]) and dustiness index (measured using a Perra pulvimeter). The results showed that as the particle breakage (weight loss) for a particular size fraction increases, the sample become less dusty. Thus, the results were in contrast to the preconceived ideas that link dustiness to fragility of materials.

Olsen [122] used two alumina powders to find a correlation between the attrition and dustiness indices. But, the author found a positive correlation between the two for one powder sample whereas no correlation for the other alumina sample.

The mechanical wear takes place using three mechanisms, i.e., abrasion, impaction, or the combination of both. A materials ability to wear by abrasion is related to its surface area, whereas wear by impaction is related to the number of particle collisions and the energy of such collisions [123].

Clearly, there is a lack of studies related to comparison of mechanisms involved in attrition and dustiness tests. Furthermore, the collision frequency and collision energy are difficult to measure at particle level but particle tracking studies such as particle trajectory in a vortex shaker experiment using Positron Emission Particle Tracking (PEPT) [124] can be one way to understand the influence of such parameters on powder dustiness.

## **2.1.6 Modelling approaches**

The goal of the modelling of powder dustiness is the development of predictive models that fit the known experimental data and are capable of foretelling new trends under original conditions. Dustiness models can be divided into empirical models and numerical models based on approaches such as CFD (Computational Fluid Dynamics) and the DEM (Discrete Element Method).

### **2.1.6.1 Empirical modelling**

Schmidt [92] remarked that the development of predictive dustiness models has not yet been successfully achieved. He developed an analytical model aiming at describing dust generation based on the competition between the cohesion and the separation forces. It relies on the fractional release rate  $R(x, t)$  that describes the probability with which a particle of

diameter  $x$  is released from the powder into the gas phase at the time point  $t$  and for the time period  $dt$ . Let  $m_{ae,tot}(t)$  be the total mass of dust in the system at the time point  $t$  and  $dm_{ae}(x,t)$  the mass of dust with particle diameters included between  $x$  and  $x + dx$  so that

$$m_{ae,tot}(t) = \int_{x=0}^{\infty} dm_{ae}(x,t) \cdot dx$$

The concentration of dust in the air is obtained by dividing the emitted mass through the volume:

$$c_{Rm,tot}(t) = \frac{m_{ae,tot}(t)}{V(t)}$$

The total fractional release rate is obtained by integrating  $R(x,t)$  over all diameters:

$$R_{3,tot}(t) = \int_{x=0}^{\infty} R(x,t) q_{3,p}(x,t) dx$$

The fraction release rate itself is a function of the cohesion forces  $F_C$  and the separation forces  $F_S$ :

$$R(x,t) = f(F_C(x,t), F_S(x,t))$$

Such a general model allows the use of both simple and complex descriptions of cohesion and separation.

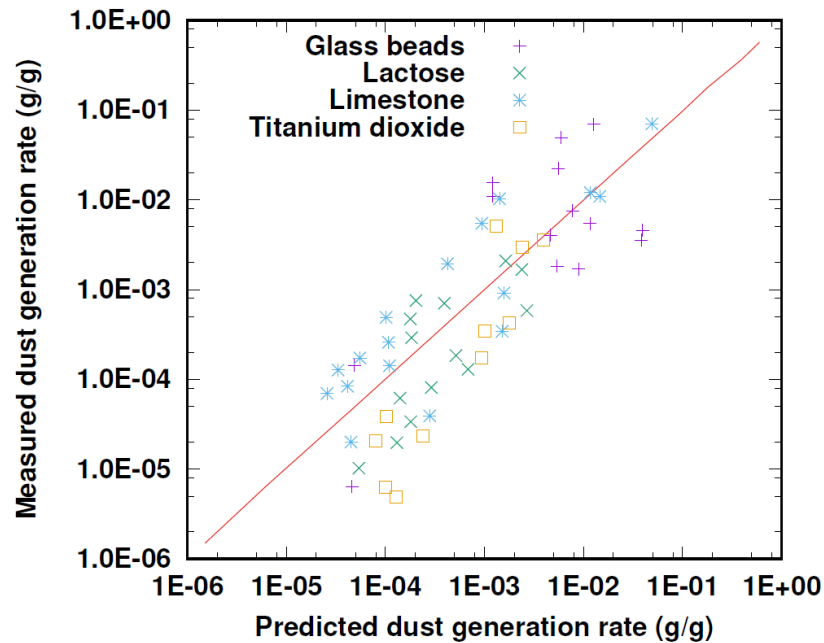


**Figure 2.5:** Plinke's dust generation rate [37]

Following a similar approach, Plinke et al. [37] expressed the dust generation rate of particles with size  $i$  as

$$G_i = x_i^a \frac{F_s^b}{F_c^c}$$

where  $a$ ,  $b$ ,  $c$  are empirical coefficients depending on the nature of the powder and of the stresses it is exposed to.  $F_c$  can be expressed as the product of the shear area and a cohesion coefficient  $C$  such that

$$C = e^{a_1} M^{a_2} d_{50}^{a_3} T_m^{a_4}$$

where  $M$  is the moisture content,  $d_{50}$  is the median size of the particle and  $T_m$  is the melting temperature of the material. They expressed the separation force in the case of a material fall-type process as:

$$F_s = e^{b_1} H^{b_2} M^{b_3} d_{50}^{b_4} \rho_p^{b_5} c_w^{b_6} AR^{b_7}$$

where  $H$  is the drop height,  $M$  is the material moisture,  $\rho_p$  is the particle density,  $c_w$  is the width of the impaction area at the top of the pile and  $AR$  is the angle of repose of the pile. They investigated dust emission from four common materials (titanium dioxide, limestone, glass beads and lactose) with three different size distributions and three moisture rates in a falling device. Using direct measures of cohesion and impaction, they were able to accurately predict the dust emission rates (see Figure 2.5).

Lanning et al. [105] applied Plinke's model to dust generation in a bench-top dustiness tester. A good agreement between measurements and model predictions were reached for limestone and titanium oxide whereas the predictions are poorer in the case of lactose and very poor in the case of glass beads. The model was further used for describing dust generation involving materials not employed during the development of Plinke's model. The values for fly ash, baby powder and toner were relatively well matched whereas those for tea mix were overestimated.

Breum [68] created a model expressing the dustiness of a material  $D_N$  as

$$D_N = \alpha M_N^\beta M T_N^\delta S A_N^\lambda$$

where  $M_N$  is the actual mass of test material normalised to the maximum of mass under testing,  $MT_N$  is the median time normalised to the test period, and  $SA_N$  is the surface adhesion. Such a model could successfully describe dust emissions from bentonite and barium sulphate in a rotating drum.

To conclude, only few empirical models accounting for dust formation and emission can be found in the literature. They succeeded in describing measurements to a significant degree but they require a relatively large number of experiments to ensure their validity.

## 2.1.6.2 Numerical modelling

### 2.1.6.2.1 CFD modelling

Since empirical models rely on a simplified description of the factors leading to dust emission, they are only valid in the relatively narrow domain in which the coefficients have been fitted to measurements. Numerical modelling offers the promise to allow reliable predictions for a much wider range of conditions because they are grounded on the real laws underlying powder dynamics. CFD (Computational Fluid Dynamics) [126] is a widespread approach to fluid mechanical problems consisting of numerically solving the underlying differential equations. Since a direct resolution would be extremely expensive for all practical systems [127], simplifications (called modelling) have to be introduced. The most popular approach used in the industry is the RANS (Reynolds-Averaged Navier-Stokes) equation approach [128]. Variables such as the pressure  $p$  and the velocity  $U$  are divided into a time-averaged part and a fluctuating part:  $p = \bar{p} + p'$  and  $U = \bar{U} + U'$ . Such a decomposition results in the RANS equations

$$\frac{\partial \bar{u}_i}{\partial t} + \rho \left( \frac{\partial \bar{u}_i \bar{u}_j}{\partial x_j} \right) = \bar{f}_i - \frac{\partial \bar{p}}{\partial x_i} + \frac{\partial}{\partial x_j} \left( \eta \left( \frac{\partial \bar{u}_i}{\partial x_j} + \frac{\partial \bar{u}_j}{\partial x_i} \right) - \rho \overline{u'_i u'_j} \right)$$

whereby  $\rho$  is the volumetric mass,  $t$  and  $x_i$  stand for the time and the spatial coordinates,  $\eta$  is the dynamic viscosity,  $f_i$  represents the forces the fluid is subjected to and  $\overline{u'_i u'_j}$  are the Reynolds stresses that have to be modelled. In the absence of thermal transfers, this equation must be solved along with the continuity equation  $\frac{\partial \bar{p}}{\partial t} + \nabla \cdot (\rho) = 0$

CFD can be used to simulate the gaseous flow in the dustiness tester, including both the air flowing through the system and the motion induced (e.g. by the rotation of a vortex shaker or of a rotating drum) and to simulate the behaviour of detached particles.

#### 2.1.6.2.2 The Eulerian-Eulerian approach

The first approach to simulating powders is the Eulerian-Eulerian method [129]. The powder is treated like a second phase for which another set of Navier-Stokes equations are solved and a new variable, the solid phase fraction  $s$ , is considered. To model the effect of the air flow on the solid phase, a momentum exchange coefficient [110, 111] is introduced:

$$K_{sf} = \frac{\alpha_s \rho_s f_d}{\tau_s}$$

where  $\rho_s$ ,  $f_d$ ,  $\tau_s$  are the density of the particle, the drag function and the particle relaxation time, respectively. The latter coefficient is itself defined as:

$$\tau_s = \frac{\rho_s d_s^2}{18 \mu_f}$$

The interaction between the solid phase and the gas phase is also represented by a solid phase stress [132] that needs to be modelled. The kinetic theory of granular flow [133] is often used to that end. It is an extension of the classical kinetic gas theory to dense particulate flows which takes non-ideal particle-particle collisions and gas-particle drag into account. The underlying concept is that the grains are in a state of continuous and chaotic restlessness within the fluid. This chaotic random motion exists at very low concentrations (due to friction between gas and particles, gas turbulence, pressure variations in the fluid, etc.) or at higher concentrations (due to grain collisions).

The Eulerian-Eulerian approach has had several applications relevant to the study of powder dustiness. Santos et al. [131] simulated the agitation of a glass bead powder in a rotating drum. The glass beads had a mean diameter of 1.09 mm and 3.68 mm and a density of 2460 kg/m<sup>3</sup>. The rotational speed was set at 1.45 rad/s, 4.08 rad/s, 8.91 rad/s, and 16.4 rad/s to spawn four different regimes of discrete solid motion: rolling, cascading, cataracting, and centrifuging. Overall, a good agreement between experimental results and the model predictions was reached. Figure 2.6 shows some results from Santo's study when the rotation speed was 2.31 rad/s. The outcomes of their investigation made it clear that the behaviour of the powder in the rotating drum can be very well described by the Eulerian-Eulerian approach with respect to both the powder distribution and the velocities of the grain.



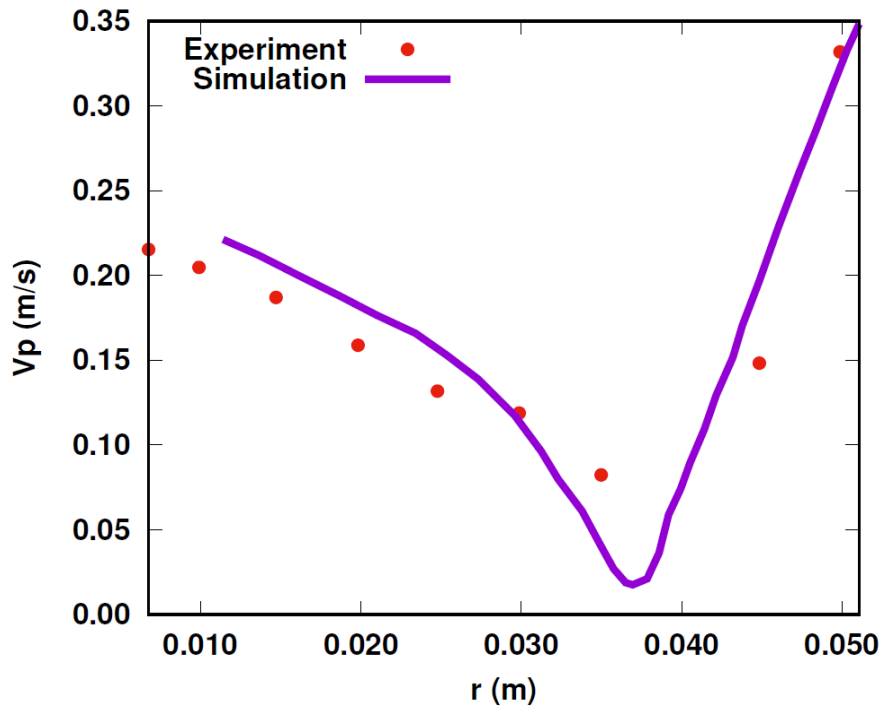


**Figure 2.6:** Results from Santos et al. [130] at 2.31 rad/s

Karunaratne et al. [134] modelled the behaviour of an unspecified powder in a rotary drum and achieved a qualitative agreement with experimental results.

Zudak and Klemens used the Eulerian-Eulerian framework to model the lifting of dust behind shock waves [135]. Experiments and simulations produced similar shapes of the dust cloud and the height reached by the dust was correctly predicted.

A number of authors have utilised the Eulerian-Eulerian approach for simulating the behaviour of powders in a fluidised bed. Cammarata et al. performed 2D and 3D CFD simulations of bubbling fluidised beds [136]. The bubble sizes were relatively well described. Li et al. studied granulation in a fluidised bed spray. Li et al. [137] combined a Two-Fluid Model with a growth model. They captured reasonably well the vertical particle velocities and the development of the particle diameter over time.

Chen et al. simulated dust emissions from conveyor transfer chutes [75]. The predicted dust emissions are close to the measurements. The model further predicted that reducing the air velocity at the discharge point of transfer lowers dust emissions.

Esmaili et al. investigated the effects of a falling stream of particles on the air velocity, as it is a crucial variable for predicting dustiness [138, 139]. They observed that increasing the diameter of particles decreases their concentration in the stream, thereby lowering the air velocity.

### 2.1.6.2.3 The Eulerian-Lagrangian approach

In the Eulerian-Lagrangian approach [140], the powder is simulated as a large number of discrete particles that are subjected to Newton's law (including the forces caused by the air flow). Equation 2.5 describes the particle's basic behaviour.

$$\frac{du_p}{dt} = F_D(u - u_p) + \frac{g_x(\rho_p - \rho)}{\rho_p} + F_x \quad (\text{Eq. 2.5})$$

$F_x$  is an additional acceleration (force/unit particle mass) term,  $F_D(u - u_p)$  is the drag force per unit particle mass and

$$F_D = \frac{18\mu C_d Re}{\rho_p d_p^2} \frac{1}{24}$$

Here,  $u$  is the fluid phase velocity,  $u_p$  is the particle velocity,  $\mu$  is the molecular viscosity of the fluid,  $\rho_p$  is the density of the particle, and  $d_p$  is the particle diameter.  $Re$  is the relative Reynolds number, which is defined as

$$Re \equiv \frac{\rho d_p |u_p - u|}{\mu}$$

The Eulerian-Lagrangian approach has been applied to several topics relevant or related to dust emission. Kolinsky et al. used the Eulerian-Lagrangian method to model dust lifting behind shock waves [141, 142]. They were able to include the effects of particle-particle and particle-wall collisions in a realistic and straightforward manner. They found that collisions play an important role in the formation of a dust cloud. While comparing the Eulerian-Lagrangian with the Eulerian-Eulerian approach, they found that the former leads to more realistic results. Murillo et al. modelled dust dispersion preceding explosions [143]. They found that the process can be divided into a fragmentation phase, the stabilisation of the dust cloud and a sedimentation phase.

### 2.1.6.2.4 The Discrete Element method (DEM)

The Eulerian-Lagrangian and the Eulerian-Eulerian method can be found in commercial CFD software such as Fluent and can be relatively easily employed. Their main disadvantage is that they do not address one fundamental aspect of dustiness: the adhesion and cohesion forces that hold the powder's particles together and that play a crucial role in the breakage of the

powder's primary particles into aerosols through processes such as abrasion [144] and fragmentation [145]. The Discrete Element Method (DEM) describes the powder particles as obeying Newton's law in a similar way to the Eulerian-Lagrangian method (see Eq. 5). There is, however, an additional term accounting for the cohesion forces and no term accounting for the interaction with the air flow that is not described so that Eq. 2.6 holds for a single particle.

$$\frac{du_p}{dt} = g_x + F_{cohesion} + F_{separation} \quad (\text{Eq.2. 6})$$

The cohesion forces may include, among other factors, the Van-Der-Waals forces, the electrostatic forces, and liquid bridges.

The DEM has been applied to several topics relevant to dustiness. Rhodes et al. employed the DEM to study fluidisation characteristics [146]. They have investigated the influence of cohesive interparticle forces on the characteristic behaviour of a gas fluidised bed. They discovered through their simulations the existence of non-bubbling fluidisation for a range of gas velocities between the minimum fluidisation velocity and the minimum bubbling velocity.

Cleary and Paul applied the DEM to particle flow modelling [147]. They found out that the particle shape is of uttermost importance and that it has a strong influence on the strength of granular materials, the situations when it will fail and flow and when it will remain stationary, the shear and dilation in flowing regions, the void fraction in granular solids, and the interaction of the linear and rotational dynamics of the granular material.

Kwapinska et al. investigated the transverse mixing of free flowing particles in horizontal rotating drums without inlets [148]. They obtained good agreements with experimental data with respect to the mixing numbers. Alchikh-Sulaiman et al. studied the mixing of polydisperse particles in a rotary drum [149]. The degree of mixing of polydisperse particles was smaller than that of monodisperse particles due to the segregation process. Mishra et al. simulated agglomeration in a rotary drum [150] Realistic predictions of the steady-state size distribution of the agglomerates could be achieved.

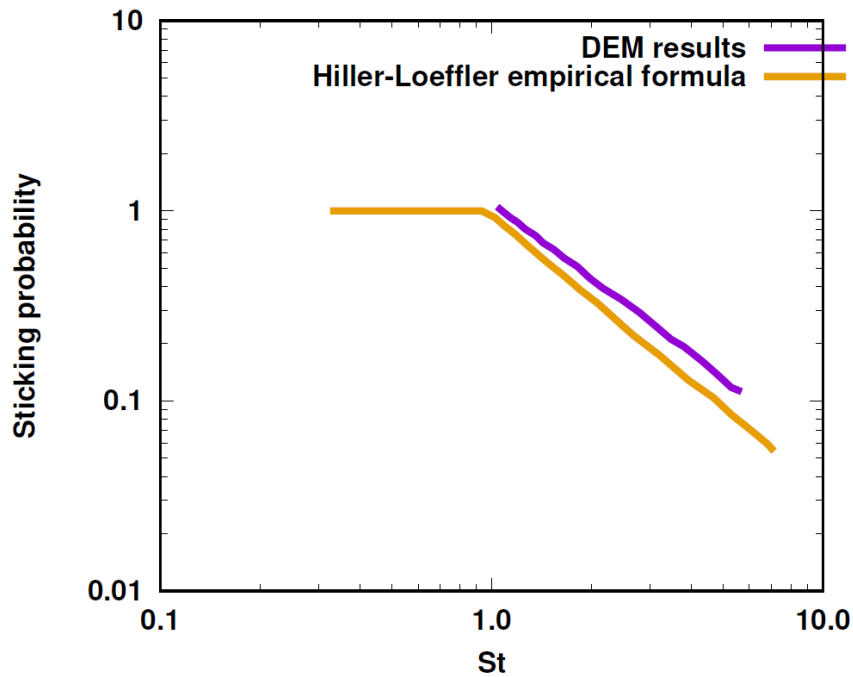


**Figure 2.7:** Results from Yang et al. [150]

Yang et al. [151] studied the impaction-sticking process during the initial deposition of fine particles on a single fibre through DEM. The balance between the sticking and the impaction forces play a crucial role in dust emission and capture [37]. The HillerLoeffler formula [152], an experimentally determined relation between the Stokes' number [153] and the sticking probability, has been compared with results from DEM computations (see Figure 2.7). The DEM predictions match well the values of the empirically obtained formula.

#### 2.1.6.2.5 CFD-DEM combinations

One significant drawback of these pure DEM studies is that they fail to take into account the air flow. But the air flow can play an important role in the behaviour of smaller primary particles and aerosols [154]. One solution consists of combining the CFD description of the gas flow seen in subsection 5.1 with the DEM modelling of particles obeying Newton's laws including the cohesion and the separation forces acting upon the powder's particles. Such a combination is referred to as DEM-CFD simulations as well as Eulerian-Lagrangian simulation. We shall, however, not use the latter designation as we think it should be limited to the CFD-based approach described in Section 2.1.6.2.1. Researchers have applied CFD-DEM to different problems related to dustiness.

Kawaguchi et al. studied two-dimensional fluidised beds [155]. The movement of the particle was computed using Newton's equation of motion and the contact forces were modelled

through the discrete element method. They used a 2-D and a 3-D model and found that both models are in good agreement once the particles are fluidised with respect to flow patterns including the period of bubble formation. However, the motion of particles near the corners is not as well captured.

Kloss et al. developed a multi-purpose CFD-DEM framework to simulate coupled fluid-granular systems [156]. Both the DEM and the CFD-DEM were successfully validated against analytical as well as experimental data. Chu et al. studied the gas-solid flow in a cyclone separator [157]. The model succeeded in capturing the crucial flow features in the gas cyclone, like the flow pattern of particles and the decrease in pressure drop and tangential velocity after loading solids.

Zhong et al. employed DEM-CFD to model non-spherical particulate systems (NSPS) [158]. They found that despite noteworthy efforts, it is still very challenging to capture the behaviour of NSPS and their interaction with the fluid flow.

Derakhshani et al. modelled dust liberation at the belt conveyor transfer point [158]. They used DEM for accounting for particle-particle and particle-wall interactions and CFD for modelling the fluid field around the particle plume. The dust release from the bulk solids hinges on particle properties such as the particle size, particle size distribution, particle shape, and bulk density.

Lamarche et al. validated quantitatively CFD-DEM simulations of small-scale fluidised beds through comparisons with large-scale experiments [160].

Bagherzadeh et al. simulated single particle settlement as the *simplest version of dust liberation problem* [161]. Tong et al. investigated the dispersion mechanisms in commercial dry powder inhalers [162]. They found that the shear stress of turbulent flow had no noticeable effects upon powder dispersion whereas strong impactions happened between the agglomerates and the chamber wall, thereby fragmenting the agglomerates into large pieces without generating many fine particles. They noticed that the dust liberation rate raises non-linearly as the wind speed increases. The accuracy of the stockpile deformation results obtained through CFD-DEM modelling were successfully compared with experimental results related to the sand pile deformation after 30 seconds.

Hilton and Cleary simulated dust production from a dynamic granular bed by using a three-dimensional coupled DEM and Navier-Stokes computational model [163]. Nevertheless, the generated dust is modelled as an Eulerian density field which is advected and diffused by the gas flow. The total imparted energy was employed for determining a dust flux inside each CFD cell that worked as a source term in a dust density advection-diffusion equation. The results of

the simulations are in good agreement with empirical expressions for both active and passive dust productions.

The main disadvantage of DEM-CFD lies in the huge computational expense it often requires. Brosh et al. worked on accelerating the CFD-DEM simulations of processes involving wide particle size distributions [164]. A detached DEM grid was employed for lowering the time required for the communication between CFD and DEM. The DEM-cells used a non-binary search to reduce the computational effort. The DEM-cells were divided into sub-cells to further speed up the computation. The stiffness of the smallest particles was reduced to permit larger time steps. The finest particles were removed from the simulation. As a result, DEM comminution simulations [165] can run approximately 300 times faster.

Overall, it can be seen that DEM and especially the combination of DEM with CFD are promising approaches to the prediction of dust emission and generation. Computational costs are being increasingly reduced [166].

### **2.1.7 Conclusion and outlook**

Dust emissions are a very important topic for the protection of workers at industrial installations and the safeguard of the environment. Between 2000 and 2010, they caused 295 incidents (combinations of fires, explosions and fires & explosions) in the UK [167]. If not held in check, they can cause toxicological damages to the environment if the underlying substance is noxious [168]. As a consequence, a good understanding of dustiness has become crucial in order to tackle these problems. In other domains of applied science, engineering and risk analyses (concerning, for instance, combustion [127], pollutant release into the air [169] or hydrology [42]), predictive models (relying on the equations of Navier-Stokes) could be successfully developed. They allow researchers and practitioners to foretell the effects of a new industrial situation or solution in a trustworthy manner. In contrast to these fields, dustiness studies are characterised by a very large number of experimental articles in comparison to the limited amount of theoretical and modelling work. This article aims at providing a useful overview of our theoretical understanding of dustiness with the goal of expanding it.

We first presented dustiness testers which have been used for studies contributing to our comprehension of dust generation. The drop tester and the rotation drum remain the main approaches used to study dustiness. There are several factors which may hamper our theoretical understanding of dustiness. Many dustiness studies suffer from a lack of independent characterisation tests: instead, the authors just state that they use the data of the manufacturer, also those have often been shown to be inaccurate. This can greatly diminish their theoretical value. There is a lack of studies related to relatively new dustiness testers (such as the vortex

shaker) which can potentially reduce the cost and risks involved with powder testing. With new advances in nano-technology, the powder quantity available for testing can be expensive and its toxicity can be unknown. As a consequence, it can be expected that such testers will be increasingly used over the years to come. However, without theorising, the results cannot be used to predict new situations, which can only be reached through the development of numerical and analytical methods. There is an overemphasis on tester comparisons rather than the comparison of powder properties although the latter might prove more helpful for improving our theoretical grasp of dustiness. There are also very few studies with the interactions of dust generation with the powder properties (such as the PSD, shape, cohesion/flowability etc.). Although there are several studies dealing with the comparison of dustiness testers and of powders, there is generally no information regarding the particle motion (trajectory) inside the testers, their average velocities, energy levels or frequency of collisions with the wall and/or other particles in the bulk.

In order to get a systematic understanding of a phenomenon, parametric studies are crucial. In Section 2.1.5, we reviewed the main parametric studies widening our comprehension of dustiness. Increasing the sample mass leads to a relative increase of dust emission (probably owing to a higher number of fines) until a critical mass is reached, beyond which dustiness decreases, which could be explained through the influence of higher cohesive forces. The mean particle size of the powder has the following influence on dustiness. Dustiness keeps increasing with the particle size until a critical diameter is attained beyond which it diminishes. The low dustiness for the smallest particle sizes can be well accounted for by the stronger Van-der-Waals forces accompanying small diameters. The lower dustiness of large powder particles could possibly be explained by higher gravitational forces they are exposed to.

Humidity causes generally a very strong reduction in dust emission which is due to the liquid bonds it spawns in the powder. It is worth noting there are very few studies investigating the effect of air humidity on dustiness. Increasing the bulk density of the powder leads to unsystematic effects, it can either lead to an increase or decrease of dust emissions. Higher values of the sphericity of the powder particles tend to reduce its dustiness. This could potentially be explained by the fact that irregularly-shaped are more fragile because of a higher number of microcracks on their surface. No strong correlations between flowability and dustiness could be established. A stronger cohesion strongly reduces dustiness as the measured cohesion values are caused by cohesive forces which oppose the separation forces that lead the powder to emit dust particles. Dust generation over long time scales can be different than dust generation over short time scales. It is worth mentioning, however, that there are very few long-term dust generation studies even though they could greatly enrich our views of dustiness.

In Section 2.1.6, we explored the relatively limited number of studies that aimed at modelling dust emission. Plinke et al. and Schmidt proposed analytical models for describing dust emission [37]. They rely on the concept that dustiness is a result of a competition between cohesion and separation forces so that the dust emission rate of particles of "size"  $i$  is given by

$$G_i = x_i^a \frac{F_s^b}{F_c^c}$$

where  $a, b, c$  are empirical coefficients depending on the nature of the powder and of the stresses it is exposed to. Plinke et al. and Lanning et al. were able to successfully model and predict the dust generation behaviour of four powders in drop testers [37]. The simplicity of that approach and the small computational power it demands could make very interesting to industrial practitioners but that research avenue has not been much pursued since the 1990s.

One of its main drawbacks is that it does not provide us with a generally valid model so that the empirical coefficients may only be valid for a limited range of boundary and initial conditions. A universal model must somehow take into account all forces a particle is subjected to which include mechanical forces (such as collisions with the wall and particle-particle collisions), cohesive forces (e.g. Van-der-Waals forces) and forces the flow exercises over the particle. CFD modelling is based on solving the Navier-Stokes equations governing the behaviour of the air in the tester. In the case of the Eulerian-Eulerian approach [170], the powder is modelled as a second fluid characterised by a solid mass fraction. The interaction of the powder with the air flow is modelled through the particle density, the drag function and the particle relaxation time that may have to be determined empirically. The Eulerian-Eulerian approach could be successfully applied to represent the behaviour of powders in rotating drums, in a fluidised bed, the lifting of dust behind shock waves and dust emissions from conveyor transfer chutes. Its limitation may be that the representation of the powder as a fluid may be too simple to account for the complex behaviour of the dust particles being emitted. An alternative consists of the Eulerian-Lagrangian method whereby each dust particle is subjected to Newton's equation including particle-particle collisions and the effect of the air flow on the particle [171]. They were applied to the simulation of dust lifting behind shock waves and dust dispersion preceding explosions. When compared to the Eulerian approach, their downside lies in the strongly rising computational time when the number of particles is increased.

Approaches purely based on traditional CFD-software suffer from the fact that they do not account for the most fundamental aspect of dustiness, namely the competition between the cohesion and the separation forces that leads to dust release. Discrete Element Simulations (DEM) describe precisely the balance between cohesion and separation forces [172]. However,



alone they fail to consider the influence of the flow on the dust particles which can be quite large for small particles. The most exhaustive approach is the combined CFD-DEM method that precisely describes all forces the particles are exposed to, which go from the Van-der-Waals forces to the shear forces caused by the air-flow [156]. Its drawback is the enormous computational expense it can involve.

To conclude, there are promising ways to model dustiness and dust generation which are increasingly being considered by research groups all around the world. Plinke's simplified approach and the complex CFD and DEM modelling approach should be parallelly pursued, as both hold the promise to increase our scientific understanding and facilitate decisions related to workplace safety and environment protection.

## 2.1.8 References

- [1] Bickis U. Hazard prevention and control in the work environment: airborne dust. *World Health* 1998; 13-16.
- [2] International Organization for Standardization. ISO 4225: Air quality - General aspects - Vocabulary 1994.
- [3] Klippel A, Schmidt M, Krause U. Dustiness in workplace safety and explosion protection - review and outlook. *Journal of Loss Prevention in the Process Industries* 2015; 34:22-29.
- [4] Junemann R, Holzhauser R. Reduction of bulk emissions in bulk handling installations. *Bulk Solids Handling* 1992; 12:217-26.
- [5] Liu Z, Wypych P, Cooper P. Dust generation and air entrainment in bulk materials handling- a review. *Powder handling & processing* 1999; 11:421-425.
- [6] for Occupational Safety NI, of Respiratory Disease Studies HD. Work-related Lung Disease Surveillance Report, 1996. 96-134. US Department of Health and Human Services, Public Health Service, Centers for Disease Control and Prevention, National Institute for Occupational Safety and Health, 1996.
- [7] Iossifova Y, Bailey R, Wood J, Kreiss K. Concurrent silicosis and pulmonary mycosis at death. *Emerging infectious diseases* 2010; 16:318.
- [8] Levy A, Kalman CJ. Handbook of conveying and handling of particulate solids, volume 10. Elsevier, 2001.
- [9] LidÉN G. Dustiness testing of materials handled at workplaces. *The Annals of occupational hygiene* 2006; 50:437-439.
- [10] CEN EN 481.(1993) Workplace Atmospheres. Size Fraction Definitions for Measurement of Airborne Particles." Brussels: Comité Européen de Normalisation 1993.
- [11] Baron P, Vincent JH. Particle size-selective sampling of particulate air contaminants. American Conference of Governmental Industrial Hygienists (ACGIH), 1999.
- [12] Malda J, Frondoza CG. Microcarriers in the engineering of cartilage and bone. *Trends in biotechnology* 2006; 24:299-304.
- [13] Bell AT. The impact of nanoscience on heterogeneous catalysis. *Science* 2003; 299:1688-1691.
- [14] Li Y, Somorjai GA. Nanoscale advances in catalysis and energy applications. *Nano letters* 2010; 10:2289-2295.
- [15] Gundogdu O, Jenneson P. Understanding nanoagglomerates. *Advanced Science Letters* 2008; 1:161-164.

- [16] Brune H, Ernst H, Grunwald A, Grunwald W, Hofmann H, Krug H, Janich P, Mayor M, Rathgeber W, Schmid G, et al. Nanotechnology: assessment and perspectives, volume 27. Springer Science & Business Media, 2006.
- [17] Plitzko S, Gierke E. Tätigkeiten mit Nanomaterialien in Deutschland-Gemeinsame Fragebogenaktion der Bundesanstalt für Arbeitsschutz und Arbeitsmedizin (BAuA) und des Verbands der Chemischen Industrie (VCI). *Gefahrstoffe-Reinhaltung der Luft* 2007; 10:419-424.
- [18] Peters TM, Elzey S, Johnson R, Park H, Grassian VH, Maher T, O'Shaughnessy P. Airborne monitoring to distinguish engineered nanomaterials from incidental particles for environmental health and safety. *Journal of occupational and environmental hygiene* 2008; 6:73-81.
- [19] Evans DE, Ku BK, Birch ME, Dunn KH. Aerosol monitoring during carbon nano fiber production: mobile direct-reading sampling. *Annals of Occupational Hygiene* 2010; 54:514-531.
- [20] Evans DE, Turkevich LA, Roettgers CT, Deye GJ, Baron PA. Dustiness of fine and nanoscale powders. *Annals of Occupational Hygiene* 2012; 57:261-277.
- [21] Hamelmann F, Schmidt E. Methods of estimating the dustiness of industrial powders-a review. *KONA Powder and Particle Journal* 2003; 21:7-18.
- [22] Brouwer DH, Links IH, De Vreede SA, Christopher Y. Size selective dustiness and exposure; simulated workplace comparisons. *The Annals of occupational hygiene* 2006; 50:445-452.
- [23] Pensis I, Mareels J, Dahmann D, Mark D. Comparative evaluation of the dustiness of industrial minerals according to european standard EN 15051, 2006. *Annals of occupational hygiene* 2009; 54(2):2014-216.
- [24] Heitbrink WA, Todd WF, Fischbach TJ. Correlation of tests for material dustiness with worker exposure from the bagging of powders. *Applied Industrial Hygiene* 1989; 4:12-16.
- [25] Heitbrink WA, Todd WF, Cooper TC, O'Brien DM. The application of dustiness tests to the prediction of worker dust exposure. *The American Industrial Hygiene Association Journal* 1990; 51:217-223.
- [26] Breum N, Schneider T, Jrgensen O, Valdbjrn Rasmussen T, Skibstrup Eriksen S. Cellulosic building insulation versus mineral wool, fiberglass or perlite: installers exposure by inhalation of fibers, dust, endotoxin and retardant additives. *Annals of occupational hygiene* 2003; 47:653-669.
- [27] Madsen A, Martensson L, Schneider T, Larsson L. Microbial dustiness and particle release of different biofuels. *Annals of Occupational Hygiene* 2004; 48:327-338.
- [28] Madsen AM. Exposure to airborne microbial components in autumn and spring during work at Danish biofuel plants. *The Annals of occupational hygiene* 2006; 50:821-831.
- [29] Cowherd C, Grelinger MA, Wong KF. Dust inhalation exposures from the handling of small volumes of powders. *American Industrial Hygiene Association journal* 1989; 50:131-138.
- [30] Class P, Deghilage P, Brown R. Dustiness of different high-temperature insulation wools and refractory ceramic fibres. *The Annals of occupational hygiene* 2001; 45:381-384.
- [31] Petavratzi E, Kingman S, Lowndes I. Particulates from mining operations: A review of sources, effects and regulations. *Minerals Engineering* 2005; 18:1183-1199.
- [32] Tsai CJ, Huang CY, Chen SC, Ho CE, Huang CH, Chen CW, Chang CP, Tsai SJ, Ellenbecker MJ. Exposure assessment of nano-sized and respirable particles at different workplaces. *Journal of Nanoparticle Research* 2011; 13:4161-4172.
- [33] Dubey P, Ghia U, Turkevich LA. Computational fluid dynamics analysis of the venturi dustiness tester. *Powder technology* 2017; 312:310-320.
- [34] Pujara C, Kildsig D. Effect of individual particle characteristics on airborne emissions. *Drugs and the Pharmaceutical Sciences* 2001; 108:29-54.
- [35] Blome H. Umgang mit partikelförmigen Schadstoffen. *Sichere Arbeit* 2001; 1:19.
- [36] Barig A, Blome H. General dust limit. hazardous substances - keeping the air clean 2002; 62:2.

- [37] Plinke MA, Leith D, Boundy MG, Löffler F. Dust generation from handling powders in industry. *American Industrial Hygiene Association Journal* 1995; 56:251-257.
- [38] Plinke MA, Leith D, Hathaway R, Löffler F. Cohesion in granular materials. *Bulk solids handling* 1994; 14:101-101.
- [39] Petavratzi E, Kingman S, Lowndes I. Assessment of the dustiness and the dust liberation mechanisms of limestone quarry operations. *Chemical Engineering and Processing: Process Intensification* 2007; 46:1412-1423.
- [40] Peters N. *Turbulent combustion*. Cambridge university press, 2000.
- [41] Holmes NS, Morawska L. A review of dispersion modelling and its application to the dispersion of particles: an overview of different dispersion models available. *Atmospheric environment* 2006; 40:5902-5928.
- [42] Blöschl G, Sivapalan M. Scale issues in hydrological modelling: a review. *Hydrological processes* 1995; 9:251-290.
- [43] Gill TE, Zobeck TM, Stout JE. Technologies for laboratory generation of dust from geological materials. *Journal of hazardous materials* 2006; 132:1-13.
- [44] Reznik G, Klenk U, Schmidt E. Untersuchungen zur staubungsneigung von braunkohle unterschiedlicher feuchte. *Chemie Ingenieur Technik* 2006; 78:1885-1889.
- [45] Bihan OLCL, Ustache A, Bernard D, Aguerre-Chariol O, Morgeneyer M. Experimental study of the aerosolization from a carbon nanotube bulk by a vortex shaker. *Journal of Nanomaterials* 2014; 2014:7.
- [46] Boundy M, Leith D, Polton T. Method to evaluate the dustiness of pharmaceutical powders. *Annals of Occupational Hygiene* 2006; 50:453-458.
- [47] Saleh K, Jaoude MTMA, Morgeneyer M, Lefrancois E, Le Bihan O, Bouillard J. Dust generation from powders: A characterization test based on stirred fluidization. *Powder Technology* 2014; 255:141-148.
- [48] Sethi S, Schneider T. A gas fluidization dustiness tester. *Journal of Aerosol Science* 1996; 27:S305-S306.
- [49] Dahmann D, Monz C. Determination of dustiness of nanostructured materials. *Gefahrstoffe Reinhaltung der Luft* 2011; 71:481-487.
- [50] Schneider T, Jensen KA. Combined single-drop and rotating drum dustiness test of fine to nanosize powders using a small drum. *Annals of Occupational Hygiene* 2007; 52:23-34.
- [51] Chung K, Burdett G. Dustiness testing and moving towards a biologically relevant dustiness index. *The Annals of occupational hygiene* 1994; 38:945-949.
- [52] EN C. 15051 Workplace atmospheres: measurement of the dustiness of bulk materials requirements and test methods. Brussels, Belgium: European committee for standardization 2006.
- [53] Morgeneyer M, Le Bihan O, Ustache A, Aguerre-Chariol O. Experimental study of the aerosolization of fine alumina particles from bulk by a vortex shaker. *Powder Technology* 2013; 246:583-589.
- [54] O'Shaughnessy PT, Kang M, Ellickson D. A novel device for measuring respirable dustiness using low-mass powder samples. *Journal of occupational and environmental hygiene* 2012; 9:129-139.
- [55] Stauber D, Beutel R. Determination and control of the dusting potential of feed premixes. *Bestimmung und Kontrolle des Staubpotentials von Futtermittelvormischungen.* *Fresenius' Zeitschrift für analytische Chemie* 1984; 318:522-524.
- [56] Hjemsted K, Schneider T. Documentation of a dustiness drum test. *The Annals of occupational hygiene* 1996; 40:627-643.
- [57] Maynard AD, Baron PA, Foley M, Shvedova AA, Kisin ER, Castranova V. Exposure to carbon nanotube material: aerosol release during the handling of unrefined single-walled carbon nanotube material. *Journal of Toxicology and Environmental Health, Part A* 2004; 67:87-107.
- [58] Ogura I, Sakurai H, Gamo M. Dustiness testing of engineered nanomaterials. In: *Journal of Physics: Conference Series*. IOP Publishing, 2009, volume 170, p. 012003.

- [59] Plinke MA, Maus R, Leith D. Experimental examination of factors that affect dust generation by using Heubach and MRI testers. *The American Industrial Hygiene Association Journal* 1992; 53:325-330.
- [60] Cawley B, Leith D. Bench-top apparatus to examine factors that affect dust generation. *Applied Occupational and Environmental Hygiene* 1993; 8:624-631.
- [61] Duan M, Wang Y, Ren X, Qu X, Cao Y, Yang Y, Nian L. Correlation analysis of three influencing factors and the dust production rate for a free-falling particle stream. *Particuology* 2017; 34:126-133.
- [62] Wang Y, Ren X, Zhao J, Chu Z, Cao Y, Yang Y, Duan M, Fan H, Qu X. Experimental study of flow regimes and dust emission in a free falling particle stream. *Powder Technology* 2016; 292:14-22.
- [63] Schofield C, Sutton H, Waters K. The generation of dust by materials handling operations. *J Powder Bulk Solids Technol.* 1979; 3:40.
- [64] Ding Y, Stahlmecke B, Kaminski H, Jiang Y, Kuhlbusch TA, Riediker M. Deagglomeration testing of airborne nanoparticle agglomerates: Stability analysis under varied aerodynamic shear and relative humidity conditions. *Aerosol Science and Technology* 2016; 50:1253--1263.
- [65] Visser GT. A wind-tunnel study of the dust emissions from the continuous dumping of coal. *Atmospheric Environment Part A General Topics* 1992; 26:1453-1460.
- [66] Chow JC, Watson JG, Houck JE, Pritchett LC, Rogers CF, Frazier CA, Egami RT, Ball BM. A laboratory resuspension chamber to measure fugitive dust size distributions and chemical compositions. *Atmospheric Environment* 1994; 28:3463-3481.
- [67] Stahlmecke B, Wagener S, Asbach C, Kaminski H, Fissan H, Kuhlbusch TA. Investigation of airborne nanopowder agglomerate stability in an orifice under various differential pressure conditions. *Journal of Nanoparticle Research* 2009; 11:1625.
- [68] Breum N. The rotating drum dustiness tester: variability in dustiness in relation to sample mass, testing time, and surface adhesion. *The Annals of occupational hygiene* 1999; 43:557-566.
- [69] Ansart R, De Ryck A, Dodds JA, Roudet M, Fabre D, Charru F. Dust emission by powder handling: comparison between numerical analysis and experimental results. *Powder Technology* 2009; 190:274-281.
- [70] Bach S, Schmidt E. Determining the dustiness of powders a comparison of three measuring devices. *Annals of occupational hygiene* 2008; 52:717-725.
- [71] Chakravarty S, Le Bihan O, Fischer M, Morgeneyer M. Dust generation in powders: Effect of particle size distribution. In: *EPJ Web of Conferences*. EDP Sciences, 2017, volume 140, p. 13018.
- [72] Han J, Zhu Z, Qian H, Wohl AR, Beaman CJ, Hoye TR, Macosko CW. A simple confined impingement jets mixer for flash nanoprecipitation. *Journal of pharmaceutical sciences* 2012; 101:4018-4023.
- [73] Jensen K, Kembouche Y, Christiansen E, Jacobsen N, Wallin H, Guiot C, Spalla O, Witschger O. The generic nanogenotox dispersion protocol: final protocol for producing suitable manufactured nanomaterial exposure media. *NANOGENOTOX Joint Action* 2011.
- [74] Ogura I, Kotake M, Sakurai H, Gamo M. Emission and exposure assessment of manufactured nanomaterials. English version. (26 october 2012). NEDO project (p06041) research and development of nanoparticle characterization methods. 2012.
- [75] Chen X, Wheeler C, Donohue T, McLean R, Roberts A. Evaluation of dust emissions from conveyor transfer chutes using experimental and cfd simulation. *International Journal of Mineral Processing* 2012; 110:101-108.
- [76] Klinzing GE, Rizk F, Marcus R, Leung L. *Pneumatic conveying of solids: a theoretical and practical approach*, volume 8. Springer Science & Business Media, 2011.
- [77] Heitbrink WA, Baron PA, Willeke K. An investigation of dust generation by free falling powders. *The American Industrial Hygiene Association Journal* 1992; 53:617-624.
- [78] Stein M, Seville J, Parker D. Attrition of porous glass particles in a fluidised bed. *Powder technology* 1998; 100:242-250.

- [79] Bemrose C, Bridgwater J. A review of attrition and attrition test methods. *Powder Technology* 1987; 49:97-126.
- [80] Bailey A. Electrostatic phenomena during powder handling. *Powder Technology* 1984; 37:71-85.
- [81] Israelachvili JN. *Intermolecular and surface forces*. Academic press, 2011.
- [82] Seville J, Willett C, Knight P. Interparticle forces in fluidisation: a review. *Powder Technology* 2000; 113:261-268.
- [83] Castellanos A. The relationship between attractive interparticle forces and bulk behaviour in dry and uncharged fine powders. *Advances in physics* 2005; 54:263-376.
- [84] Pietsch WB. *Agglomeration processes: phenomena, technologies, equipment*. John Wiley & Sons, 2008.
- [85] Calin L, Caliap L, Neamtu V, Morar R, Iuga A, Samuila A, Dascalescu L. Tribocharging of granular plastic mixtures in view of electrostatic separation. *IEEE Transactions on Industry Applications* 2008; 44:1045-1051.
- [86] Krupp H. Particles adhesion theory and experiment. *Advances in colloid and interface science* 1967; 1:111-239.
- [87] Gady B, Schleef D, Reifenberger R, Rimai D, DeMejo L. Identification of electrostatic and van der Waals interaction forces between a micrometer-size sphere and a substrate. *Physical Review B* 1996; 53:8065.
- [88] Rietema K. *The dynamics of fine powders*. Springer Science & Business Media, 2012.
- [89] Butt HJ, Kappl M. Normal capillary forces. *Advances in colloid and interface science*. 2009; 146(1-2):48-60.
- [90] Schwedes J. Review on testers for measuring flow properties of bulk solids. *Granular matter* 2003; 5:1-43.
- [91] Seville J, Tüzün U, Clift R. *Processing of particulate solids, volume 9*. Springer Science & Business Media, 2012.
- [92] Schmidt E, et al. Fractional release rate-a novel concept to quantify the dustiness of powders. *Chemie Ingenieur Technik* 2015; 87:638-643.
- [93] Davies K, Hammond C, Higman R, Wells A. Progress in dustiness estimation: British occupational hygiene society technology committee working party on dustiness estimation. *The Annals of Occupational Hygiene* 1988; 32:535-544.
- [94] Lyons C, Mark D. *Development and testing of a procedure to evaluate the dustiness of powders and dusts in industrial use*. HSE Books, 1994.
- [95] Pujara CP. *Determination of factors that affect the generation of airborne particles from bulk pharmaceutical powders* 1997; Ph.D. dissertation Purdue University, USA.
- [96] Schofield C. Dust generation and control in materials handling. *Bulk solids handling* 1981; 1:419-427.
- [97] Janhunen H, Nylander L, Heikkila P, Raunemaa T. Improved dustiness testing using a three stage impactor. In: *Proc. 3rd Finnish Aerosolsymposium, Sipoo, Finland*. 1988, pp. 1-6.
- [98] Goodfellow H, Smith J. Dustiness testing a new design approach for dust control. In: *Proc. Second Int. Symp. Ventilation for Contaminant Control*. 1989, pp. 175-182.
- [99] Farrugia T, Ahmed N, Jameson G. A new technique for measuring dustiness of coal. *Journal of Coal Quality* 1989; 8:51.
- [100] Westborg S, Cortson C. Determination of dustiness of coal by the rotating drum method. *Journal of Coal Quality* 1990; 9:77.
- [101] Bröckel U, Wahl M, Kirsch R, Feise HJ. Formation and growth of crystal bridges in bulk solids. *Chemical engineering & technology* 2006; 29:691-695.

- [102] Jensen KA, Koponen IK, Clausen PA, Schneider T. Dustiness behaviour of loose and compacted bentonite and organoclay powders: What is the difference in exposure risk? *Journal of Nanoparticle Research* 2009; 11:133-146.
- [103] Fu X, Huck D, Makein L, Armstrong B, Willen U, Freeman T. Effect of particle shape and size on flow properties of lactose powders. *Particuology* 2012; 10:203-208.
- [104] Leith D. Drag on nonspherical objects. *Aerosol science and technology* 1987; 6:153-161.
- [105] Authier-Martin M. Alumina handling dustiness. In: *Essential Readings in Light Metals*, Springer, 2016. pp. 774-782.
- [106] Hjemsted K, Schneider T. Dustiness from powder materials. *Journal of Aerosol Science* 1996; 27:S485-S486.
- [107] Olsen D, Behrens C, Hamberg K, Prytz A, Tveten E. Effects of morphology on alumina strength and dustiness. *Proceedings of the 6th International Alumina Quality Workshop* 2002; 1-9.
- [108] Pujara CP. Determination of factors that affect the generation of airborne particles from bulk pharmaceutical powders 1997.
- [109] Chakravarty S, Fischer M, Garca-Trianes P, Dalle M, Meunier L, Aguerre-Chariol O, Bihan OL, Morgeneyer M. Long-term dust generation from silicon carbide powders. *Process Safety and Environmental Protection* 2018; 116:115-25.
- [110] Prescott JK, Barnum RA. On powder owability. *Pharmaceutical technology* 2000; 24:60-85.
- [111] Ganesan V, Rosentrater KA, Muthukumarappan K. Flowability and handling characteristics of bulk solids and powders—a review with implications for DDGS. *biosystems engineering* 2008;101:425-435.
- [112] Iqbal T, Fitzpatrick J. Effect of storage conditions on the wall friction characteristics of three food powders. *Journal of Food Engineering* 2006; 72:273-280.
- [113] Teunou E, Fitzpatrick J, Synnott E. Characterisation of food powder flowability. *Journal of Food Engineering* 1999; 39:31-37.
- [114] Teunou E, Vasseur J, Krawczyk M. Measurement and interpretation of bulk solids angle of repose for industrial process design. *Powder Handling and Processing* 1995; 7:219-228.
- [115] Carr Jr RL. Evaluating flow properties of solids. *Chem Eng(Jan)* 1965;18:163-168.
- [116] Hsieh H. Measurement of flowability and dustiness of alumina. *Light Metals* 1987 1987;:139-149.
- [117] Clayton J. Reviewing current practice in powder testing. *Organic Process Research & Development* 2014; 19:102-109.
- [118] Visser J. Van der waals and other cohesive forces affecting powder fluidization. *Powder Technology* 1989; 58:1-10.
- [119] Shi H, Mohanty R, Chakravarty S, Cabisco R, Morgeneyer M, Zetzener H, Ooi JY, Kwade A, Luding S, Magnanimo V. Effect of particle size and cohesion on powder yielding and flow. *KONA Powder and Particle Journal* 2017; 2018014.
- [120] Heitbrink WA. Factors affecting the Heubach and MRI dustiness tests. *American Industrial Hygiene Association Journal* 1990; 51:210-216.
- [121] Forsythe W, Hertwig W. Attrition characteristics of fluid cracking catalysts. *Industrial & Engineering Chemistry* 1949; 41:1200-1206.
- [122] Olsen D. Alumina dustiness related to physical quality parametersuser experience and R&D in Hydro Aluminium. In *Fifth International Alumina Quality Workshop*, Bunbury, WA, Australia 1999, pp. 1-11.
- [123] Nabeel M, Liu H, Karasev A, Jönsson P. Dust generation due to mechanical wear of iron ore pellets. *Jernkontoret Teknisk Slutrapport Final report (energimyndigheten.se)*

- [124] Chakravarty S, Fischer M, García-Triñanes P, Parker D, Le Bihan O, Morgeneyer M. Study of the particle motion induced by a vortex shaker. *Powder Technology*. 2017 Dec 1; 322:54-64.
- [125] Lanning JS, BOUNDY MG, Leith D. Validating a model for the prediction of dust generation. *Particulate science and technology* 1995; 13:105-116.
- [126] Bansal RK. A textbook of fluid mechanics. Firewall Media; 2005.
- [127] Jiang X, Lai CH. Numerical techniques for direct and large-eddy simulations. CRC Press; 2016 Apr 19.
- [128] Tabatabaian M. CFD Module: Turbulent Flow Modeling. Mercury Learning & Information, 2015.
- [129] Van Wachem BG, Schouten JC, Krishna R, Van den Bleek CM. Validation of the Eulerian simulated dynamic behaviour of gas–solid fluidised beds. *Chemical Engineering Science* 1999; 54:2141-2149.
- [130] Prasad S, Gautam A. Role of momentum exchange coefficient in circulating fluidized-bed. *Indian Journal of Chemical Technology* 2007; 14(3):258-62.
- [131] Santos DA, Petri IJ, Duarte CR, Barrozo MA. Experimental and CFD study of the hydrodynamic behavior in a rotating drum. *Powder technology* 2013; 250:52-62.
- [132] Hwang G, Shen H. Modeling the solid phase stress in a fluid-solid mixture. *International Journal of Multiphase Flow* 1989; 15:257-268.
- [133] Lun CK, Savage SB, Jeffrey DJ, Chepuriniy N. Kinetic theories for granular flow: inelastic particles in Couette flow and slightly inelastic particles in a general flowfield. *Journal of fluid mechanics* 1984; 140:223-256.
- [134] Karunarathne SS, Jayarathna CK, Tokheim LA. Mixing and segregation in a rotating cylinder: Cfd simulation and experimental study. *International Journal of Modeling and Optimization* 2017; 7:1.
- [135] Zydak P, Klemens R. Modelling of dust lifting process behind propagating shock wave. *Journal of Loss Prevention in the Process Industries* 2007; 20:417-426.
- [136] Karunarathne SS, Jayarathna CK, Tokheim LA. Mixing and Segregation in a Rotating Cylinder: CFD Simulation and Experimental Study. *International Journal of Modeling and Optimization* 2017 Feb 1; 7(1):1.
- [137] i Z, Kind M, Gruenewald G. Modeling fluid dynamics and growth kinetics in fluidized bed spray granulation. *The Journal of Computational Multiphase Flows* 2010; 2:235-248.
- [138] Esmaili AA, Donohue TJ, Wheeler CA, McBride WM, Roberts AW. Cfd modeling of a coarse particle free falling material stream. 11th International Conference on Bulk Materials Storage, Newcastle, 2013.
- [139] Esmaili A, Donohue T, Wheeler C, McBride W, Roberts A. On the analysis of a coarse particle free falling material stream. *International Journal of Mineral Processing* 2015; 142:82-90.
- [140] Chiesa M, Mathiesen V, Melheim JA, Halvorsen B. Numerical simulation of particulate flow by the Eulerian–Lagrangian and the Eulerian–Eulerian approach with application to a fluidized bed. *Computers & chemical engineering* 2005; 29:291-304.
- [141] Kosinski P, Hoffmann AC, Klemens R. Dust lifting behind shock waves: comparison of two modelling techniques. *Chemical Engineering Science* 2005; 60:5219-5230.
- [142] Kosinski P, Hoffmann AC. An Eulerian–Lagrangian model for dense particle clouds. *Computers & fluids* 2007; 36:714-723.
- [143] Murillo C, Dufaud O, Bardin-Monnier N, L\_opez O, Munoz F, Perrin L. Dust explosions: Cfd modeling as a tool to characterize the relevant parameters of the dust dispersion. *Chemical Engineering Science* 2013; 104:103-116.
- [144] Zhou YQ, Zhang ZS, Yuan GZ. Powder abrasion material in simulated space state [J]. *Materials Science and Engineering of Powder Metallurgy*. 2005; 1.

- [145] Salman A, Hounslow M, Verba A. Particle fragmentation in dilute phase pneumatic conveying. *Powder Technology* 2002; 126:109-115.
- [146] Rhodes MJ, Wang XS, Nguyen M, Stewart P, Liffman K. Use of discrete element method simulation in studying fluidization characteristics: influence of interparticle force. *Chemical Engineering Science* 2001; 56:69-76.
- [147] Cleary PW. Industrial particle flow modelling using discrete element method. *Engineering Computations* 2009; 26:698-743.
- [148] Kwapinska M, Saage G, Tsotsas E. Mixing of particles in rotary drums: A comparison of discrete element simulations with experimental results and penetration models for thermal processes. *Powder Technology* 2006; 161:69-78.
- [149] Alchikh-Sulaiman B, Alian M, Ein-Moza\_ari F, Lohi A, Upreti SR. Using the discrete element method to assess the mixing of polydisperse solid particles in a rotary drum. *Particuology* 2016; 25:133-142.
- [150] Mishra B, Thornton C, Bhimji D. A preliminary numerical investigation of agglomeration in a rotary drum. *Minerals Engineering* 2002; 15:27-33.
- [151] Yang M, Li S, Yao Q. Mechanistic studies of initial deposition of fine adhesive particles on a fiber using discrete-element methods. *Powder technology* 2013; 248:44-53.
- [152] Hiller R, Löffler F. Influence of particle impact and adhesion on the collection efficiency of fibre filters. *German Chemical Engineering* 1980; 3:327-332.
- [153] Lucci F, Ferrante A, Elghobashi S. Is Stokes number an appropriate indicator for turbulence modulation by particles of Taylor-length-scale size? *Physics of Fluids* 2011; 23:025101.
- [154] Chew NY, Chan HK. Influence of particle size, air flow, and inhaler device on the dispersion of mannitol powders as aerosols. *Pharmaceutical Research* 1999; 16:1098-1103.
- [155] Kawaguchi T, Tanaka T, Tsuji Y. Numerical simulation of two-dimensional fluidized beds using the discrete element method (comparison between the two- and three-dimensional models). *Powder technology* 1998; 96:129-138.
- [156] Kloss C, Goniva C, Hager A, Amberger S, Pirker S. Models, algorithms and validation for open-source DEM and CFD-DEM. *Progress in Computational Fluid Dynamics, an International Journal* 2012; 12:140-152.
- [157] Chu KW, Wang B, Xu DL, Chen YX, Yu AB. CFD-DEM simulation of the gas-solid flow in a cyclone separator. *Chemical Engineering Science* 2011; 66:834-847.
- [158] Zhong W, Yu A, Liu X, Tong Z, Zhang H. DEM/CFD-DEM modelling of non-spherical particulate systems: theoretical developments and applications. *Powder Technology* 2016; 302:108-152.
- [159] Derakhshani SM, Schott DL, Lodewijks G. Modeling dust liberation at the belt conveyor transfer point with cfd and dem. In: 11th International Conference on Bulk Materials Storage, Handling and Transportation, ICBMH 2013. 2013.
- [160] La Marche CQ, Liu P, Kellogg KM, Weimer AW, Hrenya CM. A system-size independent validation of CFD-DEM for noncohesive particles. *AIChE Journal* 2015; 61:4051-4058.
- [161] Bagherzadeh M. Modelling single particle settlement by CFD-DEM coupling method. TU Delft Master thesis (<http://resolver.tudelft.nl/uuid:04758dc9-97c8-4449-9556-501d6dd778bb>)
- [162] Tong Z, Zheng B, Yang R, Yu A, Chan H. CFD-DEM investigation of the dispersion mechanisms in commercial dry powder inhalers. *Powder technology* 2013; 240:19-24.
- [163] Hilton J, Cleary P. Dust modelling using a combined CFD and discrete element formulation. *International Journal for Numerical Methods in Fluids* 2013; 72:528-549.
- [164] Brosh T, Kalman H, Levy A. Accelerating CFD-DEM simulation of processes with wide particle size distributions. *Particuology* 2014; 12:113-121.



- [165] Yang Y, Cheng YM. A fractal model of contact force distribution and the unified coordination distribution for crushable granular materials under confined compression. *Powder Technology* 2015; 279:1-9.
- [166] Shigeto Y, Sakai M. Parallel computing of discrete element method on multi-core processors. *Particuology* 2011; 9:398-405.
- [167] Ward M. Dust testing for DSEAR and ATEX compliance. Technical report, Explosion Hazard Testing Limited UK September 2010.
- [168] Nuyttens D, Devarrewaere W, Verboven P, Foqué D. Pesticide-laden dust emission and drift from treated seeds during seed drilling: a review. *Pest management science* 2013; 69:564-575.
- [169] Vardoulakis S, Fisher BE, Pericleous K, Gonzalez-Flesca N. Modelling air quality in street canyons: a review. *Atmospheric environment* 2003; 37:155-182.
- [170] Owoyemi O, Lettieri P, Place R. Experimental validation of eulerian– eulerian simulations of rutile industrial powders. *Industrial & engineering chemistry research* 2005; 44:9996-10004.
- [171] Patankar N, Joseph D. Modeling and numerical simulation of particulate flows by the Eulerian-Lagrangian approach. *International Journal of Multiphase Flow* 2001; 27:1659-1684.
- [172] Di Renzo A, Di Maio FP. Comparison of contact-force models for the simulation of collisions in DEM-based granular flow codes. *Chemical engineering science* 2004; 59:525-541.

## 3 Characterization of bulk properties influencing powder flow and dustiness

### 3.0 Overview

This chapter focuses on characterization of key powder parameters which influence their dustiness in the dry state. Firstly, we present a study discussing the several characterization equipment available for testing the powder flow properties (flowability, cohesivity) which were found to affect dustiness. Furthermore, the effect of powder size and size distribution on dustiness is analysed using a vortex shaker tester. Based on the test results, the powders are classified into 3 groups with varying dust generation behaviour.

From the state of the art, it was established that inter-particle binding forces described as cohesion is predominantly due to the van der Waals forces in dry powders. But, theoretical calculations to predict such attractive forces between two isolated particles is not useful with multi-particle systems with billions of particles. Thus, cohesion needs to be tested using experimental methods such as shear tests. Section 3.1 presents an extensive experimental study using different shear devices, namely the Jenike shear tester, the ELE direct shear tester, the Schulze ring shear tester and the FT4 powder rheometer focussing on the effect of particle size, thus inter-particle forces on powder bulk behaviour.

Section 2 highlights the vortex shaker dustiness tester as a promising equipment suitable for testing dustiness of fine-scale (micro- or smaller) powders with relatively less cost and risks involved with testing such powders using the traditional testers; the rotating drum and the drop test. For Section 3.2, we use the vortex shaker dustiness tester to show the effect of particle size distribution of the powder on respirable aerosol. In order to study this, eight calcium carbonate powders whose median diameter and flowability varies over two orders of magnitude. Their propensity to release respirable aerosol particles differ with respect to the particle size distribution (PSD) of the primary particles. Dustiness of fine cohesive powders shows a correlation with median particle size ( $x_{50}$ ) as well as flowability of the powder. The smaller the primary particles, the more cohesive the powder and the smallest the dust emission. Bi-modal powders with similar flowability but different PSD show similar dustiness behaviour with the powder consisting of largest fraction of particles (by volume) in the 1st mode (particularly in the respirable fraction) releases the maximum dust particles. The powder sample made of larger primary particles was the least dusty powder and its initial release might be due to the attrition of large primary particles.

### 3.1 Article (published in KONA Powder and Particle journal, 2017):

## Effect of Particle Size and Cohesion on Powder Yielding and Flow

Hao Shi<sup>1</sup>, Rahul Mohanty<sup>2,4</sup>, **Somik Chakravarty**<sup>3</sup>, Ramon Cabisco<sup>2</sup>, Martin Morgeneyer<sup>3</sup>, Harald Zetzener<sup>2</sup>, Jin Y. Ooi<sup>4</sup>, Arno Kwade<sup>2</sup>, Stefan Luding<sup>1</sup> and Vanessa Magnanimo<sup>1</sup>

<sup>1</sup> *Multi-Scale Mechanics (MSM), Faculty of Engineering Technology (ET), MESA+, University of Twente, The Netherlands*

<sup>2</sup> *Institute for Particle Technology (iPAT), TU Braunschweig, Germany*

<sup>3</sup> *Laboratoire Transformations Intégrées de la Matière Renouvelable (TIMR), Université de Technologie de Compiègne (UTC) Sorbonne Universités, France*

<sup>4</sup> *Institute of Infrastructure and Environment, School of Engineering, University of Edinburgh, UK*

#### 3.1.1 Abstract

The bulk properties of powders depend on material characteristics and size of the primary particles. During storage and transportation processes in the powder processing industry, the material undergoes various modes of deformation and stress conditions, e.g., due to compression or shear. In many applications, it is important to know when powders are yielding, i.e. when they start to flow under shear; in other cases it is necessary to know how much stress is needed to keep them flowing. The measurement of powder yield and flow properties is still a challenge and will be addressed in this study.

In the framework of the collaborative project T-MAPPP, a large set of shear experiments using different shear devices, namely the Jenike shear tester, the ELE direct shear tester, the Schulze ring shear tester and the FT4 powder rheometer, have been carried out on eight chemically-identical limestone powders of different particle sizes in a wide range of confining stresses. These experiments serve two goals: i) to test the reproducibility/consistency among different shear devices and testing protocols; ii) to relate the bulk behaviour to microscopic particle properties, focusing on the effect of particle size and thus inter-particle cohesion.

The experiments show high repeatability for all shear devices, though some of them show more fluctuations than others. All devices provide consistent results, where the FT4 powder rheometer gives lower yield/steady state stress values, due to a different pre-shearing protocol. As expected, the bulk cohesion decreases with increasing particle size (up to 150  $\mu\text{m}$ ), due to the decrease of inter-particle cohesion. The bulk friction, characterized in

different ways, is following a similar decreasing trend, whereas the bulk density increases with particle size in this range. Interestingly, for samples with particle sizes larger than 150  $\mu\text{m}$ , the bulk cohesion increases slightly, while the bulk friction increases considerably—presumably due to particle interlocking effects—up to magnitudes comparable to those of the finest powders. Furthermore, removing the fines from the coarse powder samples reduces the bulk cohesion and bulk density, but has a negligible effect on the bulk friction.

In addition to providing useful insights into the role of microscopically attractive, van der Waals, gravitational and/or compressive forces for the macroscopic bulk powder flow behaviour, the experimental data provide a robust database of cohesive and frictional fine powders for industrially relevant designs such as silos, as well as for calibration and validation of models and computer simulations.

**Keywords:** cohesive powders, shear testers, yield locus, bulk friction, bulk cohesion, particle size effect, T-MAPPP, database

### 3.1.2 Introduction

Granular materials are omnipresent in our daily life and widely used in various industries such as food, pharmaceutical, agriculture and mining. Interesting granular phenomena like yielding and jamming (Liu and Nagel, 1998; Bi et al., 2011; Luding, 2016; Kumar and Luding, 2016), dilatancy (Cates et al., 2005; Van Hecke, 2009; Yang et al., 2015), shear-band localization (Alshibi and Sture, 2000; Singh et al., 2014), history-dependence (Thakur et al., 2014), and anisotropy (Radjai et al., 1996; Majmudar and Behringer, 2005) have attracted significant scientific interest over the past decades (Savage and Hutter, 1989; Cundall, 1989; Radjai et al., 1999; Wolf et al., 2000; GDR-MiDi, 2004; Tomas, 2005; Alonso-Marroquin and Herrmann, 2004; Luding 2005a, b, 2008). Various laboratory element tests can be performed to study the bulk behaviour of granular materials (Schwedes, 2003). Element tests are also a valuable tool to understand the influence of particle properties, e.g. density, size-distribution and shape, on the macroscopic bulk response. Moreover, such element tests are commonly used for the industrial designs of silos (Jenike, 1967; Schwedes and Schulze, 1990; Schulze, 2003a).

Element tests are (ideally homogeneous and isotropic) macroscopic tests in which the force (stress) and/or displacement (strain) path are controlled. The most widely performed element test in both industry and academia is the shear test, where a granular sample is sheared until failure is reached and the material starts to flow. Shear testers are usually classified into two groups: direct and indirect methods (Schwedes, 2003; Schwedes and Schulze, 1990). In direct shear testers, the shear zone is pre-defined by the device design, and the shear failure is forced in a specific physical location. On the contrary, in the indirect devices, the shear zone

develops according to the applied state of stress. The most common indirect devices are the uni-axial compression tester (Russell et al., 2014; Thakur et al., 2014; Imole et al., 2016) and bi-axial shear box (Morgeneyer et al., 2003; Morgeneyer and Schwedes, 2003; Feise and Schwedes, 1995). Direct devices can be further categorised into two sub-groups: translational and rotational. Typical translational shear testers include the direct shear tester (Casagrande, 1936; Schwedes, 1979; Shibuya et al., 1997) and the Jenike shear tester (Jenike, 1964), while torsional or rotational shear testers include the FT4 powder rheometer (Freeman, 2007), the Schulze ring shear tester (Schulze, 1994) and the Brookfield powder flow tester (Berry et al., 2015). Detailed reviews of testers have been presented by several authors (Schwedes, 2003; Tsunakawa and Aoki, 1982; Schulze, 2008), and more (non-commercial) shear testers with higher complexity can be found in literature (Harder and Schwedes, 1985; Janssen and Zetzener, 2003; Bardet, 1997).

Quality and reproducibility of results are key aspects for proper material characterization. Although shear testing technologies have been developed and studied extensively, significant scatter in measurements is still common when testing powder flowability using different devices in different labs/environments (Freeman, 2007; Schulze, 1994; Berry et al., 2015; Schulze, 2001; Kamath et al., 1993; Kamath et al., 1994). Previous studies have been focusing on this problem by performing round-robin experimental studies on the Jenike tester (Akers, 1992), the Schulze ring shear tester (Schulze, 2001) and the Brookfield powder flow tester (Berry et al., 2015) as well as comparing different devices (Koynov et al., 2015). The earliest round-robin study (Akers, 1992) resulted in a certified material (CRM-116 limestone powder) and a common standard experimental testing procedure for determining the yield locus. Schulze (Schulze, 2011) has collected 60 yield loci obtained using the small Schulze shear tester RST-XS (21 labs) and 19 yield loci using the large Schulze shear tester RST-01 (10 labs) on one limestone powder (CRM-116). Results have been compared among them as well as with the results from reference Jenike tester. While results from RST-01 and RST-XS are in good agreement, a considerable deviation (up to 20 %) was observed when comparing results from the Schulze ring (direct rotational) shear tester to the Jenike (direct translational) shear tester. Similar outputs are found by other researchers (Berry et al., 2015; Koynov et al., 2015; Salehi et al., 2017), where yield loci from the Brookfield powder flow tester, the Schulze ring shear tester, the FT4 powder rheometer and the Jenike shear tester are compared. The Brookfield powder flow tester and the FT4 powder rheometer show systematically lower shear responses in comparison to the other two shear testers.

Other studies have compared different industrially relevant powders but only in a single device (Teunou et al., 1999; Fitzpatrick et al., 2004). Moreover, these comparative studies have

been limited to relatively low stresses. A deeper understanding of the flow behaviour of powders in several shear devices over a wide stress range is still missing.

Our collaborative network, EU/ITN T-MAPPP ([www. t-mapp.eu](http://www.t-mapp.eu)), offers the unique possibility to shed light on the complex topic of powder yielding and flow, extending beyond the boundaries of previous projects. The network involves 16 partners in both academia and industry across Europe. The present study has multiple goals. Firstly, we want to investigate the consistency and repeatability of yield loci measurements between commonly used shear testers. This can provide a robust platform to establish the reliability of the testing methodology and procedures. Secondly, we aim to study the influence of cohesion on powder flowability by testing powders that have same chemical composition but different particle size, leading to different degrees of bulk cohesion. Finally, once the agreement between the shear devices is established, measurements can be combined to characterise the powders over a wider stress range, which is not achievable with a single device. To achieve this goal, a systematic study has been carried out by testing 8 powders (Eskal limestone with median particle diameter from 2.2 to 938  $\mu\text{m}$ ) in 5 shear testers (the Jenike Shear Tester, the Direct Shear Tester, the Schulze Ring Shear Tester with two shear cell sizes, and the FT4 Powder Rheometer) at 4 partner locations by different operators. Limestone powder has been chosen due to its negligible sensitivity towards humidity and temperature changes.

The work is structured as follows: In section 3.1.3, we provide information on the limestone samples/materials, in section 3.1.4 the description of the experimental devices and in section 3.1.5 the test procedures are shown. Sections 3.1.6 and 3.1.7 are devoted to the discussion of experimental results with focus on shear devices and materials, respectively, while conclusions and outlook are presented in section 3.1.8.

### **3.1.3 Material description and characterization**

In this section, a brief description of the limestone samples along with their material properties is provided. Eight size grades with the same chemical composition, i.e. Eskal limestone (calcium carbonate), are used, with median particle sizes that almost span three orders of magnitude from  $\mu\text{m}$  to mm.

The Eskal series (KSL Staubtechnik GmbH, Germany) is extensively used in many fields including construction and automotive industries. Eskal is also used as a reference powder for standard testing and calibration of equipment in powder technology, for instance, shear testers (Feise, 1998; Zetzener and Schwedes, 2002) and optical sizing systems due to the favourable physical properties: high roundness, low porosity and an almost negligible sensitivity towards humidity and temperature changes, which allows to avoid sample pre-treatment.

Table 3-1 summarizes the physical properties of the Eskal samples. Median particle size  $d_{50}$  ranges from 2.22  $\mu\text{m}$  (cohesive, sticky primary particles that form clumps) to 938  $\mu\text{m}$  (free-flowing primary particles). In this study, all powders are named with their original commercial name (e.g. Eskal150, Eskal300), except for Eskal K0.1–0.5 and K0.5–0.8 (original product names are Eskal Körnung 0.1–0.5 and Körnung 0.5–0.8), which for sake of brevity, is referred to as “K”. The particle size distributions were determined by laser diffraction (HELOS + RODOS, Sympatec GmbH) with the dry dispersion unit. The span of the particle size distribution decreases with increasing particle size from 1.52 to 0.7, whereas the initial bulk density (bulk density measured directly after filling) increases from 540 to 1400  $\text{kg/m}^3$ . Primary particle density  $\rho_p$  is measured using a helium pycnometer at 0.9 % moisture content and is found to be independent of size. Particle roundness, which is the ratio of the perimeter of the equivalent circle to the real perimeter of the projected primary particle, was measured with the Sympatec-QICPIC imaging system. The working principle of this technique consists of a high-speed image analysis sensor capable of capturing 500 frames per second with low exposure time below 1 ns; this set-up allows to capture and measure with a high detail size and shape information of an extremely large number of particles in the size range of 1  $\mu\text{m}$  to 30 mm (Witt et al., 2006). Values are the average over approximately the range between 20000 and 8000000 particles, depending on the median size of primary particles in the powders. The median particle size,  $d_{50}$ , is used in the following as reference to the different Eskal samples.

*Table 3-1: Material parameters of the experimental samples. The initial bulk density represents bulk density from raw materials. Here, K0.1–0.5 means Körnung 0.1–0.5, which follows the commercial product naming. The initial bulk density values are provided by the manufacturer.*

Property (Eskal)	Symbol	Unit	300	500	15	30	80	150	K0.1–0.5	K0.5–0.8
Particle size by volume	$d_{10}$	$\mu\text{m}$	0.78	1.64	12	21	39	97	4.5	738
	$d_{50}$	$\mu\text{m}$	2.22	4.42	19	30	71	138	223	938
	$d_{90}$	$\mu\text{m}$	4.15	8.25	28	43	106	194	292	1148
Span	$(d_{90}-d_{10})/d_{50}$	[-]	1.52	1.50	0.84	0.73	0.94	0.70	1.29	0.44
Particle density	$\rho_p$	$\text{kg/m}^3$	2737	2737	2737	2737	2737	2737	2737	2737
Moisture content	$w$	%	0.9	0.9	0.9	0.9	0.9	0.9	0.9	0.9
Roundness	$\Psi$	[-]	0.75	0.55	0.48	0.66	0.84	0.88	0.74	0.85
Initial bulk density	$\rho_0$	$\text{kg/m}^3$	540	730	1110	1230	1330	1370	1400	1276

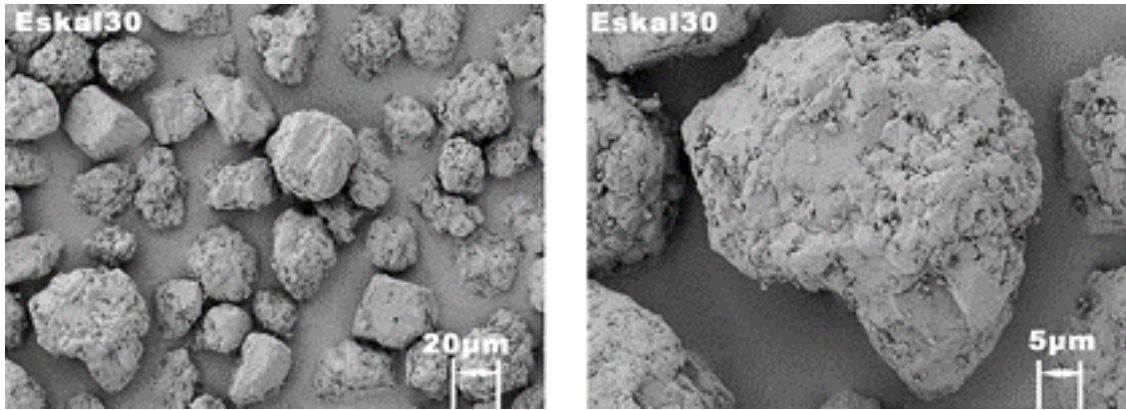


**Figure 3.1:** SEM topography images of Eskal30 ( $d_{50} = 30 \mu\text{m}$ ) in two different length scales as shown in the scale bars.

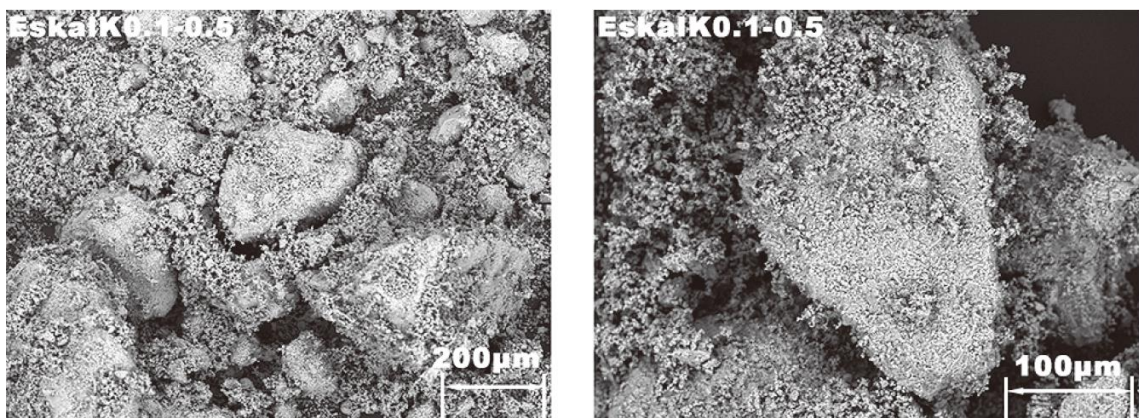


**Figure 3.2:** SEM topography images of Eskal K0.1–0.5 ( $d_{50} = 223 \mu\text{m}$ ) in two different length scales as shown in the scale bars.

Figure 3.1 and Figure 3.2 show the scanning electron microscopy images of Eskal30 and Eskal K0.1–0.5, in two different length scales. The topography of the surfaces are created using secondary electron imaging (SEI) method. In Figure 3.1, we see that all the Eskal30 primary particles have similar shapes (left) and rough surfaces (right). But for Eskal K0.1–0.5, in Figure 3.2, we observe more fines between the coarse particles (left) as well as on the surface (right).

But for Eskal K0.1–0.5, in Figure 3.2, we observe more fines between the coarse particles (left) as well as on the surface (right). The other Eskal samples have mostly similar shapes (difference in the range of 20%, considering the mean values of roundness) irrespective of the median particle size of the samples.



### 3.1.4 Experimental setup

Many testers have been devised for measuring the yielding and flow properties of bulk solids in the last 70 years, ranging from the Jenike Shear Tester to the semi-automated or fully automated testers that are being developed in the present days (Carr and Walker, 1968). Here we present a comparison between measurements in five direct shear devices, specifically the two “translational” devices, namely the ELE direct shear tester and the Jenike shear cell, and three “rotational” devices (The Schulze ring shear testers and the FT4 powder rheometer). A detailed comparison between the main features of all testers is shown in Table 3-2 and a comparison of results from all these testers is presented in section 5. Two main characteristics of these devices are the degree of automation and the normal stress regime. The Schulze ring shear tester and the FT4 powder rheometer are in most of the operational stages completely automated, which strongly reduces the operator influences. The ELE direct shear tester can reach the highest normal stress among all the devices we investigated.

Table 3-2: Specification comparison of the Schulze ring shear tester (RST-1), ELE direct shear tester (DST), FT4 powder rheometer (FT4) and Jenike shear cell (Jenike). The actual shear velocities used are indicated in parentheses, stars refer to the default value from control software programs.

Property	Jenike	DST	RST-01	RST-XS	FT4
Cell volume (cm <sup>3</sup> )	189	126	204	31.4	86.4
Cell geometry	cylinder	box	ring	ring	cylinder
Wall material	aluminium	stainless steel	aluminium	aluminium	borosilicate glass
Diameter ( <i>D</i> ) or Length ( <i>L</i> ) (cm)	9.3	6	6 (inner) 12 (outer)	3.2 (inner) 6.4 (outer)	5
Height ( <i>H</i> ) (cm)	2.8	3.5	2.4	1.3	4.4
Aspect ratio <i>H/D</i> or <i>H/L</i>	0.30	0.58	0.27	0.27	0.88
Shear displacement limit (mm)	8	10	Unlimited	Unlimited	Unlimited
Test control	Manual	Manual	Computer	Computer	Computer
Sample weighing	Offline	Offline	Offline	Offline	On-board
Compression device	Top lid	Top lid	Top ring	Top ring	Vented piston
Driving velocity	1-3 (2) (mm/min)	0.001-2 (2) (mm/min)	0.0038-22.9 (*) (°/min)	0.0038-22.9 (*) (°/min)	6-18 (6) (°/min)
Max. normal stress (kPa)	10-30	2778	50	20	22
Sample conditioning before pre-shear	Pluviation (manual)	Pluviation (manual)	Pluviation (manual)	Pluviation (manual)	Rotated blade (automatic)
Yield locus test duration	2 hours	2 hours	20 minutes	20 minutes	30 minutes
Stress measure direction	Horizontal	Horizontal and vertical	Rotational and vertical	Rotational and vertical	Rotational

### 3.1.4.1 Jenike shear tester

The Jenike tester is a direct translational shear tester, developed in the 1960s (Jenike, 1964) and it is recognized as one of the industrial standards for designing reliable bulk solids handling equipment such as storage bins, silos and hoppers. The tester consists of a shear cell ( $D = 93 \text{ mm}$ ) which includes a closed-bottom hollow base fitted to a fixed bearing plate. A shear ring capable of moving horizontally is placed over the base with a top lid, used to close the cell, see Figure 3.3(a). The shear cell is filled with the test sample, which rests within the base and the shear ring, as shown in Figure 3.3(b). A normal force is applied to the shear lid by loading weight on a hanger. A shear force is then applied using a bracket and a pin on the shear ring. The bulk solid undergoes shear deformation due to the simultaneous displacement of the upper ring and the lid against the stationary bottom ring. The stem is moved by a motor at a constant speed of around 1–3 mm/minute and the shear force is measured by a force transducer and is recorded on a computer.

For conducting a shear test, a sample of powder is uniformly filled into the shear cell using a spatula and/or a sieve. The sample is initially pre-consolidated by twisting a special lid covering the powder bed under a certain normal load. Then the lid and the filling ring are replaced with a shear lid and the pre-consolidated sample is pre-sheared until a steady state flow is reached, which is defined as a state of constant shear force and bulk density for a given normal stress. After retracting the shear stem and reducing the normal load, the shearing process is re-initiated under a reduced normal load until a maximum shear stress is recorded. This peak value represents a single point on the yield locus. The pre-shear and shear process is repeated for lower normal loads in order to get the complete yield locus. A more detailed description of the standard testing procedure is reported in the ASTM standard D-6128 (ASTM-D6128, 2006). The laborious work of filling and sample conditioning as well as a potential influence of the operator are the major drawbacks of this technique.

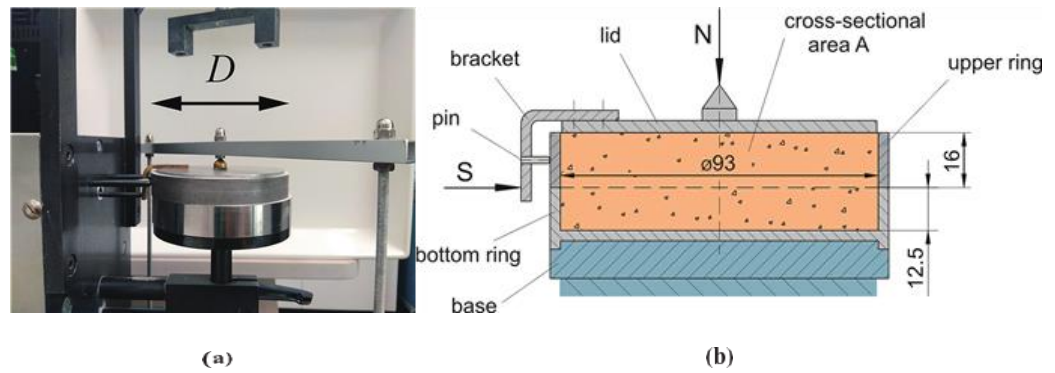


**Figure 3.3:** (a) Jenike direct shear tester and (b) the schematic representation of the Jenike shear cell. For technical details see Table 3-2. (b), reprinted with permission from author (Schulze, 2002). Copyright: (2002) Dietmar Schulze

### 3.1.4.2 ELE direct shear tester (DST)

The second direct shear tester (ELE International, United Kingdom), is illustrated in Figure 3.4(a). It operates with specimens with a square cross-section of 60 mm × 60 mm and a height of 30 mm. The apparatus is enclosed in a robustly constructed case. It is designed for and can reach shear stress up to 1250 kPa and normal stress up to 2778 kPa. The speed range is between 0.0001 to 2 mm/min. The ELE direct shear tester is designed for much higher load in soil testing, employs a simple shear principle as the Jenike shear cell, has a larger shear displacement range (up to 12 mm in horizontal direction) and the possibility of reverse box movement.

The shear test sequence starts with the filling of the shear box by dry pluviation of the powder into the box until a height of approximately 40 mm is reached; then the top excess powder is removed by a scraper to ensure that the top surface of the sample is flat. Finally the top lid is mounted and the powder sticking to the sides of the box is removed carefully using a small paint brush. In addition to the typical direct shear testers as listed in Sec. 3.1, the main drawback for this tester is the possible ejection of powder through the inter-quadrant opening. In order to compare results in DST with other devices properly, shear tests in this study are performed following the same ASTM standard D-6128 (ASTM-D6128, 2006) as in Jenike shear tester. For the steady state test, in analogy to the normal wall friction procedure, the sample is first sheared to steady state at the highest normal load chosen. Then step by step the normal load is decreased and shear is continued until steady state is reached.

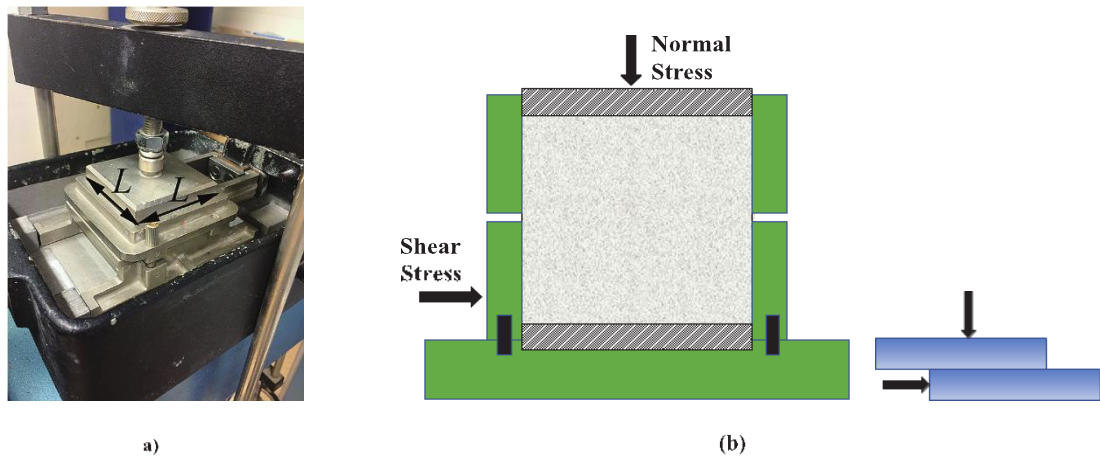


**Figure 3.4:** (a) The ELE direct shear tester and (b) the schematic representation of the ELE direct shear cell setup. For technical details see Table 3-2.

### 3.1.4.3 Schulze ring shear tester—RST-01 and RST-XS

Among the shear devices for powder characterization, the Schulze rotational ring shear tester (1994) is one of the most widely used testers. The Schulze ring shear tester (RST-01) operates connected to a personal computer running a control software that allows the user to obtain, among other things, yield loci and wall yield loci. A smaller version of the ring shear tester with exactly the same working principle is the so-called RST-XS, developed for smaller specimen volumes (3.5 ml to 70 ml, rather than 204 ml for the RST-01). For both testers, ring-shaped (annular) bottom ring of the shear cell contains the bulk solid specimen. An annular-shaped lid is placed on top of the bulk solid specimen and it is fixed at a cross-beam (Figure 3.5).

A normal force,  $F_N$ , is exerted on the cross-beam in the rotational axis of the shear cell and transmitted through the lid onto the specimen. Thus a normal stress is applied to the bulk solid. In order to allow small confining stress, the counterbalance force,  $F_A$ , acts in the centre of the cross-beam, created by counterweights and directed upwards, counteracting the gravity forces of the lid, the hanger and the cross-beam. Shearing of the sample is achieved by rotating the bottom ring with an angular velocity  $\omega$ , whereas the lid and the cross-beam are prevented from rotation by two tie-rods connected to the cross-beam. Each of the tie-rods is fixed at a load beam, so that the forces,  $F_1$  and  $F_2$ , acting on the tie-rods can be measured. The bottom of the shear cell and the lower side of the lid are rough in order to prevent sliding of the bulk solid on

these two surfaces. Therefore, rotation of the bottom ring relative to the lid creates a shear deformation within the bulk solid. Through this shearing the bulk solid is deformed, and thus a shear stress  $\tau$  develops, proportional to the forces on the tie-rods ( $F_1 + F_2$ ). All the tests performed here follow the ASTM standard (ASTM-D6773-16, 2008).

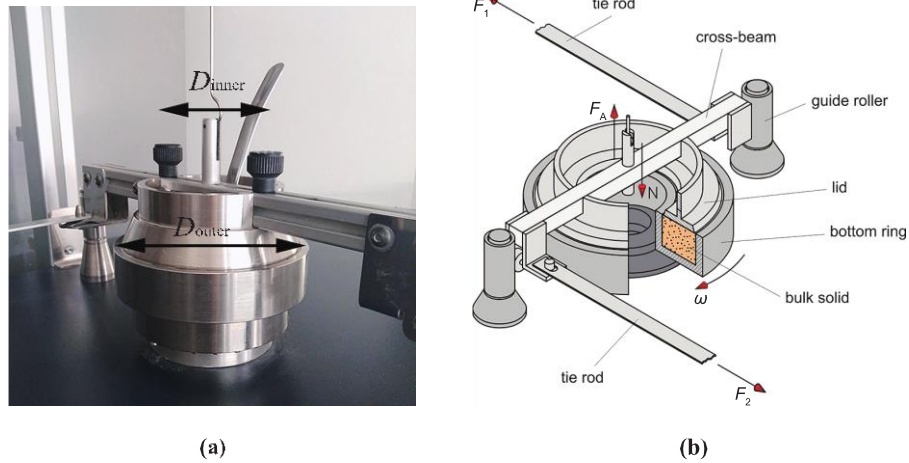


**Figure 3.5:** (a) The Schulze ring shear tester RST-01 and (b) the working principle of the Ring shear cell setup. The difference between RST-XS and RST-XS is the shear cell size. For technical details see Table 3-2. Figure 3.5(b), reprinted with permission from author (Schulz, 2003b). Copyright: (2003) Dietmar Schulze.

#### 3.1.4.4 FT4 powder rheometer

The last experimental equipment used in this work is the FT4 Powder Rheometer (Freeman technology Ltd., UK), depicted in Figure 3.6(a). Standard accessories for the shear test include the 50-mm-diameter blade for sample conditioning, the vented piston for compression, the shear head for the shearing process and the 50-mm-high with 50 mm diameter borosilicate test vessel. One advantage of the commercial FT4 Powder Rheometer is the automated nature of the test procedure requiring minimal operator intervention.

The shear test sequence under the ASTM standard D7891 (ASTM-D7891-15, 2015) can be summarized as follows: the test vessel is carefully filled with the powder of interest using a spatula after obtaining the tare weight. The conditioning procedure involves the movement of the conditioning blade into the test sample to gently disturb the powder bed for a user-defined number of cycles before it is removed slowly. A cycle consists of the inward and outward movement of the conditioning blade into the

powder bed with a constant rotation movement all the time. In order to prevent the conditioning blade from touching the base of the vessel, the direction of the blade movement is reversed as soon as it is within 1 mm of the vessel base. It is believed that this creates a uniform, loosely packed test sample that can be readily reproduced (Freeman, 2007).

In this study, we perform three pre-conditioning cycles before the shear tests are carried out (pre-conditioning does not involve a confining stress like in the other 3 testers). The portion of the base insert of the test vessel are excluded from the calculation of the vessel height, leading to a maximum vessel height of 44 mm instead of 50 mm and an aspect ratio  $\alpha$  of 0.88. Subsequent to pre-conditioning, the blade is replaced with a vented piston, which incorporates a stainless steel mesh to allow the enclosed air in the powder to escape uniformly across the surface of the powder bed. The vessel assembly is then split (and thus levelled) after the vented piston executes the compression until the pre-shear normal stress level is reached. Then the powder mass is recorded after splitting to compute the bulk density before the shear tests start. A detailed description of the vessel split-and-leveling procedure is reported by Freeman et al. (2009).

A shear test begins after changing the vented piston to the shear head as shown in Figure 3.6(b). The shear head moves downwards inserting the blades into the powder and induces a normal stress as the shear head bottom surface is in contact with the top of the powder. The shear head continues to move downwards until the required pre-shear normal stress is reached. At this point slow rotation of the shear head begins, inducing an increasing shear stress. As the powder bed resists the rotation of the shear head, the shear stress increases until failure, at the point a maximum shear stress is observed. As a consequence, a shear plane is formed just below the ends of blades. The shear head is kept moving until the shear stress does not change anymore for the pre-shear step and is stopped immediately after the maximum is reached for each shear step. A constant normal stress is maintained throughout each pre-shear or shear step. Note that pre-shear in FT4 is a multi-stage process and will be discussed in the next section. All the tests performed with the FT4 powder rheometer follow ASTM standard (ASTM-D7891-15, 2015).

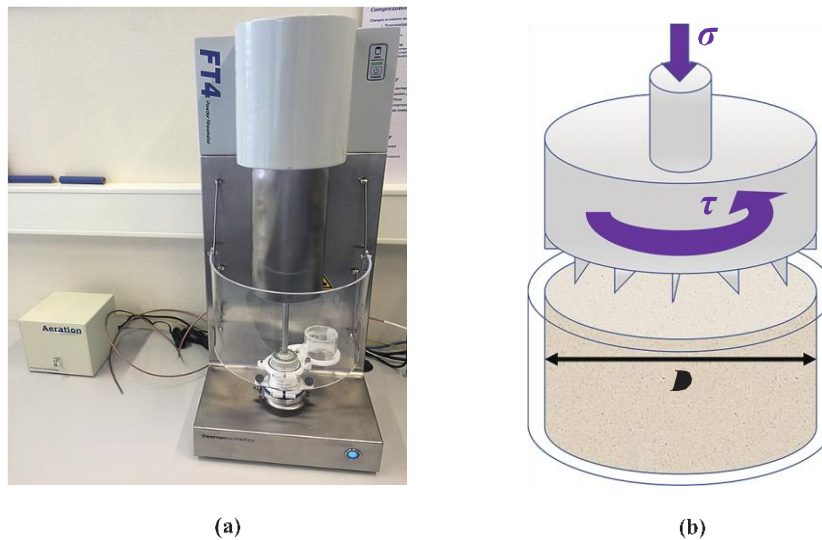


**Figure 3.6:** (a) The FT4 Powder rheometer and (b) the working principle of the FT4 shear cell set-up. For technical details see Table 3-2.

### 3.1.5 Test procedures

In this section, an overview of the testing procedures as well as all the details of the tests performed using shear devices for different limestone specimens are presented.

The diagram in Figure 3.7 illustrates the common testing procedures used for measuring the yield locus. The Schulze ring shear tester RST-01 only requires one single pre-shear cycle before the first shear point and the steady state is reached (Figure 3.7 top). And this pre-shear determination is also similar in the DST and Jenike. However, the FT4 powder rheometer involves multiple pre-shear cycles before the first shear is initiated, and it determines the steady state only when the difference between the end point shear stress values from two consecutive pre-shear cycles is within 1 % (Figure 3.7 bottom). The number of multiple pre-shear cycles in the FT4 usually varies from 4 for cohesive powders to 6 for free-flowing powders. And the influence of this difference on powder flow properties will be further elaborated in Sec. 5.3.



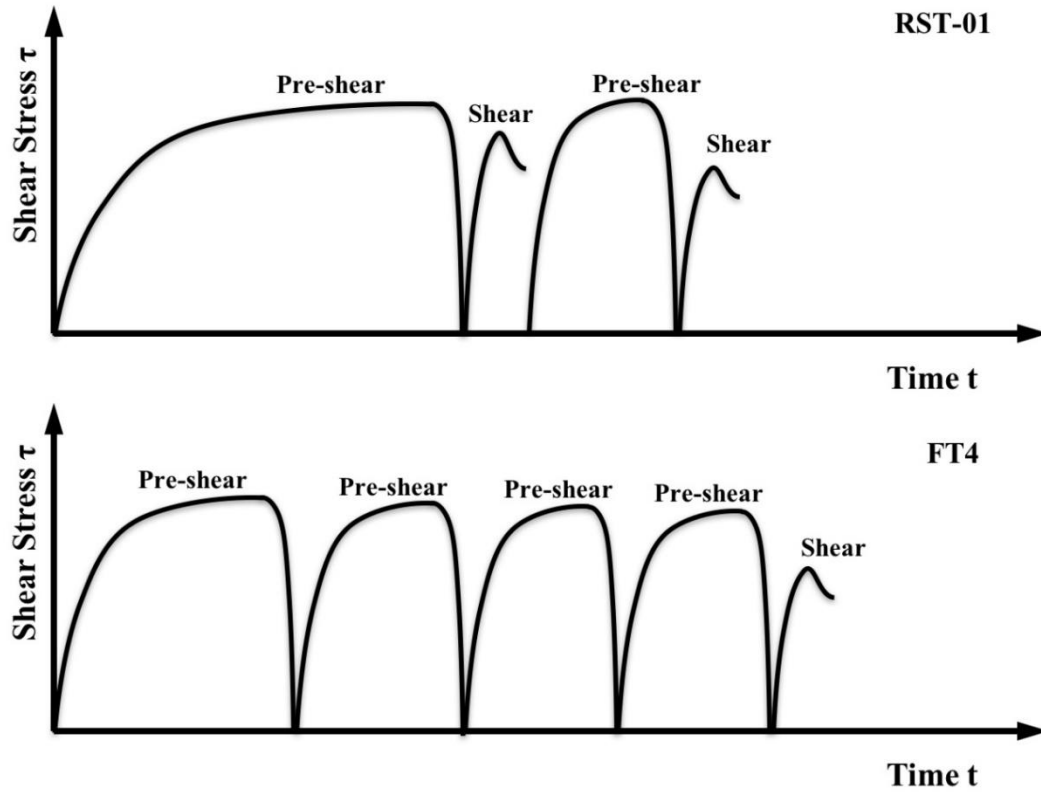
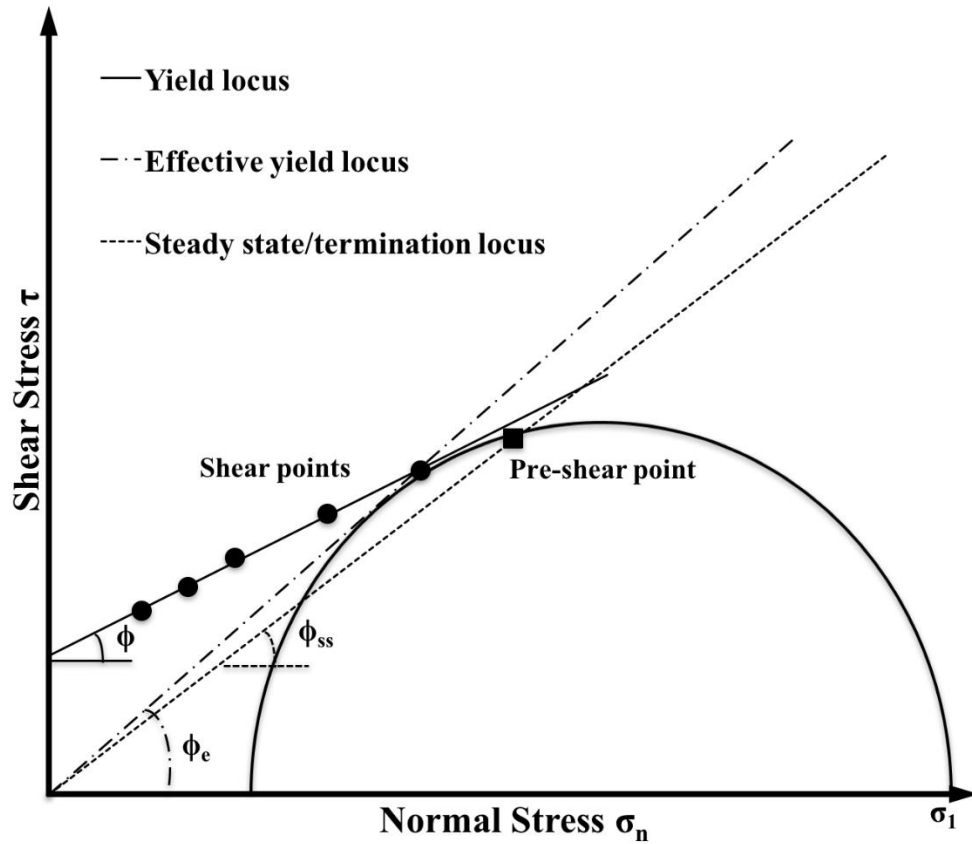


Figure 3.7: Schematic drawing of typical yield locus measurement steps for RST-01 (top) and FT4 (bottom).

The main quantities referred to in this study (linearised effective yield locus, yield locus and steady state/termination locus) are explained in Figure 3.8, where the pre-shear and shear points are the measured values as indicated in Figure 3.7. According to these three loci, three different angles can be determined: effective angle of internal friction,  $\phi_e$ , angle of internal friction,  $\phi$ , and steady state angle of internal friction,  $\phi_{ss}$  as depicted in Figure 3.8 and the details are given by Schulze (2008). The intercept of yield locus for normal stress equals to zero is named as cohesive strength, and it qualitatively indicates the bulk cohesion of a given sample under a given normal stress. Note that all the quantities measured from different testers are using the same definition here.



**Figure 3.8:** Schematic drawing of effective yield locus, yield locus and steady state locus.

Since all the devices investigated here have been designed for different purposes, they are adapted to test the materials in preferable normal stress ranges. In Figure 3.9, we show schematically the range of normal stress that each device can cover with acceptable accuracy. In the same plot, we indicate the extended normal stress ranges of Jenike and DST (dashed lines). For Jenike in higher normal stress range, the data are highly difficult to acquire and less reliable due to insufficient shear path available in shearing direction. On the other hand, low/intermediate normal stress results from DST are less accurate due to the limit of the force sensor. The actual normal stresses used for this study are also highlighted with black dots on the solid lines and summarized in Table A-1. In Figure 3.9, we divide the whole normal stress range into three regimes: i) low normal stress, where Jenike, RST-01/RST-XS and FT4 can be used; ii) moderate normal stress, where RST-01 and FT4 are available; iii) high normal stress that DST and RST-01 can be relied on.

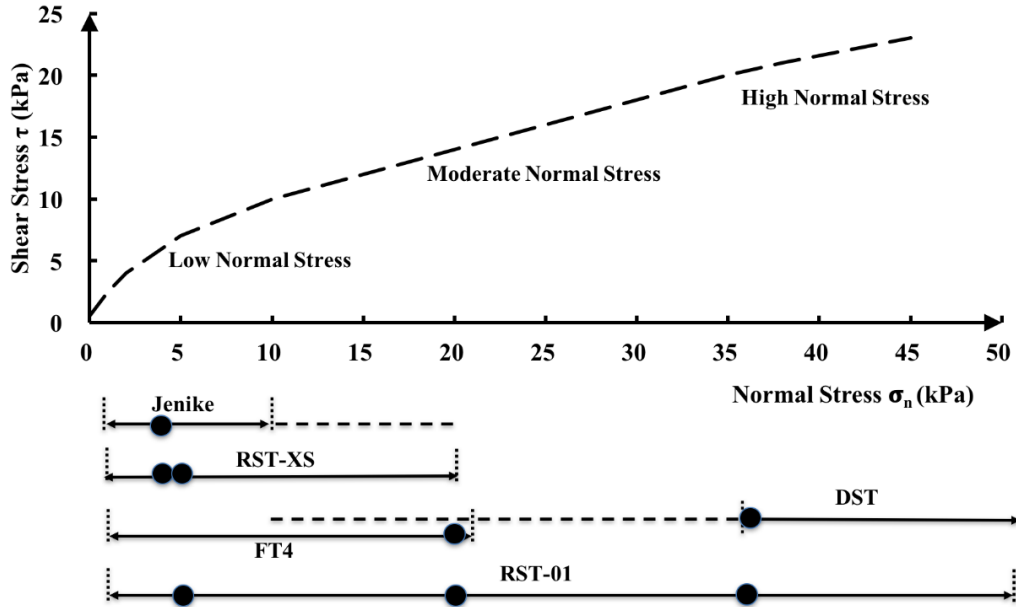


**Figure 3.9:** Schematic drawing of typical yield locus. Black arrows at the bottom: typical normal stress ranges used for each device; dashed lines are extended normal stress limits. Black points indicate the actual normal stress levels used for different shear testers.

The Schulze RST-01 was chosen as a reference device and used to test all 7 Eskal samples at 3 different pre-shear normal stress levels since it covers the widest stress range. A limited number of cases were tested with the other devices depending on the accuracy and material availability. However, for each pre-shear normal stress, tests on one powder have been performed using at least two devices in order to check the reproducibility of the results between the testers. Each test was repeated three times (3 fresh samples) to investigate the repeatability within a single device. Details on the pre-shear and shear normal stress levels used are given in Appendix (Table A-1). In addition, we have also performed steady state locus study using 4 powders in DST. We have chosen a pre-shear normal stress values between 1.4 and 36.1 kPa. The test details are summarized in Table A-2.

### 3.1.6 Comparison of shear devices

In this section, we compare the measurement from different shear devices and a general overview of the repeatability and reproducibility of the test results is given. In order to compare the yield loci from different testers, two limestone powders were chosen as reference powders (see Table 3-3), namely cohesive Eskal300 (2.22  $\mu\text{m}$ ) and free flowing Eskal150 (138  $\mu\text{m}$ ).

*Table 3-3: Summary of the tests performed. The numbering in the table are the number of powders tested with a certain device under a certain pre-shear stress level. For more details, see Table A-1. Note that the values in the parentheses refer to the pre-shear normal stress values used for a specific device.*

Device	Stress (in kPa)		
	Low stress: 5 (4.3)	Moderate stress: 20	High stress: 35 (36.1)
Jenike	2 (4.3)	[-]	[-]
DST	[-]	[-]	4 (36.1)
RST-01	7	8	7
RST-XS	4 (4.3)	[-]	[-]
FT4	[-]	4	[-]

### **3.1.6.1 Low normal stress: Schulze ring shear tester (RST-01) vs Jenike tester**

In the low normal stress regime, we first compare the RST-01 with the standard Jenike tester at pre-shear normal stress of 5 kPa. Each shear point is measured with 3 fresh samples to acquire the standard deviations. The yield loci for Eskal150 (138  $\mu\text{m}$ ) and 300 (2.22  $\mu\text{m}$ ) are shown in Figure 3.10. Both testers show quite good repeat-ability with a higher standard deviation from the Jenike tester. When we look at the individual powders, the agreement between the two shear testers for Eskal150 is good, with the difference increasing slightly with increasing normal stress. The pre-shear stress values are also close within the deviation range. For the finer Eskal300, the discrepancy between the two devices becomes higher, but still within the standard deviation. A big discrepancy is observed for the pre-shear points, where the Jenike shows lower values and higher

standard deviations compared to RST-01. This may be related to the manual control procedure of the Jenike shear cell. Often the pre-shear must be stopped to prevent the risk of running out the shear displacement.

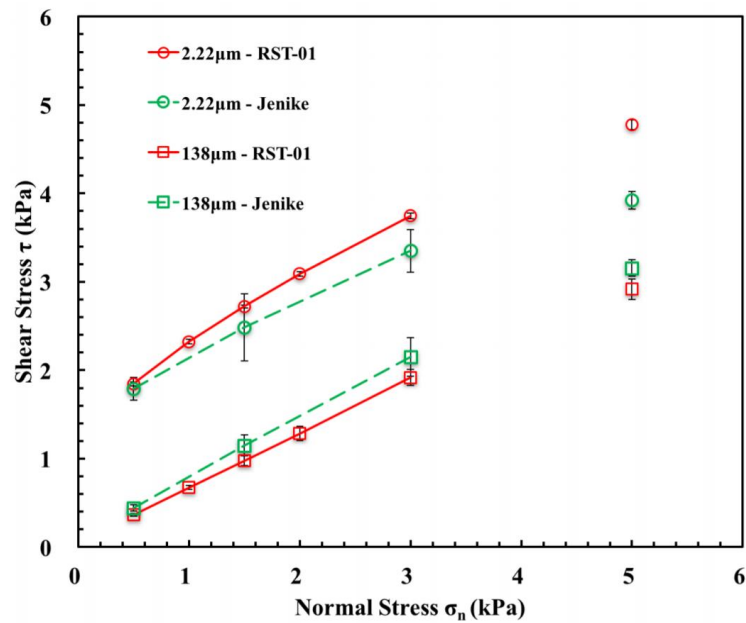


**Figure 3.10:** Yield locus (shear stress versus normal stress) of Es-kal150 (138  $\mu\text{m}$ ) and Eskal300 (2.22  $\mu\text{m}$ ) using RST-01 and Jenike. The pre-shear normal stress is kept at 5 kPa for both devices. Points with and without lines are shear and pre-shear points, respectively. Lines are guides to the eye.

### 3.1.6.2 Low normal stress: Schulze ring shear tester (RST-01) vs (RST-XS)

In the same low normal stress range, we have also tested the two reference powders using the smaller RST-XS, and the data are compared to RST-01 as shown in Figure 3.11. For both devices, the repeatability is very high, with the standard deviations within the symbol size. For the free flowing Eskal150, the yield loci measured by the two devices demonstrate a very good agreement although a slightly different pre-shear normal stresses are used. For the cohesive Eskal300, data from RST-XS are consistently lower than data from RST-01. However, both devices show a non-linear behaviour with the slope (decreasing with increasing normal stress).

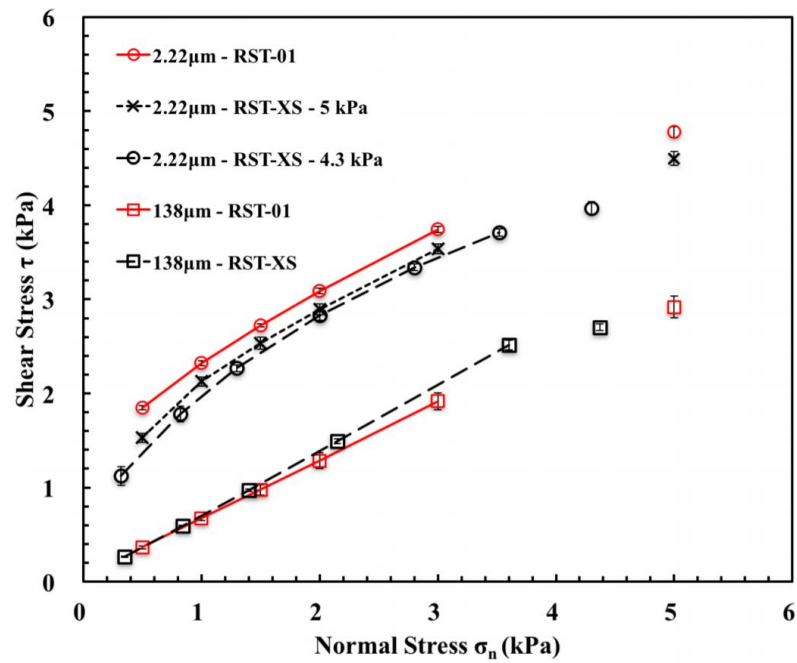


**Figure 3.11:** Yield locus (shear stress versus normal stress) of Es-kal150 (138  $\mu\text{m}$ ) and Eskal300 (2.22  $\mu\text{m}$ ) using RST-01 and RST-XS. The pre-shear normal stresses are set to 5 and 4.3 kPa for RST-01 and RST-XS, respectively (Eskal300 has one extra 5 kPa pre-shear using RST-XS). Points with and without lines are shear and pre-shear points, respectively. Lines are guides to the eye. Note that here the data for RST-01 are the same as in Figure 3.10.

To further investigate RST-XS, we have tested Eskal300 in the RST-XS using the same pre-shear and shear stress levels as in RST-01, and results are also plotted in Figure 3.11. We observe that, also in this case of same pre-shear normal stress, the RST-XS values are systematically lower than the RST-01 values (around 5 %). As the only known difference between RST-XS and RST-01 is the shear cell size, our results indicate that the powder response may be influenced by the system size in the case of cohesive material.

### 3.1.6.3 Moderate normal stress: Schulze ring shear tester (RST-01) vs FT4 powder rheometer

In the moderate normal stress regime, we compare the most commonly used rotational shear testers, the RST-01 and the FT4 rheometer. Both testers are automated and allow selection of a pre-shear normal stress value,  $\sigma_{pre}$ , which was set to 20 kPa for our comparison.

The yield loci for Eskal300 and Eskal150 are shown in Figure 3.12. Both the RST-01 and the FT4 show good repeatability for each measurement point, with the standard deviations within the symbol size. For the free-flowing Eskal150, the yield loci measured by the two devices are in very good agreement except for the pre-shear points, where the FT4 gives a much lower value than the RST-01. However, for the cohesive Eskal300, we see a pronounced difference between results obtained by the two devices (around 10–20 %), although the angle of internal friction (slope) between the two devices stays almost the same. A similar trend is observed with the other two cohesive samples: Eskal500 and Eskal15, with the values measured by FT4 systematically lower than the ones from RST-01 (data not shown here, for details see Table A-3 and Table A-4).

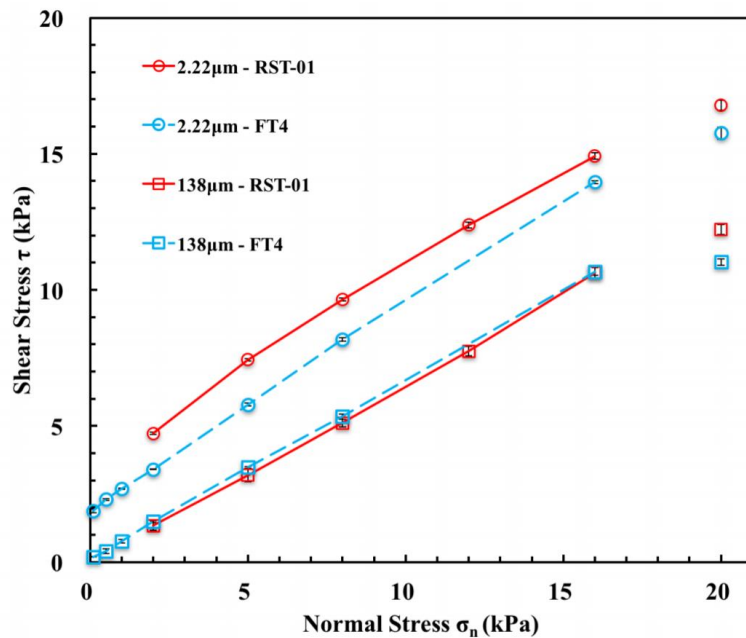


**Figure 3.12:** Yield locus (shear stress versus normal stress) of Eskal150 (138  $\mu\text{m}$ ) and Eskal300 (2.22  $\mu\text{m}$ ) using RST-01 and FT4. The pre-shear normal stress is kept at 20 kPa for both devices. Points with and without lines are shear and pre-shear points, respectively. Lines are guides to the eye.

We associate the difference in the behaviour between the two devices to the test protocols as explained in Sec. 4. The Schulze ring shear tester, based on the ASTM standard D-6773 (ASTM-D6773-16, 2008), uses the conventional pre-shear determination criterion: the steady state shear stress plateau is determined in one pre-shear stage and the following pre-shear stages after incipient flow follows this one pre-

shear state value. On the other hand, for the FT4 powder rheometer, based on the ASTM standard D7891 (ASTM-D7891-15, 2015), several pre-shear cycles are performed until the steady state reaches a constant shear stress value (within 1 % difference). This value is the assumed as pre-shear steady state and the shear stage starts. In the case of cohesive powders, the samples need 3–10 repetitions for the pre-shear to fulfil the steady state criterion in the FT4. This may lead to formation of a pre-defined shear failure plane in the sample that reduces its shearing resistance along the shear direction. We point out here that both shear devices are automated using their own test software where the test protocols are in-built and therefore impossible to change by the users. In addition, there is another significant difference between the two testers in that the Schulze ring shear tester has an annular cross-section where the shear displacement is applied fairly uniformly over the solid shearing surface; whilst the FT4 rheometer has a circular cross-section where the shearing displacement is highly non-uniform with values decreasing towards zero at the centre of the cross-section. It is thus probable that critical shearing state may not be fully achieved particularly near the central zone of the cross-section, thereby producing a smaller overall critical shear stress.

#### ***3.1.6.4 High normal stress: Schulze ring shear tester (RST-01) vs direct shear tester (DST)***

In the high normal stress regime, we compare the reference Schulze ring shear tester (RST-01) with the direct shear tester (DST) as shown in Figure 3.13. The pre-shear stress  $\sigma_{pre}$  is set to 35 kPa for the RST-01 and 36.1 kPa for the DST. This small difference in the pre-shear normal stress applied is due to the design limitation of DST, where one can only change the normal stress discontinuously.



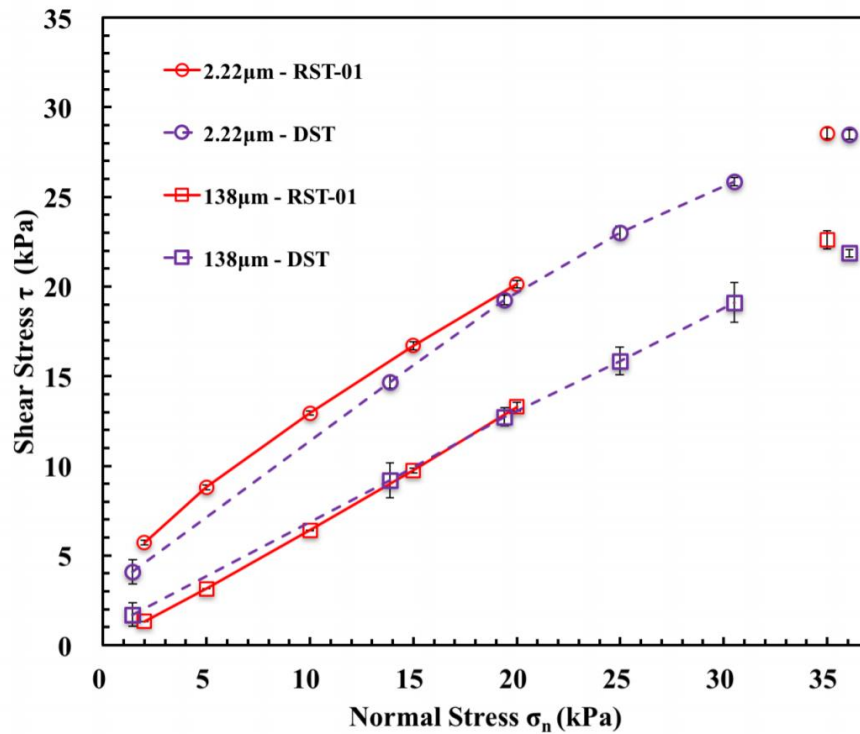


**Figure 3.13:** Yield locus (shear stress versus normal stress) of Es-kal150 (138  $\mu\text{m}$ ) and Eskal300 (2.22  $\mu\text{m}$ ) using RST-01 and DST. The pre-shear normal stresses are kept at 35 and 36.1 kPa for RST-01 and DST, respectively. Points with and without lines are shear and pre-shear points, respectively. Lines are guides to the eye.

As we can see clearly from the figure, the results from DST and RST-01 are in good agreement for both powders. The standard deviation of DST data is higher than the RST-01, and becomes more prominent for low stress levels as well as for the free-flowing sample Eskal150. In the case of pre-shear points, the DST shows a slightly lower value compared to the RST-01, but the difference is negligible. For the yield locus of Eskal150, data from the two devices overlap within the error bars. When we focus on Eskal300, DST underestimates the shear stress values on the yield locus with respect to the RST-01, especially for low normal stresses. We want to point out that the low stress data from DST may be less reliable that the shear force measurement system of DST has a lower limit value of 1 N (1 kPa).

Finally, in order to confirm the reproducibility between the two devices, we further test the steady state shear responses for Eskal K0.1–0.5 and Eskal K0.5–0.8, as shown in Figure 3.14. Results from the two shear devices show good agreements for the

tested two powders, with the data points following the two linearised yield loci within the standard deviations.

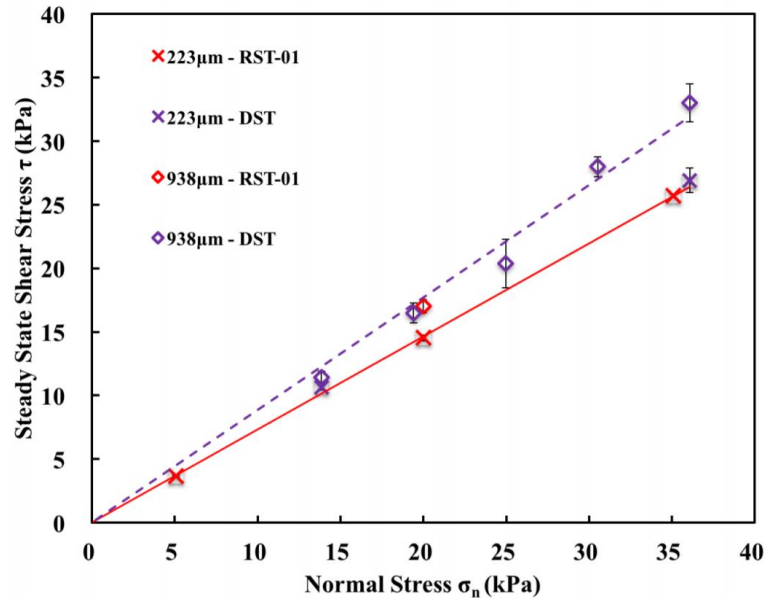


**Figure 3.14:** Steady state locus (shear stress versus normal stress) of Eskal K0.1–0.5 (223  $\mu\text{m}$ ) and K0.5–0.8 (938  $\mu\text{m}$ ) using RST-01 and DST. The lines are the least mean square linear regression to the data with angle  $\phi_{ss} = 36.2^\circ$  for Eskal K0.1–0.5 and  $41.5^\circ$  for Eskal K0.5–0.8.

### 3.1.6.5 Summary of device comparison

In order to validate the consistency of the results obtained from different shear devices, we extrapolate the linearised yield loci and compare both angle of internal friction as well as cohesive strength (interception of linearised yield locus on y-axis) for the two reference powders (Figure 3.15 and Figure 3.16). The data from different shear testers are interpreted in different ways. In the case of the yield locus from the Jenike tester and DST, the shear points are linearised using a least square method, while the RST-01, RST-XS and FT4 are linearised using the de-fault software with pro-rating method. For a free-flowing powder, Eskal150 (138  $\mu\text{m}$ ), we get a good agreement among the RST-01, the RST-XS and the FT4 for the cohesive strength,  $c$ , but higher values from the Jenike and especially from the DST with also larger standard deviations (Figure 3.15(a)). A similar observation is also found for the angle of internal friction as shown in Figure 3.15(b), but the  $\phi$  value obtained from the DST is lower than the other devices. This is caused by the limit of the direct shear tester in the low stress range (below 1.0

kPa). The direct shear tester is initially designed for measuring the strength of soil samples in civil engineering, where the stresses applied are usually high, whereas our tests were performed at much lower stress levels, close to the accuracy limit (around 0.5 kPa) of the force ring on direct shear tester, resulting in a decrease in measurement accuracy for the direct shear tester using free-flowing powders. In the case of the Jenike shear tester, the  $\phi$  value is higher than the other devices, but still within the deviation range.

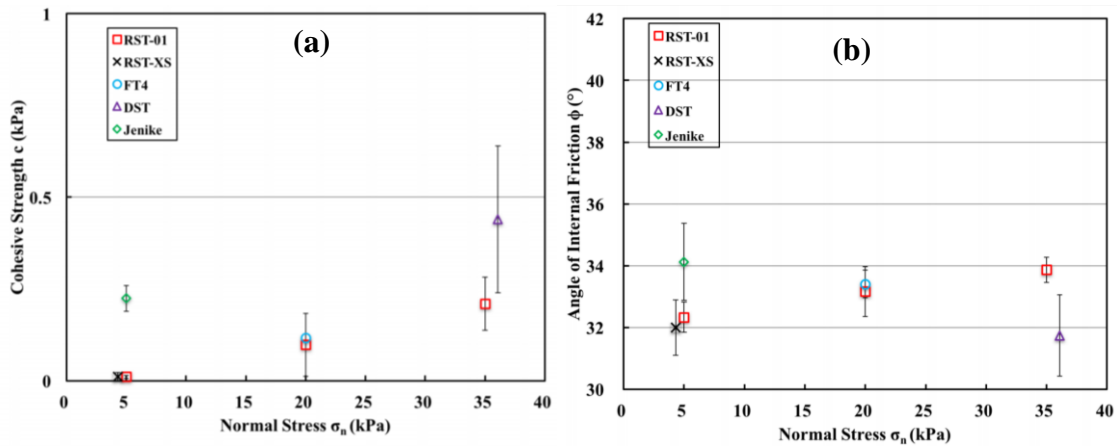


**Figure 3.15:** (a) Cohesive strength,  $c$  and (b) angle of internal friction,  $\phi$ , plotted against normal stress,  $\sigma_n$ , for Eskal150 (138  $\mu\text{m}$ ) tested using all the devices in this study.

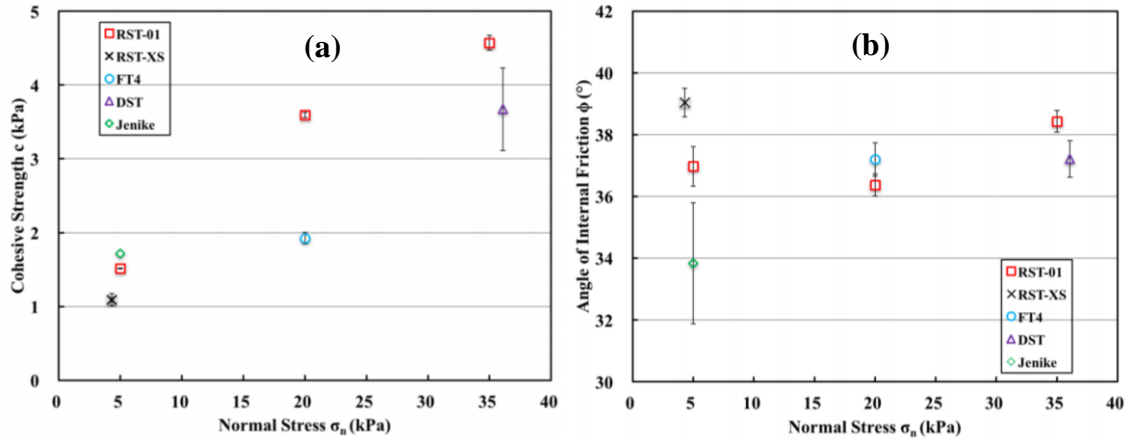


**Figure 3.16:** (a) Cohesive strength,  $c$  and (b) angle of internal friction,  $\phi$ , plotted against normal stress,  $\sigma_n$ , for Eskal300 (2.22  $\mu\text{m}$ ) tested using all the devices in this study.

In Figure 3.16, we investigate the reproducibility of all the devices by looking at the most cohesive Eskal300 powder (2.22  $\mu\text{m}$ ). DST shows a good agreement with the highest standard deviation for cohesive strength,  $c$ , (Figure 3.16(a)). However, the difference between the DST and the RST-01 is around 20 %. The RST-XS, Jenike and the RST-01 have a good agreement but FT4 shows a relatively lower value for  $c$ , thus underestimating the flowability of very cohesive powders. When we look at the  $\phi$  value as shown in Figure 3.16(b), Jenike unexpectedly gives the lowest value with the highest standard deviation. The DST shows slightly lower values than the RST-01 and the FT4 has a good agreement with the RST-01 (within deviation range). Similar behaviour is observed for two other Eskal powders tested using RST-01, RST-XS, FT4 and DST: cohesive Eskal500 and easy-flowing Eskal15 (data are not shown here, see the Tables in Appendix A). Note that the vertical axes of cohesive strength are different in Figure 3.15 and Figure 3.16.

### **3.1.7 Effects of varying particle size**

In this section, we present the comparison of seven Eskal powders tested by the Schulze ring shear tester (RST-01) at different pre-shear stresses as given in Table 3-3. For the analysis of RST-01 data, we used the standard RST-CONTROL 95 software with “N-RHOB-correction” activated (Schulze, 2011). The powder have sizes ranging from 2.22 to 938  $\mu\text{m}$ , and identical chemical composition as explained in Table 3-1. We characterize the above-mentioned seven powders in terms of bulk density, angle of internal friction, cohesive strength, steady state angle of internal friction, effective angle of internal friction and flow function as they are directly measured from the shear tester and is readily displayed in the tester software.

#### ***3.1.7.1 Bulk density at steady state***

As a first step, we look at the dependence of the bulk density on the normal stress and particle size for all the powders. Data are shown in Figure 3.17(a). Zero normal stress (arrows on bulk density axis) corresponds to the initial bulk density of the fresh samples before applying any stresses (provided by the manufacturer). By increasing normal stress,

the bulk density increases for all powders with different rates, higher for small-particle-size powder and almost zero for Eskal80 (71  $\mu\text{m}$ ) and 150 (138  $\mu\text{m}$ ). However, for Eskal K0.1–0.5 (223  $\mu\text{m}$ ), the bulk density increases with increasing normal stress. We associate this trend to the wider particle size distribution (large span value 1.29 as shown in Table 3-1) and the visible huge amount of fines as shown in Figure 3.2. A wider particle size distribution allows easy rearrangement of the packing structure when applying external load.

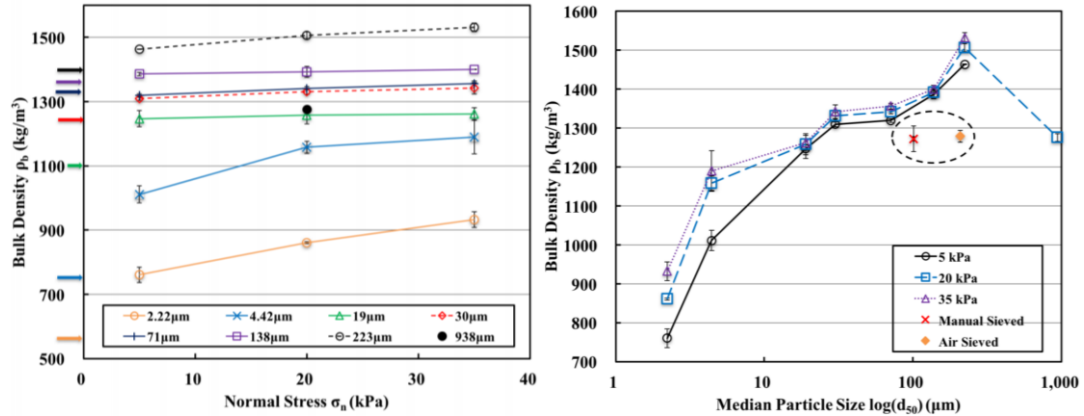


**Figure 3.17:** Bulk density in steady state,  $\rho_b$ , plotted against (a) normal (pre-shear) stress,  $\sigma_n$ , (b) median particle size,  $d_{50}$ . Arrows represent the initial bulk density of the raw samples before stress and shear are applied. Symbols in the dashed area are sieved Eskal K0.1–0.5 (223  $\mu\text{m}$ ) sample sheared at  $\sigma_n = 20 \text{ kPa}$ . Lines are guides to the eye.

In Figure 3.17(b), we plot the bulk density with respect to the median particle size for different normal stresses. We observe an increasing trend with increasing particle size consistent for all normal stresses. This can be explained by the presence of cohesive forces (van der Waals) between primarily particles other than gravitational forces. Since Eskal powders are relatively dry, the presence of liquid bridging and other forces are expected to be small, the dry cohesive interaction will result in forming clusters and create many voids in the bulk, and therefore decrease the bulk density. As cohesive forces become smaller with increasing size, particles will have mainly frictional and gravitational forces without forming clusters and therefore the material can form a denser bulk solid. One extra powder, Eskal K0.5–0.8 (938  $\mu\text{m}$ ), is also tested under 20 kPa normal stress. This powder breaks the trend seen previously and shows a lower bulk density associated with the largest median particle size. In order to investigate further the role of the span in the bulk density behaviour, we perform sieving on the sample with

largest span, Eskal K0.1–0.5 (223  $\mu\text{m}$ ). Two sieving methods are used: standard vibration sieving and high pressure air sieving. The median particle sizes reduce to 101  $\mu\text{m}$  and 208  $\mu\text{m}$ , in the case of vibration sieving and air sieving, respectively. The vibration sieving is only effective in removing the coarse particle but not the fines and thus leads to an increase of the span from 1.289 to 2.173. While the air sieving is effective enough to remove both coarse and fines and decrease the span to 0.395. The bulk densities for Eskal K0.1–0.5 (223  $\mu\text{m}$ ) after sieving are plotted in the dashed area of the same Figure 3.17(b). The bulk density of the sieved samples both decrease to values that are similar to the values of the largest median particle size powder, Eskal K0.5–0.8 (938  $\mu\text{m}$ ). This indicates that for a given median particle size, the span has a dominating effect on the bulk density of a powder.

### ***3.1.7.2 Bulk responses from incipient and steady state flow***

#### ***3.1.7.2.1 Angle of internal friction from incipient flow***

The angle of internal friction describes the bulk friction during incipient flow of a powder, which is determined from the linearised yield locus as shown in Figure 3.8. Although the yield locus for cohesive powder is non-linear by nature, the linearised yield locus can still be used to estimate the angle of internal friction in a certain stress range. This estimated value is one important property that determines the maximum bulk friction of a powder from a given pre-consolidation history. Here, unless specified, all angles of internal friction originate from linearised yield loci.

In Figure 3.18, we plot the angle of internal friction against normal stress at three different pre-shear normal stress and particle size for the 7 powders studied (Eskal K0.5–0.8 is also included here but with only one point). Within the stresses investigated, there is no apparent dependence of the angle of internal friction on the normal stress (Figure 3.18(a)). However, if we focus on the dependence on the particle size as shown in Figure 3.18(b), we observe that when  $d_{50}$  is lower than approximately 30  $\mu\text{m}$ ,  $\phi$  decreases with increasing particle size. Then, for  $30 < d_{50} < 150 \mu\text{m}$ , we observe that the  $\phi$  is almost constant with changing particle size for the three pre-shear normal stresses chosen. Interestingly, if the particle size keeps rising to  $d_{50} < 150 \mu\text{m}$ ,  $\phi$  follows a parallel rise

and achieves similar values to the ones obtained for samples smaller than 30  $\mu\text{m}$ . For Eskal K0.1–0.5 ( $d_{50} = 223 \mu\text{m}$ ), the angle of internal friction increases back to around  $38^\circ$ .

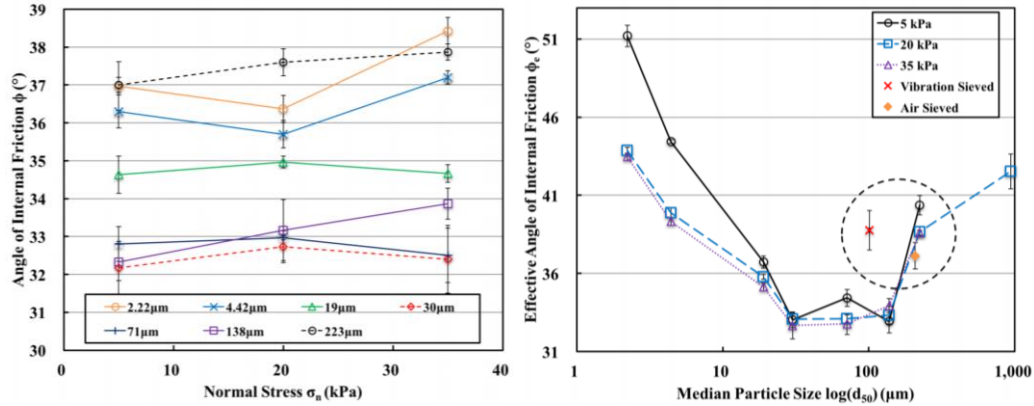


**Figure 3.18:** Angle of internal friction,  $\phi$ , plotted against (a) pre-shear normal stress,  $\sigma_n$ , (b) median particle size,  $d_{50}$ . Symbols in the dashed area are sieved Eskal K0.1–0.5 ( $223 \mu\text{m}$ ) sample sheared at  $\sigma_n = 20 \text{ kPa}$ . Lines are guides to the eye.

We have run several tests/checks with the goal of elucidating the non-monotonic behavior that observed in Figure 3.18(b). First, we further test another sample in the range of  $d_{50} > 150 \mu\text{m}$ , namely Eskal K0.5–0.8 ( $d_{50} = 938 \mu\text{m}$ ), at 20 kPa pre-shear stress. The  $\phi$  value of Eskal K0.5–0.8 increases even further to around  $42^\circ$ . This confirms that the increasing trend is not limited only to a specific sample. As second step, we have measured the angle of internal friction for the two sieved samples obtained after sieving Eskal K0.1–0.5 ( $223 \mu\text{m}$ ) via vibration and air methods that are already introduced in Sec. 6.2.1. While the bulk density strongly reduces after sieving, the angle of internal friction remains unaffected as shown in the dashed area of Figure 3.18(b), which indicates that the span of particle size distribution is not the primary factor influencing the bulk friction. Finally, in order to check the influence of the devices, we have further tested Eskal K0.1–0.5 ( $223 \mu\text{m}$ ) and K0.5–0.8 ( $938 \mu\text{m}$ ) in the direct shear tester (DST), and the results are reported in Figure 3.14. The flow behaviour of both powders are very similar using RST-01 and DST. This agreement clarifies that the behaviour originates from material properties rather than from a specific shear device.

One possible explanation of this interesting behaviour on bulk friction would be that the different size particles have a similar shape (this is visible by comparing the

roundness between Eskal K0.1–0.5 and K0.5–0.8 in Table 3-1) but different surface roughness/asperity, but this has to be further investigated and it is far beyond the scope of this study. Another possibility is the competition between the inter-particle cohesion and inter-particle friction (caused by shape). When the particles are small, the inter-particle cohesion dominates the flow behaviour and enhances the shear resistance. Also when a sample is confined under a given confining stress, if the inter-particle cohesion is high, the sample bulk density will be low, which gives more free spaces for particles to move around. Therefore, the geometrical interlocking does not play an important role here. When the particle size is large, we have almost no influence from inter-particle cohesion and the whole powder is more densely packed, so that the inter-particle friction/interlocking (shape/geometry) is the ruling mechanism of the bulk friction behaviour. For an intermediate particle size, these two effects are both reducing but still competing with each other, and they cannot be distinguished.

#### *3.1.7.2.2 Cohesive strength from incipient flow*

As a complement to the angle of internal friction, one has to also look at the cohesive strength, which is the extrapolated intercept from the linearised yield locus, and gives an indication of the strength of the powder under zero confining stress ( $\sigma_n$ ). In Figure 3.19(a), we plot the cohesive strength against the pre-shear normal stress. As expected, the values of cohesive strength at given stress levels are higher for powders with finer particle size. The cohesive strength of all powders increases with increasing normal stress, but with different slopes. The cohesive strength of the two finest powders, Eskal300 (2.22  $\mu\text{m}$ ) and Eskal500 (4.42  $\mu\text{m}$ ), increase conspicuously with normal stress as we focus on the particle size dependence in Figure 3.19(b), we see a monotonically decreasing bulk cohesion with increasing particle size for all the normal stress levels investigated. However, the cohesive strength for raw Eskal K0.1–0.5 (223  $\mu\text{m}$ ) increases above this trend (as shown in the dashed area in the figure). This apparent discrepancy was also observed in the bulk density and the angle of internal friction, as explained earlier. We further investigated this behaviour by sieving the sample using different techniques. It seems that our air sieving procedures are effective and reduce the cohesive strength of the powder by separating the fines from the coarse fractions. The theory that



smaller particles have the strongest cohesive forces, acting most effectively on each other, is consistent with the strongest decrease in cohesion for the air-sieved samples in which the fines are most effectively removed. The observation of removing fines reduces bulk cohesion but does not affect bulk friction supports the hypothesis that frictional flow behaviour of powders in the range of  $d_{50} > 150 \mu\text{m}$  is governed by particle interlocking.

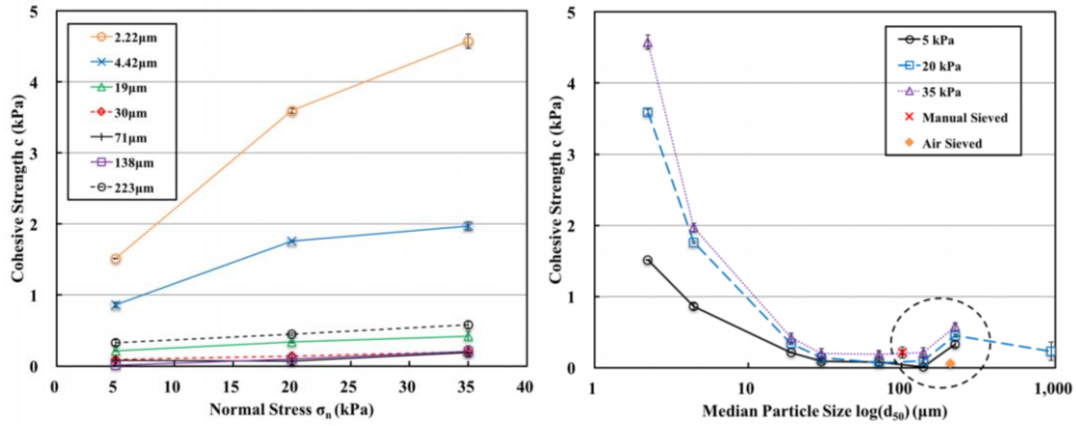


**Figure 3.19:** Cohesive strength,  $c$ , plotted against (a) pre-shear normal stress,  $\sigma_n$ , (b) median particle size,  $d_{50}$ . Symbols in the dashed area are sieved Eskal K0.1–0.5 (223  $\mu\text{m}$ ) sample sheared at  $\sigma_n = 20 \text{ kPa}$ . Lines are from the fit-ted function:  $c(d_{50}) = \sigma_{pre}^* (d_c/d_{50})$  with  $d_c = 0.6919, 0.3953$  and  $0.2809 \mu\text{m}$  for  $\sigma_{pre} = 5, 20$  and  $35 \text{ kPa}$ , respectively.

In Figure 3.19(b), we have also given fitted lines based on the equation as shown in the caption. All our data fitted well with a power law dependence and this power has its origin from the adhesive forces between two particles, as introduced by Rumpf in 1990 (Rumpf 1990, Rabinovich et al. 2000), where the adhesion force between two particles is linearly proportional to particle diameter:  $F_{ad} \propto d$ . While for the cohesive strength, it is a bulk property with an unit of stress. Therefore, cohesive strength is proportional to the adhesion force divided by effective contact area:  $c \propto F_{ad}/d^2$ , and finally we get  $c \propto d^{-1}$ , which is the relation used for our fitting.

### 3.1.7.2.3 Bulk friction from steady state flow

Along with the bulk density (volume fraction), angle of internal friction and cohesive strength, the steady state angle of internal friction,  $\phi_{ss}$ , also plays a major role in

determining the powder flow behaviour. The steady state flow does not depend on time change or sample history and one could get a unique bulk friction response to shearing for each normal stress level for a given sample. We first look at the  $\phi_{ss}$  with respect to the applied normal stress in Figure 3.20(a). For samples with median particle size higher than 20  $\mu\text{m}$  (Eskal30, 80, 150 and K0.1–0.5), the  $\phi_{ss}$  behaves similarly as  $\phi$ , no clear dependence on normal stress is observed. However, for samples smaller than 20  $\mu\text{m}$  (Eskal300, 500 and 15),  $\phi_{ss}$  decreases with increasing normal stress.

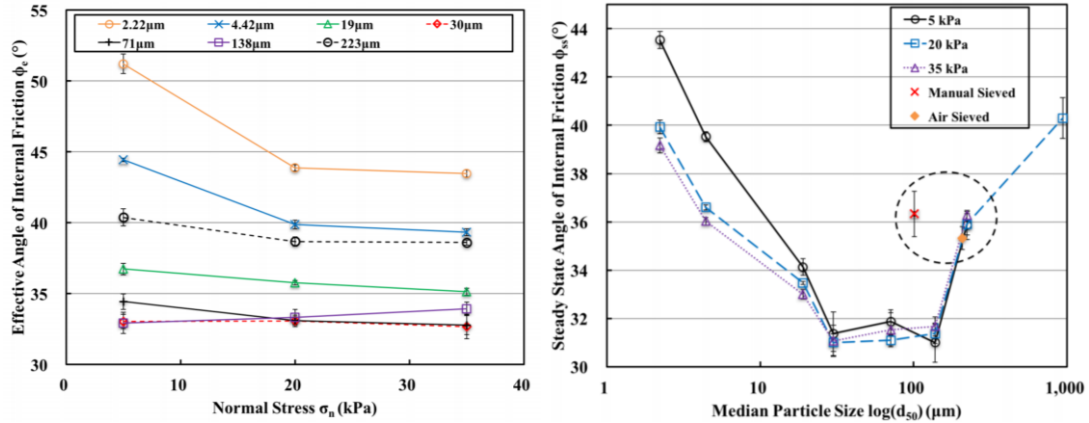


**Figure 3.20:** Steady state angle of internal friction,  $\phi_{ss}$ , plotted against (a) pre-shear normal stress,  $\sigma_n$ , (b) median particle size,  $d_{50}$ . Symbols in the dashed area are sieved Eskal K0.1–0.5 (223  $\mu\text{m}$ ) sample sheared at  $\sigma_n = 20$  kPa. Lines are guides to the eye.

When we look at the size influence on  $\phi_{ss}$  in Figure 3.20(b), we observe a very similar trend to the angle of internal friction in Figure 3.18(b). However, the value of  $\phi_{ss}$  for largest size powder is lower than the value of the finest powder, where  $\phi$  of the coarsest powder exceeds the finest. This indicates that the inter-particle cohesion contributes more to the shear resistance at steady state flow than at incipient flow. When looking at the behaviour of the two sieved samples,  $\phi_{ss}$  stay almost unchanged after sieving, which is consistent with Figure 3.18(b).

### 3.1.7.3 Quantities relevant for silo design

The parameters mentioned in the sections above are determined directly from the physical response of powders in the shear tester, e.g., bulk friction values can be directly calculated from the measured normal and shear stresses, and are very useful for understanding the powder's physical behaviour. However, for designing a silo, some

additional parameters play an important role (Jenike, 1976; Schulze, 2008, 2014b). These will be discussed in the following sections.

### 3.1.7.3.1 Effective angle of internal friction

The effective angle of internal friction is defined as the angle of the effective yield locus, which is the line starting at the origin of the  $\sigma_n - \tau$  plane and tangent to the Mohr circle (see Figure 3.8). And this property is crucial for designing the hopper angle in order to achieve mass flow in a silo.

In Figure 3.21, the effective angle of internal friction is plotted against the normal stress and median particle size. Within the stress levels investigated,  $\phi_e$  decreases with increasing normal stress, except for two intermediate size powders—Eskal30 (30  $\mu\text{m}$ ) and 150 (138  $\mu\text{m}$ ), which shows a consistent behaviour with  $\phi_{SS}$  independent of the normal stress. Interestingly, for even higher particle size, Eskal K0.1–0.5 (223  $\mu\text{m}$ ),  $\phi_e$  again decreases with applied normal stress.

When we focus on the dependence of the effective angle of internal friction on the particle size as shown in Figure 3.21(b), we observe a very similar trend as  $\phi$  and  $\phi_{SS}$ , especially with values of  $\phi_e$  consistently higher than  $\phi_{SS}$  for both very fine and very coarse powders. Also in this case, sieving barely affects the behaviour of the powders, see dashed area in Figure 3.21(b).

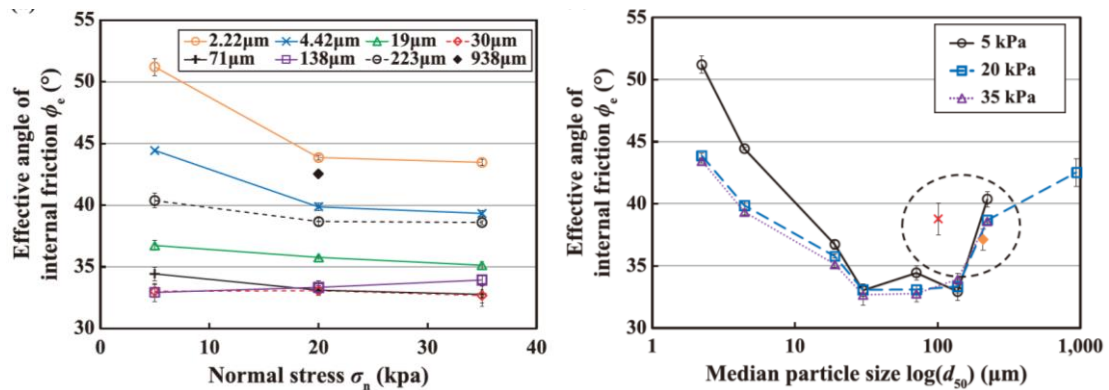


**Figure 3.21:** Effective angle of internal friction,  $\phi_e$ , plotted against (a) pre-shear normal stress,  $\sigma_n$ , (b) median particle size,  $d_{50}$ . Symbols in the dashed area are sieved Eskal K0.1–0.5 (223  $\mu\text{m}$ ) sample sheared at  $\sigma_n = 20$  kPa. Lines are guides to the eye.

### 3.1.7.3.2 Flow function and powder flowability

Finally, we process the results to look at the powder flowability in the form of the flow function to evaluate how a given powder would fail/flow under a given major consolidation stress (see Figure 3.8). This is also of great significance for designing the outlet diameter of a silo (Schulze, 2014a). When a powder sample is compressed in a confined geometry, e.g. a cylinder in a uni-axial tester, the major consolidation stress is named as  $\sigma_1$ , which indicates the maximum compressive stress achieved in the sample. If the powder is sufficiently cohesive, it will form an intact bulk/block after the confinement is removed. If the block is compressed again, the minimum stress needed to achieve sample failure/breakage is called the unconfined yield strength,  $\sigma_c$ . Note that the sample stress paths in uni-axial testers and shear testers are different, but the stress states could be linked using Mohr's Circle. The curve  $\sigma_c = f(\sigma_1)$  is called flow function in powder engineering, which can be used to characterize material flowability,  $ffc = (\sigma_1/\sigma_c)$  (Schulze, 2008). The flowability is defined as follows:

- $ffc < 1$       not flowing
- $1 < ffc < 2$     very cohesive    •  $2 < ffc < 4$     cohesive
- $4 < ffc < 10$     easy flowing    •  $ffc > 10$       free flowing

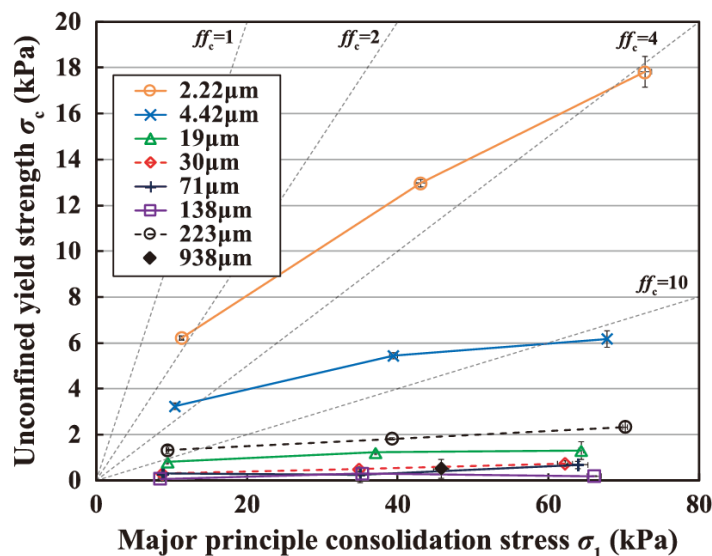


**Figure 3.22:** Flow function: unconfined yield strength,  $\sigma_c$ , plotted against major consolidation stress,  $\sigma_1$  under 3 different pre-shear stresses using RST-01. Different symbols/colours represent different materials. Note that for Eskal K0.5–

*0.8, there is only one point, and we have error bars with both  $\sigma_c$  and  $\sigma_1$ . Lines are guides to the eye.*

In Figure 3.22, we plot the flow functions for 7 limestone powders. As we can see, our powders cover almost the whole range of flowability, from cohesive to free flowing. In the stress range we investigated,  $\sigma_c$  increases for all the samples with increasing  $\sigma_1$ . As expected, the slope of the increase trend becomes higher with decreasing particle size, with the maximum slope of Eskal300 (minimum particle size). The flowability of a certain powder depends not only on the major consolidation stress  $\sigma_1$ , but also on particle size.

### **3.1.8 Conclusion and outlook**

In this study, we have systematically examined the powder flow behaviour of limestone powder samples with varying median particle sizes in different shear testers at different confining stress levels. The major goal is to understand the relation between microscopic properties such as particle size and contact cohesion and macroscopic, bulk properties such as bulk density, cohesive strength and shear resistance (characterized by the effective angle of internal friction, the internal friction at steady state flow, and the internal friction).

All shear testers investigated show highly repeatable reproducible results and good overall, consistent agreement among each other. Direct shear devices (Jenike and ELE direct shear tester) give the highest standard deviations. The yield loci obtained by the Schulze ring shear tester (RST-01) are consistently slightly higher than the results from other testers, which, on the practical side, results in a more conservative but safer silo design. The shear protocol evidently influences the measurements as shown by comparing the RST-01 and the FT4, where the latter gives a significantly lower yield locus, which we attribute to a different pre-shear protocol. As a conclusion, while the automated devices minimize the operator influence, the output should be carefully interpreted, as differences in the protocol can result in considerable deviations in the measured material response even if the qualitative trends are found to be consistent among different testers.

In order to study the material behaviour, eight limestone powders with identical chemical composition and median particle size ranging from 2.2  $\mu\text{m}$  to 938  $\mu\text{m}$  have been tested in a wide range of normal stresses (5, 20 and 35 kPa). Both factors, size and stress, are found to influence the bulk flow significantly. As expected, the bulk density and cohesive strength increase with increasing normal stress, the effect being stronger for finer particles. On the other hand, the angle of internal friction seems to be unaffected by the normal stress (at least in the range investigated here), while the effective angle of internal friction and the steady state angle of internal friction show a decreasing trend with normal stress.

When we look at the dependence of the macroscopic flow on particle size, two regimes can be distinguished, above and below the median particle size of about 150  $\mu\text{m}$ . For the fine particle regime, contact cohesion dominates the bulk behaviour, the effect getting smaller with increasing particle size. The bulk density increases monotonically with particle size, and the bulk cohesion (cohesive strength) decreases to nearly zero. The friction angles (effective angle of internal friction, angle of internal friction and steady state angle of internal friction), follow a similar decreasing trend as bulk cohesion.

In the coarse particle regime (150 to 938  $\mu\text{m}$ ), the bulk behaviour is less obvious. The bulk cohesion slightly increases while bulk density increases, then decreases. The bulk friction angles increase with increasing particle size up to values comparable to those of the finest powders. In order to check the effect of small particles in this regime, fines are removed from the coarse samples via air sieving. This results in a significant reduction in bulk density and bulk cohesion, while the bulk friction angles are barely affected. This proves that the fine particles being the main source of cohesion. The competition between contact cohesion and geometrical effects can explain the transition between the two regimes. For dry powders consisting of large particles, the inter-particle cohesive forces, especially the van der Waals forces, become negligible. The interlocking between particles due to the surface roughness and shape dominates the bulk behaviour of coarse samples, while cohesion is the key contribution that governs the shear strength of fine powders. The geometrical interlocking effect is further enhanced by the increase of the bulk density for coarse samples. On the other hand, low density is associated with small median particle size, due to the presence of clusters and large pores.

For the sake of completeness, we also look at the flow behaviour of our powders, as relevant for the silo-design procedure. Overall, the flowability increases when increasing normal stress (powders become more free flowing) for finer samples, with the effect becoming weaker for coarse samples that are more free flowing anyway.

The present paper is the beginning of a collection of experimental data that, in the future, can be enriched with more data from many more materials of both industrial and academic interest. Our speculations on the interesting bulk cohesion and friction behaviour with increasing particle size have to be further investigated. Furthermore, this experimental database can be used as a source for design (e.g. silo) procedures and as a benchmark for further experimental studies. Last but not least, the development, calibration and validation of particle models and simulations, especially the DEM contact models, and simulations of element tests (shear tests), require experimental data as presented here.

### 3.1.9 Nomenclature

$\rho_p$	Particle density (kg/m <sup>3</sup> )
$\rho_0$	Initial bulk density (kg/m <sup>3</sup> )
$\rho_b$	Bulk density (kg/m <sup>3</sup> )
$w$	Moisture content (%)
$d_{10}$	Particle diameter where 10 % of distribution is below this value (µm)
$d_{50}$	Particle median size where 50 % of distribution is below this value (µm)
$d_{90}$	Particle diameter where 90 % of distribution is below this value (µm)
$\Psi$	Roundness ([–])
$\tau$	Shear stress (kPa)
$\tau_{ss}$	Steady state shear stress (kPa)
$\tau_p$	Peak failure shear stress (kPa)
$\sigma_n$	Normal stress (kPa)
$\sigma_{pre}$	Pre-shear normal stress (kPa)
$c$	Cohesive strength of yield locus or bulk cohesion (kPa)
$c_{ss}$	Cohesive strength of steady state locus (kPa)
$\sigma_c$	Unconfined yield strength (kPa)
$\sigma_1$	Major consolidation stress (kPa)
$\sigma_2$	Minor consolidation stress (kPa)
$\phi$	Angle of internal friction (°)
$\phi_e$	Effective angle of internal friction (°)

- $\phi_{ss}$  Steady state angle of internal friction ( $^{\circ}$ )  
 $ffc$  Flowability ([-])

### 3.1.10 References

- Akers R.J., The certification of a limestone powder for Jenike shear testing (CRM 116), *EUR (Luxembourg)*, 1992.
- Alonso-Marroquin F., Herrmann, H.J., Ratcheting of granular materials, *Physics Review Letter*, 92 (2004) 54301.
- Alshibli K.A., Sture, S., Shear band formation in plane strain experiments of sand, *Journal of Geotechnical and Geoenvironmental Engineering*, 126 (2000) 495–503.
- ASTM-D6128-16, Standard test method for shear testing of bulk solids using the Jenike shear cell, West Conshohocken, PA: ASTM International, 2006.
- ASTM-D6773-16, Standard shear test method for bulk solids using the Schulze ring shear tester, West Conshohocken, PA: ASTM International, 2008.
- ASTM-D7891-15, Standard test method for shear testing of powders using the freeman technology FT4 powder rheometer shear cell, West Conshohocken, PA: ASTM International, 2015.
- Bardet J.P., *Experimental Soil Mechanics*, Prentice-Hall, Upper Saddle River, New Jersey, 1997.
- Berry R.J., Bradley M.S.A., McGregor R.G., Brookfield powder flow tester-Results of round robin tests with CRM-116 limestone powder, *Proceedings of the Institution of Mechanical Engineers, Part E: Journal of Process Mechanical Engineering*, 229 (2015) 215–230.
- Bi D., Zhang J., Chakraborty B., Behringer R.P., Jamming by shear, *Nature*, 480 (2011) 355–358.
- Carr J.F., Walker D.M., An annular shear cell for granular materials, *Powder Technology*, 1 (1968) 369–373.
- Casagrande A., The determination of the pre-consolidation load and its practical significance, *Proceedings of the international conference on soil mechanics and foundation engineering*, 3 (1936) 60–64.
- Cates M.E., Haw M.D., Holmes C.B., Dilatancy, jamming, and the physics of granulation, *Journal of Physics: Condensed Matter*, 17 (2005) S2517.
- Cundall P.A., Numerical experiments on localization in frictional materials, *Ingenieur-Archiv*, 59 (1989) 148–159.
- Feise H.J., A review of induced anisotropy and steady-state flow in powders, *Powder Technology*, 98 (1998) 191–200.
- Feise H., Schwedes J., Investigation of the Behaviour of Cohesive Powder in the Biaxial Tester, *KONA Powder Particle Journal*, 13 (1995) 99–104.
- Fitzpatrick J.J., Barringer S.A., Iqbal T., Flow property measurement of food powders and sensitivity of Jenike's hopper design methodology to the measured values, *Journal of Food Engineering*, 61 (2004) 399–405.
- Freeman R., Measuring the flow properties of consolidated, conditioned and aerated powders—A comparative study using a powder rheometer and a rotational shear cell, *Powder Technology*, 174 (2007) 25–33.
- Freeman R.E., Cooke J.R., Schneider L.C.R., Measuring shear properties and normal stresses generated within a rotational shear cell for consolidated and non-consolidated powders, *Powder Technology*, 190 (2009) 65–69.
- GDR-MiDi, On dense granular flows, *European Physical Journal E–Soft Matter*, 14 (2004) 341–365.
- Harder J., Schwedes J., The development of a true biaxial shear tester, *Particle & Particle Systems Characterization*, 2 (1985) 149–153.
- Imole O.I., Paulick M., Magnanimo V., Morgeneyer M., Montes B.E., Ramaioli M., Kwade A., Luding S., Slow stress relaxation behavior of cohesive powders, *Powder Technology*, 293 (2016) 82–93.
- Janssen R.J.M., Zetzener H., Measurements on cohesive powder with two biaxial shear testers, *Chemical Engineering & Technology*, 26 (2003) 147–151.
- Jenike A.W., Storage and Flow of Solids, Bulletin No. 123, Bulletin of the University of Utah, 53 (1964).



- Jenike A.W., Quantitative design of mass-flow bins, *Powder Technology*, 1 (1967) 237–244.
- Jenike A.W., Storage and flow of solids. bulletin no. 123, vol. 53, no. 26, November 1964, Technical report, Utah University, Salt Lake City (USA), 1976.
- Kamath S., Puri V.M., Manbeck H.B., Flow property measurement using the Jenike cell for wheat flour at various moisture contents and consolidation times, *Powder Technology*, 81 (1994) 293–297.
- Kamath S., Puri V.M., Manbeck H.B., Hogg R., Flow properties of powders using four testers-measurement, comparison and assessment, *Powder Technology*, 76 (1993) 277–289.
- Koynov S., Glasser B., Muzzio F., Comparison of three rotational shear cell testers: Powder flowability and bulk density, *Powder Technology*, 283 (2015) 103–112.
- Kumar N., Luding S., Memory of jamming—multiscale models for soft and granular matter, *Granular Matter*, 18 (2016) 1–21.
- Liu A.J., Nagel S.R., Nonlinear dynamics: Jamming is not just cool any more, *Nature*, 396 (1998) 21–22
- Luding S., Anisotropy in cohesive, frictional granular media, *Journal of Physics: Condensed Matter*, 17 (2005a) S2623–S2640.
- Luding S., Shear flow modeling of cohesive and frictional fine powder, *Powder Technology*, 158 (2005b) 45–50.
- Luding S., Cohesive, frictional powders: contact models for tension, *Granular Matter*, 10 (2008) 235–246.
- Luding S., Granular matter: So much for the jamming point, *Nature*, 12 (2016) 531–532.
- Majmudar T.S., Behringer R.P., Contact force measurements and stress-induced anisotropy in granular materials, *Nature*, 435 (2005) 1079–1082.
- Morgeneyer M., Brendel L., Farkas Z., Kadau D., Wolf D.E., Schwedes J., Can one make a powder forget its history?, *Proceedings of the 4th international conference for conveying and handling of particulate solids*, Budapest, 2003, pp. 12–118.
- Morgeneyer M., Schwedes J., Investigation of powder properties using alternating strain paths, *Task Quarterly*, 7 (2003) 571–578.
- Rabinovich Y.I., Adler J.J., Ata A., Singh R.K., Moudgil B.M., Adhesion between nanoscale rough surfaces: I. Role of asperity geometry, *Journal of Colloid and Interface Science*, 232 (2000) 10–16.
- Radjai F., Jean M., Moreau J.J., Roux S., Force distribution in dense two-dimensional granular systems, *Physical Review Letters*, 77 (1996) 274–277.
- Radjai F., Roux S., Moreau J.J., Contact forces in a granular packing, *Chaos: An Interdisciplinary Journal of Nonlinear Science*, 9 (1999) 544–550.
- Rumpf H., *Particle technology*, Chapman & Hall, London/New York, 1990.
- Russell A., Müller P., Shi H., Tomas J., Influences of loading rate and preloading on the mechanical properties of dry elasto-plastic granules under compression, *AIChE Journal*, 60 (2014) 4037–4050.
- Salehi H., Barletta D., Poletto M., A comparison between powder flow property testers, *Particology*, 32 (2017) 10–20.
- Savage S.B., Hutter K., The motion of a finite mass of granular material down a rough incline, *Journal of Fluid Mechanics*, 199 (1989) 177–215.
- Schulze D., Entwicklung und Anwendung eines neuartigen Ringschergerätes, *Aufbereitungs-Technik*, 35 (1994) 524–535.
- Schulze D., Flow properties of bulk solids (v), *Deutsche Keramische Gesellschaft und Nederlandse Keramische Vereniging, Annual Meeting 2002, Eindhoven.*, 2002, pp. 21–23.10.
- Schulze D., Time- and velocity-dependent properties of powders effecting slip-stick oscillations, *Chemical Engineering & Technology*, 26 (2003a) 1047–1051.
- Schulze D., Towards more reliability in powder testing (v), *Proceedings of the 4th international conference for conveying and handling of particulate solids (CHoPS)*, Budapest, 2003b, pp. 5–31.
- Schulze D., *Powders and bulk solids: behavior, characterization, storage and flow*, Springer, 2008.
- Schulze D., Round robin test on ring shear testers, *Advanced Powder Technology*, 22 (2011) 197–202.
- Schulze D., Beispiele gemessener Fließeigenschaften, in ‘*Pulver und Schüttgüter*’, Springer, 2014a, pp. 249–268.

- Schulze D., Verfahrenstechnische Siloauslegung, in 'Pulver und Schüttgüter', Springer, 2014b, pp. 335–360.
- Schwedes J., Vergleichende Betrachtungen zum Einsatz von Schergeräten zur Messung von Schüttguteigenschaften, Proceedings of PARTEC, Nürnberg, 1979, pp. 278–300.
- Schwedes J., Review on testers for measuring flow properties of bulk solids, *Granular Matter*, 5 (2003) 1–43.
- Schwedes J., Schulze D., Measurement of flow properties of bulk solids, *Powder Technology*, 61 (1990) 59–68.
- Shibuya S., Mitachi T., Tamate S., Interpretation of direct shear box testing of sands as quasi-simple shear, *Geotechnique*, 47 (1997) 769–790.
- Singh A., Magnanimo V., Saitoh K., Luding S., Effect of cohesion on shear banding in quasistatic granular materials, *Physical Review E*, 90 (2014) 022202.
- Teunou E., Fitzpatrick J.J., Synnott E.C., Characterisation of food powder flowability, *Journal of Food Engineering*, 39 (1999) 31–37.
- Thakur S.C., Ahmadian H., Sun J., Ooi J.Y., An experimental and numerical study of packing, compression, and caking behaviour of detergent powders, *Particuology*, 12 (2014) 2–12.
- Tomas J., Product design of cohesive powders – Mechanical properties, compression and flow behavior, *Chemical Engineering & Technology*, 27(6) (2005) 605–618.
- Tsunakawa H., Aoki R., Measurements of the failure properties of granular materials and cohesive powders, *Powder Technology*, 33 (1982) 249–256.
- Van Hecke M., Jamming of soft particles: geometry, mechanics, scaling and isostaticity, *Journal of Physics: Condensed Matter*, 22 (2009) 033101.
- Witt W., Altrogge D., Rutsch O., High speed image analysis and dispersion for size and shape characterisation on fibres, Proceedings of 5th World Congress of Particle Technology, 2006.
- Wolf B., Scirocco R., Frith W.J., Norton I.T., Shear-induced anisotropic microstructure in phase-separated biopolymer mixtures, *Food Hydrocolloids*, 14 (2000) 217–225.
- Yang Y., Fei W., Yu H.-S., Ooi J., Rotter M., Experimental study of anisotropy and non-coaxiality of granular solids, *Granular Matter*, 17 (2015) 189–196.
- Zetzener, H. Schwedes, J., Relaxation and creep of dry bulk solids, *Particle & Particle Systems characterization*, 19 (2002) 144–148.

### 3.2 Article (published in peer-reviewed EPJ Web of Conferences, EDP Sciences, 2017)

## Dust generation in powders: Effect of particle size distribution

Somik Chakravarty<sup>1</sup>, Olivier Le Bihan<sup>2</sup>, Marc Fischer<sup>1,2</sup>, and Martin Morgeneyer<sup>1</sup>

<sup>1</sup> *Laboratoire Transformations Intégrées de la Matière Renouvelable (TIMR), Université de Technologie de Compiègne (UTC) Sorbonne Universités, France*

<sup>2</sup> *Institut National de l'Environnement Industriel et des Risques (INERIS), NOVA/CARA/DRC/INERIS, Parc Technologique Alata, BP2, F-60550 Verneuil-En-Halatte, France*

#### 3.2.1 Abstract

This study explores the relationship between the bulk and grain-scale properties of powders and dust generation. A vortex shaker dustiness tester was used to evaluate 8 calcium carbonate test powders with median particle sizes ranging from 2  $\mu\text{m}$  to 136  $\mu\text{m}$ . Respirable aerosols released from the powder samples were characterised by their particle number and mass concentrations. All the powder samples were found to release respirable fractions of dust particles which end up decreasing with time. The variation of powder dustiness as a function of the particle size distribution was analysed for the powders, which were classified into three groups based on the fraction of particles within the respirable range. The trends we observe might be due to the interplay of several mechanisms like de-agglomeration and attrition and their relative importance.

#### 3.2.2 Introduction

Granular matter or bulk solids makes up for roughly 50% of products and 75% of the raw material used in industrial applications [1]. Applications and processes involving handling or transportation of bulk solids generate dust, referred to as small solid particles which remain suspended in the air for a prolonged period of time [2]. The propensity of a material to generate dust upon handling is known as its dustiness [3]. The risks of dust emission in a contained area such as in an occupational environment can involve

inhalation of dust particles by industrial workers [4,5] or explosion of volatile dust cloud capable of creating substantial financial and human loss [6]. Regulatory measures such as the 2008/50/EC directive [7] or ATEX [8] in the EU underpins the need for assessment and containment of dust concentration in ambient air with an emphasis on the generation and exposure of fine particles such as PM<sub>2.5</sub> and respirable fraction, responsible for significant negative impacts on human health.

Dustiness of a material and thus the risk of exposure while handling a material depends on its physical properties and the type of process at work [9]. Testing of dust generation is often practical when developing new products in industries before producing and distributing them in bulk scale. Lab scale testing of dustiness of granular material requires a low-cost tester capable of testing a wide range of material with relatively simple operations. Standardized testers such as the continuous drop and the rotating drum method according to the EN 15051 '*Workplace atmospheres — Measurement of the dustiness of bulk materials—Requirements and reference test methods*' requires large amounts of powder (35 cm<sup>3</sup> or 500 g) and can give disparate results for a range of industrial minerals [4] due to the difference in stressing/agitation energy and the timescale of agitation, pointed out by several authors [4,10].

New testers such as the vortex shaker (VS) enable testing dustiness of powders using a small fraction of the powder quantity required for the standardized testers [3]. They are especially suitable for testing micro- and nano- scale powders typically used in catalysts and pharmaceutical industries where the powder test quantity is low and costs are high. Furthermore, they are capable of testing powders for different energy levels by varying vortex speed and time. Morgeneyer et al. [3] and [11] used the VS method to study the effects of tester parameters on dust generation of micron-sized alumina particles and carbon nano-tubes (CNTs), respectively. In [3], the effect of the VS speed and sample mass on the dust generated from alumina were studied whereas [11] dealt with the effect of change in tube diameter in addition to vortex speed on dustiness of CNTs.

Measuring dustiness and the risk of exposure in different environmental conditions requires testing and characterizing powder properties by their effect on dustiness as it can enable understanding the role of different powder properties on the dust generation mechanisms. Since dustiness of a powder depends on several parameters, studying the effect of each physical parameter on dust generation requires testing the

same material while changing one parameter at a time keeping the other powder parameters and environmental conditions constant.

In this study, respirable dustiness for eight calcium carbonate powders with similar physico-chemical properties were tested. The results were used to analyze the effect of particle size distribution (PSD) on the evolution of aerosol concentrations and size distributions. The powder samples were divided into three groups based on their PSD (and especially respirable fractions of particles already present in the powder) and attempted to identify 'potential scenarios' or generation mechanisms prevalent in each group.

### **3.2.3 Material and experimental methods**

#### ***3.2.3.1 Sample material***

The Eskal series of calcium carbonate powders (KSL Staubtechnik GmbH, Germany) were used as the test material. They are standard test powders used in various industries and also as a reference powder for calibration of equipment [12] due to their high roundness (close to 0.9), and insensitivity to moisture and temperature changes. All powder samples were manufactured with the same process/technology with the same particle density ( $2,710\text{kg/m}^3$ ), as reported by the manufacturer.

The volumetric size distribution of the powders (Table 3-4) were measured 'as received' using laser diffraction size analyser (Malvern Mastersizer 2000, Scirocco 2000M, UK). The samples were measured using dry dispersion of the powders with nozzle air pressure of 3 bars and the obscuration rate ranging from 1% to 5%, depending on grain size of the samples.

Table 3-4: Volumetric size distribution of the tests samples.

	Sample	$X_{10}$ , $\mu\text{m}$ COV (in %)	$X_{50}$ , $\mu\text{m}$ COV (in %)	$X_{90}$ , $\mu\text{m}$ COV (in %)
A1	Eskal 300	0.96 (3.3)	2.2 (3.1)	4.6 (3.4)
A2	Eskal 500	1.6 (0.57)	4.1 (0.12)	8.2 (0.34)
A3	Eskal 1000	1.7 (4.8)	4.6 (1.4)	10 (3.7)
B1	Eskal 10	5.7 (1.2)	10 (1.1)	16 (1.2)
B2	Eskal 14	8.3 (0.1)	14 (0.3)	23 (0.7)
B3	Eskal 15	8.8 (0.3)	16 (0.13)	25 (0.11)
B4	Eskal 20	11 (1.6)	20 (0.2)	33 (2.1)
C1	Eskal 150	99 (0.5)	136 (0.1)	187 (0.5)

The primary selection criteria for the Eskal powders were their median particle size ( $x_{50}$ ), their PSD and the respirable fraction of particles already present in the powder. The powder samples were classified in three groups with group A (A1, A2 and A3) consisting mainly of particles with size smaller than  $10\mu\text{m}$ , i.e., the maximum particle size sampled by a respirable cyclone. Group B (B1, B2, B3 and B4) consists of bi-modal powders, with modes at ( $1.1\mu\text{m}$ ,  $11\mu\text{m}$ ) B1, ( $1.9\mu\text{m}$ ,  $15\mu\text{m}$ ) B2, B3 ( $2.2\mu\text{m}$ ,  $17\mu\text{m}$ ), and B4 ( $2.9\mu\text{m}$ ,  $23\mu\text{m}$ ). Group C (C1) powder did not consist of particles in the respirable size range. Test samples from each group were designated by their group name followed by the sample number arranged in ascending order of their  $x_{50}$ . For example, A1, A2 and A3 are the three samples from group A arranged in ascending order of their  $x_{50}$ . Please note the differences in values in Table 3-4 and Table 3-1 are due to the measurements performed at different locations by different users with different instruments (with the laser diffraction technique).

### 3.2.3.2 The vortex shaker dustiness tester

The experimental setup was similar to the one used by Morgeneyer et.al. [3] except that the released aerosol was sampled using a respirable cyclone (BGI GK2.69). The setup consists of 4 sections: generation, sampling, dilution, and measurement (Figure

3.23). Aerosol is generated through the turbulent agitation of a powder-filled glass test-tube mounted on a digital vortex shaker (VWR Signature Digital Vortex Mixer).

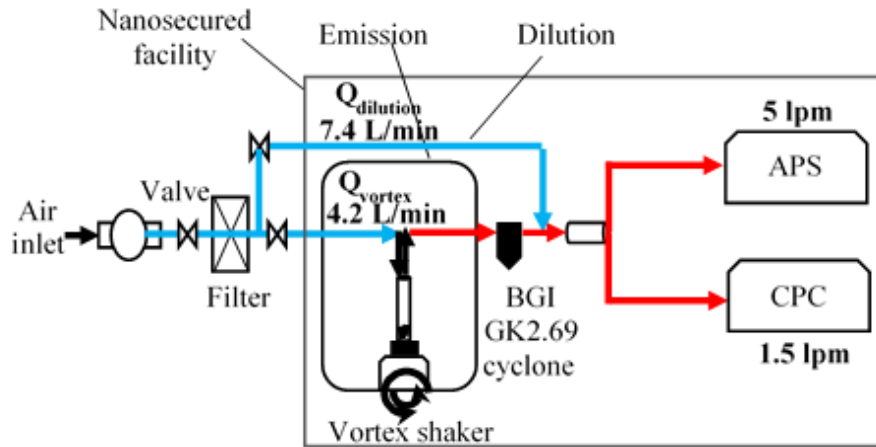


**Figure 3.23:** Schematic of the vortex shaker experimental setup.

The experimental setup was similar to the one used by Morgeneyer et.al. [3] except that the released aerosol was sampled using a respirable cyclone (BGI GK2.69). The setup consists of 4 sections: generation, sampling, dilution, and measurement (Figure 3.23). Aerosol is generated through the turbulent agitation of a powder-filled glass test-tube mounted on a digital vortex shaker (VWR Signature Digital Vortex Mixer).

Airborne aerosol particles from the test-tube is carried to the respirable cyclone (50% cut point of  $4\mu\text{m}$ ) by the inlet flow ( $Q_V$ ) of  $4.2\text{L}/\text{min}$  ( $7\text{e-}05\text{m}^3/\text{s}$ ). While the cyclone separates the larger particles, the respirable aerosol particles permeates through the cyclone and is diluted with ( $Q_D$ ) of  $7.4\text{L}/\text{min}$  ( $1.2\text{e-}04\text{m}^3/\text{s}$ ) of filtered air before splitting into 2 channels for measurement and characterization [13]. The aerosol number concentration NCPC over the  $4\text{nm}$  to  $3\mu\text{m}$  size range was measured using a condensation particle counter (CPC TSI 3775, TSI Inc.), whereas the aerosol number concentration  $N_{APS}$  and mass  $M_{APS}$  over the size range of  $0.54\mu\text{m}$  to  $20\mu\text{m}$  were measured by an aerodynamic particle sizer (APS TSI 3321, TSI Inc.). The APS records the particle numbers by their aerodynamic size which is based on times of flight of individual aerosol particles [3].

Three replicates were used for each test sample. Each test used 2g of powder weighed with an accuracy of  $\pm 0.001\text{g}$  using an analytical balance (MS1003S, Mettler-

Toledo Inc.), manually filled in a centrifuge glass tube (diameter 0.025m, height 0.15m). The filled tube was sealed using a rubber stopper and carried to the isolator system. The powders were weighed within 1 hour of performing the experiments to limit the number of variables affecting the powder condition. The VS operated at 1500rpm and was run for 10 minutes ( $T$ ). The background reference concentrations were measured for two minutes before the beginning and two minutes after the end of the vortex-shaker operation.

The total respirable aerosol number concentration measured by the CPC (4nm to 3 $\mu$ m) and the APS (3 $\mu$ m to 19.5 $\mu$ m) were combined to calculate the total number of generated particles using Eq. 3.1 and Eq. 3.2, adapted from Jensen [13], whereby:

$$S_{CPC}^{Number} = [Q_V + Q_D]. \Delta t_{CPC} \cdot \sum_{i=0}^{T/\Delta t_{CPC}} N_{CPC}(t_0 + i. \Delta t_{CPC}) \quad (\text{Eq. 3.1})$$

$$S_{APS>3\mu m}^{Number} = [Q_V + Q_D]. \Delta t_{APS} \cdot \sum_{i=0}^{T/\Delta t_{APS}} N_{APS>3\mu m}(t_0 + i. \Delta t_{APS}) \quad (\text{Eq. 3.2})$$

where,  $\Delta t_{CPC}$  (1s) and  $\Delta t_{APS}$  (5s) are the time-step set for the CPC and the APS, respectively.  $dN_{CPC}(t_0 + i. \Delta t_{CPC})$  and  $dN_{APS>3\mu m}(t_0 + i. \Delta t_{APS})$  are the aerosol number concentration ( $\#/cm^3$ ) for the  $i^{\text{th}}$  time interval measured by the CPC and the APS, respectively. The differences between the aerodynamic and electrical mobility diameters measured by the APS and the CPC, respectively needs to be determined for the spherical Eskal powders in future works.

### 3.2.4 Results and discussion

In general, CPC and APS results reveal that all test samples emit respirable fractions of aerosol. The number concentration ( $N_{CPC}$ ) curves from CPC (Figure 3.24) are the average values over 3 repetitions. Also,  $S_{Total} = S_{CPC}^{Number} + S_{APS>3\mu m}^{Number}$  calculated for the test samples are shown (Figure 3.24, top-right corner of each figure). All samples show an initial peak of  $N_{CPC}$  at the onset of the VS activity (around 120s to 135s from the start of the measurement). It is followed by a decline.



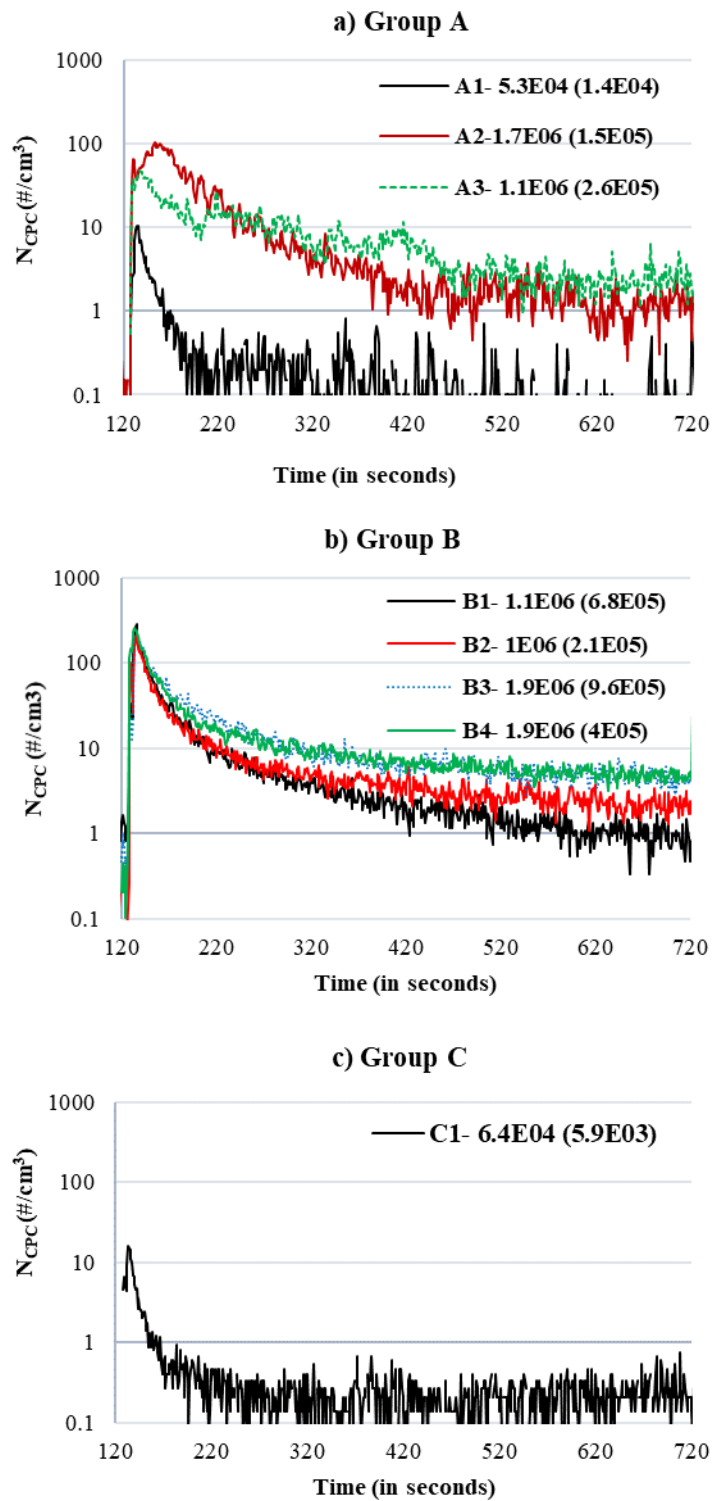


**Figure 3.24:** Temporal evolution of respirable aerosol number concentration from the CPC (4 nm to 3  $\mu\text{m}$ ) for a) Group A; b) Group B; c) Group C. The total number of aerosol particles released and their SD were calculated using (1) and (2) (see top-right corner).

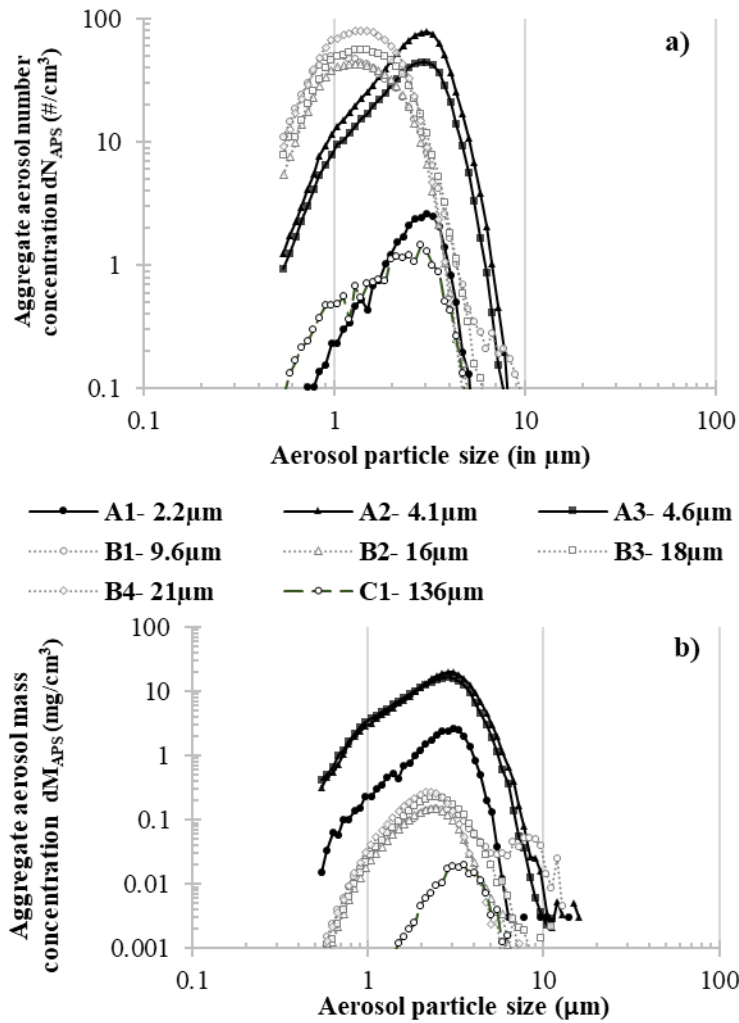


**Figure 3.25:** APS ( $0.54 \mu\text{m} - 0.54 \mu\text{m}$ ) measurements for aggregate aerosol concentration by particle size by a) number concentration ( $dN$ ); b) mass concentration ( $dM$ ).

### 3.2.4.1 Group A (fine powders)

Samples A2 and A3 show qualitatively similar dust generation behaviour, whereby they initially emit aerosols with concentrations up to  $104 \#/\text{cm}^3$  (A2) and  $47 \#/\text{cm}^3$  (A3) before a gradual decline. This stands in contrast to A1 which attains its maximum concentration of  $10 \#/\text{cm}^3$  before swiftly descending into emission of aerosols comparable to the background reference values (usually between  $0.1$  to  $0.2 \#/\text{cm}^3$ ). This

relies on the assumption that the overwhelming majority of aerosol particles are in the size range measured by the CPC.

Measurements from the CPC (Figure 3.24a) and APS (Figure 3.25) shows the cumulative aerosol concentrations generated by A2 and A3 are greater than one order of magnitude higher than A1. Furthermore, the modal aerosol sizes of the three samples measured by the APS are similar and amount to approximately 3  $\mu\text{m}$  (Figure 3.25).

Group A powders are cohesive in nature [14] and exist in the form of agglomerates of sizes greater than their primary particles. The dust generated from such powders could stem from the breaking and dispersion of the agglomerates into primary particles due to agglomerate-agglomerate collision or impacts against the wall. In the case of the VS, the centrifugal forces acting upon the agglomerates lead to collisions and impacts in the shaker which could result in the breakage and disintegration of agglomerates into particles. Such small disintegrated particles are more prone to be elutriated within a turbulent air flow developed in the VS. They follow a Stokesian flow regime [15].

A1 with a relatively small particle sizes (Table 3-4) forms agglomerates with high cohesive binding energies [14] (see appendix B, Table B-1, Figure B 1) such that the vortex agitation at 1,500 rpm might not be enough to separate and aerosolize high concentrations of primary particles. Contrarily to A1, samples A2 and A3 consist of particles relatively larger in size and displaying broader PSD. Thus, based on the theoretical relationship between particle sizes and Van der Waals cohesive forces [16], the cohesivities of A2 and A3 must be inferior to that of A1 (as seen appendix B, Table B-1).

For A2 and A3 (similar in size) the temporal evolution of the total number of released aerosols and their PSD are similar (Figure 3.24 and Figure 3.25). At the onset of vortex agitation, both samples emit relatively elevated concentrations of aerosols with small particle sizes. This might be due to the fact that such particles are more prone to be elutriated within the turbulent air flow [17].

### **3.2.4.2 Group B (bi-modal powders)**

The four bi-modal powders in group B display similar aerosol emissions during the test, whereby a sharp initial peak is followed by a gradual decline of the aerosol concentration into values between 1 and 10 #/cm<sup>3</sup>. B1 and B2 with the lowest  $x_{50}$  in this group emit relatively less respirable aerosols compared to B3 and B4. The modal aerosol size for all the samples measured from the APS is approximately 1  $\mu\text{m}$  (Figure 3.25), which is in close proximity to the first mode particle size of B1 (1.1 $\mu\text{m}$ ), B2 (1.9 $\mu\text{m}$ ), B3 (2.2 $\mu\text{m}$ ), and B4 (2.9 $\mu\text{m}$ ) (see Figure B 2 in Appendix B from Section 8.2). Thus the respirable fraction of aerosols from group B could originate from small particles with sizes inferior to the respirable size fraction.

Furthermore, laser diffraction measurements of volume fractions of particles with diameters smaller than 4  $\mu\text{m}$  present in group B shows that the respirable dustiness of a sample increases with an increase in the volume of particles in the first population. The volume fraction of the group B samples are measured as 3.7% (B1), 4.9% (B2), 5.2% (B3), and 6.5% (B4), with their mode particle size close 1 $\mu\text{m}$ .

### **3.2.4.2 Group C (coarse powder)**

Group C represents powders with almost no particles within the respirable range. C1 initially releases an aerosol concentration peak at the onset of the VS followed by a rapid descent to aerosol concentration of 0 to 0.2 #/cm<sup>3</sup>, similar to background aerosol concentrations used as reference. The initial emission can be due to the presence of small impurities present in the powder or due to the generation of small fragments of powder due to the attrition of larger sized particles.

Several mechanisms can be responsible for the attrition of particles which depends on the particle mechanical properties, shape and mode of loading [18]. Large brittle particles are prone to generate dust by attrition as they contain more faults in the form of micro cracks or imperfections which can lead to fracture or breakage when compared to smaller particles.

An aerosol particle sampler, the mini-particle-sampler (MPS®) [13] could be used to capture and deposit aerosol particles on copper grids for off-site transmission electron

microscope (TEM) analyses. This might provide evidence of the role of attrition in the generation of respirable aerosols.

### 3.2.5 Conclusion

The theoretical relationship between the properties of a powder and its dustiness remains poorly understood so that further experimental works are required [3,11]. We use a vortex shaker to test respirable dust generation from eight powders with similar physical properties except their particle size distributions which differ from each other. The powders were divided into three groups based on the fraction of particles within the respirable range. The interplay of several mechanisms like de-agglomeration and attrition and their relative importance might account for our observations.

Further studies combining experimental (atomic force microscopy in micro-scale and shear test in meso-scale) and numerical (discrete element method) techniques are required in order to confirm this.

### 3.2.6 References

- [1] R. Nedderman, *Statics and kinematics of granular materials* (2005). Cambridge University Press.
- [2] International Organization for Standardization, ISO 7708: Air quality—particle size fraction definitions for health-related sampling. Geneva, Switzerland: *International Organization for Standardization*, 1995.
- [3] M. Morgeneyer, O. Le Bihan, A. Ustache, O. Aguerre-Chariol, Experimental study of the aerosolization of fine alumina particles from bulk by a vortex shaker, *Powder Technol.* 246 (2013) 583–589. doi:10.1016/j.powtec.2013.05.040.
- [4] I. Pensis, J. Mareels, D. Dahmann, D. Mark, Comparative evaluation of the dustiness of industrial minerals according to European standard en 15051, 2006, *Ann. Occup. Hyg.* 54 (2010) 204–216. doi:10.1093/annhyg/mep077.
- [5] C. Pujara, D. Kildsig, Effect of individual particle characteristics on airborne emissions, *DRUGS AND THE PHARMACEUTICAL SCIENCES* 108 (2001): 29-54.
- [6] A. Klippel, M. Schmidt, U. Krause, Dustiness in workplace safety and explosion protection – Review and outlook, *J. Loss Prev. Process Ind.* 34 (2015) 22–29. doi:10.1016/j.jlp.2015.01.011.
- [7] EU, Directive 2008/50/EC of the European Parliament and of the Council of 21 May 2008 on ambient air quality and cleaner air for Europe, *Off. J. Eur. Communities.* 152 (2008) 1–43.
- [8] European Union, ATEX Guidelines, *Eur. Comm.* Edition 4 (2012) 1–76.
- [9] M.A.E. Plinke, Dust generation from handling powders in industry, *Am. Ind. Hyg. Assoc. J.* 56 (1995) 251-257.
- [10] S. Bach, E. Schmidt, Determining the Dustiness of Powders — A Comparison of three Measuring Devices. *Annals of occupational hygiene* 52 (2008) 717–725. doi:10.1093/annhyg/men062.
- [11] O.L.C. Le Bihan, A. Ustache, D. Bernard, O. Aguerre-Chariol, M. Morgeneyer, Experimental Study of the Aerosolization from a Carbon Nanotube Bulk by a Vortex Shaker, *J. Nanomater.* 2014 (2014) 1–11. doi:10.1155/2014/193154.
- [12] H. Zetzener, J. Schwedes, Relaxation and Creep of Dry Bulk Solids, *Part. Part. Syst. Charact.* 19 (2002) 144–148.
- [13] K.A. Jensen, Towards a method for detecting the potential genotoxicity of nanomaterials. D4.6: Dustiness of NANOGENOTOX nanomaterials using the NRCWE small rotating drum and the

- INRS Vortex shaker, Copenhagen, DENMARK, 2012. [www.nanogenotox.eu](http://www.nanogenotox.eu).
- [14] H. Shi, S. Luding, V. Magnanimo, Limestone Powders Yielding and Steady State Resistance under Shearing with Different Testers, *Powder, granule and bulk Solids: Innovations and Applications*. PGBSIA (2016).
- [15] S.C. Liang, T. Hong, L.S. Fan, Effects of particle arrangements on the drag force of a particle in the intermediate flow regime, *Int. J. Multiph. Flow.* 22 (1996) 285–306. doi:10.1016/0301-9322(95)00070-4.
- [16] H. Rumpf, K. Sommer, K. Steier, Mechanismen der Haftkraftverstärkung bei der Partikelhaftung durch plastisches Verformen, Sintern und viskoelastisches Fließen, *Chemie Ing. Tech.* 48 (1976) 300–307.
- [17] K. Saleh, M. Jaoude, M. Morgeneyer, E. Lefrancois, Dust generation from powders: A characterization test based on stirred fluidization, *Powder Technol.* (2014).

## **4 Experimental dustiness tester: particle motion and parametric study of the vortex shaker dustiness tester**

### **4.0 Overview**

New dustiness testers such as the vortex shaker remain somewhat of a ‘black box’ as there is lack of understanding of the intricate physical processes involved with dust generation at the particle level. An understanding of such processes is necessary to develop and validate numerical models which may be used to predict dustiness based on material and geometrical parameters of the material and tester, respectively.

Chapter 4 analyses the particle motion (trajectory) inside the testers using positron emission particle tracking (PEPT) method which can provide a large set of information at the particle level including particle average velocities, energy levels or frequency of collisions with the wall and/or other particles in the bulk. A vortex shaker is used as the dustiness tester as it proves to be an efficient device for studying the dustiness of powders using a fraction of material required for testing with traditional methods as mentioned in Chapter 2 and Section 3.2.

Section 4.1 entails a brief description of the PEPT technique and the statistical methodology developed and validated for standard test conditions (as previously used in the experiments, see Section 3.2). The methodology allows the calculation of particle velocities filtering out non-physical particle movement due to experimental noise and can be used for analysing results from other testers with small geometries.

Section 4.2 shows a parametric study which was performed to estimate the influence of diverse features of the powder and of the tester on the particle's movements. The study included the influence of parameters including the powder mass, the size of the tracer particle and the rotation speed which were varied along with the air flow passing through the test tube being agitated by a vortex shaker.

## 4.1 Article (published in Powder Technology, 2017)

### Study of the particle motion induced by a vortex shaker

Somik Chakravarty<sup>1</sup>, Marc Fischer<sup>1,2</sup>, Pablo García-Tríñanes<sup>3</sup>, David Parker<sup>4</sup>, Olivier Le Bihan<sup>5</sup> and Martin Morgeneyer<sup>1</sup>

<sup>1</sup> *Laboratoire Transformations Intégrées de la Matière Renouvelable (TIMR), Université de Technologie de Compiègne (UTC) Sorbonne Universités, France*

<sup>2</sup> *Institut National de l'Environnement Industriel et des Risques (INERIS), NOVA/CARA/DRC/INERIS, Parc Technologique Alata, BP2, F-60550 Verneuil-En-Halatte, France*

<sup>3</sup> *Wolfson Centre for Bulk Solids Handling Technology, University of Greenwich, Faculty of Engineering and Science, Central Avenue, Chatham Maritime, Kent, ME4 4TB, United Kingdom*

<sup>4</sup> *School of Physics and Astronomy, University of Birmingham, Birmingham, United Kingdom*

#### 4.1.1 Abstract

The behaviour of a traced alumina particle lying on limestone powders with similar features has been studied in a test tube agitated by a vortex shaker aiming at studying dust emissions from powders. PEPT (Positron Emission Particle Tracking) was used for measuring the particle's position. Population densities were computed as the frequency of the particle's presence in different regions dividing the two horizontal axes and the vertical axis, respectively. The velocities of the particle were calculated by filtering out all displacements inferior to a critical distance  $d_{crit}$  so as not to consider spurious movements caused by experimental noise. After its validation, the methodology was applied to the standard condition of a vortex shaker experiment ( $y = 1500$  rpm, 2 g of powder and open test tube). While the horizontal coordinates and velocity components follow a symmetric distribution, the vertical coordinate is characterised by a large asymmetrical plateau. The heights reached by the particle (up to 24.3 mm) are small in comparison to that of the test tube (150 mm). The greatest velocities are found near the inner wall of the test tube and at the highest heights where the population densities are the lowest. The median velocity of the particle is



0.0613 m.s<sup>-1</sup> whereas its median kinetic energy is 8.4E-12 J. The method explicated in the present study is directly applicable to any other sets of data obtained through PEPT, especially if the system is of small dimension.

**Keywords:** PEPT, Powder, Vortex-shaker, Dustiness

#### **4.1.2 Introduction**

One necessary condition for reaching a better theoretical understanding of dust emission in a tester is a good understanding of the detached particle's motion within the system. This prompted us to undertake the present work where the motion of a single particle has been followed in a test tube agitated by a vortex shaker for several hundreds of seconds. Dust aerosols are small solid particles, conventionally taken as those particles below 75 µm in diameter, which settle out under their own weight but which may remain suspended for some time, according to the International Standardisation Organization (ISO 4225 - ISO, 1994) [1]. The tendency of materials to form aerosols upon handling is known as their dustiness [2,3]. Dustiness studies are important for analysing the industrial risks posed by a bulk material in terms of worker exposure to particles by inhalation, contamination of products and equipment, loss of material and release to the environment [4].

The dustiness of a material is not only related to its physical parameters but also depends on the nature and intensity of the stresses exerted on it alongside external conditions such as humidity and ventilation [2,5]. The tendency of a material to generate dust under certain conditions can be evaluated using meso-scale lab testers [6,7]. For a specific amount of powder, they provide energy to the system for a given period of time. The amount of energy is ideally selected in such a way that it is enough to over-come the adhesive forces between the particles of the bulk solids, thereby emitting dust particles in the air beyond the threshold of measurability. The aerosol concentration and the particle size distribution are then measured as a function of time. Although the dustiness testers are generally designed in such a way that the input energy and dust generation mechanisms are close to industrial situations [8,9], there are only few studies which directly compare the experimental and industrial conditions [10]. This limits our ability to understand, simulate and predict dustiness under industrially relevant circumstances [11].

There exists a wide range of such testers which have been reviewed by several authors [12–14], yet no universal dustiness testing method delivering consistent results under all circumstances could be developed [13]. The European standard 15051 on the Measurement of dustiness of bulk material [15] mentions the continuous drop tester and the rotating drum method but their applicability to the test of micro- and nano-scale powders has been limited as they require large amounts of powder (35 cm<sup>3</sup> or 500 g), thus increasing the experimental cost and also the risk of exposure to aerosol particles of the persons conducting the test [16].

The vortex shaker (VS) [17,18] (or vortex mixer) enables the measure of dustiness with only a fraction (2 g) of the powder which would have been required by other standardised testers. The system is relatively cheap and easy to operate. It seems to be a promising approach to measuring the dustiness of fine cohesive powders [8]. Aerosols are generated through the agitation of a powder-filled symmetrical cylindrical test tube mounted on a digital vortex shaker capable of achieving rotation speeds along the vertical axis. There have been several studies looking into the effect of the VS speed and sample mass on the aerosol concentration (expressed with respect to their masses and numbers) [3,6,17]. However, to the best of our knowledge there has not been any study investigating the effect of the rotational agitation on the powder particle motion.

While there are optical methods, such as the laser Doppler anemometer (LDA) [19] and the particle image velocimetry (PIV) [20], for studying the average velocity fields in a range of flow systems [21–23], they are not well suited for opaque systems [24,25] and consider generally rather low concentrations of particles in the fluid phase [26,27]. Our own approach consists of the Lagrangian tracking of an individual particle [28,29] placed in the powder bed of the test tube which is then agitated by the vortex shaker. The cyclical trajectory of the particle measured at a high frequency over a large duration provides us with statistical information about the behaviour of a powder primary particle detached from the bulk.

We use the Positron Emission Particle Tracking (PEPT) method for tracking a single radioactive tracer particle. It is a non-invasive study of the motion of a particle representative of the other detached powder particles subjected to the same stress conditions. A PEPT analysis of a particle's trajectory over a wide interval (largely superior to one period) can provide us with valuable statistical information such as

population densities, velocities or kinetic energies. These, in turn, would provide us with the first experimental data that can subsequently be used for the validation of CFD (Computationally Fluid Dynamics) and DE (Discrete Elements) models. Such studies would prove very valuable for assessing the frequency and effects of particle-particle and particle-wall interactions.

The goal of our work are to establish a well-founded methodology for studying the traced particle's behaviour within the agitated test tube and then to apply it to the standard case of the vortex shaker induced agitation (1500 rpm) with a vertical gaseous flow of  $0.7 \text{ L}\cdot\text{min}^{-1}$  going through the agitated test tube filled with 2 g of powder.

In Section 4.1.3, we go into the technique of PEPT, and its application to the vortex shaker experimental setup. In Section 4.1.4, we present and validate the statistical strategy we use to determine the particle's position, velocity and kinetic energy. In Section 4.1.5, we apply our methodology to the particle's movement in our reference case ( $\gamma = 1500 \text{ rpm}$ , open test tube, 2 g of powder). Finally, in Section 4.1.6, conclusions are drawn and an outlook for future studies is given.

### **4.1.3 Experimental foundations**

#### ***4.1.3.1 Vortex shaker dustiness tester***

The use of a vortex shaker as a method for generating dust particles from powders is a relatively new and promising technique which has the advantage of being able to use very small quantities of powder [8, 17]. This makes the vortex shaker method a practical and inexpensive dustiness tester when compared to the standardised dustiness testers including the rotating drum and the drop-test.

A vortex shaker can be seen in Figure 4.1. The vortex shaker method used for this study consists of a digital vortex shaker (VWR Signature Digital Vortex Mixer, USA). Such shakers or mixers are commonly used in laboratories to mix small quantities of liquids. It consists of an electric motor with a drive shaft oriented vertically, which is connected to a rubber cup mounted slightly off-center. Dust is generated from a small amount (around 2 g) of bulk solid sample contained in a glass centrifuge tube (diameter 0.025 m, height 0.150 m) firmly mounted on the rubber cup. As the motor runs, the rubber cup oscillates rapidly in a circular motion and the motion is transmitted to the

solid sample inside the cylindrical tube. The shaker is capable of generating a uniform vortex action with rotational velocities ranging between 500 rpm and 2500 rpm along the vertical axis.

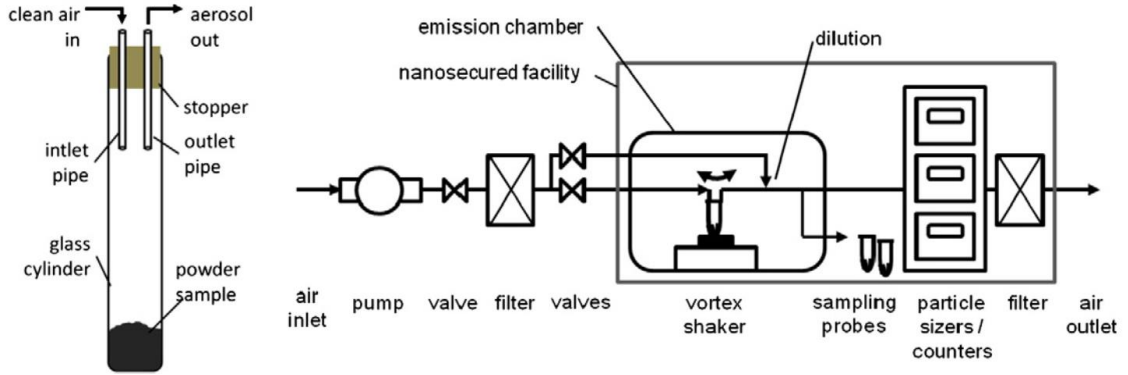


**Figure 4.1:** *The vortex shaker experiment [17].*

Due to the centrifugal forces generated in the vortex shaker setup, the particles in the bulk sample can be assumed to undergo the outward centrifugal force acting as a separation force, the vertical gravitational force and attractive surface forces between the particles acting as binding forces. This phenomenon can be qualitatively seen after each vortex shaker experiment where the bulk sample generates a hollow centre whereas the particles accumulate towards the wall and can also adhere to the wall surface (as shown in the appendix C, see Figure C.1).

#### **4.1.3.2 PEPT and the tracer particle**

Positron emission particle tracking (PEPT) is an experimental technique allowing one to follow the movements of a radioactive tracer particle [30]. This method has been adapted from Positron Emission Tomography (PET) and it is used in particle technology for studying the dynamic behaviour of dry particulate systems such as gas-fluidised beds, tumbling mills, pneumatic conveying etc. used in various industrial processes [31–34]. PEPT allows for non-invasive particle imaging and tracking deep within the particulate system for an extended period of time, thus enabling the analysis of the in-situ kinematics and dynamics of the particle flow [35,36]. We briefly describe the use of a tracer particle in the PEPT technique. For more detailed descriptions of the technique, we refer the

interested reader to the following works [34,37-39]. A scanning device detects the positrons (sub-atomic particles) emitted by a single tracer particle coated (labelled) with the radionuclide. The tracer particle labelled with a positron emitter  $^{18}\text{F}$  [40] with a half-life of 109 min decays via  $\beta^+$  decay, resulting in two gamma rays, each of which travelling

in exactly opposite directions with an energy of 511 keV. The simultaneous detection of the two gamma rays in an array of detectors (using a positron camera) defines a line along which the annihilation of positrons with electrons occurs. The detection of many such events in a short time interval of approximately 10 ms allows the position of the tracer particle to be triangulated in three dimensions. This, in turn, makes the analysis of the trajectory of the tracer particle possible. The spatial location of the tracer particle may be achieved at a frequency reaching values as high as 250 Hz with an accuracy which depends on the speed and activity of the tracer particle. Using an ADAC Forte positron camera [41] installed at the Positron Imaging Centre at the University of Birmingham, a tracer particle moving at 1 m/s can be located within 0.5 mm of its actual position, 250 times per second. To capture the dynamic behaviour of the system, the tracer particle used for a PEPT study should ideally be identical or very similar with respect to its physical characteristics to the bulk material used in the system [42,43].

Also, the radio activity of the tracer should be high enough (preferably 300–1000  $\mu\text{Ci}$ ) for uninterrupted tracking of the particle [44]. Thus, PEPT allows for the analysis of the motion of the particle in a complex physical system such as the vortex shaker, where it is influenced by a combination of forces including the centrifugal forces, vibration and particle-particle and particle-wall interactions. In addition to that, it can be used to determine the density of particles at each point of the setup, under the assumption that the behaviour of the traced particle over a large time period is a good approximation of the average behaviour of the ensemble of detached particles.

#### ***4.1.3.3 Test protocol***

The experiments were performed at the Positron Imaging Centre, Nuclear Physics research group, University of Birmingham. A detailed description of the PEPT is

mentioned in [34,37,45] and here we mention only the procedures related to the vortex shaker dustiness tester.

We took 2 g of Eskal 150 calcium carbonate powder weighed with an accuracy of  $\pm 0.01$  g using an analytical balance (Mettler Toledo MS104TS), manually filled in the centrifuge tube (diameter 0.025 m, height 0.15 m). The size distribution of the primary particles is such that the median diameter is 138  $\mu\text{m}$ ,  $d_{10} = 97$   $\mu\text{m}$  and  $d_{90} = 194$   $\mu\text{m}$  (see [46]). The diameter of the tracer particle has been chosen in such a way to be between 80  $\mu\text{m}$  and 150  $\mu\text{m}$ . The density is 2710  $\text{kg}\cdot\text{m}^{-3}$ .

We first labelled such a  $\text{CaCO}_3$  particle using  $^{18}\text{F}$  radionuclide (whose half-life is 109 min). However, due to the poor activation and insufficient radioactivity of the Eskal limestone particles, the calcium carbonate tracer particle was replaced by a gamma-alumina particle which showed sufficient radioactivity for more than few hours after the activation. The  $^{18}\text{F}$  radionuclide in the tracer particle exists as structural elements about 0.3  $\mu\text{m}$  under the tracer surface and is most likely unaffected by the existing ions or worn out during the test [44]. The used gamma-alumina particles from Alfa Aesar, USA had diameters between 80  $\mu\text{m}$  and 150  $\mu\text{m}$  with a purity of 99.9% and a particle density of 2950  $\text{kg}\cdot\text{m}^{-3}$  similar to the features of the Eskal 150 powder used as the bulk powder during the vortex shaker experiment.

For the experiments, the powder-filled centrifuge tube was sealed using a rubber stopper (0.02 m in depth) with an opening for the inlet and outlet using two stainless steel pipes (inner diameter, 0.003 m) placed beyond 30 mm inside the tube opening piercing through the rubber stopper. The air was sucked in by a low-pressure pump ( $0.7 \pm 0.01$  L  $\cdot$  min $^{-1}$  or  $1\text{e-}05 \pm 1.6\text{e-}07$   $\text{m}^3\cdot\text{s}^{-1}$ , Gilian LFS-113DC). The tracer particle was prepared using an indirect (water based) radioactive labelling technique in contrast to the direct bombardment of the particle itself. A heat lamp assisted then the evaporation of the radioactive water. The particle tracer was then manually transferred from its holder to a powder-filled centrifuge tube, which was mounted on the vortex shaker system placed between the positron camera (detectors). The transfer of the tracer particle into the tube and its presence in the test tube through the test duration was ensured using a Geiger counter. The vortex shaker was rotated at 1500 rpm and run for 12 min. The trial was repeated once. The powder bed covered a height of 6 mm lying on the round bottom of the test tube. It was not possible to determine the initial position of the traced particle.

#### 4.1.4 Presentation of the statistical methodology

This section aims at defining and illustrating a sound methodology suitable for studying the movement of the particle inside the agitated test tube.

##### 4.1.4.1 Raw data and measurement uncertainties

The raw data come in the form of relative coordinates of the traced particle measured in very short time intervals (of roughly 10 ms). The position of the test tube with respect to the detectors may change from trial to trial because of its being mounted and unmounted. As a consequence, only the relative movements of the particle can be seen. Therefore, we defined the coordinate system as follows. We defined the height in such a way that  $y = 0$  corresponds to the lowest position of the particle which has ever been measured during the trial under consideration. We defined the horizontal coordinates  $x$  and  $z$  in such a way that  $x = 0$  and  $z = 0$  become the median position which are stabler statistical indicators than the means [47]. Given the symmetrical nature of the system, this proved a good strategy. We show the three axes within the test tube in Figure 4.2. The PEPT data are given in a cartesian frame and can thus be more readily interpreted in that way. Researchers interested in cylindrical coordinates could easily transform our results into that system of representation.

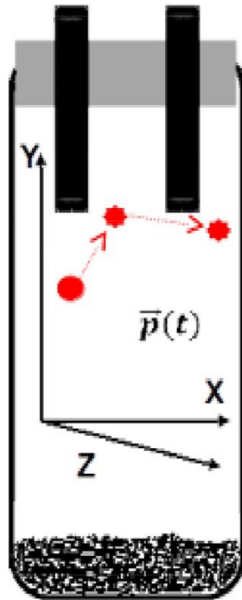


**Figure 4.2:** Axes within the test tube.

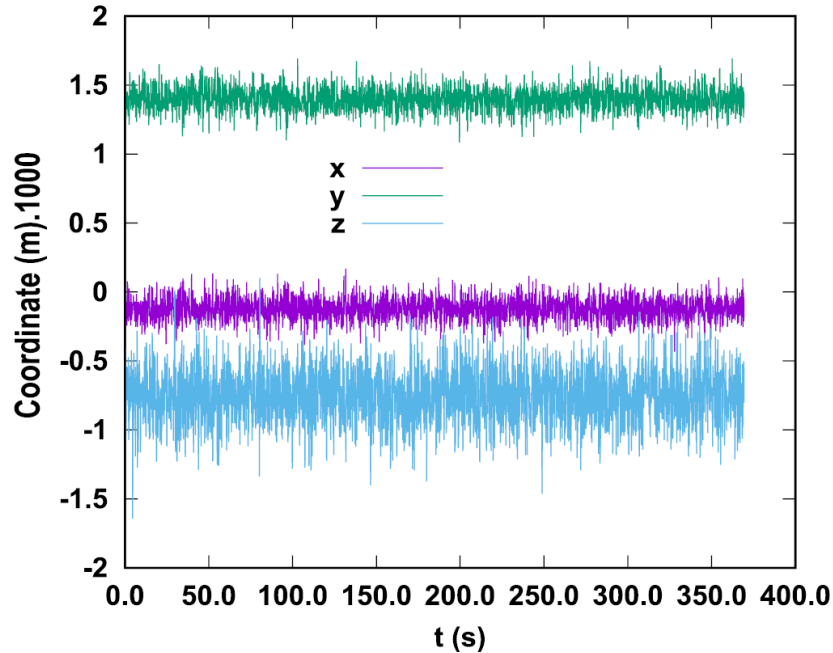


**Figure 4.3:** *Measured position in a closed non-agitated vortex-shaker.*

In order to compute velocities and other quantities based on the raw data, it is necessary to make a distinction between random experimental uncertainties and fluctuations of the position stemming from turbulence or other physical phenomena. For that sake, a trial where the particle position was tracked in a non-agitated and closed test tube (i.e.  $\omega = 0$  rpm) has been considered. If the diffusion of particles whose aerodynamic diameters are higher than  $50 \mu\text{m}$  can be neglected, random errors should be the only cause of any observed change. In Figure 4.3, the “position” ( $x,y,z$ ) is represented as a function of time. It can be clearly seen that the measurement uncertainties cause rapid chaotic oscillations of the values which cannot be attributed to the physical state of the system. As a consequence, it is not possible to define velocities locally as this could artificially attribute a highly fluctuating speed to an immobile particle. In Figure 4.4, the averaged coordinates of the particle are given for different numbers of time points utilised to compute the local means (e.g. around  $t = 300.0$  s). Even if relatively large numbers of time points are considered to calculate the mean values, the quantities are not constant, which means that the experimental noise is not erased. What is more, we noticed that averaging over more than 30 points may hide many of the physical trends observed during non-stationary trials. Consequently, another approach was adopted.



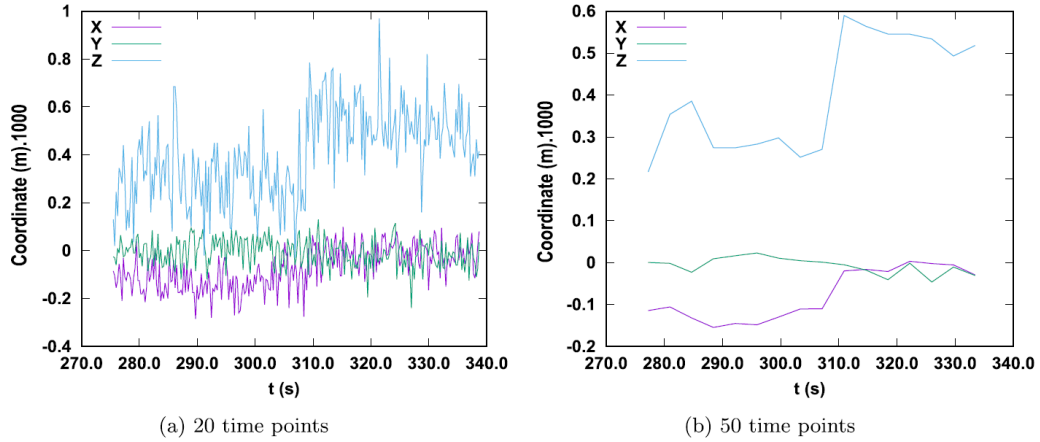


**Figure 4.4:** Locally averaged coordinates. Length units are in mm.

#### 4.1.4.2. Definition of the strategy

These considerations led us to devise the following strategy for studying the particle’s behaviour in the test tube.

- Only the steady state of the experiment is considered. It is the time period after the transition following the starting of the vortex shaker and before the device is switched off. It was determined in each case by analysing the raw data  $(x,y,z)$  as a function of time.
- The frequency of the particle being at the position  $x$ ,  $y$  or  $z$  is estimated as the number of times its position belongs to the interval  $[x \pm D_x]$ ,  $[y \pm D_y]$  or  $[z \pm D_z]$ , respectively. Since the measurement errors follow more or less a random distribution (see appendix C, Figure C.3), they can be expected to cancel out while considering the large samples we have at our disposal.
- Every time the particle displays a change in position equal to or greater than a critical distance (i.e.  $d \geq d_{crit}$ ), a velocity is defined as the ratio of  $d$  and the time  $D_t$  corresponding to the displacement. The value of the critical distance  $d_{crit}$  must be chosen in such a way that ideally as few spurious coordinate fluctuations as possible are considered while the real physical movements of the particle are captured. Such a trade-off requires a process of trials and

errors. The trajectory is filtered in such a way that the displacement from a point P1 to a point P2 is only considered as a genuine movement if the covered distance  $d$  is greater than or equal to  $d_{crit}$ .

- Frequency distributions of the values of the above velocities and kinetic energies are computed.
- The locally averaged velocities  $V$ ,  $V_x$  (horizontal motion) and  $V_y$  (vertical motion) have been expressed as a function of  $x$  and  $y$ .

#### 4.1.4.3 Analysis of the strategy

We then analysed the consistency of our filtering approach, partially relying on the data considered in Section 4.

The first step was to check that the filtered velocity defined above corresponds to genuine trajectories. Ideally, the measurement errors should be filtered out without overlooking important features of the traced particle trajectory. In Figure 4.5, the vectors corresponding to the pseudo-trajectory under stationary conditions (i.e. closed test tube,  $y = 0$  rpm) have been represented before and after the filtering in the  $(x,y)$  plane. It can be seen that the measurement errors are randomly distributed and do not show any consistent trajectory. The artificial displacement vectors are erased upon filtering.

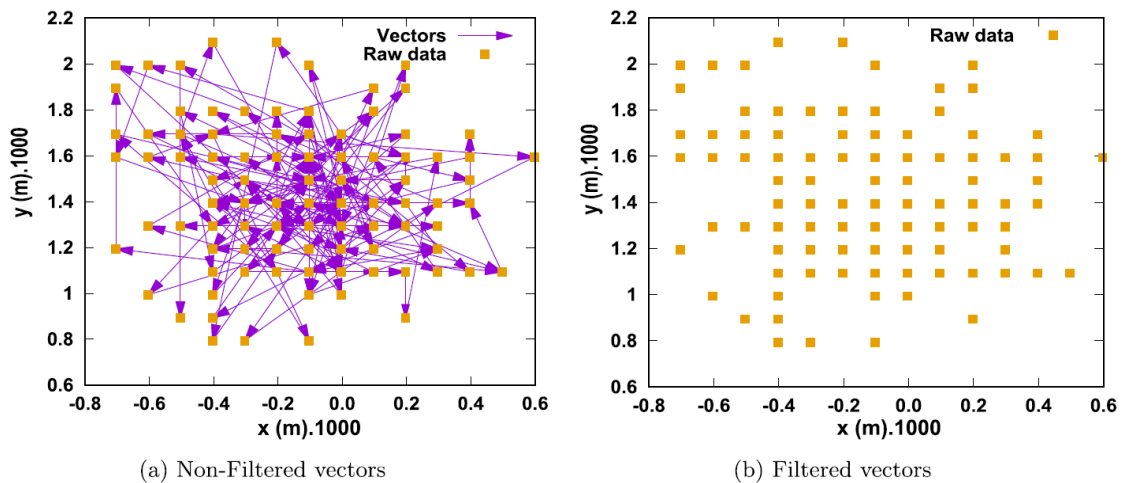


**Figure 4.5:** Pseudo-trajectory for the stationary trial. Length units are in mm.

It is worth noting that authors such as [34] used averaging over a relatively long period of time (e.g. 10 s) to carry out their analyses. Such an approach would not work in our case as the particle can considerably change its direction (up to ten times) within only 2 s. Averaging would thus lead us to unphysical velocities which do not correspond to the real movements of the particle. Ansart et al. [33] utilised an alternative approach consisting of smoothing the velocity using a given number of neighbouring points. In the case of 10 neighbouring points, the velocity with respect to the coordinate  $i$  is defined as follows:

$$u_{p,i}(t_k) = 0.1 \left( \frac{P_{k+5,i} - P_{k,i}}{t_{k+5} - t_k} \right) + 0.15 \left( \frac{P_{k+4,i} - P_{k-1,i}}{t_{k+4} - t_{k-1}} \right) + 0.25 \left( \frac{P_{k+3,i} - P_{k-2,i}}{t_{k+3} - t_{k-2}} \right) + 0.25 \left( \frac{P_{k+2,i} - P_{k-3,i}}{t_{k+2} - t_{k-3}} \right) + 0.1 \left( \frac{P_{k+1,i} - P_{k-4,i}}{t_{k+1} - t_{k-4}} \right) + 0.15 \left( \frac{P_{k,i} - P_{k-5,i}}{t_k - t_{k-5}} \right)$$

(Eq. 4.1)

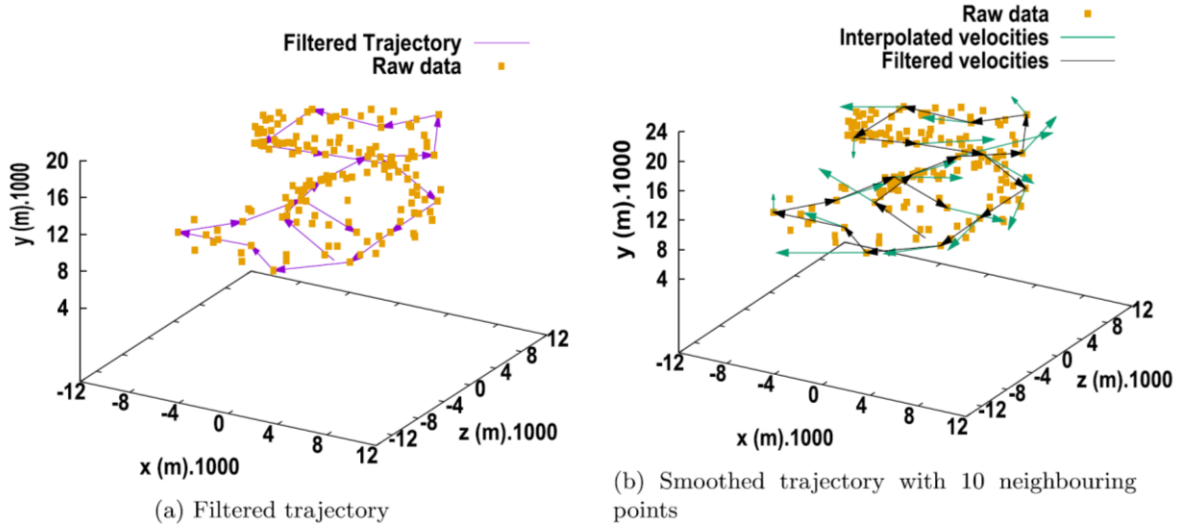


**Figure 4.6:** Filtering and smoothing for  $y = 1500$  rpm, close test tube and  $t \in [100:102, 0]$  s. Length units are in mm.

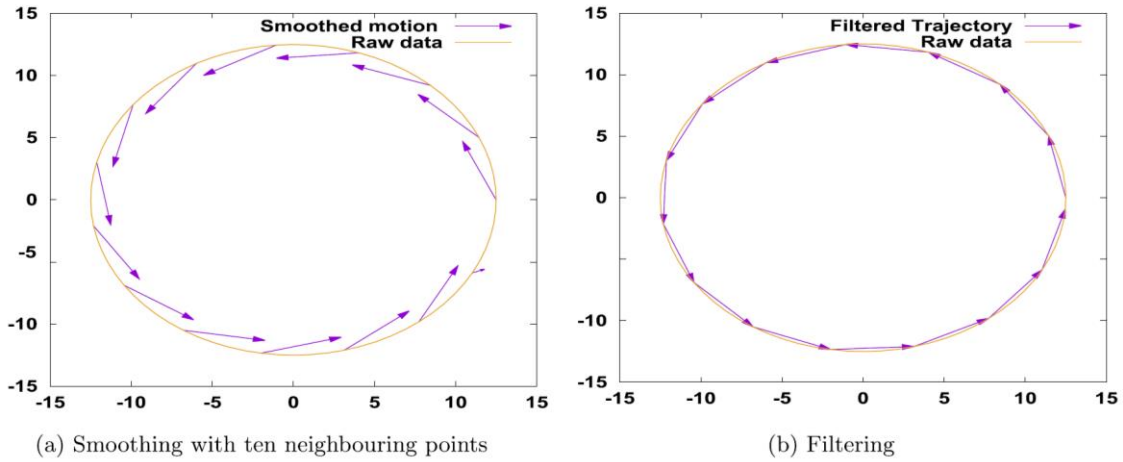


**Figure 4.7:** Smoothing and filtering of a circular movement (units: mm).

The points directly surrounding  $k$  receive a weight of 0.5 whereas the most distant ones receive the smallest coefficients. In Figure 4.6, the filtered and smoothed trajectory during one trial at  $\omega = 1500$  rpm in a test tube with inlet and outlet flow have been represented for a duration of 2 s. One can recognise that the main trends of the trajectory are well represented by the filtered vector field. Thus, our filtering appears to be a good compromise for removing most random experimental errors without losing track of the genuine movements of the particle. The optimal value used for obtaining these curves proved to be  $d_{crit} = 5$  mm. The interpolated velocity has been systematically multiplied by the difference in time  $D_t$  between two points of the filtered trajectory. In this way, the magnitude of the motion can be compared as well. It can be seen that both the directions and values of the smoothed velocity can differ significantly from those of the filtered one. No improvement could be achieved for other numbers of neighbouring points.

We also applied filtering and smoothing to a perfectly circular movement of radius 12.5 cm taking place for 1 s, which is the duration of a real circular movement happening between  $t = 100.30$  s and  $t = 101.30$  encompassing 76 points. The results are shown in Figure 4.7. While the filtered velocities correspond to real distances covered by the particle, there is a priori no guarantee that the smoothed velocities are a good approximation to the particle's real behaviour, regardless of the number of neighbouring points. The same can be said about the averaging over 20 points, despite the fact that such a number is not large enough to even out the experimental noise, as can be seen in Figure

4.4. All these difficulties led us to consider filtering as a straightforward and easily implementable approach for estimating the velocity distribution of the traced particle.

As can be seen in Section 4 and in the appendix C (see Figure C.4 – Figure C.8), the population densities (frequencies of presence) computed using all unfiltered points during the steady state and the frequencies of the velocity and the kinetic energy values based on the filtered trajectory are coherent and similar for two repeated trials.

#### 4.1.5 Analysis of the particle’s behaviour under standard conditions

The population densities and frequency distributions of the velocity and kinetic energy were considered to assess the movement of the particle under standard conditions (open test tube,  $\gamma = 1500$  rpm and 2 g of powder). For that sake, the two repeated trials were taken into consideration. We refer the reader to the appendix for seeing graphics systematically comparing the two repeated trials for every variable (see Figure C.4 – Figure C.8). In what follows, we only show the first trial in the graphics. Q1 and Q2 are the first and second quartile, respectively. Along with the median, they are robust statistical indicators of trends in a series of data [47]. The frequency distribution of the coordinates and velocity components are shown in Figure 4.8 whereas the corresponding statistical indicators are given in Table 4-1 and Table 4-2.

**Table 4-1:** *Statistics related to the movement.*

<b>Trial</b>	<b>Min</b>	<b>Max</b>	<b>Q<sub>1</sub></b>	<b>Median</b>	<b>Q<sub>3</sub></b>	<b>Std dev</b>
<i>x</i> (mm)						
1	-10.90	10.90	-3.50	0.00	3.50	4.68
2	-11.01	11.00	-3.31	0.00	3.10	4.61
<i>z</i> (mm)						
1	-12.80	11.80	-3.40	0.00	3.40	4.48
2	-11.50	12.21	-3.30	0.00	3.00	4.38
<i>y</i> (mm)						
1	0.00	23.80	6.60	11.01	15.60	5.44
2	0.00	24.30	6.00	11.10	15.81	5.68

**Table 4-2:** Statistics related to the velocity components.

<b>Trial</b>	<b>Min</b>	<b>Max</b>	<b>Q<sub>1</sub></b>	<b>Median</b>	<b>Q<sub>3</sub></b>	<b>Std dev</b>
<i>V<sub>x</sub>(x)(m/s)</i>						
1	-0.2339	0.2857	-0.0325	-0.0004	0.0311	0.0495
2	-0.2769	0.2851	-0.0294	0.0000	0.0304	0.0506
<i>V<sub>z</sub>(z)(m/s)</i>						
1	0.3231	0.2395	-0.0317	-0.0008	0.0333	0.0513
2	-0.3894	0.4188	-0.0309	-0.0008	0.0315	0.0549
<i>V<sub>y</sub>(y)(m/s)</i>						
1	-0.2105	0.1584	-0.0184	-0.0025	0.0103	0.0214
2	-0.2762	0.1682	-0.0212	-0.0031	0.0112	0.0250

The frequency distributions of the horizontal coordinates  $x$  and  $z$  and of the corresponding velocity components seem to follow a symmetric normal distribution. The particle's behaviour with respect to  $x$  and  $z$  is the same, as shown by the statistical indicators. The width of the  $x$  values (21.8 and 22.1 mm) is slightly smaller than the inner diameter of the test tube (24 mm). The higher width of the  $z$  values (24.6 and 23.71 mm) are likely due to the higher values of the random errors (see appendix C, Figure C.3). The frequency distribution of  $y$  is characterised by an increase, a plateau and a steep decrease at the highest heights. The largest measured height (24.30 mm) represents only 16.2% of the total height of the test tube (150 mm) and 4.05 times the height of the powder bed (6 mm). This means that the particle considered here (whose diameters are between 80  $\mu\text{m}$  and 150  $\mu\text{m}$ ) are apparently too large and heavy for reaching the height where they could exit the test tube over the duration of the experiment. The frequency distribution of the vertical velocity  $V_y$  is non-symmetrical and biased towards negative values. This can be plausibly attributed to the effect of gravity and the smaller numbers of collisions with other aerosols as shall be seen later.

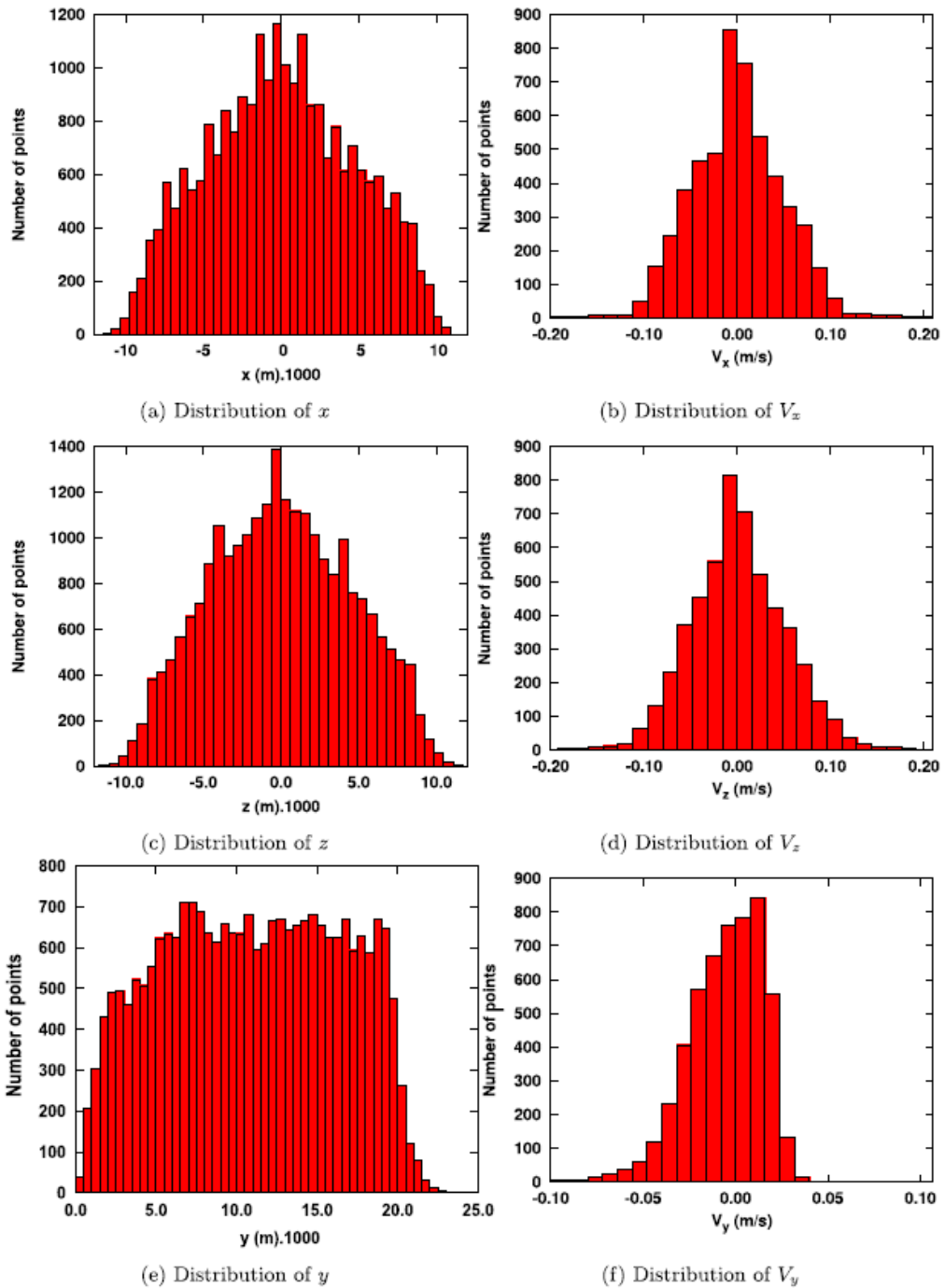


**Figure 4.8:** Distribution of the coordinates and velocity components. Length units are in mm.

In Figure 4.9 and in Table 4-3, the features of the velocity and the kinetic energy are shown.

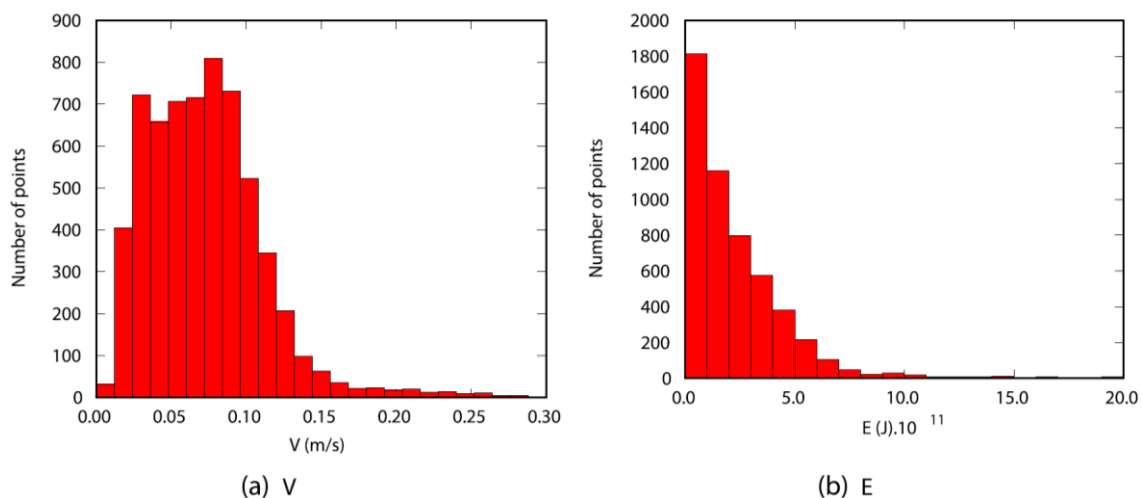


**Figure 4.9:** Frequency distribution of the velocity and kinetic energy.

**Table 4-3:** Statistics related to  $pV$ .

Trial	Min	Max	Q <sub>1</sub>	Median	Q <sub>3</sub>	Std dev
$V$ (m/s)						
1	0.0024	0.3491	0.0385	0.0615	0.0854	0.0366
2	0.0052	0.4477	0.0355	0.0611	0.0883	0.0422
Average			0.0370	0.0613	0.0869	0.0394
$E \cdot 10^{11}$ (J)						
1	0.0012	27.3551	0.3326	0.8490	1.6382	1.7089
2	0.0061	44.9969	0.2822	0.8374	1.7511	2.3108
Average			0.3074	0.8432	1.6947	2.0099

The kinetic energy distribution follows a decreasing exponential shape. The frequency distribution of the velocity  $V$  is asymmetrical and is u by a smooth increase followed by a steep decrease in both cases. To explore the cause of this, we represented the average values of the velocity (and velocity components) as a function of the horizontal coordinate  $x$  and the vertical coordinate  $y$  in Figure 4.10. We show the results of the repeated trials in the appendix C (see Figure C.7 and Figure C.8). The largest values of the velocity  $V$  are found at the highest heights where the highest descending values of  $V_y$  are also seen. This indicates that these highest velocities might stem from the effects of gravity on the particle. As function of the horizontal coordinate  $x$ , the highest velocity values are found near the wall of the test tube. It is worth noting that



$V_y(x)$  points upwards at the middle of the test tube but downwards when  $x$  approaches the extremity of the test tube.

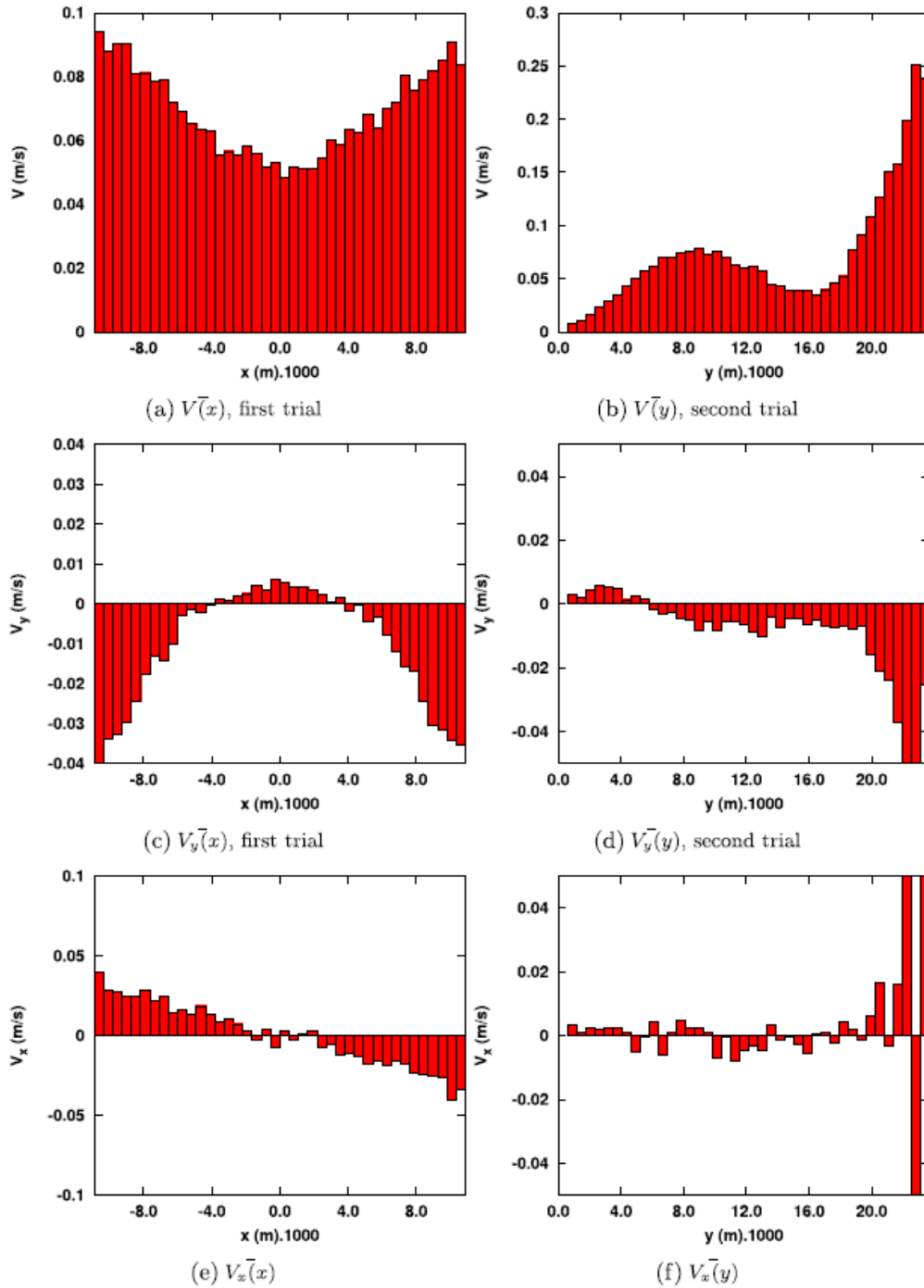


**Figure 4.10:** Time-averaged velocity as a function of  $x$  and  $y$ . Length units are in mm.

In Figure 4.11, all points where the particle goes upwards and downwards are represented with respect to the horizontal coordinates  $x$  and  $z$ . It can be seen that the

particle rarely moves downward around the middle of the test tube. On the other hand, the particle also seldom moves upward near the wall of the test tube. The region where the upward and downward motions overlap is narrow. It is noteworthy that the highest values of the average velocity  $V$  are found in regions where the presence frequency of the particle is the lowest (highest heights and areas close to the inner wall). Besides the gravity, the higher values of the velocity might stem from a decrease in the number of shocks due to lower population densities.

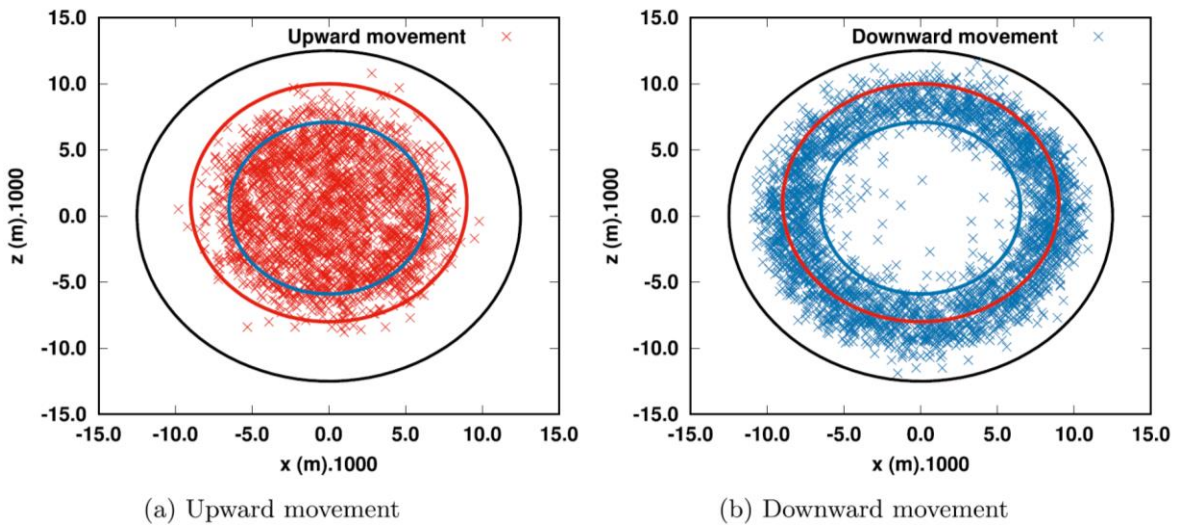


**Figure 4.11:** Distribution of the upward and downward movement. Large circle: inner wall. Small markings: imaginary boundaries of the upward and downward movements.

In Figure 4.12, the local circulation (from  $t = 200$  s to  $t = 207$  s) and the average circulation (over the whole steady state, i.e. between  $t = 20$  s and  $t = 700$  s) have been represented. On average, the particle tends to move upward with a low velocity around the middle of the test tube whereas it falls back at a much higher speed beside the inner wall of the test tube. The time-averaged velocities are considerably smaller in the horizontal middle of the test tube. The local values are much less regular.

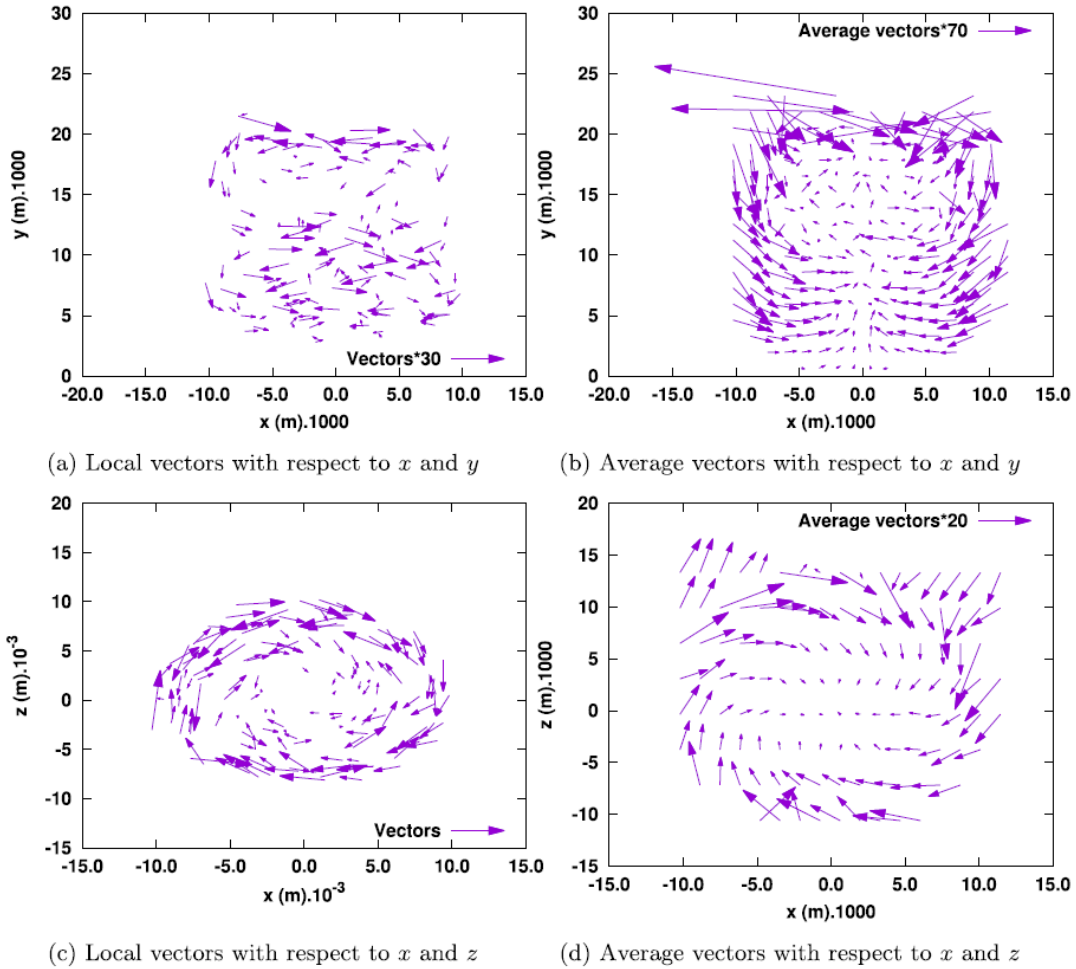


**Figure 4.12:** Local instantaneous ([200.00;217.00] s) and time-averaged velocity vectors. Length units are in mm.

#### 4.1.6 Conclusions and outlook

In this work, we wanted to develop a methodology allowing us to study the behaviour of detached aerosol particles in a test tube agitated by a vortex shaker and apply it to our standard conditions, as such data are necessary for understanding dust emission and developing predictive models.

In Section 2, we describe PEPT and the vortex shaker. In Section 3, we describe and validate the statistical methods we used. Giving the short-range motion of the particle and the small dimension of the test tube, averaging and smoothing did not prove to be good strategies for computing a physically realistic velocity. Instead, a filtering approach was adopted, in that only a motion covering at least a critical distance  $d_{crit}$  is considered.

Based on this, we assessed the particle's behaviour under standard conditions that is at a rotation speed of 1500 rpm while an air flow goes through the open test tube filled with 2 g of powder. We considered  $\text{CaCO}_3$  powder whose aerodynamic diameters are between 80  $\mu\text{m}$  and 150  $\mu\text{m}$ . Since we could not radio-activate its particles, we used a tracer particle of alumina with similar physical characteristics instead. The local instantaneous trajectory of the particle has a chaotic aspect which makes it hard to identify any trends apart from the circular nature of the motion. A statistical treatment of the measured positions and filtered velocities allows one, however, to identify important features of the macroscopic behaviour of the particle. The frequency distributions of the horizontal coordinates  $x$  and  $z$  and of the corresponding velocity components  $V_x$  and  $V_z$  follow approximately a Gaussian shape. The frequency distribution of the height  $y$  is characterised by a strong increase, an even stronger decrease and a plateau between  $y = 5$  mm and  $y = 20$  mm. The heights reached by the particle are much inferior to the height of the test tube (150 mm). The highest values of the velocity are found at the highest heights and close to the inner wall of the test tube, where the population densities are thinner.

The data we obtained in the present study are the first step for establishing numerical models building a bridge between theory and experiments, which is in itself one of the main goals of powder technology [48]. A combination of CFD (Eulerian - Lagrangian) and DEM (Direct Element Modelling) seems to be a promising way to develop predictive models [49]. Wangchai et al. [50] investigated the particle flow mechanisms of powders within a rotating drum dustiness tester through a combination of experimental work and DEM. They found out that while useful, DEM cannot capture all the flow patterns in a dustiness tester which are crucial for understanding the behaviour of the produced aerosols. CFD appears to be a good complementary approach to reaching a truly holistic view of the phenomena under-lying dust generation. We intend to use the data of this study as a basis for simulating the motion of the particles within the agitated test tube. This, in turn, shall allow us to model the whole aerosolisation process, including the movement of the particles in the bulk, the interaction between particles and the formation of the first aerosols. Our study opens up another research endeavour that is worth mentioning. Kahrizsangi et al. [51,52] conducted a parametric study of dustiness within a fluidised bed vibrating with different frequencies and accelerations. While they could well account for the effects stemming from changes in the acceleration, they were

not able to provide an intuitive physical explanation of the bearing of the frequency on dustiness. We intend to perform a similar parametric study of our system relying on PEPT which will concern the most important variables, i.e. the mass, the rotation speed and the size of the tracer particle.

#### 4.1.7 References

- [1] E. Petavratzi, S. Kingman, I. Lowndes, Particulates from mining operations: a review of sources, effects and regulations, *Miner. Eng.* 18 (2005) 1183–1199.
- [2] D. Dahmann, C. Monz, Determination of dustiness of nanostructured materials, *Gefahrstoffe - Reinhalt. Luft* 71 (2011) 481–487.
- [3] I. Ogura, H. Sakurai, M. Gamo, Dustiness testing of engineered nanomaterials, *J. Phys. Conf. Ser.* 170 (2009) 012003.
- [4] A. Klippel, M. Schmidt, U. Krause, Dustiness in workplace safety and explosion protection-review and outlook, *J. Loss Prev. Process Ind.* 34 (2015) 22–29.
- [5] D.E. Evans, L.A. Turkevich, T. Roettgers, G.J. Deye, P.A. Baron, Dustiness of fine and nanoscale powders, *Ann. Occup. Hyg.* 57 (2013) 261–277.
- [6] A. Maynard, P. Baron, M. Foley, Exposure to carbon nanotube material: aerosol release during the handling of unrefined single-walled carbon nanotube material, *J. Toxicol.* (2004)
- [7] A.D. Maynard, E.D. Kuempel, Airborne nanostructured particles and occupational health, *J. Nanopart. Res.* 7 (2005) 587–614.
- [8] O.L.C. Le Bihan, A. Ustache, D. Bernard, O. Aguerre-Chariol, M. Morgeneyer, Experimental study of the aerosolization from a carbon nanotube bulk by a vortex shaker, *J. Nanopart.* 2014 (2014) 7.
- [9] Y. Ding, B. Stahlmecke, H. Kaminski, Y. Jiang, T.A. Kuhlbusch, M. Riediker, Deagglomeration testing of airborne nanoparticle agglomerates: stability analysis under varied aerodynamic shear and relative humidity conditions, *Aerosol Sci. Technol.* 50 (2016) 1253–1263.
- [10] S. Kamath, V. Puri, H. Manbeck, R. Hogg, Flow properties of powders using four testers measurement, comparison and assessment, *Powder Technol.* 76 (1993) 277–289.
- [11] W.A. Heitbrink, W.F. Todd, T.C. Cooper, D.M. O'Brien, The application of dustiness tests to the prediction of worker dust exposure, *Am. Ind. Hyg. Assoc. J.* 51 (1990) 217–223.
- [12] S. Bach, U. Eickmann, E. Schmidt, Comparison of established systems for measuring the dustiness of powders with the UNC dustiness tester developed especially for pharmaceutical substances, *Ann. Occup. Hyg.* (2013) met022.
- [13] F. Hamelmann, E. Schmidt, Methods of estimating the dustiness of industrial powders-a review, *KONA Powder Particle J.* 21 (2003) 7–18.
- [14] M.A. Plinke, R. Maus, D. Leith, Experimental examination of factors that affect dust generation by using Heubach and MRI testers, *Am. Ind. Hyg. Assoc. J.* 53 (1992) 325–330.
- [15] C.E.N. 15051, 15051 Workplace Atmospheres Measurement of the Dustiness of Bulk Materials Requirements and Test Methods, European committee for standardization, Brussels, Belgium, 2006.
- [16] M. Boundy, D. Leith, T. Polton, Method to evaluate the dustiness of pharmaceutical powders, *Ann. Occup. Hyg.* 50 (2006) 453–458.
- [17] M. Morgeneyer, O. Le Bihan, A. Ustache, O. Aguerre-Chariol, Experimental study of the aerosolization of fine alumina particles from bulk by a vortex shaker, *Powder Technol.* 246 (2013) 583–589.

- [18] S. Chakravarty, O. LeBihan, M. Fischer, M. Morgener, Dust generation in powders: effect of particle size distribution, EPJ Web of Conferences, vol. 140, EDP Sciences. 2017, pp. 13018.
- [19] F. Durst, A. Melling, J.H. Whitelaw, Principles and Practice of Laser-Doppler Anemometry, NASA STI/Recon Technical Report A, 76. 1976.
- [20] R.J. Adrian, J. Westerweel, Particle Image Velocimetry, 30, Cambridge University Press. 2011.
- [21] J.G. Santiago, S.T. Wereley, C.D. Meinhart, D. Beebe, R.J. Adrian, A particle image velocimetry system for microfluidics, Exp. Fluids 25 (1998) 316–319.
- [22] C. Willert, Stereoscopic digital particle image velocimetry for application in wind tunnel flows, Meas. Sci. Technol. 8 (1997) 1465.
- [23] I. Nezu, W. Rodi, Open-channel flow measurements with a laser Doppler anemometer, J. Hydraul. Eng. 112 (1986) 335–355.
- [24] A.P. Yoganathan, W.H. Corcoran, E.C. Harrison, In vitro velocity measurements in the vicinity of aortic prostheses, J. Biomech. 12 (1979) 135–152.
- [25] A. Ochieng, M. Onyango, K. Kiriamiti, Experimental measurement and computational fluid dynamics simulation of mixing in a stirred tank: a review, S. Afr. J. Sci. 105 (2009) 421–426.
- [26] Z.-C. Liu, C. Landreth, R. Adrian, T. Hanratty, High resolution measurement of turbulent structure in a channel with particle image velocimetry, Exp. Fluids 10 (1991) 301–312.
- [27] R. Ettema, I. Fujita, M. Muste, A. Kruger, Particle-image velocimetry for whole-field measurement of ice velocities, Cold Reg. Sci. Technol. 26 (1997) 97–112.
- [28] B. Guo, D.F. Fletcher, T.A. Langrish, Simulation of the agglomeration in a spray using Lagrangian particle tracking, Appl. Math. Model. 28 (2004) 273–290.
- [29] P.W. Longest, J. Xi, Effectiveness of direct Lagrangian tracking models for simulating nanoparticle deposition in the upper airways, Aerosol Sci. Technol. 41 (2007) 380–397.
- [30] J. Seville, A Single Particle View Of Fluidization, The 13th International Conference on Fluidization - New Paradigm in Fluidization Engineering. 2010, pp. 1–11.
- [31] J. Chaouki, F. Larachi, M. Dudukovic, Non-invasive monitoring of multiphase flows, Elsevier. 1997.
- [32] J.A. Laverman, I. Roghair, M. v. S. Annaland, H. Kuipers, Investigation into the hydrodynamics of gas-solid fluidized beds using particle image velocimetry coupled with digital image analysis, Can. J. Chem. Eng. 86 (2008) 523–535.
- [33] R. Ansart, P. Garcia-Trinanes, B. Boissiere, H. Benoit, J. Seville, O. Simonin, Dense gas-particle suspension upward flow used as heat transfer fluid in solar receiver: PEPT experiments and 3D numerical simulations, Powder Technol. 307 (2017) 126–137.
- [34] D. Parker, A. Dijkstra, I. Martin, J.P.K. Seville, Positron emission particle tracking studies of spherical particle motion in rotating drums, Chem. Eng. Sci. 52 (1997) 2011–2022.
- [35] T. Volkwyn, A. Buffler, I. Govender, J.-P. Franzidis, A. Morrison, A. Odo, N. Van Der Meulen, C. Vermeulen, Studies of the effect of tracer activity on time-averaged positron emission particle tracking measurements on tumbling mills at PEPT Cape Town, Miner. Eng. 24 (2011) 261–266.
- [36] M. Stein, Y. Ding, J. Seville, Experimental verification of the scaling relationships for bubbling gas-fluidised beds using the PEPT technique, Chem. Eng. Sci. 57 (2002) 3649–3658.
- [37] D.J. Parker, C.J. Broadbent, P. Fowles, M.R. Hawkesworth, Positron emission particle tracking—a technique for studying flow within engineering equipment, Nucl. Instrum. Methods Phys. Res., Sect. A 326 (1993) 592–607.
- [38] M. Tan, D. Parker, P. Dee, PEPT Data Presentation Software, Manual, Birmingham University, UK, 1997.
- [39] J. Seville, A. Ingram, X. Fan, D. Parker, Positron emission imaging in chemical engineering, Adv. Chem. Eng. 37 (2009) 149–178.

- [40] D. Valdesueiro, P. Garcia-Tri nanes, G. Meesters, M. Kreutzer, J. Gargiuli, T. Leadbeater, D. Parker, J. Seville, J. van Ommen, Enhancing the activation of silicon carbide tracer particles for PEPT applications using gas-phase deposi-tion of alumina at room temperature and atmospheric pressure, *Nucl. Instrum. Methods Phys. Res., Sect. A* 807 (2016) 108–113.
- [41] D. Parker, R. Forster, P. Fowles, P. Takhar, Positron emission particle tracking using the new Birmingham positron camera, *Nucl. Instrum. Methods Phys. Res., Sect. A* 477 (2002) 540–545.
- [42] M. Van de Velden, J. Baeyens, J.P.K. Seville, X. Fan, The solids flow in the riser of a circulating fluidised bed (CFB) viewed by positron emission particle tracking (PEPT), *Powder Technol.* 183 (2008) 290–296.
- [43] M. Marigo, M. Davies, T. Leadbeater, D.L. Cairns, A. Ingram, E.H. Stitt, Applica-tion of positron emission particle tracking (PEPT) to validate a discrete element method (DEM) model of granular flow and mixing in the Turbula mixer, *Int. J. Pharm.* 446 (2013) 46–58.
- [44] D.J. Parker, X. Fan, Positron emission particle tracking application and labelling techniques, *Particuology* 6 (2008) 16–23.
- [45] D. Parker, P. McNeil, Positron emission tomography for process applications, *Meas. Sci. Technol.* 7 (1996) 287.
- [46] H. Shi, R. Mohanty, S. Chakravarty, R. Cabisco, M. Morgeneyer, H. Zetzener, J. Ooi, A. Kwade, S. Luding, V. Magnanimo, Effect of particle size and cohesion on powders yielding and flow, *KONA Powder Particle J.* (2017) accepted for the publication.
- [47] W.H. Press, S.A. Teukolsky, W.T. Vetterling, B.P. Flannery, *Numerical Recipes in C (2Nd Ed.): The Art of Scientific Computing*, Cambridge University Press, New York, NY, USA, 1992.
- [48] I. Tomasetta, D. Barletta, M. Poletto, Correlation of powder flow properties to interparticle interactions at ambient and high temperatures, *Particuology* 12 (2014) 90–99.
- [49] L.E. Stone, P.W. Wypych, D.B. Hastie, S. Zigan, et al. CFD-DEM modelling of powder flows and dust generation mechanisms-a review, 12th International Conference on Bulk Materials Storage, Handling and Transportation (ICBMH 2016), The, Engineers Australia, 2016, pp. 417.
- [50] S. Wangchai, D.B. Hastie, P.W. Wypych, The investigation of particle flow mechanisms of bulk materials in dustiness testers, *Part. Sci. Technol.* 34 (2016) 241–254.
- [51] H.S. Kahrizangi, D. Sofia, D. Barletta, M. Poletto, Dust generation in vibrated cohesive powders, *Chem. Eng.* 43 (2015) 769–774.
- [52] D. Barletta, P. Russo, M. Poletto, Dynamic response of a vibrated fluidized bed of fine and cohesive powders, *Powder Technol.* 237 (2013) 276–285.

## 4.2 Article (submitted to Powder Technology, December 2017):

### Parametric study of the particle motion induced by a vortex shaker

Marc Fischer<sup>1,2</sup>, Somik Chakravarty<sup>1</sup>, Olivier Le Bihan<sup>2</sup> and Martin Morgeneyer<sup>1</sup>

<sup>1</sup> *Laboratoire Transformations Intégrées de la Matière Renouvelable (TIMR), Université de Technologie de Compiègne (UTC) Sorbonne Universités, France*

<sup>2</sup> *Institut National de l'Environnement Industriel et des Risques (INERIS), NOVA/CARA/DRC/INERIS, Parc Technologique Alata, BP2, F-60550 Verneuil-En-Halatte, France*

#### 4.2.1 Abstract

A rotating vertical test tube placed on a vortex shaker can be used to study the dustiness of powders. The motion of an alumina tracer particle has been followed through PEPT (Positron Emission Particle Tracking). A parametric study has been performed to estimate the influence of diverse features of the powder and of the device on the particle's movements. The powder mass, the size of the tracer particle and the rotation speed have been varied and the air stream going through the test tube has been deactivated, respectively. Deactivating the air flow has almost no effect on the particle movements. Increasing the powder mass from 2 g to 4 g has no effect on the horizontal

coordinates but increases the height and tends to decrease the velocity. Using a larger tracer particle does not affect the height but it increases the width of the horizontal coordinates and the velocity. Increasing the rotation speed from 1000 rpm to 2500 rpm leads to smaller horizontal coordinates and a larger vertical coordinate and velocity. The effects on the other variables are unsystematic and depend on whether 2 g or 4 g of powder have been used. Plausible explanations could be offered for several of the trends but numerical modelling will be necessary for accounting for all findings.



## 4.2.2 Introduction

The use, the handling and the transportation of powders is often accompanied by the release of dust particles [1]. Dust aerosols are small solid particles, conventionally defined as those particles below 75  $\mu\text{m}$  in diameter, which settle out under their own weight but which may remain suspended for some time, according to the International Standardisation Organisation (ISO 4225 - ISO, 1994) [2]. The tendency of a powder to generate dust is known as its dustiness, which is a function of both its physical properties and of the characteristics of the process and corresponds to the ratio between cohesion forces and separation forces [3]. Dust emissions from powders are deeply problematic from the standpoint of disease prevention [4], explosion risk management [5] and economic loss minimisation [6]. To reduce them, it is necessary to systematically study them and to develop predictive models dependent on the physical parameters used to describe the powder and the process in question [7, 8]. Meso-scale lab testers are utilised to simulate diverse industrial processes [1]. While the dustiness testers are usually conceived in such a way that the input energy and dust generation mechanisms are close to industrial situations [9, 10], there are only few works which straightforwardly compare the experimental and industrial conditions [11]. This limits our ability to understand, simulate and predict dustiness under industrially relevant circumstances [12].

One widespread dustiness technique is the free falling method where a powder is released on top of a test chamber and falls through the action of gravity [13]. Another technique is the rotating drum where a powder is placed in drum whose rotation axis is horizontal [14]. Both techniques require a relatively large amount of powder (such as 50 g) [15, 16]. The Vortex Shaker Dustiness Tester (VS) represents an alternative to these two approaches [17]. Like in the case of the rotating drum, the powder is strained through rotation but this time along the axis of a vertically placed test tube (see Figure 4.1). Besides allowing one to investigate situations that are not captured by the rotating drum, it can be employed with a significantly lower quantity of powder (2 g). It has been successfully used for investigating the aerosolisation of the alumina powders [17], calcium carbonate powders [7] and of a carbon nanotube bulk [9] and further works are ongoing. The next step would consist of developing

predictive numerical models that can deduce dust emissions from a given powder as a function of its features and the parameters of the VS [8]. This demands first a thorough understanding of the particles' trajectory within the rotating test tube, as dust is usually generated during particle-particle and particle-wall collisions [7].

To obtain the relevant experimental measurements, we used PEPT (Positron Emission Particle Tracking) [18] to follow the behaviour of a 1 traced alumina particle over a period of 700 s and at the standard operating conditions (namely  $\omega = 1,500$  rpm, air flow going through the test tube and 2 g of powder). The results we already obtained [8] (and that are to be shortly described in Section 2) gave us deep insights into the nature of the particle's motion within the test tube. In the current study, we endeavoured to better our understanding of the tester through a parametric study where the influence of the powder mass, of the rotation speed, of the traced particle's size and of the closing of the test tube were investigated, respectively. The influence of these parameters on the movements of the traced particle was systematically studied and interpretations of the different trends have been offered.

In Section 2, we go into the methodology of the present study and our former results. In Section 3, we present the results of the parametric study along with their potential interpretations. Finally, in Section 4, conclusions are presented and an outlook for the future is given.

### **4.2.3 Experimental foundation and prior results**

#### ***4.2.3.1 Test protocol***

The utilisation of a vortex shaker as a technique for the generation of dust particles out of powders is a relatively novel and promising approach whose advantage is to be able to employ very small amounts of powder [9, 17]. This renders the VS method a practical and cheap dustiness tester in comparison to the standardised dustiness testers comprising the rotating drum [19] and the dropping test [20]. A vortex shaker can be viewed in Figure 4.1. The vortex shaker utilised for this investigation consists of a digital vortex shaker (VWR Signature Digital Vortex Mixer, USA). Such shakers or mixers are often used in laboratories to mix up small

amounts of liquids. It is made of an electric motor with a drive shaft oriented vertically, which is connected to a rubber cup mounted slightly off-centre (orbital length 4.5 mm). Dust is generated from a small quantity (around 2 g) of bulk solid sample contained in a glass centrifuge tube (diameter 0.025 m, height 0.150 m) firmly mounted on the rubber cup. As the motor runs, the rubber cup oscillates rapidly in a circular movement and the motion is transmitted to the solid sample inside the cylindrical tube. The shaker is able to generate a uniform vortex action with rotational velocities ranging from 500 rpm to 2,500 rpm along the vertical axis. Due to the centrifugal forces spawned in the vortex shaker set-up, the particles in the bulk sample can be assumed to be subjected to the outward centrifugal force acting as a separation force, the vertical gravitational force and surface forces between the particles binding them together. The powder bed is initially located at the bottom of the test tube. The position of an alumina particle has been traced by using the technique PEPT [21-23] that provides one with a highly noisy temporal trajectory [8]. In our last article, we wanted to study the behaviour of limestone powders ( $\text{CaCO}_3$ ). Since limestone primary particles could not be marked radioactively, we used instead a gamma-alumina particle ( $\text{Al}_2\text{O}_3$ ) with similar physical properties to those of the powder. For the present parametric study, we decided to only use gamma-alumina for the sake of consistency, which means that both the powders and the tracer particles were made of alumina and have the very same physical properties. The alumina powder is sieved for 3 different sizes, namely 50  $\mu\text{m}$ , 80  $\mu\text{m}$  and 150  $\mu\text{m}$ . A particle is selected between 50 and 80  $\mu\text{m}$  (and referred to as small) whereas another particle (referred to as big) is selected between 80 and 150  $\mu\text{m}$ .

One particle of the powder is radio-activated and followed by the detector camera thanks to its regular emissions of gamma rays. The experiments were performed at the Positron Imaging Centre, Nuclear Physics research group, University of Birmingham. The reader is referred to our previous publication for more details about the experimental setup [8]. The primary size distribution of the alumina powder remains always the same and is characterised by the following values:  $d_{10} = 57.55 \mu\text{m}$ ,  $d_{25} = 63.64 \mu\text{m}$ ,  $d_{50} = 70.43 \mu\text{m}$ ,  $d_{75} = 76.13 \mu\text{m}$ , and  $d_{90} = 80.75 \mu\text{m}$ . The size distribution of the sample used to produce the tracer article, varies, however, between the "small" and the "big" tracer particle, as defined above. The particle density of the

used alumina powder is  $2950 \text{ kg.m}^{-3}$ . The trial was always repeated once. The powder bed covered a height of 6 mm lying on the round bottom of the test tube.

#### 4.2.3.2 Statistical methodology

The particle's movement is studied for the whole duration of the steady state that is only slightly shorter than the entire experiment (720 s). The population densities of the particle have been computed using all data as the frequency with which the particle is present in a given region. Since the motion of the particle has a cyclical shape whose "period" (roughly 1 s) is much inferior to the duration of the experiments, we can identify these frequencies with the population densities under the assumption of ergodicity [24]. To remove the experimental noise, we considered a displacement  $d$  as legitimate only if  $d > d_{\text{crit}}$  where  $d_{\text{crit}}$  is a critical distance. As illustrated by Figure 4.6a (taken from our previous article [8], setting  $d_{\text{crit}} = 5 \text{ mm}$  is a good compromise between erasing spurious pseudo-movements and keeping genuine tendencies. After the filtering, the velocity and velocity vectors ( $V$ ,  $V_x$ ,  $V_y$ , and  $V_z$ ) are defined locally between two points of the filtered trajectory. The angle between two consecutive filtered vectors can be computed according to the formula:

$$\phi = \arccos\left(-\frac{\vec{a} \cdot \vec{b}}{|\vec{a}| |\vec{b}|}\right) \quad \text{Eq. (4.2)}$$

#### 4.2.4 Results and discussion

In what follows, the effects of the powder mass, the size of the tracer particle, the deactivation of the air stream throughout the test tube and the rotation speed on the particle's behaviour have been investigated. The frequency distribution of the coordinates ( $x$ ,  $y$ ,  $z$ ) and of the velocity vectors ( $V$ ,  $V_x$ ,  $V_y$ , and  $V_z$ ) have been systematically computed along with the frequency with which two consecutive vectors form an angle smaller than  $90^\circ$ . The particle's kinetic energy  $E$  has only been considered for studying the influence of the particle size, as  $V$  contains all its

information otherwise. All variables have been characterised by their third quartiles  $Q_3$  (75%) except  $V_y$  that is characterised by both its third quartile ( $V_y^+$  for the upward movements) and its first quartile ( $V_y^-$  for the downward movements) because its frequency distribution is asymmetrical.

#### **4.2.4.1 Powder mass**

The effects of increasing the powder mass (and consequently the height of the powder bed) have been investigated at different rotation speeds while the test tube was open (i.e. while air was flowing through the top of the test tube at a speed included between 0.6 L/min and 0.7 L/min) and the tracer particle was small, as defined in Section 4.2.3.1 Test protocol. The effects on the horizontal coordinates and velocities are shown in Figure 4.13. The changes in the  $x$  and  $z$  directions are not significant. However,  $V_x$  and  $V_z$  are much higher at 1000 rpm and 1500 rpm and significantly higher at 2000 rpm. At 1000 rpm and 1500 rpm, the values are more than three times higher for 2 g than for 4 g. The effects on the vertical coordinate and velocity are shown in Figure 4.14. The heights reached by the particle lying on 4 g of powder are 2 mm or more higher than those corresponding to 2 g of powder. The upward velocity (represented by the third quartile  $Q_3(y)$ ) is considerably smaller for 4 g of powder. However, the downward velocity (represented by the first quartile  $Q_1(y)$ ) is only significantly smaller for 4 g of powder at 1000 rpm.

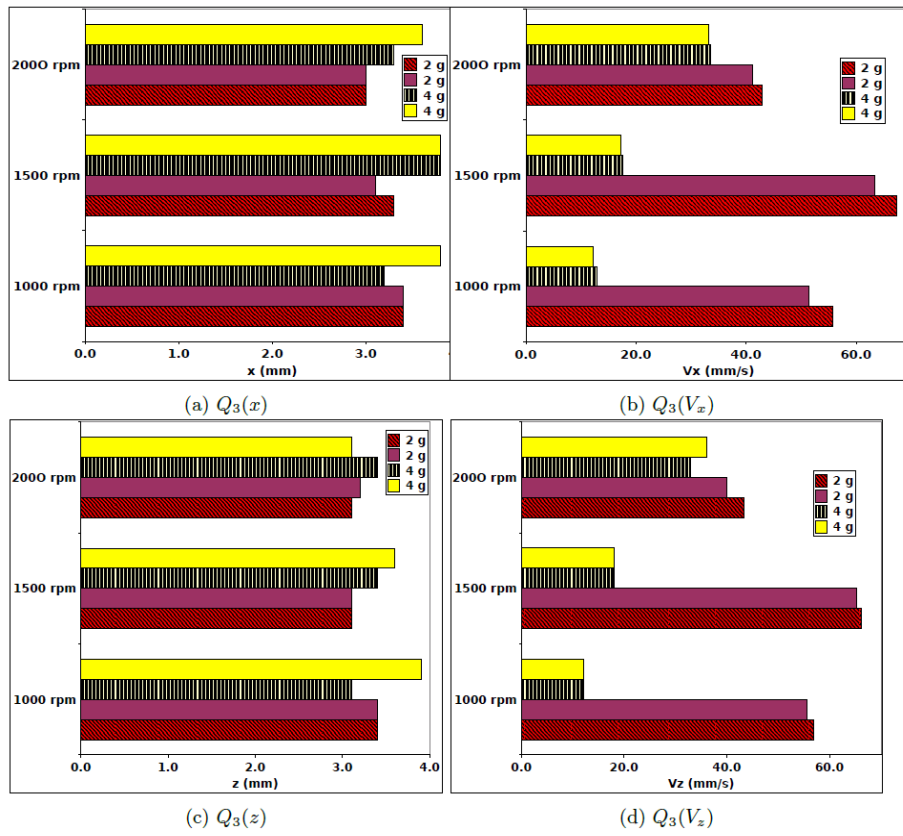


Figure 4.13: Effects of the powder mass on the horizontal coordinates and velocities.

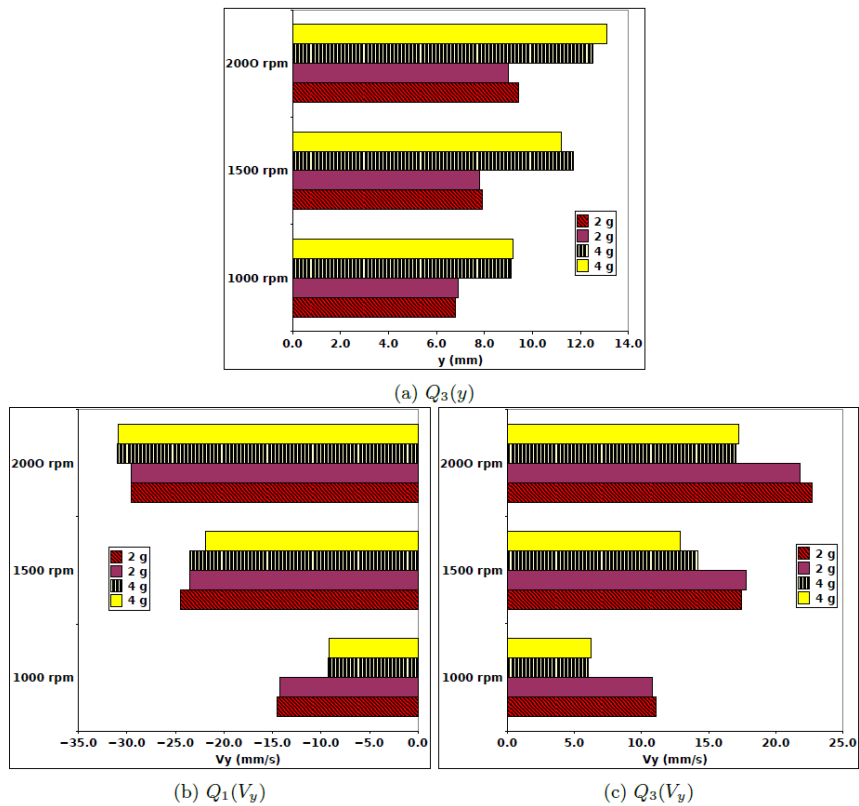
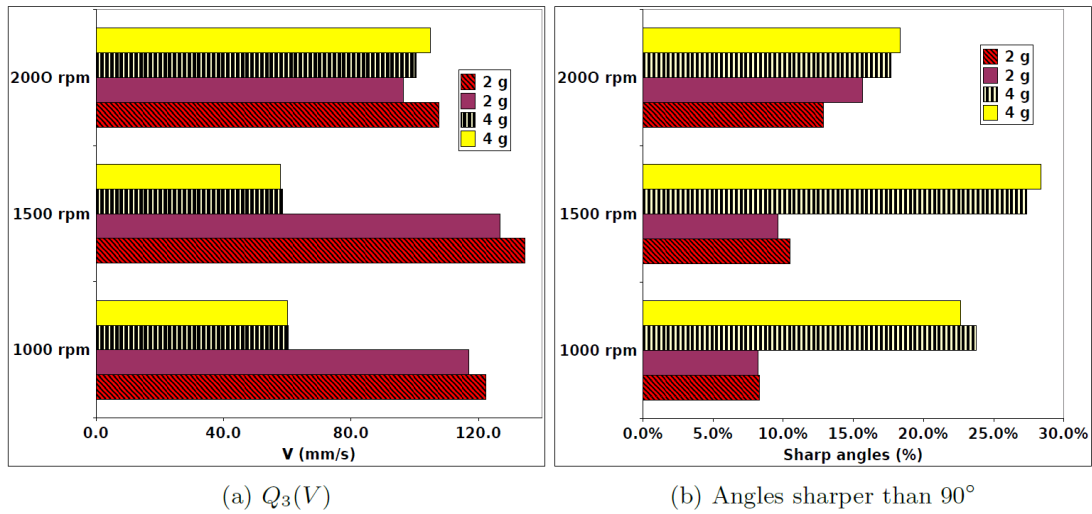


Figure 4.14: Effects of the powder mass on the height and vertical velocity.

Finally, Figure 4.15 shows the particle's velocity  $V$  along with the proportion of abrupt changes in direction (defined as the angles inferior or equal to  $90^\circ$ ), as defined above. Increasing the mass strongly decreases  $V$  at 1000 rpm and 1500 rpm but it has an insignificant effect at 2000 rpm. A powder mass of 4 g is associated with a higher proportion of sharp angles, whereby the increase is much stronger at 1500 and 1000 rpm. The results of increasing the powder mass are summarised in **Table 4-4**.



**Figure 4.15:** Effects of the powder mass on the velocity and sharp angles.

**Table 4-4:** Effects of increasing the powder mass from 2 g to 4 g.

Variable	1000 rpm	1500 rpm	2000 rpm
$ x ,  z $	Insignificant	Insignificant	Insignificant
$ y $	Higher	Higher	Higher
$ V_x ,  V_z $	Much lower	Much lower	Slightly lower
$ V_y^+ $	Lower	Lower	Lower
$ V_y^- $	Lower	Insignificant	Insignificant
$V$	Much lower	Much lower	Insignificant
Sharp angles	Much more	Much more	Slightly more

The higher percentage of sharp angles might stem from a greater number of particle-particle collisions when 4 g of powder is present due to the higher particle concentration in the gas phase. This interpretation is supported by the work of Morgeneyer et al. [17] who investigated the aerosolisation of a pseudo-bimodal alumina powder and found that the aerosol mass concentration rises more than linearly in proportion to the sample mass. Such an effect could then be weaker at 2000 rpm where there is already a large number of collisions. The higher number of collisions would, in turn, considerably decrease the horizontal velocity  $|V_x|$  and  $|V_z|$  while having a more limited effect on the vertical velocity  $|V_y|$ , especially in the downward direction where gravity may play a role. Despite the lower  $|V_x^+|$ , the higher heights reached for 4 g can be well explained as the effect of significantly increasing the bed height.

#### ***4.2.4.2 Air stream through the test tube***

The effects of closing the air stream flowing through the test tube (across an inlet and an outlet at its top at  $y = 150$  mm) have been investigated using a small tracer particle lying on 2 g of powder. Due to power limitation, we could not reach our usual value of 4.2 L/min (utilised because of our specific cyclone) and had to content ourselves with 0.7 L/min, which is a value that is industrially relevant. The results are shown in Figure 4.16, Figure 4.17, and Figure 4.18.



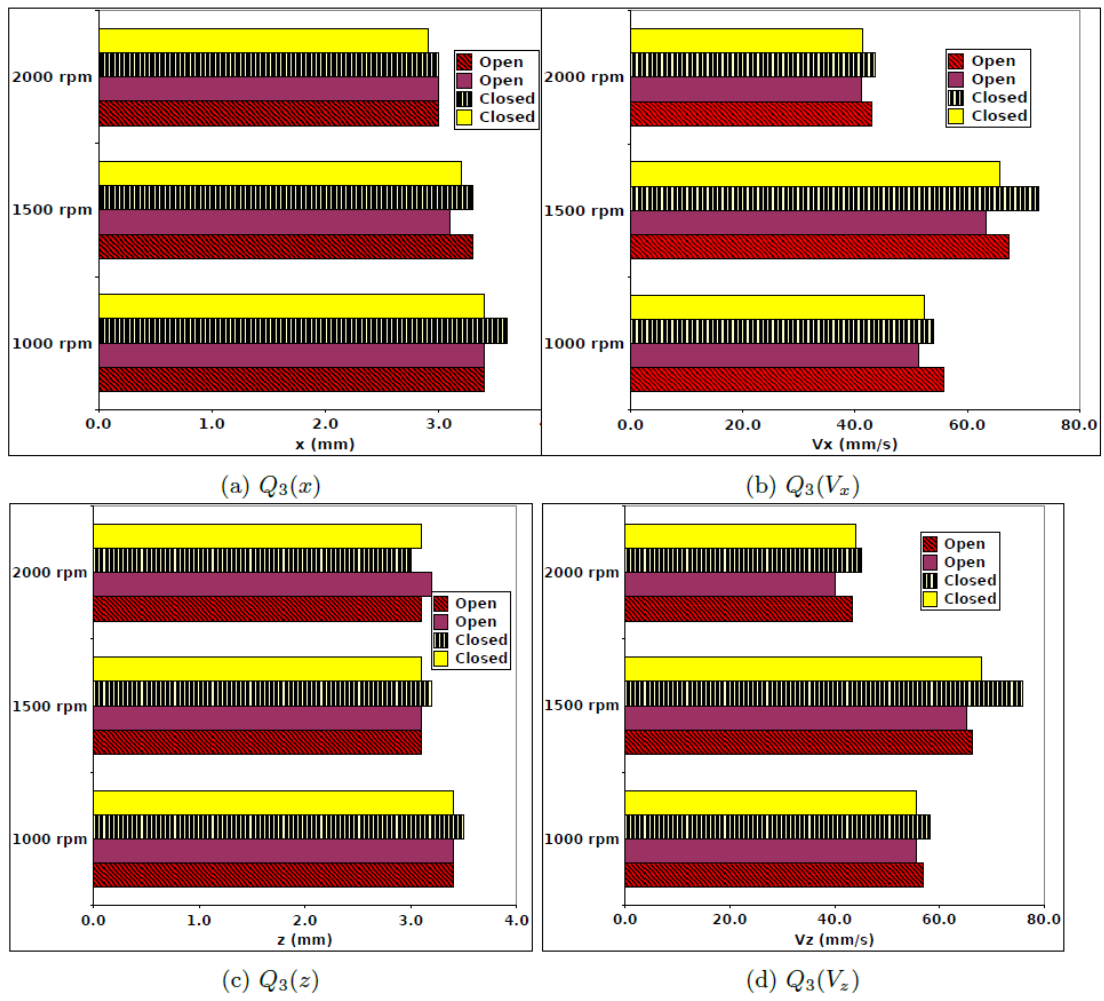
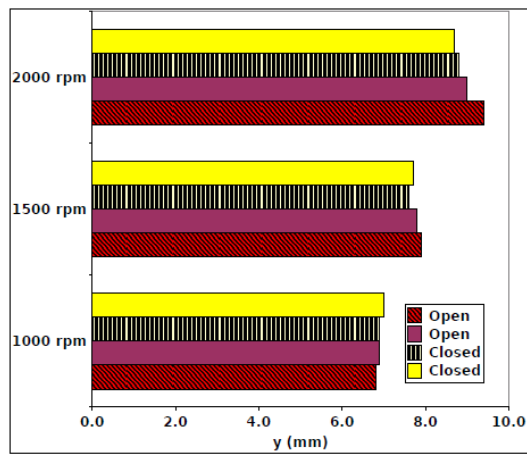
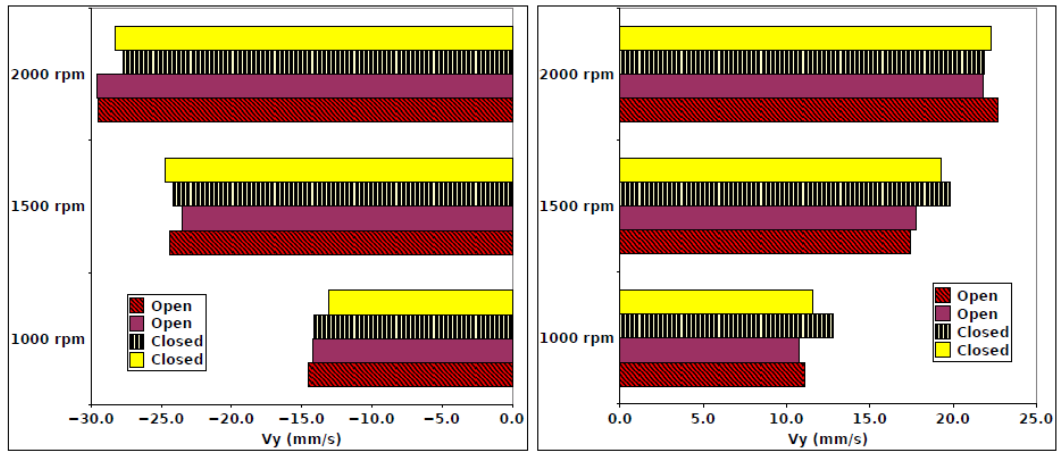


**Figure 4.16:** Effects of the air stream on the horizontal coordinates and velocities.



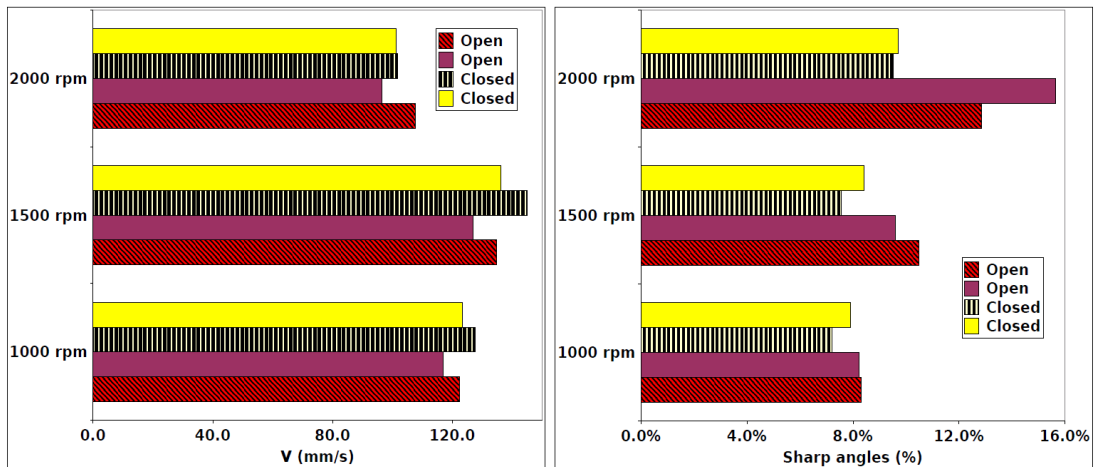
(a)  $Q_3(y)$



(b)  $Q_1(V_y)$

(c)  $Q_3(V_y)$

**Figure 4.17:** Effects of the air stream on the height and vertical velocity.



(a)  $Q_3(V)$

(b) Angles sharper than  $90^\circ$

**Figure 4.18:** Effects of the air stream on the velocity and sharp angles.

It can be seen that the effects of switching off the air stream are negligible, except at 2000 rpm where it leads to less sharp angles although the variation range between two repeated trials for the open case is half as large as the difference between the closed and open case. Given the fact that all other variables are unaffected and that the opening is much higher than the highest heights reached by the particle (namely 20 mm), there does not appear to be any intuitive explanation for this anomaly other than its being an artefact stemming from the limitation of repeatability.

Future simulations could shed light onto this result. Given that the inner diameter of the inlet tube is 3 mm and that the flow rate is 0.7 L/min, the value of the velocity of the flow is 1.65 L/s. This value approaches the velocity of the rotating test tube at 1500 rpm (1.884 m/s). Nevertheless, given the fact that the inlet and outlet are more than 100 mm above the powders surface [17], we can expect the flow to only have a small influence on the behaviour of the particle that only reaches heights inferior to 25 mm. Because of the limitations of the PEPT experimental setup, we could not use the usual value of 4.2 L/min which is 6 times higher than 0.7 L/min. As a consequence, we do not know if this higher flow rate could have a stronger influence on the particle's behaviour. The future CFD studies we plan to do will shed further light on the role of the flow rate value.

#### ***4.2.4.3 Size of the tracer particle***

The role of the size of the tracer particle has been examined at 1500 rpm while the air stream was closed and 2 g of powder were used. The effects on the vertical coordinate and velocity are shown in Figure 4.19. The big particle occupies a larger horizontal space and reaches stronger horizontal velocities. Figure 4.20 displays the effects on the vertical motion.

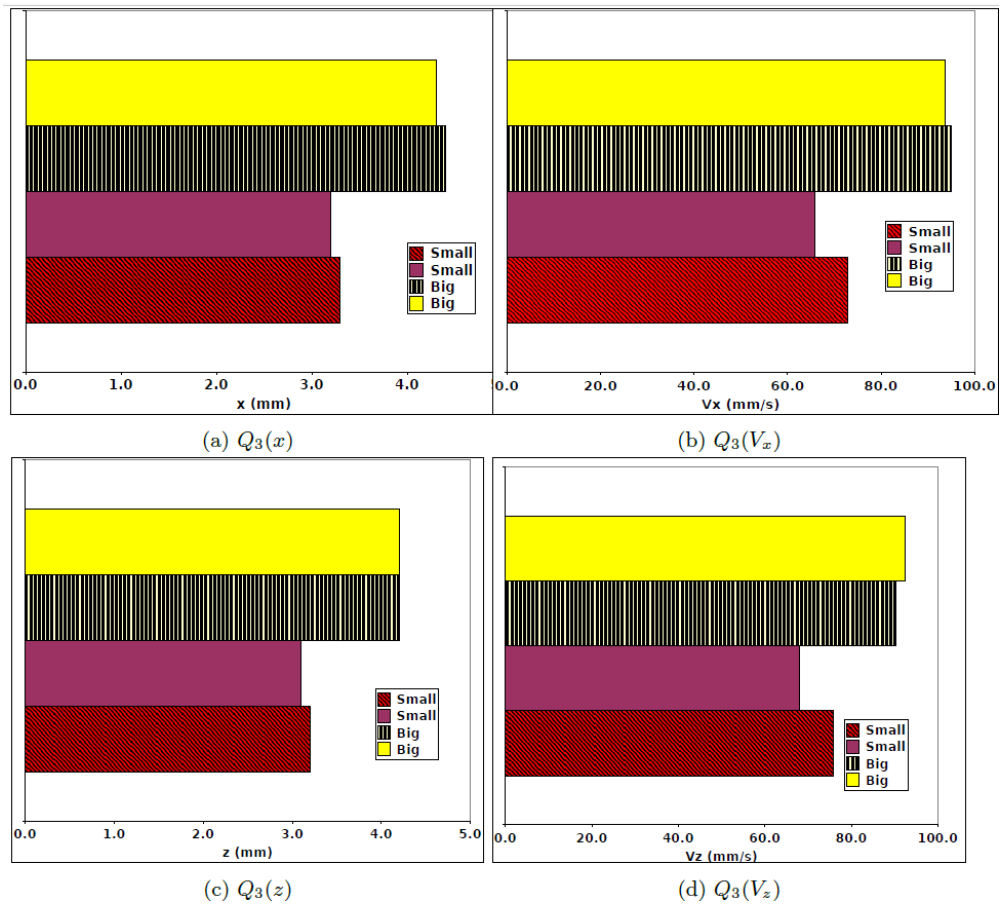


Figure 4.19: Effects of the particle size on the horizontal coordinates and velocities.

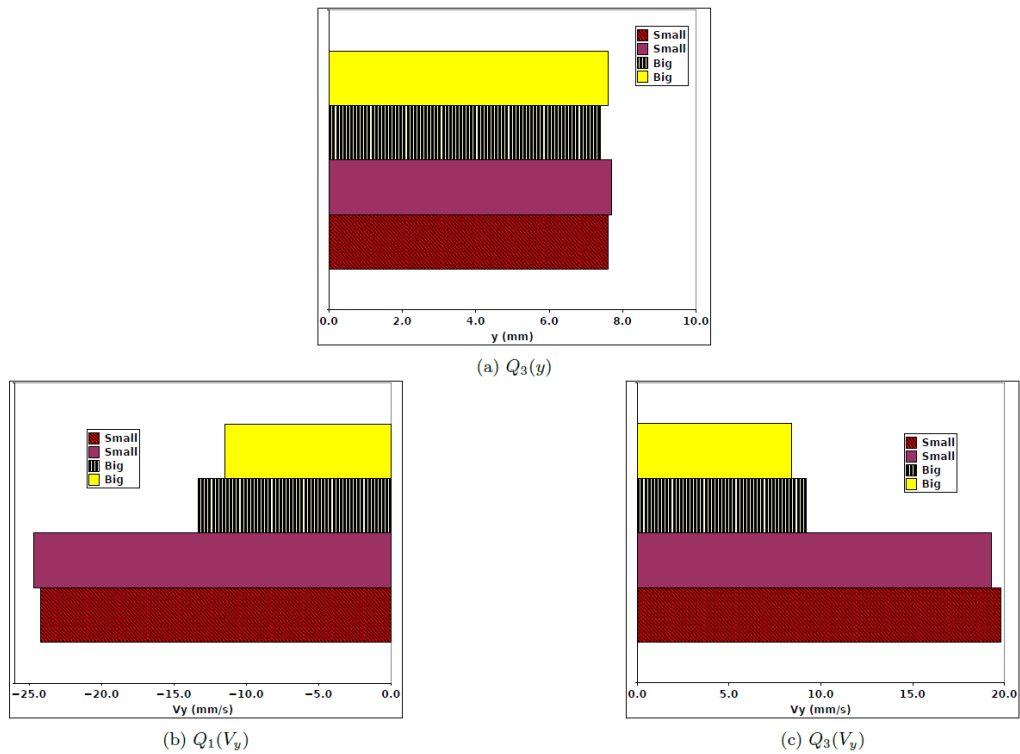
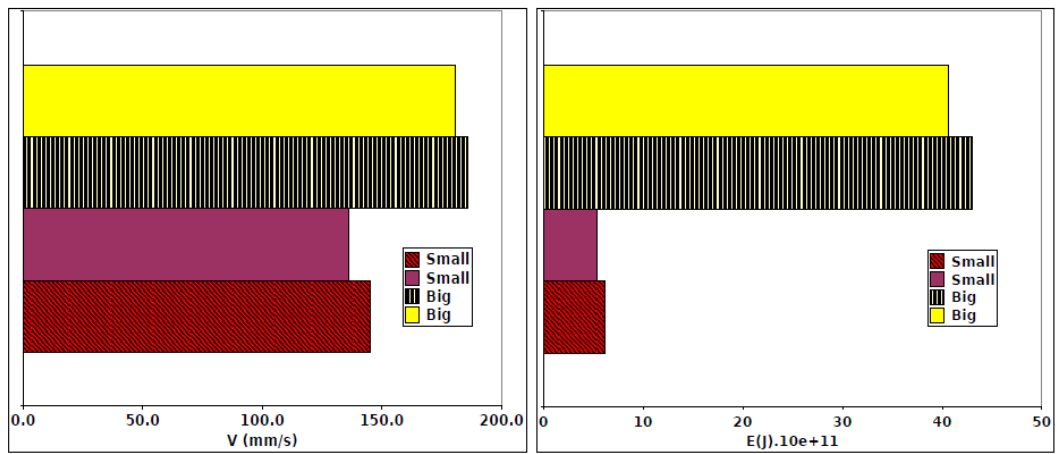


Figure 4.20: Effects of the particle size on the height and vertical velocity.

Whilst the vertical volume the particle's movement takes up is not influenced by the particle's size, the bigger particle has a much lower upward and downward velocity. Figure 4.21 shows the particle's velocity  $V$  along with its kinetic energy and the proportion of abrupt changes in direction (defined as the angles inferior or equal to  $90^\circ$ ). Increasing the size leads to a relatively higher velocity  $V$  and to a much stronger kinetic energy  $E$  and a larger number of sharp angles. The results of increasing the tracer particle's size are summarised in Table 4-5.

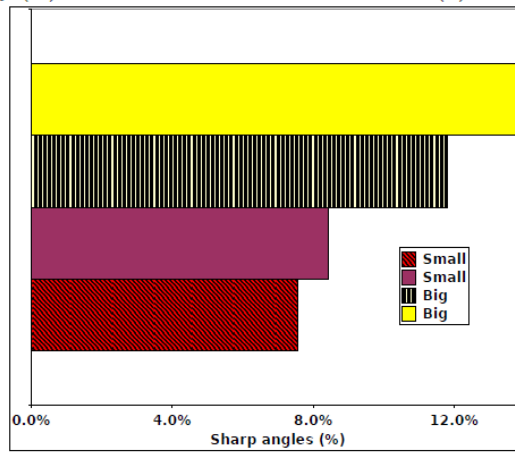
**Table 4-5:** Effects of increasing the tracer particle's size from small (50-80  $\mu\text{m}$ ) to large (80-150  $\mu\text{m}$ ).

Variable	Effect
$ x ,  z $	Increase
$ y $	Unchanged
$ V_x ,  V_z $	Increase
$ V_y^+ $	Lower
$ V_y^- $	Lower
$V$	Increase
$E$	Strong increase
Sharp angles	Much more



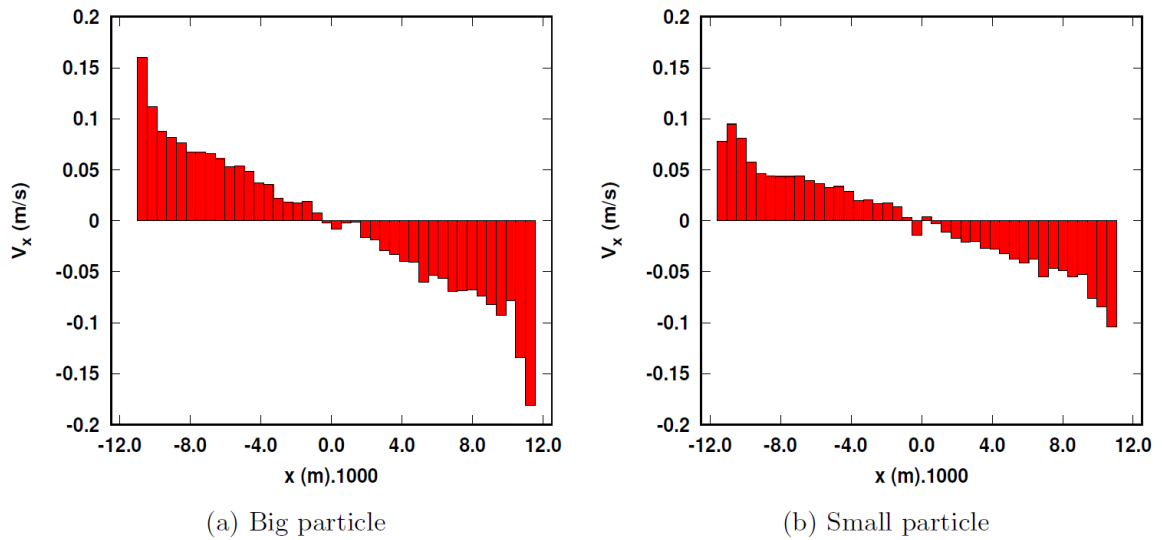
(a)  $Q_3(V)$

(b) Kinetic energy



(c) Angles sharper than  $90^\circ$

**Figure 4.21:** Effects of the particle size on the velocity and sharp angles.



(a) Big particle

(b) Small particle

**Figure 4.22:**  $V_x$  as function of  $x$ .

We can tentatively formulate hypotheses to account for some of these observations. The higher values of the horizontal velocity when the tracer particle is large leads to a larger horizontal space occupied by the particle and thus to higher values of  $|x|$  and  $|z|$ . The larger size of the tracer particle could make it more susceptible to undergo collisions, hence the higher proportion of sharp angles. These collisions could, in turn, lower the values of the vertical component of the velocity, both downwards and upwards. Since the decrease in  $|V_y^-|$  and  $|V_y^+|$  is roughly the same (namely approximately 10 mm/s), the heights reached by the particle remain unaffected.

The cause of the increase in  $|V_x|$  and  $|V_z|$  is harder to explain. The centrifugal force [25] is given by the following formula  $F_{FC} = m\omega^2 R$ , where  $m$  is the particle's mass,  $\omega$  the rotational speed of the particle and  $R$  the radius of its cyclic trajectory. Consequently, the acceleration it spawns is independent of the particle's mass and diameter and cannot be influenced by them. The drag force caused by the air on the particle [26] is given by the following formula  $F_D = \frac{1}{2}\rho v^2 C_D A$ , where  $\rho$  is the density of the fluid,  $v$  is the speed of the object relative to the fluid,  $A$  is the cross sectional area, and  $C_D$  is the drag coefficient. Since the particle's mass is proportional to  $d_p^3$  and  $A$  is proportional to  $d_p^2$ , the corresponding acceleration is proportional to  $d_p^{-1}$  multiplied by  $v^2$ . An integration shows that the drag force would cause the velocity of the large particle to be lower and not higher than that of the small particle. Figure 4.22 shows the horizontal velocity profile  $V_x(x)$  for the small and the big particle. It can be seen that  $V_x$  is always considerably higher for the big particle than for the small one. One explanation might be that the big particle loses less velocity through collisions thanks to its larger mass.

#### **4.2.4.4 Rotation speed**

The effects of the rotation speed on the small particle have been investigated. Figure 4.23 shows the horizontal coordinates and velocities. Under consideration of the uncertainty,  $|x|$  and  $|z|$  tend to decrease with higher rotation speeds. However,  $|V_x|$  and  $|V_y|$  follow two different trends for 2 g and 4 g. While they increase in the

case of 4 g of powder, in the case of 2 g, they increase till 1500 rpm before decreasing. The height and vertical velocity are shown in Figure 4.24. The heights reached by the particle and both the upward and the downward velocities constantly rise with the rotation speed. Figure 4.25 shows the velocity  $V$  along with the sharp angles. With 4 g of powder,  $V$  remains constant between 1000 and 1500 rpm before increasing whereas with 2 g,  $V$  increases until 1500 rpm, decreases between 1500 rpm and 2000 rpm before increasing again at 2000 rpm. For 2 g of powder, the percentage of sharp angles increases constantly between 1000 and 2000 rpm before increasing abruptly between 2000 rpm and 2500 rpm.

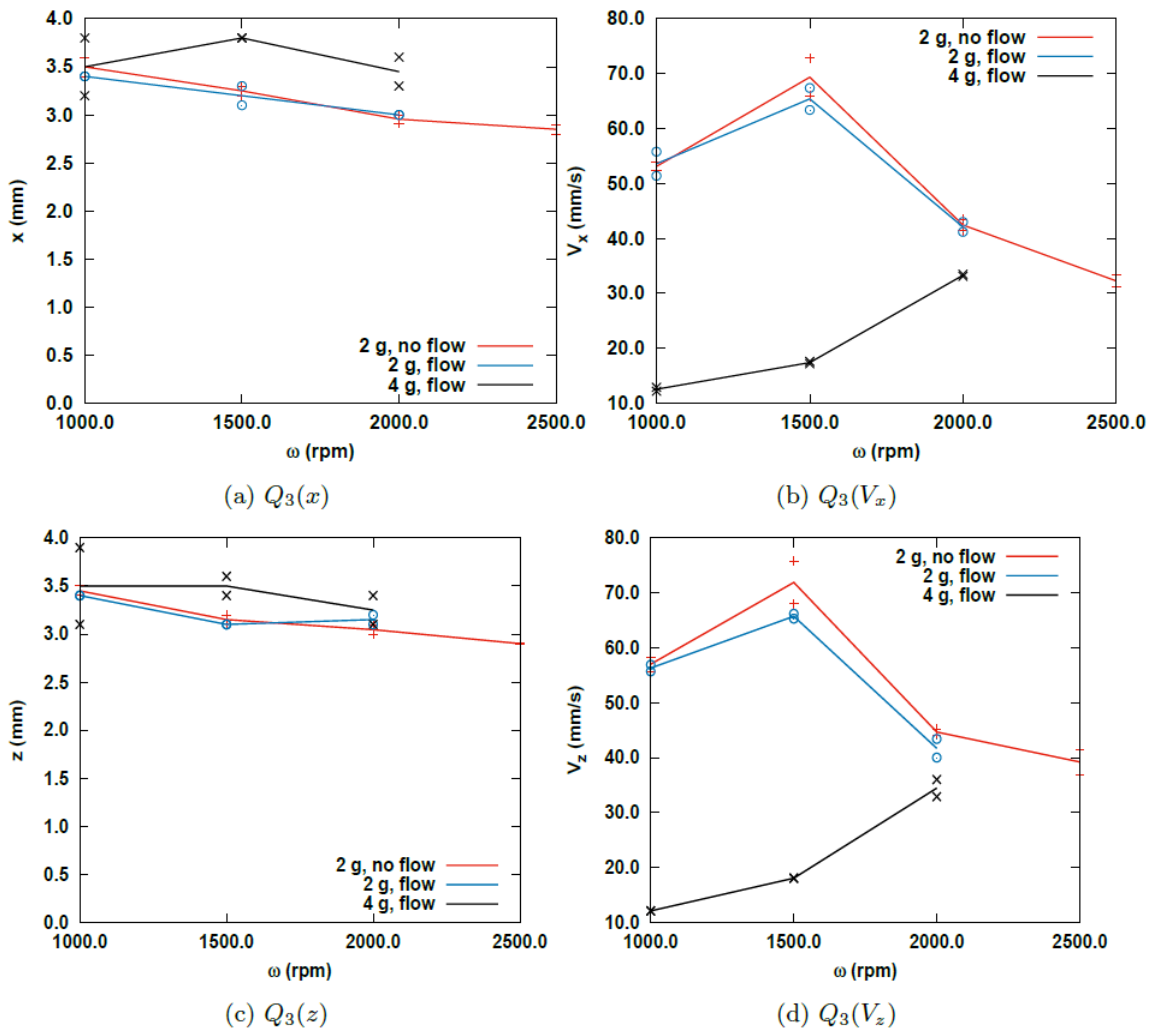
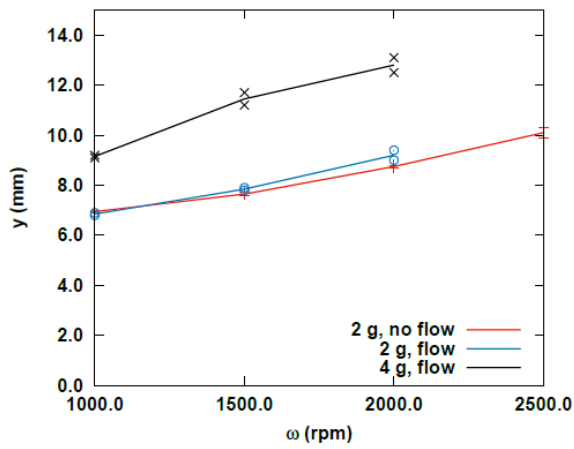
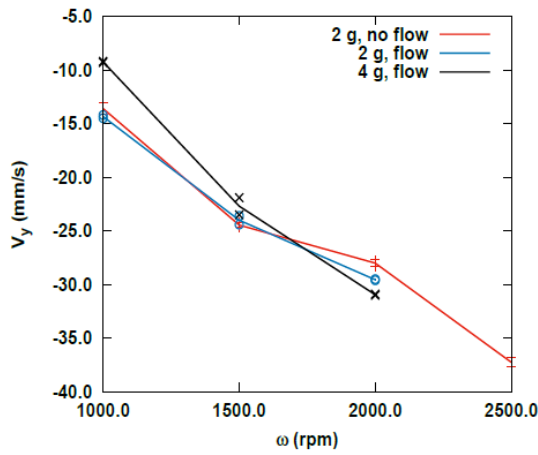


**Figure 4.23:** Effects of the rotation speed on the horizontal coordinates and velocities.

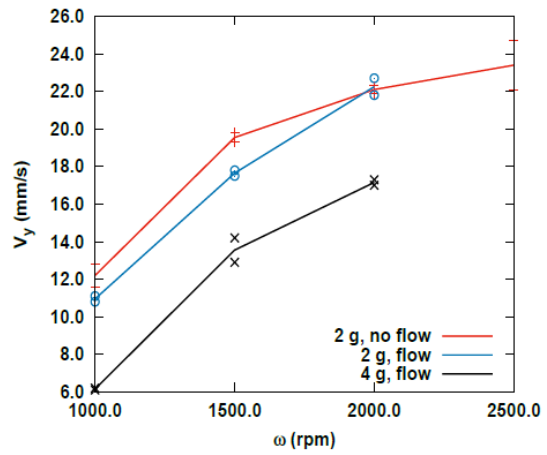




(a)  $Q_3(y)$

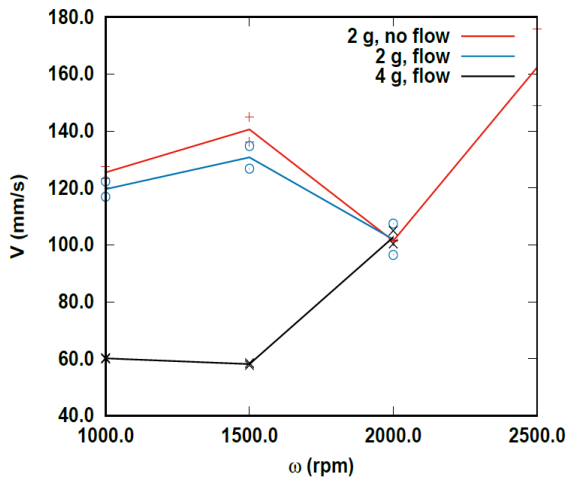


(b)  $Q_1(V_y)$

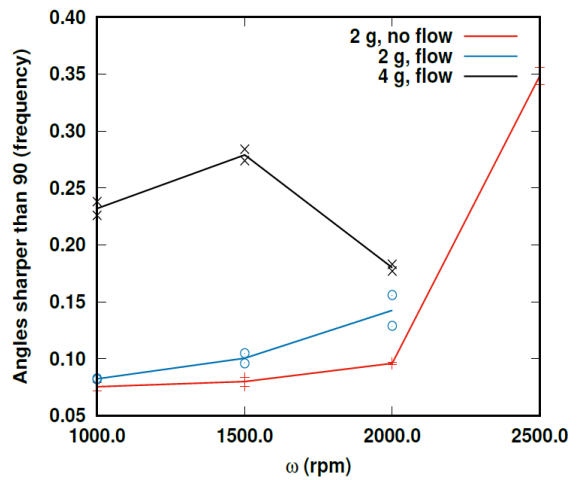


(c)  $Q_3(V_y)$

**Figure 4.24:** Effects of the rotation speed on the vertical coordinates and velocities.



(a)  $Q_3(V)$



(b) Angles sharper than  $90^\circ$

**Figure 4.25:** Effects of the rotation speed on the velocity  $V$  and sharp angles.

With 4 g of powder, the percentage of sharp angles increases until 1500 rpm before decreasing. The trends have been summed up in Table 4-6.

**Table 4-6:** Effects of increasing the rotation speed.

Variable	2g	4g
$ x ,  z $	Smaller	Smaller
$ y $	Larger	Larger
$ V_x ,  V_z $	Peak at 1500 rpm	Larger
$ V_y^+ $	Larger	Larger
$ V_y^- $	Larger	Larger
$V$	Increases, decreases, increases	Much lower
Sharp angles	Increases, abruptly increases	Peak at 1500 rpm

Some trends can potentially be accounted for. The higher rotation speed transfers more energy to the particle which allows it to reach higher heights, hence the larger values for  $|y|$ ,  $|V_y^+|$  and  $|V_y^-|$ . With 4 g of powder, the higher rotation speed can readily cause higher  $|V_x|$  and  $|V_z|$ . With 2 g of powder, the slow and then rapid increase of the percentage of sharp angles can be well explained through the stronger shocks accompanying the increase in rotation speed. Nevertheless, there is no intuitive explanation for the peaks characterising  $|V_x|$  and  $|V_z|$  for 2 g of powder and the oscillation of  $V$  and the number of sharp shocks for 4 g. It is worth noting that Morgeneyer et al. [17] found out in their study that the aerosolised particle mass concentration increases monotonously with the rotation speed.

Hence, the existence of the peaks for  $V_x$ ,  $V_z$ ,  $V$  and the proportion of sharp angles cannot be directly correlated with dust generation.

#### 4.2.5 Conclusion and outlook

The vortex shaker is a promising dustiness tester which allows one to estimate the propensity of a powder to emit dust whilst only necessitating a small quantity of material (2 g) [17]. Understanding the physical factors responsible for dustiness and developing models permitting numerical predictions is extremely important as this could greatly diminish the cost of studies aiming at minimising the risks related to dust emission [27]. Since dust emissions are due to a complex set of particle-wall and particle-particle collisions and particle-fluid interactions, it is necessary to comprehend and to be able to predict the movements of the powder primary particles in the test tube agitated by the vortex shaker. This prompted us to undertake a series of PEPT experiments to measure the motion of a traced primary particle and grasp the influence of the parameters of the tester and of the powder on it. Our previous study [8] evidenced that, on average, the particle rises at the middle of the test tube at a small speed while descending near the walls much more rapidly. In the present work, we investigated the effects of closing the air stream through the test tube, of increasing the powder mass, the rotation speed and the size of the primary particle. Overall, the air stream considered for the experiments has a very small if not negligible effect on the particle's behaviour and hence also on dust generation. Increasing the powder mass (and thereby the powder bed height) tends to increase the heights reached by the particle and to decrease its velocity. Increasing the size of the tracer particle raises the velocity and the breadth of the horizontal coordinates. An increase in the rotation speed leads to a narrower range of horizontal coordinates but also to higher heights reached by the particle. Many of these observations can be well accounted for on intuitive grounds. Nevertheless, others (such as the oscillations of the particle's velocity with the rotation speed) do not lend themselves well to intuitive explanations. We intend to perform a CFD (Computational Fluid Dynamics) and DEM (Discrete Element Method) study modelling the system as both discrete particles within the gaseous phase (following the Eulerian-Lagrangian approach [28]) and as the powder being treated as a continuous phase (Eulerian-Eulerian approach [29]) and we expect these results to shed light on our counter-intuitive findings.

## 4.2.6 References

- [1] F. Hamelmann, E. Schmidt, Methods of estimating the dustiness of industrial powders - a review, *KONA Powder and Particle Journal* 21 (2003) 7-18.
- [2] E. Petavratzi, S. Kingman, I. Lowndes, Particulates from mining operations: A review of sources, effects and regulations, *Minerals Engineering* 18 (2005) 1183-1199.
- [3] M. Plinke, B. Homburg, Vorhersage der Staubentstehung bei der industriellen Handhabung von Pulvern, VDI, 1995.
- [4] T. Kraus, K. Schaller, J. Angerer, S. Letzel, Aluminium dust-induced lung disease in the pyro-powder-producing industry: detection by high-resolution computed tomography, *International archives of occupational and environmental health* 73 (2000) 61-64.
- [5] R. K. Eckhoff, *Dust explosions in the process industries: identification, assessment and control of dust hazards*, Gulf professional publishing, 2003.
- [6] H. Y. Aruntaş, M. Gürü, M. Dayı, I. Tekin, Utilization of waste marble dust as an additive in cement production, *Materials & Design* 31 (2010) 4039-4042.
- [7] S. Chakravarty, O. Le Bihan, M. Fischer, M. Morgeneyer, Dust generation in powders: Effect of particle size distribution, in: *EPJ Web of Conferences*, volume 140, EDP Sciences, p. 13018.
- [8] S. Chakravarty, M. Fischer, P. García-Triñanes, D. Parker, O. Le Bihan, M. Morgeneyer, Study of the particle motion induced by a vortex shaker, *Powder Technology* (2017).
- [9] O. L. C. Le Bihan, A. Ustache, D. Bernard, O. Aguerre-Chariol, M. Morgeneyer, Experimental study of the aerosolization from a carbon nanotube bulk by a vortex shaker, *Journal of Nanomaterials* 2014 (2014) 7.
- [10] Y. Ding, B. Stahlmecke, H. Kaminski, Y. Jiang, T. A. Kuhlbusch, M. Riediker, Deagglomeration testing of airborne nanoparticle agglomerates: Stability analysis under varied aerodynamic shear and relative humidity conditions, *Aerosol Science and Technology* 50 (2016) 1253-1263.
- [11] S. Kamath, V. Puri, H. Manbeck, R. Hogg, Flow properties of powders using four testers measurement, comparison and assessment, *Powder technology* 76 (1993) 277-289.
- [12] W. A. Heitbrink, W. F. Todd, T. C. Cooper, D. M. O'Brien, The application of dustiness tests to the prediction of worker dust exposure, *The American Industrial Hygiene Association Journal* 51 (1990) 217-223.
- [13] W. A. Heitbrink, P. A. Baron, K. Willeke, An investigation of dust generation by free falling powders, *The American Industrial Hygiene Association Journal* 53 (1992) 617-624.
- [14] R. G. Sherritt, J. Chaouki, A. K. Mehrotra, L. A. Behie, Axial dispersion in the three-dimensional mixing of particles in a rotating drum reactor, *Chemical Engineering Science* 58 (2003) 401-415.
- [15] N. Breum, The rotating drum dustiness tester: variability in dustiness in relation to sample mass, testing time, and surface adhesion, *Annals of Occupational Hygiene* 43 (1999) 557-566.
- [16] M. Boundy, D. Leith, T. Polton, Method to evaluate the dustiness of pharmaceutical powders, *Annals of Occupational Hygiene* 50 (2006) 453-458.
- [17] M. Morgeneyer, O. Le Bihan, A. Ustache, O. Aguerre-Chariol, Experimental study of the aerosolization of fine alumina particles from bulk by a vortex shaker, *Powder Technology* 246 (2013) 583-589.
- [18] M. Tan, D. Parker, P. Dee, PEPT data presentation software, manual, Birmingham University, UK (1997).
- [19] D. Parker, A. Dijkstra, I. Martin, J. P. K. Seville, Positron emission particle tracking studies of spherical particle motion in rotating drums, *Chemical Engineering Science* 52 (1997) 2011-2022.
- [20] S. Bach, E. Schmidt, Determining the dustiness of powders a comparison of three measuring devices, *Annals of occupational hygiene* 52 (2008) 717-725.

- [21] M. Van de Velden, J. Baeyens, J. P. K. Seville, X. Fan, The solids flow in the riser of a Circulating Fluidised Bed (CFB) viewed by Positron Emission Particle Tracking (PEPT), *Powder Technology* 183 (2008) 290-296.
- [22] D. Valdesueiro, P. García-Triñanes, G. Meesters, M. Kreutzer, J. Gargiuli, T. Leadbeater, D. Parker, J. Seville, J. van Ommen, Enhancing the activation of silicon carbide tracer particles for PEPT applications using gas phase deposition of alumina at room temperature and atmospheric pressure, *Nuclear Instruments and Methods in Physics Research Section A: Accelerators, Spectrometers, Detectors and Associated Equipment* 807 (2016) 108-113.
- [23] M. Marigo, M. Davies, T. Leadbeater, D. L. Cairns, A. Ingram, E. H. Stitt, Application of Positron Emission Particle Tracking (PEPT) to validate a Discrete Element Method (DEM) model of granular flow and mixing in the Turbula mixer, *International journal of pharmaceutics* 446 (2013) 46-58.
- [24] T. Royama, *Analytical population dynamics*, volume 10, Springer Science & Business Media, 2012.
- [25] M. A. Abramowicz, Centrifugal force-a few surprises, *Monthly Notices of the Royal astronomical society* 245 (1990) 733.
- [26] G. K. Batchelor, *An introduction to fluid dynamics*, Cambridge university press, 2000.
- [27] L. E. Stone, P. W. Wypych, D. B. Hastie, S. Zigan, et al., CFD-DEM modelling of powder flows and dust generation mechanisms-a review, in: *12th International Conference on Bulk Materials Storage, Handling and Transportation (ICBMH 2016)*, The, Engineers Australia, p. 417.
- [28] B. Van Wachem, J. Van der Schaaf, J. Schouten, R. Krishna, C. Van den Bleek, Experimental validation of Lagrangian-Eulerian simulations of fluidized beds, *Powder Technology* 116 (2001) 155-165.
- [29] D. Santos, I. Petri, C. Duarte, M. Barrozo, Experimental and CFD study of the hydrodynamic behavior in a rotating drum, *Powder technology* 250 (2013) 52-62.

## **5 Application of the vortex shaker: Dust generation from long-term industrial operations and comparison with a pilot-scale fluidized bed attrition tester**

### **5.0 Overview**

This chapter focusses on the role of time-scale, a process parameter, on the dust generation behaviour of powders. Since majority of the dustiness studies span over few seconds to minutes, there is a lack of information regarding the evolution of dust emissions, the powder parameters affecting dust generation and the changes in powder parameters with time. Such information can be useful in understanding the risks from the powders being used in long-term industrial applications which can span anywhere between few weeks to months.

Dust generation patterns and dustiness levels over time depending on the material and operation can be used as important descriptors for understanding the dust generation mechanisms as the dust generation mechanisms during the initial few moments of operation may be different from those governing the dust released over an extended period of time.

While particle size and size distribution were seen to influence powder mechanical and dustiness behaviours in calcium carbonate powders (in Section 3.2), this chapter discusses the effect of particle shape on the dust generation process. This chapter also discusses the application of particle size analysis by number, which is relatively time and labour intensive, but useful in determining the fractions of very fine particles present in the bulk which may not be reflected in the particle size analysis by volume.

Dust generation can modify the material quality and characterization for change in bulk material properties due to long-term dust generation and release is important but often overlooked in dustiness tests. Powder properties such as particle size, distribution, shape etc. can change with time due to the long-term powder processing and dustiness, which may cause changes in physical, mechanical and chemical behaviour of a bulk material diverging from its intended use.

Dustiness tests are not intended to comminute particles (due to high impact or shear stresses) and generate new particles. However, depending on the material and

process conditions, particles may undergo attrition (abrasion) even under low stresses, which can lead to the production and emission of small dust particles.

This chapter uses two case studies related to the long-term use of silicon carbide powders in solar thermal application (Section 5.1) and aluminium oxide and acetylene coke used in automotive, petroleum and iron & steel industry (Section 5.2) to highlight the need for sufficiently long dustiness tests to support the selection of material and quantify the risk associated with the handling of new and used particles.

Section 5.1 evaluates the effect of time-scale on powder dust generation while considering the effect of dustiness testing on the particle size distribution and particle shape properties of the tested samples compared to their pristine state. Based on the time-evolution of dust generation, we propose stages of dust generation mechanisms which can possibly provide explanations concerning the emission of dust and its subsequent effect on physical properties of the powder sample.

In Section 5.2 we use the methodology developed in Section 5.1 to compare the evolution of dust mass and the size distribution and shape properties of the particles with a pilot-scale attrition tester. The study allows to highlight the similarities and differences between the small-scale dustiness tester and pilot-scale attrition tester, in terms of evolution of mass of dust/fines generated and the effect of testing on PSD and shape properties of the particles.

## 5.1 Article (published in *Process Safety and Environmental Protection*, 2018)

### Long-term dust generation from silicon carbide powders

Somik Chakravarty<sup>1</sup>, Marc Fischer<sup>1,2</sup>, Pablo García-Triñanes<sup>3</sup>, Morgane Dalle<sup>2</sup>, Laurent Meunier<sup>2</sup>, Olivier Aguerre-Chariol<sup>2</sup>, Olivier Le Bihan<sup>2</sup> and Martin Morgeneyer<sup>1</sup>

<sup>1</sup> *Laboratoire Transformations Intégrées de la Matière Renouvelable (TIMR), Université de Technologie de Compiègne (UTC) Sorbonne Universités, France*

<sup>2</sup> *Institut National de l'Environnement Industriel et des Risques (INERIS), NOVA/CARA/DRC/INERIS, Parc Technologique Alata, BP2, F-60550 Verneuil-En-Halatte, France*

<sup>3</sup> *Wolfson Centre for Bulk Solids Handling Technology, Faculty of Engineering and Science, University of Greenwich, Chatham Maritime, Chatham, Kent ME44TB, UK*

#### 5.1.1 Abstract

Most dustiness studies do not measure dust release over long durations, nor do they characterize the effect of dust release on bulk powders. In this study, we tested the dustiness of two different samples of silicon carbide (SiC) powders (referred to as F220 and F320) over six hours using a vortex shaker. Additionally, we characterized the bulk sample for change in shape and size distribution due to the testing. Both powders release respirable fractions of dust particles but differ in their dust generation behavior. The numbers of released respirable particles for powder F220 are more than two times higher than those of powder F320.

The dust generation mechanism might include the release of aerosols due to the attrition of particles owing to inter-particle and particle-wall impaction. This study emphasizes the need for long duration dustiness tests for hard materials like SiC and characterization for change in bulk material properties due to dust generation and release. Furthermore, the results can aid in selecting the bulk material for long-term applications based on dustiness.



### 5.1.2 Introduction

Hard particles, such as silicon carbide (SiC) having diameters in the range of 30-100  $\mu\text{m}$  are widely used in high endurance applications such as the production of abrasives and wear-resistant machineries (Harris, 1995). Considering their excellent physical and mechanical properties (high strength, durability and heat capacity), SiC powders have recently been adopted as a heat transfer and storage fluid (HTF) for concentrated solar thermal plants (CSP) (Benoit et al., 2015; García-Triñanes et al., 2016). The HTF particles conveyed pneumatically or mechanically are used to transfer heat energy from different sections of the solar thermal plant. The conveying of HTF material generates dust as it undergoes mechanical stresses due to screw feeder or rotary valves, kinetic stresses due to high-velocity jets, conveyors, collision with tubes, and shear stresses while being conveyed in a closed circulating loop. Further, such stresses engender attrition in particulate systems which can potentially influence the physical, mechanical and thermal properties of the HTF material and therefore, the operation of the CSP plant. Thus, the handling of such material requires the knowledge of the powder ability to generate dust and monitor its consequent change in physical and mechanical properties which may be different from their original state.

According to ISO 4225 (International Organization for Standardization, 1994), dust is made of small airborne solid particles, usually of sizes inferior to 75  $\mu\text{m}$  in diameter which settle under their own weight but may remain suspended for some time. The tendency of a material to generate dust upon handling is known as its dustiness (Hamelmann and Schmidt, 2003). The exposure and deposition of airborne dust in various regions of the human respiratory tract depends on several factors including the size of the dust particle. Based on the size of a dust particle and its ability to penetrate and deposit in lungs, the three dust size fractions include the inhalable fraction (mouth/nose), the thoracic fraction (respiratory tract below the larynx) and the respirable fraction (the alveolar region in the lung) (Baron and Vincent, 1999; EN 481, 1993; ISO 7708, 1995). The size fractions depend on the aerodynamic diameter of the dust particles (Hinds, 1999) and are classified based on dust median particle size with 100  $\mu\text{m}$  for inhalable, 10  $\mu\text{m}$  for thoracic, and 4  $\mu\text{m}$  for respirable fractions, for 50% sampling efficiency. The exposure to dust generated from the handling of silicon carbide powders

in industries can lead to increased rates of chronic bronchopulmonary diseases and bronchial hyper-reactivity (Governa et al., 1997; Petran et al., 2000).

In an occupational setting, handling of materials including silicon carbide particles, may pose major challenges including the risk of inhalation of dust, changes in material quality, contamination of plant equipment, and in some cases, can even cause fire and explosion (Eckhoff, 2005). Dustiness of a powder depends on several factors including powder parameters such as particle size and particle morphology and external factors such as ambient humidity (Plinke, 1995). Testing for dustiness of a material involves measuring dust particles aerosolized from a specific amount of bulk material, subjected to a precise amount and type of energy for a defined period of time (Plinke et al., 1992). The time of suspension of a dust particle is directly related to its size, shape and density (Green, 2007; Klippel et al., 2013). Thus, it is important to not only test and report dustiness of HTF material (SiC) in their original pristine state but also at their used form in order to assess the risks of handling such material and to select powders with suitable properties. The results could aid in quantifying and mitigating risks associated not only with planned activities such as handling and transportation of new and used HTF material but also with major incidents, such as an HTF leak in the plant. Thus measurement of the long-term dust generation of HTF powders is possibly as important as characterizing short-term dust generation (associated with activities such as the loading and unloading of powders) as the HTF powders continuously circulate in CSP plants for months without changing.

There are a wide range of dustiness testers including the air jet dispersion (Boundy et al., 2006) and gas fluidization systems (Saleh et al., 2014; Sethi and Schneider, 1996), drop test (Cowherd et al., 1989; Dahmann and Monz, 2011), the rotating drum (Breum, 1999; Schneider and Jensen, 2008). Among them, the latter two are the standard testers for measuring dustiness of bulk materials according to EN 15051 (EN, 2006). But these testers need large amounts of powders ( $35 \text{ cm}^3$  or 500 g) (Morgeneyer et al., 2013; O'Shaughnessy et al., 2012) and can give disparate results for industrial minerals (Pensis et al., 2010). Hamelmann and Schmidt's (Hamelmann and Schmidt, 2004) review of several dustiness testers shows the lack of comparability between the testers due to differences in the bulk sample and generation techniques, and thus a single standardized test is not suitable for all powders and applications.

Furthermore, most of the testers mentioned have only been used for short time durations (less than 1 hour) and may not be representative of the dust generated from processes with longer durations.

The vortex shaker (VS) method (Chakravarty et al., 2017a, 2017b; Le Bihan et al., 2014; Morgeneuer et al., 2013) is a promising dust generation method which is capable of functioning with very small sample quantities (less than 4g). (Morgeneuer et al., 2013) and (Le Bihan et al., 2014) used the VS method to test dust generation of micron-sized alumina particles and nanoscale carbon nano-tubes (CNTs) for one hour with sample mass as small as 0.5 g, respectively. (Morgeneuer et al., 2013) studied the minimum level of bulk mass and optimum vortex speeds necessary to aerosolize micron-sized alumina particles. They report a minimum sample mass of 2 g and a vortex speed of 1500 rpm - 1,800 rpm as suitable parameters for aerosolizing alumina particles without impacting the particle size distribution (PSD) of the powder. The VS setup also allows one to retrieve the used bulk sample after the end of the dustiness test for further analysis, but such results have not been reported in previous studies with the VS setup.

In this study, an experimental setup similar to (Morgeneuer et al., 2013) was used for testing the respirable dust generated by silicon carbide powders. Further, the tested powders were characterized for any change in PSD and shape properties due to testing. As HTFs in CSP plants are circulated for a prolonged duration, they require long-term monitoring of dust and change in powder properties. This study was focused on dust generation over six hours of vortex agitation for the worst case conditions, i.e., a dry filtered air flow and a vortex speed of 1500 rpm. This is a novel approach for studying dust generation in hard materials used for long-duration applications. Results from this study can support the selection process of an HTF material and appraise the need for further dust generation monitoring with different test conditions.

The primary objective of this study is to test and evaluate the dust generation behavior of two samples of silicon carbide particles subjected to vortex rotation for six hours. The ultimate purpose is to gain insights into the physical mechanisms underlying dustiness and how various factors lead to differences in dust emission. The results of these studies can be used for material selection based on their dust generation behavior and change in physical properties over long periods of time.

The grain shape properties and size distributions of the bulk powders were compared for the tested and untested (pristine) bulk powder samples using laser diffraction and image analysis (described in the materials and methods section 2.3). Finally, hypotheses accounting for our observations were proposed along with recommendations regarding the choice of powders in such industrial operations.

## 1.1.1 Materials and Methods

### 5.1.3.1 Silicon carbide particles

Two sets of silicon carbide powders (CAS Number: 409-21-2), SiC F220 and SiC F320 (from Mineralex, France) were used "as-received" following the EN standard 15051 (CEN, 2006). The test samples consisted of 99% of silicon carbide obtained from high purity sand or quartz, fused in an oven with pet coke at temperatures above 2000 °C. The powder test samples were characterized for volumetric and number size distribution by laser diffraction (3D measurement) and image analysis (2D measurement), respectively. Also, the samples' specific surface area and water content were measured using the gas adsorption surface area analyzer (BET) and a halogen moisture analyzer, respectively. The material parameters are mentioned in Table 5-1.

F220 and F320 have the same particle density ( $3,210 \text{ kg/m}^3$ ) and contain less than 0.1% of moisture by mass, measured before the dustiness test (Table 5-1). The volumetric size distribution of the samples measured in wet mode shows F220 and F320 with normal size distribution, and F220 with a broader size distribution than F320 (Figure 5.1a).

In order to compute number size distributions, the samples were prepared, dispersed automatically for measurement using the Morphologi G3s image analyzer (explained in section 2.3) according to the Malvern G3s user manual (*Morphologi G3 User Manual*, 2008). F220 shows a bi-modal size distribution with its first mode within the size bin of 0-5  $\mu\text{m}$  in circle equivalent diameter (CED), i.e, the diameter of a circle with the same areas as the measured 2D image of the particle (Figure 5.2b).

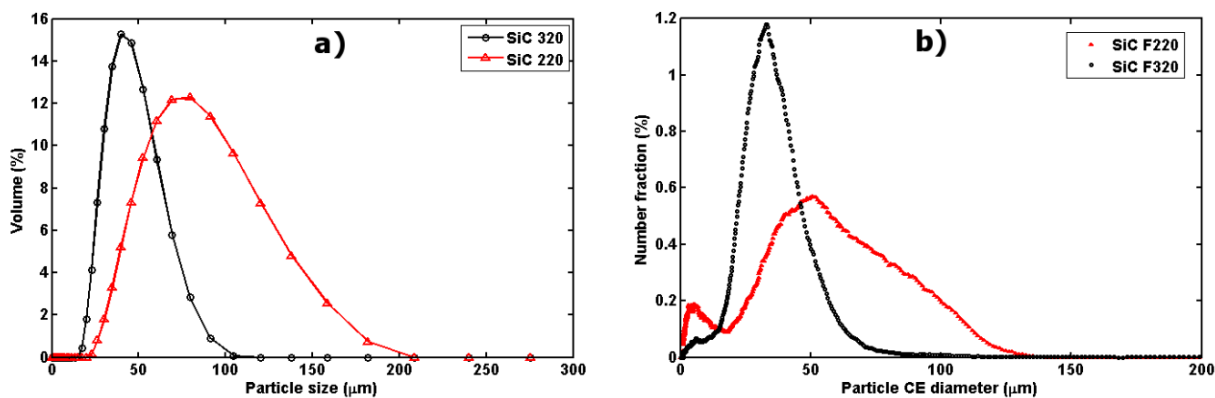


**Figure 5.1:** Particle size distribution of SiC samples F220 and F320. (a) by volume from laser diffraction analysis (b) by number from image analysis represented as relative distribution (in %).

**Table 5-1:** Powder properties of SiC F220 and F320 test samples.

	Units	F220	F320
Particle density <sup>a</sup> , $\rho_p$	kg/m <sup>3</sup>	3,210	3,210
Size distribution by volume <sup>b</sup>			
$x_{10}$ (SD)		38.7 (0.02)	24.7 (0.04)
$x_{50}$ (SD)	$\mu\text{m}$	68.2 (0.08)	38.5 (0.06)
$x_{90}$ (SD)		115 (0.15)	59.8 (0.11)
Span <sup>b</sup>			
$[(x_{90} - x_{10})/x_{50}]$	-	1.12	0.91
Surface weighted mean, $D[3,2]$ <sup>b</sup> (SD)	$\mu\text{m}$	60 (0.18)	36 (0.02)
Specific surface area <sup>c</sup>	m <sup>2</sup> /g	0.029	0.052
Moisture content <sup>d</sup>	%	< 0.1	< 0.1

<sup>a</sup> Data provided by the manufacturer

<sup>b</sup> Three replicates were measured for each powder sample using Mastersizer 2000 laser particle size analyzer (Malvern Instruments, UK) for sizes 0.01  $\mu\text{m}$  - 10,000  $\mu\text{m}$ . The samples were stirred in de-mineralized water for 5 min before measuring.

<sup>c</sup> Nitrogen adsorption surface area analyzer (Micromeritics Gemini, Norcross, USA)

<sup>d</sup> Moisture content (by mass) measured using a halogen moisture analyzer (Mettler Toledo, USA)

### 5.1.3.2 Vortex shaker dustiness tester

The VS setup was used as the dustiness tester due to its low requirements of sample sizes, ease of operation and the ability to retain the powder sample after the test. The experimental setup used by (Chakravarty et al., 2017b; Jensen, 2012) was adopted for the present study. The setup broadly consists of 4 sections; generation, sampling, dilution, and measurement (Figure 5.2).

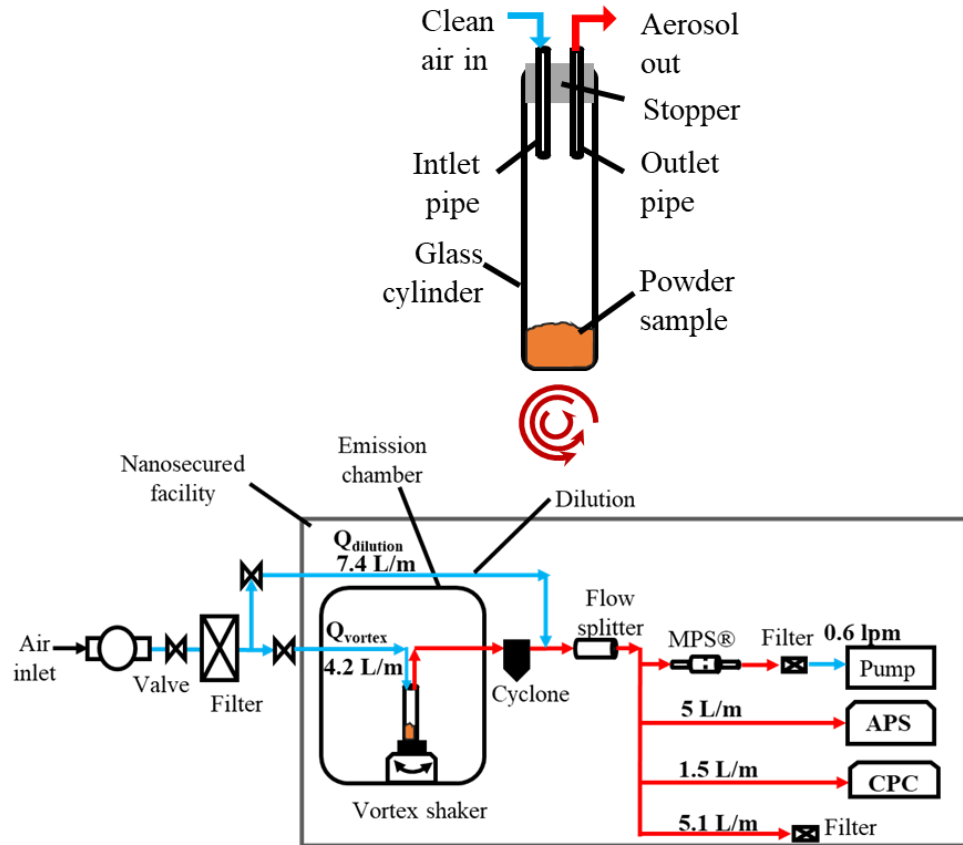


**Figure 5.2:** The vortex shaker setup. Centrifuge tube with filled sample (top) and the schematic of the experimental setup (bottom).

For aerosol generation, a powder-filled centrifuge test-tube (made of glass) was mounted on a digital vortex shaker (VWR Signature Digital Vortex Mixer). The shaker which is capable of achieving constant rotational speeds, was set to rotate at 1500 rpm along the vertical axis. The centrifuge tubes were sealed using a rubber stopper with provisions for an inlet to channel HEPA filtered dry air (at 4.2 L/min or  $7e-05$  m<sup>3</sup>/s) and an outlet to emit air containing aerosolized particles (also at 4.2 L/min).

Airborne dust particles were sampled using a BGI GK 2.69 cyclone operated at a volumetric flow rate of 4.2 L/min ( $7 \times 10^{-5} \text{ m}^3/\text{s}$ ) to meet the requirements of sampling for respirable size fraction (Jensen, 2012). The respirable fraction of aerosol released is then diluted with 7.4 L/min ( $1.2 \times 10^{-4} \text{ m}^3/\text{s}$ ) of filtered air (HEPA) and split into 3 channels for measurement and characterization. Particles with size larger than the respirable size fraction fall into the grit pot and are discarded. The flow through the sampler was checked and calibrated before starting each experiment.

The aerosol concentration of the respirable dust is measured at different bin size ranges using an aerodynamic particle sizer (APS TSI 3321, TSI Inc., Shoreview, MN). The APS records the particle counts by their aerodynamic size measured based on the time-of-flight of individual aerosol particles. It measured the aerosol number concentration over 51 size channels from 0.54  $\mu\text{m}$  to 20  $\mu\text{m}$ , recorded every 5 sec with a total flow rate of 5 L/min. Furthermore, it calculates the mass of individual spherical particles for a given particle density (TSI, APS Application notes). Since the minimum APS size detection limit inhibits its ability to quantify all particles in the respirable range ( $<4 \mu\text{m}$ ), a condensation particle counter (CPC TSI 3775, TSI Inc., Shoreview, MN) is used to measure the concentration of aerosol particles with size ranging from 0.004  $\mu\text{m}$  to 3  $\mu\text{m}$ . The CPC measurements span over a wide concentration ranging from 0 to  $10^7$  particles or  $\#/\text{cm}^3$  with high accuracy. An aerosol particle sampler, the Mini-Particle-Sampler (MPS®) (R'mili et al., 2013) was used to capture and deposit aerosol particles on copper grids for off-site transmission electron microscope (TEM) analysis.

Measures to minimize electrostatic charging during the transportation of dust included grounding the conductive aerosol outlet tube (stainless) and silicone tubes (diameter,  $4.8 \times 10^{-3} \text{ m}$ ) especially designed for particle transport (TSI Inc., USA). The total length of tubes connecting the aerosol source to the measurement devices was reduced to 0.9 m as compared to 1.2 m used by (Morgeneyer et al., 2013) to minimize the settling of dust particles in tubes. For ensuring safety while conducting the dustiness tests, all the experimental equipment were installed and operated inside a state-of-the-art closed isolator system at the Nanosecured (S-NANO) platform at the INERIS in Verneuil-en-Halatte, France. A more detailed description of the setup and powder handling process has been reported in (Le Bihan et al., 2014; Morgeneyer et al., 2013)

dealing with the aerosolization of micron-size alumina and nano-sized carbon nanotubes, respectively.

### ***5.1.3.3 Optical microscopy and particle morphology***

Particles from powder samples, F220 and F320 were quantitatively characterized with respect to their size and morphology using dry dispersion of powder in the particle image analyzer (Morphologi G3S, Malvern, UK) *before and after* the dustiness test. The particles were measured at a magnification of 20x with a 5-megapixel CCD camera to enable the digital analysis of particles shapes.

The analysis captures a 2D image of a 3D particle and calculates various size and shape parameters of the 2D image such as the circle equivalent diameter (CED), high sensitivity circularity (HSC) and convexity. CED is the diameter of the circle with the same surface area as the projected area of the particle. HSC values indicate the degree of roundness of the particles when compared to a perfect circle. It is calculated using the equation,

$$\text{HSC} = (4\pi \times A)/P^2 \quad \text{Eq. (5.1)}$$

where, A and P are the projected area and the perimeter, respectively. A perfect circle has an HSC value of 1 whereas an irregularly shaped object has a value closer to 0. Further, convexity is the measure of surface roughness in a particle, calculated as the ratio of “convex hull perimeter” by the actual perimeter of a particle (*Morphologi G3 User Manual*, 2008). A smoothly shaped particle has a convexity of 1 whereas a “spiky” or irregularly shaped particle has a value closer to 0. Aspect ratio (AR) is the ratio of the width to the length of the particle, where the width and length of the particle is the longest length of the projected particle on the major and minor axis, respectively.

### ***5.1.3.4 Test protocol***

Three trials were performed for each of the two powders, F220 and F320. Each test used 2 g of powder weighed with an accuracy of  $\pm 0.001$  g using an analytical balance (MS1003S, Mettler-Toledo, Inc., Columbus, OH, USA), manually filled in a centrifuge



glass tube (diameter 0.025 m, height 0.15 m). The filled tube was sealed using a rubber stopper and carried to the isolator system. The powders were weighed within 1 hour of performing the experiments to limit the number of variables affecting the experimental condition.

The sample filled centrifuge tube was then mounted on the VS using a rubber cup to hold the tube firmly. Prior to starting the vortex shaker, the APS and CPC sampling were turned on along with the inlet flow (4.2 L/min or  $7 \times 10^{-5}$  m<sup>3</sup>/s) and dilution flow (7.4 L/min or  $1.2 \times 10^{-4}$  m<sup>3</sup>/s) for 2 minutes. Opening the inlet flow shows a peak in the particle concentration (close to 10 particles/cm<sup>3</sup>) which rapidly decreases to the background values, usually lower than the detection limit of the APS (0.1 particles/cm<sup>3</sup>) and CPC (0.2 particles/cm<sup>3</sup>). Thus, the inlet air flow is only used to transport the aerosol generated through the vortex motion and does not influence the generation of dust particles in the system.

The VS operated at 1500 rpm, was run for six hours to test the powder samples, with a short break of 5 minutes after every 1-hour interval to avoid the overheating of the electric motor. Since the air flow is not interrupted, the peaks in the dustiness variables are entirely due to the mechanical action of the vortex shaker. The measured values begin and end 2 minutes before and after the vortex shaker running time, respectively. Each test was analyzed as an individual case. Using a low-pressure pump (0.6 L/min or  $1 \times 10^{-5}$  m<sup>3</sup>/s, Gilian LFS-113DC) attached to the sampler (MPS®), dust particles were collected on Quantifoil copper-carbon grids (Oxford Instruments, UK) (R'mili et al., 2013). The dust particles confined in these grids were further analyzed for their morphology using a Transmission electron microscope (TEM, JEOL JEM-2100F, operated at 100 kV).

## Calculation

Total respirable particle number concentrations measured for different particle size ranges from CPC (0.004 μm to 3 μm) and APS (3 μm to 19.5 μm) were combined to calculate the total number of generated particles,  $S_{\text{Vortex}}^{\text{Number (Total)}}$  using Eq. (5.2) to (5.4), modified from (Jensen, 2012).

$$S_{\text{Vortex}}^{\text{Number (CPC)}} = [Q_{\text{Vortex}} + Q_{\text{Dilution}}] \times \Delta t_{\text{CPC}} \times \sum_{i=0}^{T/\Delta t_{\text{CPC}}} C_{n,\text{CPC}}(t_0 + i \times \Delta t_{\text{CPC}}) \quad \text{Eq. (5.2)}$$

$$S_{\text{Vortex}}^{\text{Number (APS)}} = [Q_{\text{Vortex}} + Q_{\text{Dilution}}] \times \Delta t_{\text{APS}} \times \sum_{i=0}^{T/\Delta t_{\text{APS}}} C_{n,\text{APS}}(t_0 + i \times \Delta t_{\text{APS}}) \quad \text{Eq. (5.3)}$$

$$S_{\text{Vortex}}^{\text{Number (Total)}} = S_{\text{Vortex}}^{\text{Number (CPC)}} + S_{\text{Vortex}}^{\text{Number (APS)}} \quad \text{Eq. (5.4)}$$

where  $Q_{\text{Vortex}}$  and  $Q_{\text{Dilution}}$  are the flow rates for the filtered air directed towards the vortex tube ( $7e-05 \text{ m}^3/\text{s}$ ) and for dilution ( $1.2e-04 \text{ m}^3/\text{s}$ ), respectively.  $T$  is the time of the test for which the aerosol particles are calculated (6 intervals of 3,600 seconds).  $\Delta t_{\text{CPC}}$  (1s) and  $\Delta t_{\text{APS}}$  (5s) are the time-step set for the CPC and the APS, respectively.  $C_{n,\text{CPC}}(t_0 + i \cdot \Delta t_{\text{CPC}})$  and  $C_{n,\text{APS}}(t_0 + i \cdot \Delta t_{\text{APS}})$  are the aerosol number concentrations (in particles/ $\text{cm}^3$ ) for the  $i^{\text{th}}$  time interval measured by the CPC and the APS, respectively.

Additionally, APS number concentrations ( $C_{n,\text{APS}}$ , in particles/ $\text{cm}^3$ ) were used to calculate the volume of the assumed spherical particles, which is then transformed to mass concentration ( $C_{m,\text{APS}}$ , in  $\text{mg}/\text{m}^3$ ) for each size channel adjusted for the particle density of the SiC particle,  $\rho_p$  ( $3,210 \text{ kg}/\text{m}^3$ ) using Eq. (5.5). The APS software uses a pre-installed algorithm for Stokes correction reported by (Wang and John, 1987).

$$C_{m,\text{APS}} = \rho_p V_{\text{APS}} = \rho_p \times \sum_l^u \left[ \frac{\pi}{6} \left( D_a \sqrt{\frac{\rho_0}{\rho_p}} \right)^3 \times C_{n,\text{APS}} \right] \quad \text{Eq. (5.5)}$$

where  $V_{\text{APS}}$  is the total volume concentration ( $\mu\text{m}^3/\text{cm}^3$ ),  $D_a$  is the aerodynamic diameter of the particle and  $\rho_0$  is the unit density ( $1 \text{ g}/\text{cm}^3$  or  $1000 \text{ kg}/\text{m}^3$ ). The total mass of the respirable fraction of particles,  $M_{\text{Vortex}}^{\text{APS}}$  is then calculated using Eq. (5.6),

$$M_{\text{Vortex}}^{\text{APS}} = [Q_{\text{Vortex}} + Q_{\text{Dilution}}] \times \Delta t_{\text{APS}} \times \sum_{i=0}^{T/\Delta t_{\text{APS}}} C_{m,\text{APS}}(t_0 + i \times \Delta t_{\text{APS}}) \quad \text{Eq. (5.6)}$$

Furthermore, number and mass based dustiness indices (DI) were calculated for the dust generated per unit mass of powder, using Eq. (5.7) and Eq. (5.8)

$$DI_{\text{number}} \left( \frac{1}{\text{mg}} \right) = S_{\text{Vortex}}^{\text{Number (Total)}} / m \text{ (in mg)} \quad \text{Eq. (5.7)}$$

(5.7)

$$DI_{\text{mass}} \left( \frac{\text{mg}}{\text{kg}} \right) = M_{\text{Vortex}}^{\text{APS}} (\text{in mg}) / m (\text{in kg}) \quad \text{Eq. (5.8)}$$

whereby, m stands for the mass of the test sample.

## 1.1.2 Results

### 5.1.4.1 Respirable dustiness measurements

#### 5.1.4.1.1 Evolution of aerosol release

The standard deviations of the dustiness variables (particle count, aerosol mode size) are generally smaller than the differences between the averaged values for the two powders. It thus appears to be a statistically significant difference regarding the behaviour of the two agitated powders that needs to be accounted for. In general, both samples (F220 and F320) release respirable fractions of aerosol but their dust generation behaviour differs (Figure 5.3 bottom). During the six-hour test, the aerosol mode particle size by mass (Figure 5.3 top) for F220 shows a greater deviation towards smaller particle sizes compared to the F320 sample.

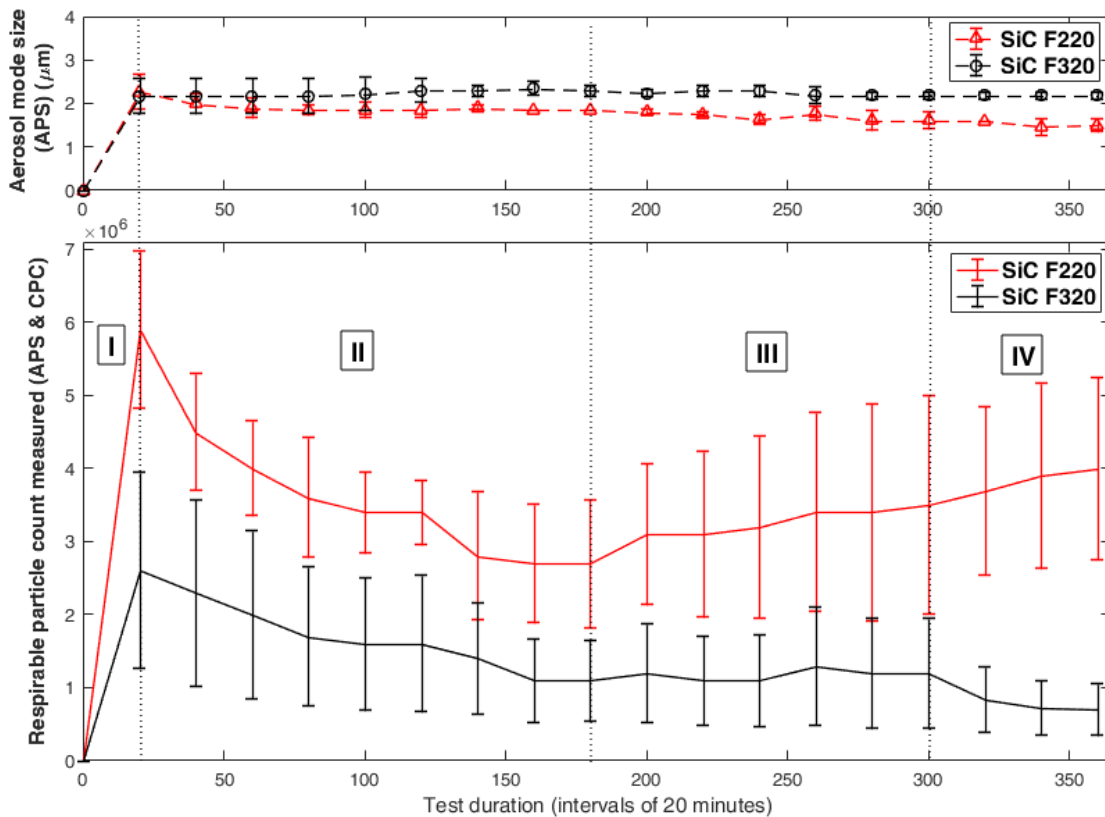


**Figure 5.3:** Evolution of aerosol mode particle size (top) and total respirable aerosol particle counts measured for F220 and F320 over stage I, II, III and IV. The counts are summed over 20-minute intervals. The error bars show the standard deviations calculated from three repeated trials. Vertical error bars are shown for both figures.

Aerosol generated from F220 and F320 can be classified into four stages based on the evolution of the total respirable aerosol counts (Figure 5.3).

#### Stages IV-IV:

**Stage I (Rapid Emission):** At the onset of the VS, F220 rapidly emits aerosol with the maximum number of aerosol released (approximately 5 to 7e+06) within the 20<sup>th</sup> minute of the test duration. F320 shows a similar behavior but with an aerosol count about 2-3 times lower than F220. Furthermore, the mode aerosol size measured for F220 and F320 using the APS shows similar values at the start of the experiment (Figure 5.3 top).

**Stage II (Reduction):** From its maximum at the 0-20<sup>th</sup> minute interval, the F220 and F320 aerosol numbers decrease to some local minima (2.7e+06 for SiC F220 and 1.1e+06 for SiC F320) within the 160<sup>th</sup> - 180<sup>th</sup> minute-intervals of the test.

**Stage III (Steady generation and release-1):** Aerosol released from F320 are relatively stable from the 180<sup>th</sup> minute to the 300<sup>th</sup> minute, but F220 shows a slight increase in

particle emission compared to F320 with some variation in the aerosol release measured by the CPC and APS, combined.

**Stage IV (Slow generation):** From the 300<sup>th</sup> minute till the end of the vortex shaker test, aerosol counts for F220 gradually increases by 14% as compared to a decrease of 42% for F320, for the same time interval.

#### 5.1.4.1.2 Aerosol size distribution

Aerosol mode particle size ( $D_{p,mode}$ ) (shown in Figure 5.3 (top)) was used as an indicator of change in aerosol size distribution with vortex time duration. Cumulative aerosol mass concentration ( $\sum_{i=0}^{T/\Delta t_{APS}} C_{m,APS}(t_0 + i \cdot \Delta t_{APS})$ ) from the APS, split in 20-minute time intervals were grouped and analyzed for change in aerosol mode particle size ( $D_{p,mode}$ ). For the APS size range of 0.5  $\mu\text{m}$  to 19.5  $\mu\text{m}$ , the average  $D_{p,mode}$  released by F320 lies within a stable range of 2.2  $\mu\text{m}$  to 2.3  $\mu\text{m}$  whereas aerosol from F220 shows a slightly wider size range of 1.5  $\mu\text{m}$  and 2.3  $\mu\text{m}$  for the six hours of testing.

#### 5.1.4.1.3 Number dustiness index

Respirable number dustiness indices for samples F220 ( $DI_{n,F220}$ ) and F320 ( $DI_{n,F320}$ ) are calculated from real-time aerosol concentration from the CPC and the APS using Eq. (5.7). For F220,  $DI_{n,F220}$  (7098/mg) at the 1<sup>st</sup> hour of vortex decreases by 27% and 21% by the 2<sup>nd</sup> and 3<sup>rd</sup> hour-intervals, respectively, followed by an increase of 14%, 10%, 12% in the 4<sup>th</sup> to 6<sup>th</sup> hour-intervals (Figure 5.4). As for F320,  $DI_{n,F320}$  in the 1<sup>st</sup> hour (3455/mg) decreases by 29%, 28%, 5%, 9% and 6% in the progressing 2<sup>nd</sup>, 3<sup>rd</sup>, 4<sup>th</sup>, 5<sup>th</sup> and 6<sup>th</sup> hour-intervals. Thus, both the micron-scale powders show  $DI_n$  in the range of 1E+03 to 1E+04, which are typically one to two orders of magnitude lower than the VS dustiness tests using nano-powders for different time durations (Dazon et al., 2017; Jensen, 2012). Furthermore, the increasing trend of  $DI_n$  (measured by APS and CPC) after 3 hours for SiC F220 is different from the stable profile of  $DI_{mass}$  (measured by APS, Figure 5.4) for the same time means the increasing trend is due to the emission of finer particles lower than the measurement range of the APS.

A parabolic fit for F220 (Eq. 5.9) and a power law fit for F320 (Eq. 5.10) can provide a reasonable approximation to the average respirable number dustiness over the 6-hour test duration.

$$DI_{n,F220} = 1168 (t_h^2) - 323 (t_h) + 4373 \quad \text{Eq. (5.9)}$$

$$DI_{n,F320} = 3457 (t_h)^{-0.53} \quad \text{Eq. (5.10)}$$

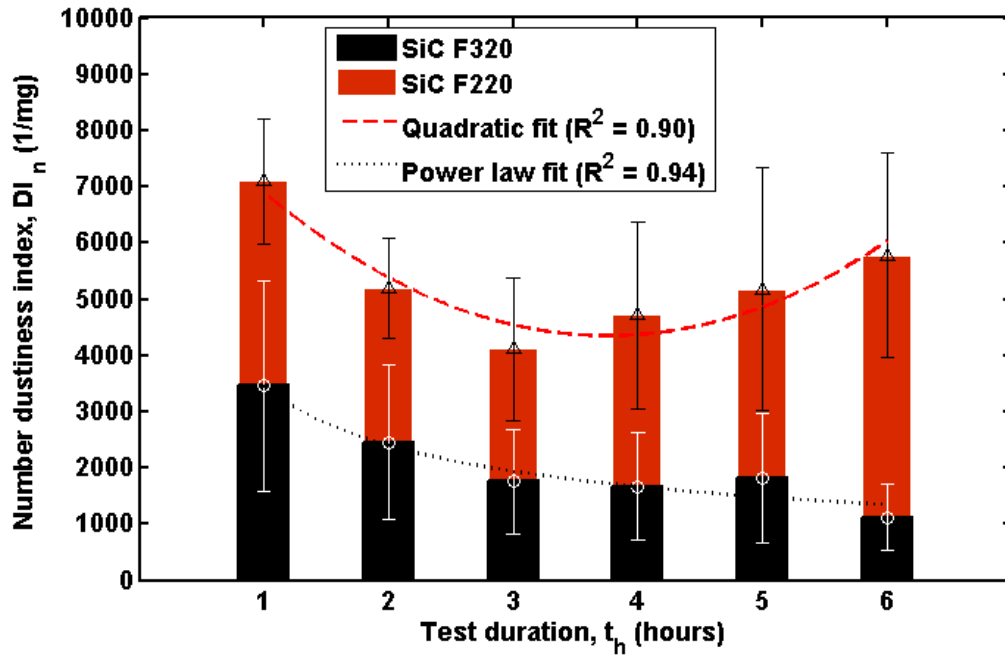


**Figure 5.4:** Number dustiness ( $DI_n$ ) indices for F220 and F320 from APS and CPC measurements summed over six 1-hour intervals. The error bars show the standard deviations calculated from three repeated trials.

#### 5.1.4.1.4 Mass dustiness index

Respirable mass dustiness indices for F220 ( $DI_{m,F220}$ ) and F320 ( $DI_{m,F320}$ ) are calculated using Eq. (5.8) based on the APS measurements. Similar to  $DI_n$  (Figure 5.4),  $DI_{m,F220}$  and  $DI_{m,F320}$  show maximum values at the start of the test (Figure 5.5). With time, while both  $DI_{m,F220}$  and  $DI_{m,F320}$  decreases,  $DI_{m,F220}$  shows an increase of 16% from the 3<sup>rd</sup> to the 6<sup>th</sup> hour of the test duration. The average  $DI_m$  values for F220 and F320 are fitted to a quadratic (in Eq. (5.11)) and power law (in Eq. (5.12)) expressions, respectively. Compared to the VS tests with nano-powders (Dazon et al., 2017; Jensen, 2012), the  $DI_m$  values for the F220 and 320 powders are around one order magnitude lower.

$$DI_{m,F220} = 750 (t_h^2) - 6412 (t_h) + 17310 \quad \text{Eq. (5.11)}$$

$$DI_{m,F320} = 5643 (t_h)^{-0.70} \quad \text{Eq. (5.12)}$$

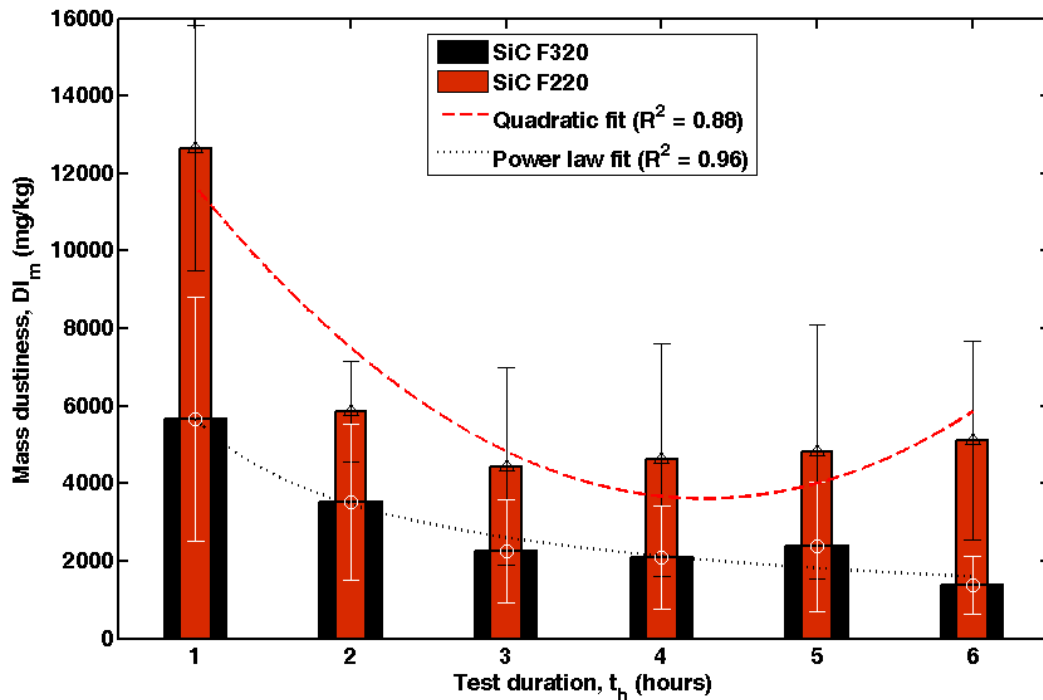


**Figure 5.5:** Mass dustiness indices ( $DI_m$ ) for F220 and F320 from APS measurements summed over six 1-hour intervals. The error bars show the standard deviations calculated from three repeated trials.

#### 5.1.4.1.5 TEM micrographs

Examining approximately 50 photomicrographs from each sample (F220 and F320) shows a wide range of sizes and shapes of the respirable aerosol particles generated from the F220 and F320 samples. The aerosol particles sampled between the 350<sup>th</sup> and the 360<sup>th</sup> minute (Figure 5.6: c, d, g, h) show angular shaped particles with at least one smooth surface (marked with a dotted line) with fewer surface asperities compared to the aerosols with rugged surfaces sampled between the 25<sup>th</sup> to 30<sup>th</sup> minute interval (Figure 5.6: a, b, e, f).

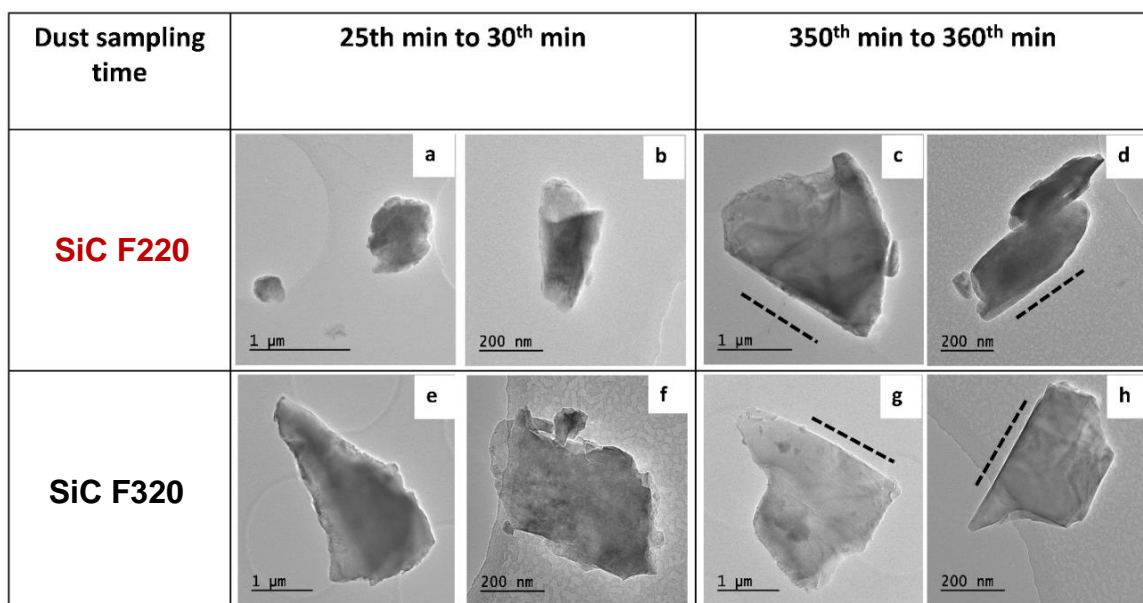


**Figure 5.6:** TEM micrographs for SiC F220 (top; a,b,c,d) and SiC F320 (bottom; e,f,g,h) aerosol particles captured at 25th- 30th minute interval and from 350th minute - 360th minute interval.

#### 5.1.4.2 Characterization of the tested powder samples

##### 5.1.4.2.1 Size distribution of the powder

###### Volumetric size distribution

After 6-hours of VS operation, the tested powder samples were characterized with respect to changes in their PSD by volume using a laser diffraction particle size analyzer (Figure 5.7a and Table 5-2). The testing of the F320 sample (F320\_tested) shows negligible change in its size distribution compared to the pristine samples (F320). The differences with respect to volumetric  $x_{10}$ ,  $x_{50}$  and  $x_{90}$  of the powder range from 0.6, 0.3 and  $-0.3$ , respectively which are close or inferior to the standard deviation stemming from the four repeated trials.

On the other hand, the tested F220 sample (F220\_tested) shows noticeable changes in powder PSD where volumetric  $x_{90}$  and  $x_{50}$  decreases by 6, and 1.7, respectively although  $x_{10}$  increases by 1.1. Those changes are significantly higher than the standard deviations for the 4 repeated trials.



**Table 5-2:** Volumetric PSD of the fresh (F220 and F320) and tested powder samples (F220\_tested and F320\_tested).

Test Samples	Distribution by volume			
	$x_{10}$ ( $\mu\text{m}$ ) (SD)	$x_{50}$ ( $\mu\text{m}$ ) (SD)	$x_{90}$ ( $\mu\text{m}$ ) (SD)	Span
<b>F220</b>	38.7 (0.02)	68.2 (0.08)	115 (0.15)	1.12
<b>F220_tested</b>	39.8 (0.01)	66.5 (0.02)	109 (0.6)	1.04
<b>F320</b>	24.7 (0.04)	38.5 (0.06)	59.8 (0.11)	0.91
<b>F320_tested</b>	25.3 (0.45)	38.9 (0.04)	59.5 (1.1)	0.88

### Number size distribution

Circle Equivalent Diameters (CED) of individual grains from fresh (F220 and F320) and tested (F220\_tested and F320\_tested) samples were measured using image analysis. A minimum of 30,000 particles were analyzed for each of the 3 trials per sample. Similar to the volume size distribution (Table 5-2), F320 samples shows negligible changes in PSD for the pristine and tested powders whereas the F220 shows a distinguishable change in PSD from its pristine to tested state.

The tested samples for both SiC F220 and SiC F320 powders show an increase in the population of particles with sizes less than 20 $\mu\text{m}$ , indicating the availability of aerosolizable fine particles even after 6 hours of testing (Figure 5.7b). In comparison to their pristine samples, the tested F320 samples show a slight increase in the number of particles less than 20 $\mu\text{m}$ , whereas tested F220 shows about 20% increase for the particular size range.

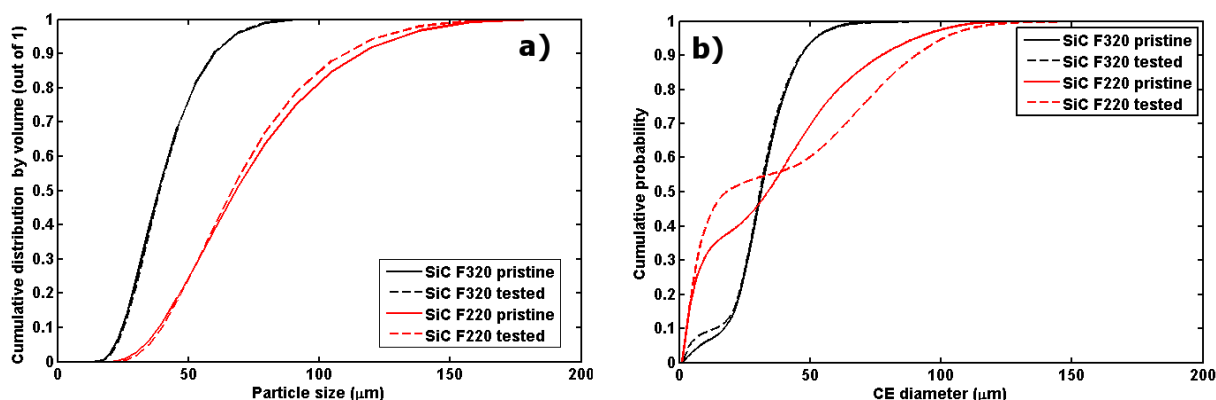


**Figure 5.7:** Cumulative particle size distribution of pristine and tested SiC powders (a) by volume measured using laser diffraction (b) by number measured using image analysis. Changes in F220 (F220 and F220\_tested) was more prominent than F320 (F320 and F320\_tested).

#### 5.1.4.2.2 *Change in particle morphology*

The Morphologi G3s analyzer was used for static image analysis and corresponding measurement of particle shape properties including high sensitivity (HS) circularity, convexity and aspect ratio (AR). The principles it relies on are laid out in section 2.3. The measured average values of HS circularity (0.81) and AR (0.73) for SiC F320 were 16% and 18% greater than the larger sized SiC F220 particles, shows the F320 particles as more circular in shape compared to SiC F220 (see Table 5-3). Also, there were almost no differences in the average convexity for both the powders, thus indicating no detectable ‘spikiness’ or roughness in in the particle shape.

Compared to the measurements from the pristine samples, F320\_tested shows no change in mean HS circularity or aspect ratio (Table 5-3). But, tested samples of F220 (F220\_tested) shows a 6% increase in both HS circularity and aspect ratio, respectively (Table 5-3).

While F320 particles shows mostly circular particles with a Gaussian-like distribution over particle sizes 5-50  $\mu\text{m}$  (Figure 5.8c and Figure 5.8d), there are few changes observed in the distribution of F220 particles over circularity and particle size (Figure 5.8a and Figure 5.8b). The fine particles (close to 0-10  $\mu\text{m}$ ) for the tested particles show a wide range of HS circularity from 0.2 to 1. Also, the tested F220 particles show a decrease in the proportion of particles within the sizes of 15  $\mu\text{m}$  - 50  $\mu\text{m}$  and an increase in particles (with relatively greater circularity) with sizes 50  $\mu\text{m}$  - 100  $\mu\text{m}$ , as compared to the F220 pristine.

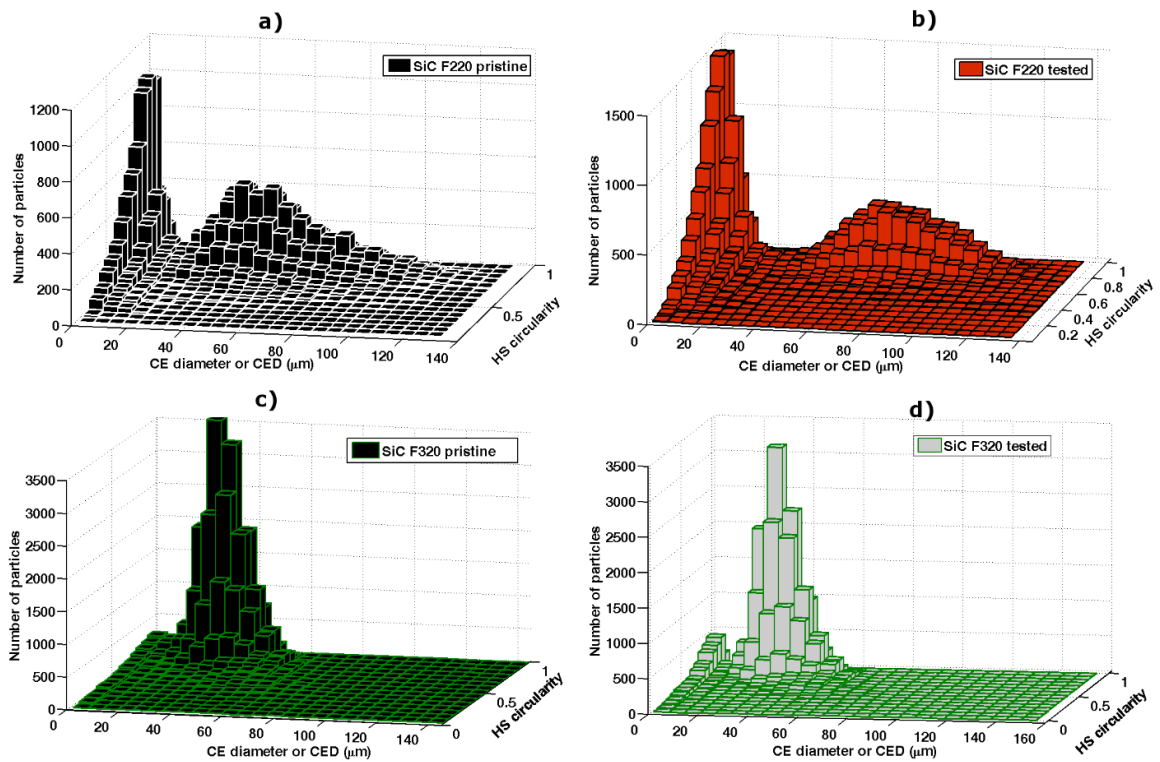


**Figure 5.8:** 3-D histogram illustrating distribution of particles by size (CED) and HS circularity measured for: SiC F220 (top): pristine (a), tested (b) and SiC F320 (bottom): pristine (c), tested (d).

**Table 5-3:** Particle size (CED) and shape factors for the fresh (F220 and F320) and tested (F220\_tested and F320\_tested) samples measured based on particle number using image analysis.

Test Samples	$x_{50}$ (in $\mu\text{m}$ )	Mean HSC (SD) (max. 1)	Mean Convexity (SD) (max. 1)	Mean Aspect ratio (SD) (max. 1)
F220	35.68	0.70 (0.08)	0.97 (0.01)	0.62 (0.03)
F220_tested	18.11	0.74 (0.01)	0.97 (0.00)	0.66 (0.00)
F320	31.59	0.81 (0.01)	0.98 (0.00)	0.73 (0.01)
F320_tested	31.58	0.81 (0.01)	0.98 (0.00)	0.72 (0.01)

## 5.1.5 Discussion

### 5.1.5.1 Aerosol measurement

The combination of APS and CPC was found suitable for determining the respirable dustiness by number and mass, for micron-sized F220 and F320. A powder mass of 2 g and a vortex speed of 1500 rpm were enough to measure the respirable aerosols within the lower and upper bounds of the APS and the CPC, similarly to the study of dustiness in alumina particles (Morgeneyer et al., 2013).

The number and mass dustiness indices of powders can be used to compare dustiness from different powder samples (Jensen, 2012). The ratio of  $DI_n$  for SiC F220 and F320 shows a progressive increase from 2.1 to 5.1 during the experiment, whereas the ratio of  $DI_m$  decreases from 2.2 (1<sup>st</sup> hour) to 1.6 (2<sup>nd</sup> hour), before reaching its maximum value 3.7 in the 6<sup>th</sup> and final 1-hour interval. We postulate that the disparity in the trends of hourly numbers and mass dustiness indices for SiC F220 measured using the CPC and APS, respectively (Figure 5.4 and Figure 5.5) may stem from the difference in the aerosol size ranges measured by the CPC (0.004  $\mu\text{m}$  to 3  $\mu\text{m}$ ) and the APS (3  $\mu\text{m}$  to 19.5  $\mu\text{m}$ ). Dust released in the initial hour is a combination of coarser and fine particles but with time, there is reduction in dust emission for both powders but the SiC F220 shows an increase in small fine-scale dust particles, unlike the SiC F320 samples. These fine-scale aerosols (whose sizes are smaller than 0.5  $\mu\text{m}$ ) are counted by the CPC and can be seen in TEM micrographs (Figure 5.6c and Figure 5.6d). Furthermore, the mass of the sub-micron sized aerosol particles with sizes lower than the APS detection limit ( $d_{ae} < 0.5 \mu\text{m}$ ) has little contribution to the total mass measured (O'Shaughnessy et al., 2012)

The TEM micrographs for F220 and F320 show aerosol particles with at least one smooth edge (marked by a dotted line in Figure 5.6c, Figure 5.6d, Figure 5.6g, Figure 5.6h). The smooth surface of the aerosol particles can be due to the chipping of small angular fragments from the original SiC particles. An analysis of the aerosol shapes and sizes between the 1<sup>st</sup> and the 6<sup>th</sup> hour could further improve our understanding of the evolution of the aerosol particles generated from F220 and F320.

### 5.1.5.2 Dustiness due to particle attrition

F220 and F320 undergo mechanical stresses due to inter-particle collisions and particle-wall impacts in the VS. Although hard materials like SiC particles are resistant to breakage or fragmentation, they can undergo attrition due to abrasion or combination of fragmentation and abrasion, depending on the stresses they are subjected to (Ness and Zibbell, 1996; Quercia et al., 2001). Generally, the abrasion of particles leads to the rounding of the primary mother particles by reducing surface asperities resulting in the generation of fine-scale particles, thus creating a bi-modal number size distribution without any significant changes in the PSD by volume (Yang, 2003).

Based on the present results of the dustiness tests of SiC particles, the initial dust generation strongly depends on the population size of the aerosolizable particles present in the bulk material. The abrasion of larger particles generates fine aerosolizable particles and is a crucial part of the overall dust generation mechanism. The dust generation mechanism can be broadly divided into two stages (Figure 5.9):

A: direct release of aerosolizable primary particles,

B: release of aerosolizable fines generated through the attrition of larger primary particles.

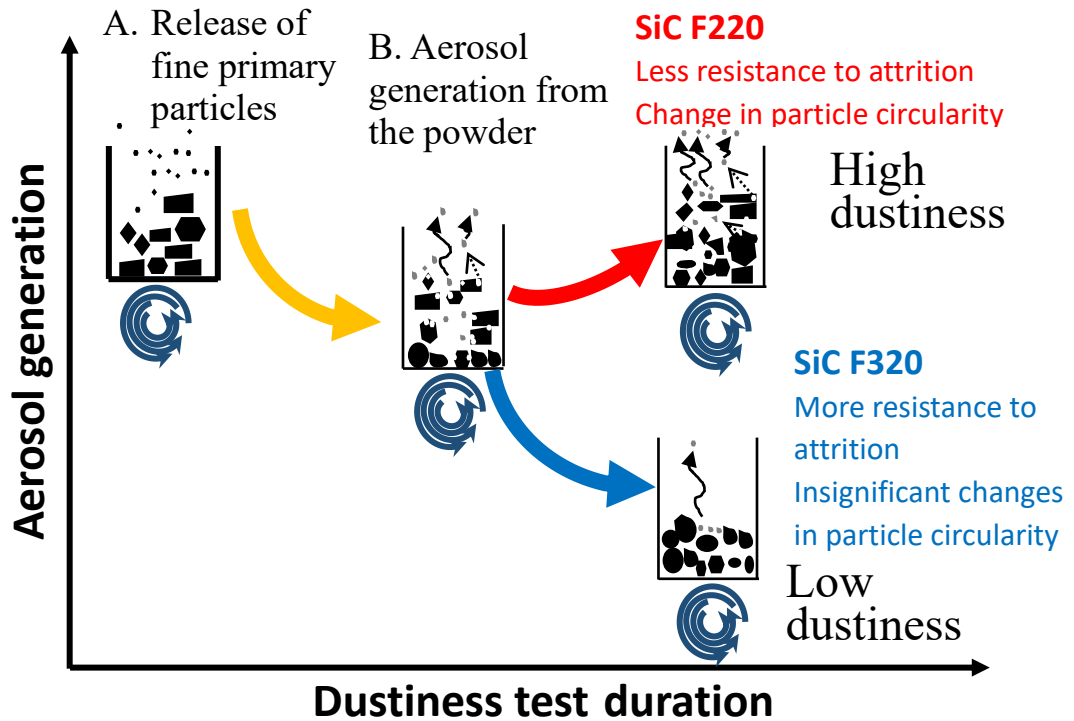


**Figure 5.9:** Dust generation mechanisms identified for F220 and F320. A: direct release of aerosol from bulk, B: release of aerosolizable particles generated from attrition of larger particles.

While the volumetric PSD does not show particles in the respirable size range (Figure 5.1a, Figure 5.7a) with respect to F220 and F320, the number PSD for both F220 and F320 show bi-modal size distributions revealing the presence of particles with CED smaller than 10  $\mu\text{m}$  (Figure 5.1b, Figure 5.7b). Such fine-scale particles already present in the bulk samples can contribute to the initial release of respirable aerosol for F220 and F320 (Figure 5.9). With 32% of particles with CED smaller than 10  $\mu\text{m}$ , F220 generates 2.3 times more respirable aerosol particles in the initial 20 minutes of the vortex shaker test (Stage I, Figure 5.3) compared to F320 consisting of less than 6% of particles smaller than 10  $\mu\text{m}$ .

Stage II can be considered as the relatively gradual reduction in dust emission after the peak of dust emission (Stage I) shown by both SiC F220 and F320 powders. The end of Stage II lies at the 160<sup>th</sup> - 180<sup>th</sup> minute-interval for both powders (Figure 5.3), where the respirable aerosol counts for F220 and F320 reaches their respective local minima, which indicates diminished reserves of aerosolizable dust particle for both SiC powders.

In stage III, the respirable aerosol counts for both F220 and F320 levels off to a relative steady-state (180<sup>th</sup> to 300<sup>th</sup> minute, Figure 5.3). One possible interpretation of this stage may be that the rate of generation of respirable aerosols in the bulk equals the rate of aerosols released from the bulk. In comparison to the smaller sized SiC F320 particles, F220 powder shows an increasing tendency to release dust, i.e., an increase in generation of respirable aerosols with time. The increase in fine production allows SiC 220 to maintain a reservoir of fine-scale aerosolizable particles (with CED up to 10  $\mu\text{m}$ ) thus showing an increase in the population of particles with sizes smaller than 10  $\mu\text{m}$ . The coarser particles in F220 (CED up to 125  $\mu\text{m}$ ) are particularly prone to attrition due to abrasion as they tend to contain more faults in the form of microcracks or imperfections and a higher surface area for particle-wall interactions compared to smaller sized particles present in SiC F320.

In Stage IV there is an observable change in the powder emission behavior for both powders. F320 emissions decreases by 42% till the end of the 6-hour test duration. The decrease in F320 aerosol counts with time (Figure 5.3) suggests a diminishing number of fines generated from attrition, that is to say, the F320 particles resist attrition and thus limits the production and generation of fine-scale respirable dust. The smaller,

more attrition resistant SiC F320 shows hardly any change in PSD by number or volume due to the 6 hours of vortex shaker test.

Contrarily to SiC F320 powders, F220 emissions increase by 14%. Characterization of the tested F220 powders show a decrease in median particle size ( $x_{50}$ ) of 49% and 2.5% based on the number (Figure 5.7b, Table 5-3) and volume (Figure 5.7a, Table 5-2) size distributions, respectively. The aerosolization of fine-scale particles from a specific quantity of particles present in the bulk can lead to an increase in  $x_{10}$  due to the absence of the aerosolized particles at the end of the vortex test (PSD by volume shown in Figure 5.7, Table 5-2). Further, a decrease in  $x_{90}$  suggests a reduction in the size of large-sized particles, potentially due to the attrition of small fragments from the larger particles inside the VS system.

Results from the image analysis of the particle shape properties show SiC F320 particles as relatively more circular in shape with higher average aspect ratio compared to the larger SiC F220 particles. The F220 tested particles show small increases in particle HS circularity and aspect ratio compared to almost no change measured for the tested and pristine SiC F320 particles. The relatively larger and sharply shaped fresh F220 particles show inclination towards becoming rounder (increasing HSC and AR in F220\_tested) by shedding angular corners in collisions (Figure 5.8, Table 5-3). This phenomena has been reported for other particles such as sodium benzoate with increasing particle impaction (Laarhoven et al., 2012). On the contrary, the less dusty F320 particles are smaller in size and retains its circularity and aspect ratio during the 6 hours of vortex. There are indications in the literature that circular particles are more resistant to attrition than non-circular ones (Laarhoven et al., 2012; Van Laarhoven, 2010). This might account for the fact that primary particles from F320 that have more circular shapes generate less fines than primary particles from F220 which have an irregular shape while there are no discernable changes particle surface roughness (convexity values in Table 5-3).

### 5.1.6 Conclusion and Perspective

Particles used for applications extending over a long period of time, such as HTFs in CSP solar thermal plants require results from sufficiently long dustiness tests to

support the selection of material and quantify the risk associated with the handling of new and used particles. In this case study, we investigate dust release over six hours for two potential silicon carbide HTFs (F220 with  $x_{50}$  by volume = 68  $\mu\text{m}$  and F320 with  $x_{50}$  by volume = 38  $\mu\text{m}$ ) using the VS method.

Test results show the release of the respirable fraction of dust particles from both samples, but F220 is found to be more prone to generate dust than F320. The hourly dustiness index (by number) ratio of F220 and F320 increases from 2.1 in the 1<sup>st</sup> hour to 5.1 at the 6<sup>th</sup> hour. For F320, an initial rise in the aerosol release is followed by a gradual decrease with time, following a power law distribution. Unlike F320, aerosol generation and release from F220 is more complex and the dust released over time shows a quadratic fit.

F220 and F320 not only differ in dustiness but also in the mechanism of dust generation and release. Two dust generation mechanisms are proposed which can potentially explain the dustiness behaviour of F220 and F320 over a 6-hour duration. Results from the dustiness measurement, TEM micrographs of the aerosol particles and characterization of pristine and tested powder samples by their size and shape suggest that the dust generation from F220 and F320 is related to the presence of aerosolizable fine-scale particles already present in the bulk as well as the particles generated from powder attrition.

The tested F220 powders show changes in particle size distribution and shape properties compared to their pristine form, indicating abrasion as the dominant source of attrition. On the contrary, the F320 powders show barely any changes in particle size distribution or shape factors with vortex testing.

Understanding the difference of aerosol generation behavior based on particle shape requires further work and the effect should be more observable for materials softer and more fragile than SiC F220 and F320 bulk samples could be further characterized by their particle size distribution and shape properties for every hour to analyze the evolution of particle properties with dust generation. The handling of F220 (SiC 220) may generate fine-scale particles which may affect the safe and efficient operation of SiC HTFs in CSP plants. Our study underlines the importance of characterizing both before and after the dustiness test, as changes in its properties are crucial to understand the underlying dust generation mechanisms.



In the industrial world, powders which have already undergone an *ageing process* for several weeks or months are employed in the CSP plants. Studying such aged powders with respect to their dust generation behavior appears worthwhile. The fact that the dustiness of powder F320 diminishes with time might make it potentially more interesting for industrial applications compared to its counterpart F220 whose dustiness index ends up increasing with time. Further studies are necessary to investigate its potential greater suitability for long-term uses.

### 5.1.7 References

- Baron, P., Vincent, J., 1999. Particle size-selective sampling of particulate air contaminants.
- Benoit, H., Pérez López, I., Gauthier, D., Sans, J.-L., Flamant, G., 2015. On-sun demonstration of a 750°C heat transfer fluid for concentrating solar systems: Dense particle suspension in tube. *Sol. Energy* 118, 622-633. <https://doi.org/10.1016/j.solener.2015.06.007>
- Boundy, M., Leith, D., Polton, T., 2006. Method to Evaluate the Dustiness of Pharmaceutical Powders 50, 453-458. <https://doi.org/10.1093/annhyg/mel004>
- Breum, N.O., 1999. The Rotating Drum Dustiness Tester : Variability in Dustiness in Relation to Sample Mass , Testing Time , and Surface Adhesion 43, 557-566. [https://doi.org/http://dx.doi.org/10.1016/S0003-4878\(99\)00049-6](https://doi.org/http://dx.doi.org/10.1016/S0003-4878(99)00049-6)
- Chakravarty, S., Fischer, M., García-Tríñanes, P., García-Tríñanes, P., Parker, D., Le Bihan, O., Morgeneyer, M., García-Tríñanes, P., Parker, D., Bihan, O.L.O. Le, Morgeneyer, M., 2017a. Study of the particle motion induced by a vortex shaker. *Powder Technol.* 322, 54-64. <https://doi.org/10.1016/j.powtec.2017.08.026>
- Chakravarty, S., Le Bihan, O., Fischer, M., Morgeneyer, M., 2017b. Dust generation in powders: Effect of particle size distribution, in: *EPJ Web of Conferences*. EDP Sciences, p. 13018. <https://doi.org/10.1051/epjconf/201714013018>
- Cowherd, C., Grelinger, M.A., Englehart, P.J., Kent, R.F., Wong, K.F., 1989. An apparatus and methodology for predicting the dustiness of materials. *Am. Ind. Hyg. Assoc. J.* 50, 123-130.
- Dahmann, D., Monz, C., 2011. Determination of dustiness of nanostructured materials. *Gefahrstoffe - Reinhaltung der Luft* 71, 481-487.
- Dazon, C., Witschger, O., Bau, S., Payet, R., Beugnon, K., Petit, G., Garin, T., Martinon, L., 2017. Dustiness of 14 carbon nanotubes using the vortex shaker method. *J. Phys. Conf. Ser.* 838. <https://doi.org/10.1088/1742-6596/838/1/012005>
- Eckhoff, R., 2005. Current status and expected future trends in dust explosion research. *J. loss Prev. Process Ind.*
- EN, C., 2006. EN 15051 Workplace atmospheres—measurement of the dustiness of bulk materials—requirements and test methods. Brussels, Belgium Eur. Comm. Stand.
- EN, C., 1993. 481 Workplace atmospheres: specification for conventions for measurement of suspended matter in workplace atmospheres. Brussels, Belgium Eur. Comm. ....
- García-Tríñanes, P., Seville, J., Boissière, B., 2016. Hydrodynamics and particle motion in upward flowing dense particle suspensions: Application in solar receivers. *Chem. Eng.*
- Governa, M., Valentino, M., Amati, M., Visonà, I., Botta, G.C., Marcer, G., Gemignani, C., 1997. Biological effects of contaminated silicon carbide particles from a workstation in a plant producing abrasives. *Toxicol. Vitr.* 11, 201-207. [https://doi.org/10.1016/S0887-2333\(97\)00018-0](https://doi.org/10.1016/S0887-2333(97)00018-0)

- Green, D.W., 2007. Perry's chemical engineering handbook. McGrawHill Prof.
- Hamelmann, F., Schmidt, E., 2004. Methods for characterizing the dustiness estimation of powders. *Chem. Eng. Technol.* 27, 844-847. <https://doi.org/http://dx.doi.org/10.1002/ceat.200403210>
- Hamelmann, F., Schmidt, E., 2003. Methods of Estimating the Dustiness of Industrial Powders - A Review. *KONA Powder Part. J.* 21, 7-18. <https://doi.org/10.14356/kona.2003006>
- Harris, G., 1995. Properties of silicon carbide. Institution of Engineering and Technology.
- Hinds, W.C., 1999. *Aerosol technology: Properties, Behavior, and Measurement of Airborne Particles.*, Wiley-Interscience Publication. [https://doi.org/10.1016/0021-8502\(83\)90049-6](https://doi.org/10.1016/0021-8502(83)90049-6)
- International Organization for Standardization, 1995. ISO 7708: Air quality—particle size fraction definitions for health-related sampling. Geneva, Switzerland: International Organization for Standardization.
- International Organization for Standardization, 1994. ISO 4225: Air quality - General aspects - Vocabulary.
- Jensen, K.A., 2012. Towards a method for detecting the potential genotoxicity of nanomaterials. D4.6: Dustiness of NANOGENOTOX nanomaterials using the NRCWE small rotating drum and the INRS Vortex shaker. Copenhagen, DENMARK.
- Klippel, A., Scheid, M., Krause, U., 2013. Investigations into the influence of dustiness on dust explosions. *J. Loss Prev. Process.*
- Laarhoven, B. van, Schaafsma, S., Meesters, G.M.H., 2012. Toward a desktop attrition tester; validation with dilute phase pneumatic conveying. *Chem. Eng. Sci.* 73, 321-328.
- Le Bihan, O.L.C., Ustache, A., Bernard, D., Aguerre-Chariol, O., Morgeneyer, M., 2014. Experimental Study of the Aerosolization from a Carbon Nanotube Bulk by a Vortex Shaker. *J. Nanomater.* 2014, 1-11. <https://doi.org/10.1155/2014/193154>
- Morgeneyer, M., Le Bihan, O., Ustache, A., Aguerre-Chariol, O., 2013. Experimental study of the aerosolization of fine alumina particles from bulk by a vortex shaker. *Powder Technol.* 246, 583-589. <https://doi.org/10.1016/j.powtec.2013.05.040>
- Morphologi G3 User Manual, MAN0410 Is. ed, 2008. . Malvern Instruments Ltd. United Kingdom.
- Ness, E., Zibbell, R., 1996. Abrasion and erosion of hard materials related to wear in the abrasive waterjet. *Wear* 196, 120-125. [https://doi.org/10.1016/0043-1648\(95\)06886-4](https://doi.org/10.1016/0043-1648(95)06886-4)
- O'Shaughnessy, P.T., Kang, M., Ellickson, D., 2012. A Novel Device for Measuring Respirable Dustiness Using Low-Mass Powder Samples. *J. Occup. Environ. Hyg.* <https://doi.org/10.1080/15459624.2011.652061>
- Pensis, I., Mareels, J., Dahmann, D., Mark, D., 2010. Comparative evaluation of the dustiness of industrial minerals according to European standard en 15051, 2006. *Ann. Occup. Hyg.* 54, 204-216. <https://doi.org/10.1093/annhyg/mep077>
- Petran, M., Cocarla, A., Baiescu, M., 2000. Association between Bronchial Hyper-reactivity and Exposure to Silicon Carbide. *Occup. Med. (Chic. Ill).* 50, 103-106. <https://doi.org/10.1093/occmed/50.2.103>
- Plinke, M.A.E., 1995. Dust generation from handling powders in industry. *Am. Ind. Hyg. Assoc. J.*
- Plinke, M., Maus, R., Leith, D., 1992. Experimental examination of factors that affect dust generation by using Heubach and MRI testers. *Am. Ind. Hyg.*
- Quercia, G., Grigorescu, I., Contreras, H., 2001. Friction and wear behavior of several hard materials. *Hard Mater.*
- R'mili, B., Le Bihan, O.L.C., Dutouquet, C., Aguerre-Chariol, O., Frejafon, E., 2013. Particle Sampling by TEM Grid Filtration. *Aerosol Sci. Technol.* 47, 767-775. <https://doi.org/10.1080/02786826.2013.789478>
- Saleh, K., Moufarej Abou Jaoude, M.T., Morgeneyer, M., Lefrancois, E., Le Bihan, O., Bouillard, J., 2014. Dust generation from powders: A characterization test based on stirred fluidization. *Powder Technol.*

255, 141-148. <https://doi.org/10.1016/j.powtec.2013.10.051>

Schneider, T., Jensen, K.A., 2008. Combined Single-Drop and Rotating Drum Dustiness Test of Fine to Nanosize Powders Using a Small Drum. *Ann. Occup. Hyg.* 52, 23-34.  
<https://doi.org/10.1093/annhyg/mem059>

Sethi, S.A., Schneider, T., 1996. A gas fluidization dustiness tester. *J. Aerosol Sci.* 27, S305-S306.  
[https://doi.org/10.1016/0021-8502\(96\)00225-X](https://doi.org/10.1016/0021-8502(96)00225-X)

TSI, 1998. Estimation of Mass with the Model 3321 APS, tsi.com.

Van Laarhoven, B., 2010. Breakage of Agglomerates: Attrition, Abrasion and Compression.

Wang, H., John, W., 1987. Particle density correction for the aerodynamic particle sizer. *Aerosol Sci. Technol.*

Yang, W.-C., 2003. Handbook of fluidization and fluid-particle systems, Chemical Engineering.  
[https://doi.org/10.1016/S1672-2515\(07\)60126-2](https://doi.org/10.1016/S1672-2515(07)60126-2)

## 5.2 Article (submitted to Powder Technology, March 2017):

### Dust generation behaviour of alumina and coke powders using a vortex shaker and a fluid-jet attrition tester

Somik Chakravarty<sup>1</sup>, Marc Fischer<sup>1,2</sup>, Miguel A. Romero Valle<sup>3</sup>, Olivier Le Bihan<sup>2</sup> and Martin Morgeneyer<sup>1</sup>

<sup>1</sup> *Laboratoire Transformations Intégrées de la Matière Renouvelable (TIMR), Université de Technologie de Compiègne (UTC) Sorbonne Universités, France*

<sup>2</sup> *Institut National de l'Environnement Industriel et des Risques (INERIS), NOVA/CARA/DRC/INERIS, Parc Technologique Alata, BP2, F-60550 Verneuil-En-Halatte, France*

<sup>3</sup> *BASF SE, Carl-Bosch-Straße 38, 67063 Ludwigshafen am Rhein, Germany*

#### 5.2.1 Abstract

The vortex shaker method is a relatively new technique for assessing the dustiness of fine powders which requires significantly smaller amounts of test powder (2 g) in comparison to other dust generation methods. The purpose of this study was to compare the dust generation behaviour while using the vortex shaker tester (1500 rpm, 2 g) and the Montecatini fluid-jet (F-jet) attrition tester (290 lph, 60 g) over 6 to 8 hours. Two powders were considered: acetylene coke ( $x_{50} = 271 \mu\text{m}$ ) and alumina ( $x_{50} = 112 \mu\text{m}$ ), which are referred to as C300 and P100, respectively. The changes in the powder properties (number fractions, volume fractions, circularity) and the dust mass released as a function of time were measured. In the case of C300, both testers cause a decrease in the percentage of particles bigger than  $240 \mu\text{m}$  and an increase in the percentage of particles smaller than  $240 \mu\text{m}$  and a decrease in the proportion of fines. The differences consist of smaller proportions of big particles and more evenly distributed intermediary size particles in the case of the F-jet tester whereas the VS leads to a higher increase in circularity and aspect ratio. The dust mass that is released is considerably higher in the case of the F-jet. As for P100, both testers lead to larger fractions of big particles (from  $80 \mu\text{m}$  for the VS and  $120 \mu\text{m}$  for the attrition bed) remaining in bulk and a decrease in those of smaller particles (between 30 and 60

um). The initial evolution of the dust generation rate is similar for the testers, but it rapidly decreases in the case of the VS whereas rises in the case of the F-jet. Our study indicates that the results of the two testers are not interchangeable and that they correspond to two different types of industrial situations.

### **5.2.2 Introduction**

Testing of powders is essential in industrial processing and to ensure smooth plant operation (Schulze, 2008; Svarovsky, 1987). Although there are many powder tests, this study focuses on two such tests; the dustiness test and the attrition test. Dustiness tests allow the assessment of a material's propensity to produce and emit dust upon handling, whereas attrition tests are used to evaluate the material life-time and material loss over time.

Dusts are small solid particles suspended in the air when separated from their bulk state due to mechanical stimulus (Dubey, Ghia, & Turkevich, 2017). Dust generation and suspension in an occupational setting may pose major challenges including the risk of inhalation of potentially hazardous dust (Brouwer, Links, Vreede, & Christopher, 2006), loss of valuable material, changes in material quality, contamination of plant equipment, and in some cases, dust can even cause fire and explosion (Cashdollar, 2000; Eckhoff, 2005; Turkevich, Dastidar, Hachmeister, & Lim, 2015). The dustiness of a powder depends on several factors, including the powder parameters, process specific parameters and operation time-scales (Liu, Wypych, & Cooper, 1999; Organization, 1999). Because of their complexity, the dustiness of a bulk material cannot yet be reliably predicted theoretically and needs to be measured using lab-scale dustiness testers (F. Hamelmann & Schmidt, 2004).

Similar to dustiness, handling or any kind of movement of particulate material results in some degree of attrition in particles. The effects of attrition can be loss of material, a need for recycling lost material, a required filtration system, the loss of flowability and environmental pollution due to the emission of dust (Bemrose & Bridgwater, 1987). Attrition in the form of the wearing, fracturing or chipping of particles can be initiated either when the applied stresses (impact, compression or

shear) overcomes the material's resistance to such causes of failure or when the stress loads are repeated and the material fails below the critical stress levels due to fatigue. There exists several attrition testers to characterize and assess the attrition of particulate matter that have been reviewed by (Bemrose & Bridgwater, 1987; Kalman, 2000) among others.

Dustiness testing of powders consists of generating and emitting dust from bulk, when the bulk is under some mechanical stimulus. It also involves characterization of the emitted dust by its size, concentration (mass or number), and other physico-chemical properties of the dust particles. The duration of dustiness tests lies anywhere between few seconds to several minutes and it is often selected based on the process or event time-scale. However, there is a lack of dustiness tests spanning over long durations and most dustiness studies consists of specific industrial cases which may last few seconds to minutes. But, a test duration of few minutes to an hour may not be enough to make a suitable prediction for applications running over several days to weeks, such as circulation of powder in a fluidized bed (Chakravarty et al., 2018). Unlike attrition test studies, there is only a limited knowledge of the underlying dust generation mechanisms involved when testing different materials over prolonged durations using different testing methods.

To facilitate the understanding of dust generation mechanisms involved over prolonged durations we use a vortex shaker (VS) [(Chakravarty, Fischer, et al., 2017; Le Bihan, Ustache, Bernard, Aguerre-Chariol, & Morgeneyer, 2014; Morgeneyer, Le Bihan, Ustache, & Aguerre-Chariol, 2013)] to test dustiness of alumina and acetylene coke powders. The vortex shaker is a relatively new dustiness tester, suitable for testing fine micro-scale powders using only 2g of test sample compared to 35 cm<sup>3</sup> or 500g of sample by the standardized dustiness testers (EN, 2006).

In this study, the vortex shaker test results obtained as total mass of the dust emitted as a function of time is compared to the mass of the dust emitted from the a fluidized bed attrition tester, also known as the Montecatini method (referred to F-jet tester in this study) (Schubert et al., 2012) using an alumina and an acetylene coke powder. Furthermore, the particle size distribution and particle shape properties of the pristine and tested samples are to analyse the differences between the two testers. The F-

jet technique is used for this study due to its wide application for mimicking powder stresses from long-term industrial processes such as FCC cracking.

Using the experimental results, we emphasize the need for long-term dustiness tests to evaluate the risk of dust exposure with application time. Additionally, the results can be used to evaluate the suitability of the vortex shaker as a small-scale attrition tester using a fraction of the powder sample used by the F-jet attrition tester.

### **5.2.3 Experimental method and test samples**

#### ***5.2.3.1 Powder dustiness tester: Vortex shaker***

There exists a wide range of dustiness testers including the air jet dispersion (Boundy, Leith, & Polton, 2006) and gas fluidization systems (Saleh et al., 2014; Sethi & Schneider, 1996), drop test (Cowherd, Grelinger, Englehart, Kent, & Wong, 1989; Dahmann & Monz, 2011), and the rotating drum (Schneider & Jensen, 2008)(Breum, 1999)(Chung & Burdett, 1994) (Jensen, 2012). Among these, the drop test and the rotating drum are the standard testers for measuring the dustiness of bulk materials according to EN 15051 (EN, 2006). But these testers need large amounts of powders (35 cm<sup>3</sup> or 500 g) (Morgeneyer et al., 2013; O'Shaughnessy, Kang, & Ellickson, 2012) and can give disparate results for industrial minerals (Pensis, Mareels, Dahmann, & Mark, 2010). Hamelmann and Schmidt's (F. Hamelmann & Schmidt, 2004) review of several dustiness testers shows the lack of comparability between the testers due to differences in the bulk sample and generation techniques, and thus a single standardized test is not suitable for all powders and applications. Furthermore, most of the testers mentioned have only been used for short time durations of less than 1 hour (HSE UK, 1996) and may not be representative of the dust generated from processes with longer durations (García-Triñanes, Seville, & Boissière, 2016).

The vortex shaker (VS) method (Chakravarty, Fischer, et al., 2017; Chakravarty, Le Bihan, Fischer, & Morgeneyer, 2017)(Le Bihan et al., 2014; Morgeneyer et al., 2013; Ogura, Kotake, Sakurai, & Gamo, 2012) is a relatively new and promising dust generation method capable of functioning with very small sample quantities of matter (around 2g). (Morgeneyer et al., 2013) and (Le Bihan et al., 2014) used the VS method to

test dust generation of micron-sized alumina particles and nanoscale carbon nano-tubes (CNTs) for one hour with sample mass as small as 0.5 g, respectively. (Morgeneyer et al., 2013) studied the minimum level of bulk mass and the optimum vortex speeds necessary to aerosolize micron-sized alumina particles. They report a minimum sample mass of 2 g and a vortex speed of 1,500 rpm – 1,800 rpm as suitable parameters for aerosolizing alumina particles without impacting the particle size distribution (PSD) of the powder. The VS setup also allows one to retrieve the used bulk sample after the end of the dustiness test for further analysis, but such results have not been reported in previous studies with the VS setup.

The VS was used for this study due to its low requirements of sample sizes, ease of operation and the ability to retain the powder sample after the test. The current setup uses the recommended specifications for powder mass (2 g) and vortex speed (1500 rpm) from (Morgeneyer et al., 2013) and is similar to (Chakravarty, Le Bihan, et al., 2017).

The setup consists broadly of 3 sections; generation, sampling, and measurement (Figure 5.1). Aerosol is generated from a powder-filled centrifuge test-tube (glass) mounted on a digital vortex shaker (VWR Signature Digital Vortex Mixer) rotated at 1500 rpm along the vertical axis. Clean filtered air (HEPA filtered dry air) is introduced from the top of the tube at 4.2 L/min or  $7e-05$  m<sup>3</sup>/s and an outlet, also situated on top of the tube draws out air containing aerosolized particles (also at 4.2 L/min).

Airborne dust particles were sampled using a BGI GK 2.69 respirable cyclone operated at 4.2 L/min with a cut-off point close to a particle aerodynamic size of 4  $\mu$ m at 50% sampling efficiency (Jensen, 2012). Particles with a larger size than the respirable size fraction fall into the grit pot and are weighed and characterized as coarse dust. The finer respirable fraction of aerosols released is diluted with 7.4 L/min ( $1.2e-04$  m<sup>3</sup>/s) of filtered air (HEPA) and split into 3 channels for measurement and characterization. The flow through the sampler was checked and calibrated prior to starting each experiment.

The aerosol concentration of the respirable dust is measured based on its size (0.54  $\mu$ m to 20  $\mu$ m, for unit particle density) using an aerodynamic particle sizer (APS TSI 3321, TSI Inc., Shoreview, MN) operating at 5 L/min. The APS aerosol mass concentration ( $C_{m,APS}$ , in mg/m<sup>3</sup>) and the aerosol mass ( $M_{Vortex}^{APS}$ ) are calculated using the



APS number concentrations ( $C_{n,APS}$ , in particles/cm<sup>3</sup>) for a given particle density, assuming spherical aerosol particles.

Since the mass of a particle is proportional to the cubic exponent of the diameter, the mass of such fine is assumed to have a relatively low effect on the total mass of the particles emitted during the tests. Although mass concentration is the most common form of dustiness test reporting, there is a growing interest in controlling and reducing the particle number concentrations of very fine respirable particles as studies suggest that number concentrations could be a better tool to indicate and predict potential health risks, when compared to mass concentrations (Donaldson, Stone, Clouter, Renwick, & MacNee, 2001; Oberdörster, 1995; Peters, Wichmann, Tuch, Heinrich, & Heyder, 1997). However, in this particular study aimed at *comparing* the two testers, we only considered the mass of the emitted dust as dustiness by number could only have been measured in the case of the VS but not in the case of the F-jet.

#### ***5.2.3.2 Powder attrition tester: Fluidized bed (F-jet) attrition tester***

A fluidized bed attrition tester (the Montecatini method) is used for this study which impinges a vertical gas jet from the bottom of an orifice plate to a bulk resting on top of the plate (Figure 5.10). The attrition test mimics the mechanical stresses subjected to the fluidized material to evaluate the attrition behaviour of the material, usually measured as proportion of fines generated.

A lab-scale fluidized bed (F-jet) apparatus similar to the one mentioned by (Schubert et al., 2012) was used for this study. The attrition apparatus comprised of an orifice plate, glass attrition tube, a steel settling tube, and a fines collector (filter paper thimble). Instead of compressed air, an inert gas (nitrogen) was used to minimize the risks of dust explosion (Klippel, Scheid, & Krause, 2013). The incoming gas flow is impinged vertically up through a single-orifice plate (diameter = 0.5 mm) contrary to the three-orifices in a plate according to the ASTM D5757 (ASTM, 2011). The orifice plate is attached to the bottom of the attrition glass tube (inner diameter of 30 mm) in a gastight and solids-tight manner. Also, a conical-widening settling tube (steel) is mounted and sealed on top of the glass tube. The combined height of the glass and seal tube is

about 800 mm. The fines collector used an extraction filter paper thimble (pore size: 10-15  $\mu\text{m}$ ) attached to the top of the steel tube bent to an angle of  $125^\circ$ . The clean gas flows out of the filter into the exhaust air system of the laboratory (1 bar,  $20^\circ\text{C}$ ).

The fluid entrains the particles in its flow field and particles are attrited mostly due to the collisions and shearing of particles with other particles and the wall (Bemrose and Bridgwater 1987). The key regions of attrition in the F-jet testers are the jetting region with high solid concentration and local velocity and the bubble induced region (Werther and Reppenhagen 1999). Furthermore, the key parameters affecting the attrition of particles in a fluidized bed tester are the particle properties, fluidization conditions and the bed structure parameters (Werther and Reppenhagen 1999).

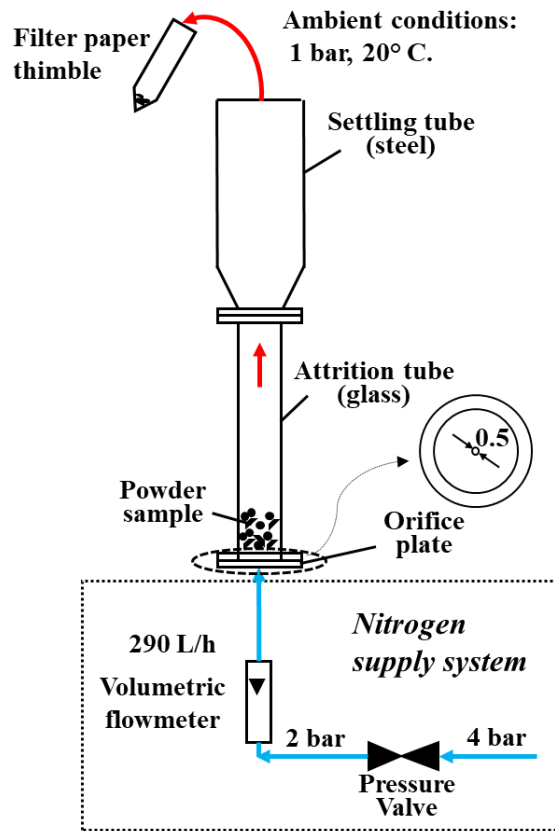


**Figure 5.10:** Schematic of the fluid-jet attrition tester.

Attrition can be broadly divided into two types, namely, particle surface abrasion and particle fragmentation (see Figure 5.11). Surface abrasion is often associated with material loss due to low energy shearing of particle surface, which leads to the production of daughter particles with dimensions much lower than those of the mother primary

particles. On the other hand, particle fragmentation is associated with high energy impaction owing to inter-particle and particle-wall collisions and the resultant daughter particles have sizes of similar order as those of the primary mother particles.

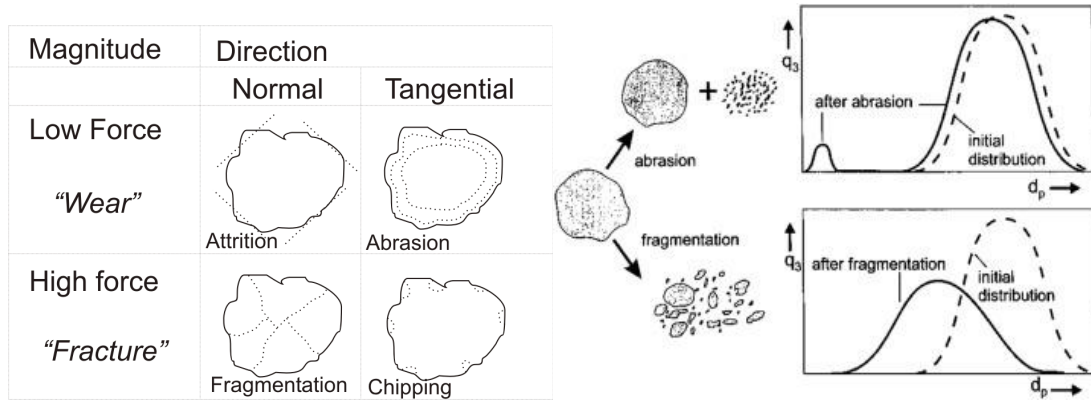


**Figure 5.11:** Particle attrition: (left) Breakage mechanisms, classified in normal and tangential forces and in low and high magnitude forces; (right) Effect of abrasion and fragmentation on the particle size ( $q_3 =$  mass density distribution of particle size  $d_p$ ) [Laarhoven et al. 2012 (left); Debras et al., 2016(right)]

An attrition process is time-dependent and can be divided into an initial non-steady state (with high attrition rate) followed by a steady state (with relatively low and stable attrition rate). The non-steady state is observed during the initial stages when using fresh powders whereas the attrition rate decreases and reaches a steady-state with time (Ray, Jiang, & Wen, 1987).

(Gwyn 1969) proposed an empirical model for predicting material loss (mass of fines) for a given sample mass over the attrition time ( $t$ ) based on jetting fluidized bed using silica-alumina cracking catalysts. The formulation uses a power law relation:

$$\frac{m_{fines,cumulative}}{m_{0,powder}} = K \cdot t^n \quad \text{Eq. (5. 13)}$$

where  $m_{fines,cumulative}$  is the cumulative mass (in kg or g) of the attrited fines,  $m_{0,powder}$  is the sample mass at  $t = 0$ ,  $K$  and  $n$  are constants related to test material, process conditions and the initial particle size of the test material.  $K$  reflects the attrition property at the initial stages of attrition, and is suggested to be related to the material properties and the fluidization conditions (Neil & Bridgwater, 1999). On the other hand, the exponent  $n$  is related to the attrition mechanism as suggested by (Gwyn, 1969; Neil & Bridgwater, 1999). The values for  $n$  were found to be between 0.43 and 0.90, based on

extensive attrition testing of different materials (Neil & Bridgwater, 1999). This rather simple expression assumes that particle attrition is only due to abrasion and it does not consider the fragmentation of the particles (Jones, Russell, Lim, Ellis, & Grace, 2017).

### 5.2.3.3 Powder sample: alumina and acetylene coke

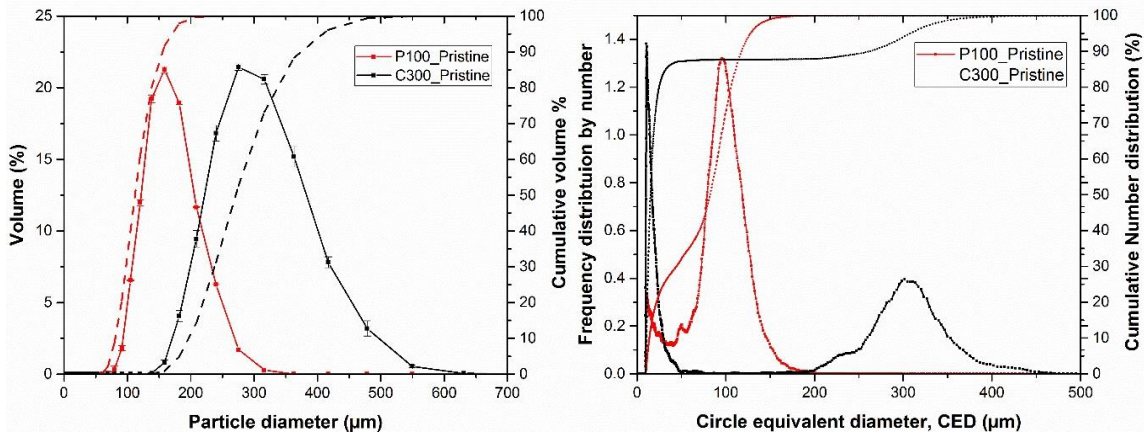


**Figure 5.12:** Particle size distribution by (a) Volume (b) number for P100 alumina powder (red) and C300 acetylene coke powder (black). Solid lines - distributive; Dotted lines – cumulative.

The tests powders, gamma-alumina ( $\gamma\text{-Al}_2\text{O}_3$ ) and acetylene coke (C) are extensively used in the industry as a catalyst and catalyst support in the automotive and petroleum industries (Oberlander, 1984) and as a recarburiser for the iron and steel industry (Gandy, 2007), respectively. Two sets of powders: alumina (Puralox 100/100 with  $x_{50} = 110 \mu\text{m}$ ) and acetylene coke (Carbolux  $\text{\textcircled{R}}$  with  $x_{50} = 274 \mu\text{m}$ ) were used for this study. The powders are commercially available from Sasol, Germany (alumina), and CS Additive, Germany and were used “as received” following the EN standard 15051 (CEN, 2006). We characterized the powder test samples for volumetric and number size distributions (Figure 5.12) by laser diffraction (Malvern Mastersizer 2000,  $0.01 \mu\text{m} - 10,000 \mu\text{m}$ ) (Sperazza, Moore, & Hendrix, 2004) and image analysis (Malvern Morphologi G3S,  $0.5\mu\text{m} - 1000\mu\text{m}$ ) (Ulusoy & Kursun, 2011), respectively. The particle density for the alumina and acetylene coke particles were measured using gas pycnometry (Micromeritics Accupyc II 1340) (Thakur, Ahmadian, Sun, & Ooi, 2014). The measurement results and the specific instruments and settings used for the measurements are mentioned in Table 5-4.

The volumetric particle size distribution analysis was carried out under wet dispersion conditions (using demineralized water) with the laser obscuration rate ranging from 5% to 17%, depending on the grain sizes of the samples. For number size distributions, the dry samples were prepared and dispersed at a gauge pressure of 1 bar and a minimum of 10,000 particles were measured for each sample following the guidelines from the Malvern G3s user manual (*Morphologi G3 User Manual*, 2008). The details have been mentioned in Section 0. Three trials were performed for each sample for both the laser diffraction and image analysis.

The volumetric size analysis shows C300 acetylene coke to have a greater range of particle sizes in comparison to P100 alumina with sizes ranging from 140  $\mu\text{m}$  to sizes in excess of 600  $\mu\text{m}$ . The PSD analysis of the samples by number (Figure 5.12 (b)) indicates bi-modality for both samples which is not evident from the PSD analysis by volume (Figure 5.12 (a)). With about 85% of the measured C300 particles below the size of 30  $\mu\text{m}$ , C300 shows a significantly high proportion of fine particles compared to P100 with only 26%. In addition, it is worth noting that unlike P100, C300 does not have particles of intermediate sizes between the fines and the largest particles.

**Table 5-4:** Powder properties of alumina and acetylene coke test samples.

Test sample	Units	Alumina P100/100	Acetylene coke C300
Particle density, $\rho_p$	kg/m <sup>3</sup>	3,247	1,823
PSD by volume			
$x_{10}$ (SD)	$\mu\text{m}$	81 (0.1)	200 (0.3)
$x_{50}$ (SD)	$\mu\text{m}$	115 (0.1)	275 (0.5)
$x_{90}$ (SD)	$\mu\text{m}$	164 (0.2)	376 (0.8)
Span [( $x_{90} - x_{10}$ )/ $x_{50}$ ]	-	0.72	0.64
PSD by number			
$x_{10}$ (SD)	$\mu\text{m}$	13.6 (0.34)	10.7 (0.3)
$x_{50}$ (SD)	$\mu\text{m}$	86.3 (5.7)	15.4 (0.5)
$x_{90}$ (SD)	$\mu\text{m}$	120 (4.2)	276 (5.4)
Span [( $x_{90} - x_{10}$ )/ $x_{50}$ ]	-	1.23	17.2

#### 5.2.3.4 Test protocol

A minimum of two trials were performed for each of the 3 powder samples using the vortex shaker and the F-jet tester. The powders were weighed and tested in their “*as received*” condition. The tests were carried out at room temperature (usually between 16 and 21 °C). In order to work safely while conducting the dustiness tests, all the experimental equipment were installed and operated under a closed isolator system protecting the operators from the dispersion of dust particles. The vortex shaker dustiness tests were performed at the Nanosecured (S-NANO) platform at the INERIS in France, whereas the F-jet attrition tests were performed at the attrition test labs at the BASF SE in Ludwigshafen, Germany.

The vortex shaker used 2 g of powder for each test, weighed with an accuracy of  $\pm 0.001$  g using an analytical balance (MS1003S, Mettler-Toledo, Inc., Columbus, OH, USA), and manually filled in a centrifuge glass tube (diameter 0.025 m, height 0.15 m). The sample-filled centrifuge tube was then mounted on the VS using a rubber cup to hold the tube firmly. Prior to starting the vortex shaker, the APS and CPC sampling were turned on along with the inlet flow (4.2 L/min) and dilution flow (7.4 L/min) for 2 minutes. The background values of the aerosols released with the VS in the absence of rotation was usually lower than the detection limit of the APS (0.1 particles/cm<sup>3</sup>) and CPC (0.2 particles/cm<sup>3</sup>). Thus the inlet air flow is only used to transport the aerosols generated through the vortex motion and does not influence the generation of dust particles in the system.

The VS was operated at 1500 rpm and was run for six hours to test the powder samples, with a short break of 5 minutes after every hour to avoid the overheating of the electric motor. Since the air flow is not interrupted, the peaks in the dustiness variables are entirely due to the mechanical action of the vortex shaker. Each test was analyzed as an individual case.

The F-jet attrition tester used 60 g of sample manually introduced into the apparatus (Schubert et al., 2012). A flow of 290 L/hour of nitrogen was fed to the powder to fluidize the powder samples. The filters (extraction thistles) were weighed before starting the experiment and the mass of the attrited fines as a function of time was determined through successive weighing after every hour, rather than weighing after one

hour and after 5 hours as mentioned by (Schubert et al., 2012). The cumulative mass of the fines generated  $m_{F-jet,cum}$  is then calculated for each test case. The tester was cleaned by fluidizing the 60g of the same sample powder for 10 minutes before performing the actual experiment. After the cleaning, that mass was disposed off. The tester was given an occasional knock to make the small quantity of fines which adhered to the walls of the attrition tube fall down on the powder bed.

The tested powder (and the fines adhering to them and to the wall) collected from the VS and the F-jet testers were gathered in sealed glass bottles and characterized before and after the test for changes in PSD by volume and number using the same characterization equipment as in Section 5.2.3.2, i.e. the laser diffraction particle sizer instrument (Malvern Mastersizer 2000) (Sperazza et al., 2004) and the static image analyser (Morphologi G3s) (Ulusoy & Kursun, 2011) using the same test protocol. In addition to PSD by number, the image analysis also allowed for the characterization of particle shape properties such as aspect ratio and circularity.

The static image analysis used a magnification of 5x and 10x with a 5-megapixel CCD camera to enable the digital analysis of individual particle sizes and shapes for the alumina and coke particles. The analysis captures a 2D image of a 3D particle and calculates various size and shape parameters of the 2D image such as the circle equivalent diameter (CED), aspect ratio (AR) and circularity (Morphologi G3 User Manual, 2008). In the Morphologi instrument, the major and the minor axes pass through the centre of mass of the object perpendicular to each other, with the major axis oriented such that it corresponds to minimum rotational energy of the shape. Out of all possible lines between two points on the perimeter, the length is defined as the largest distance projected onto the major axis, whereas the width is the largest distance projected onto the minor axis.

Assuming that particles are spherical, the CED is defined as the diameter of the circle with the same surface area as the projected area of the particle (BS 2955:1993, 1993), as defined in Eq. 5.14:

$$CED = \sqrt{\frac{4 \times A}{\pi}} \quad (\text{Eq. 5.14})$$

where, A is the particle area.

The shape parameters, aspect ratio (AR) and circularity (ISO 9276-6:1998(E), 1998) are defined as: The shape parameters, aspect ratio (AR) and circularity (ISO 9276-6:1998(E), 1998) are defined as:

$$AR = \frac{width}{length} \quad \text{Eq. (5.15)}$$

$$Circularity = \sqrt{(4\pi \times A)/(Perimeter)^2} \quad \text{Eq. (5.16)}$$

The AR values varies from approaching zero for very elongated particles to near unity for equiaxed particles. Circularity, on the other hand indicates the degree of roundness of the particles when compared to a perfect circle according to Eq. 5.16. A perfect circle has a circularity of unity whereas an irregularly shaped object has a value closer to 0.

## 5.2.4 Results and discussion

### 5.2.4.1 Acetylene coke C300

#### 5.2.4.1.1 Characterization of particle size distributions of the samples

The changes in particle size distributions of the samples before and after the testing can indicate the attrition mechanisms (Ghadiri, Ning, Kenter, & Puik, 2000; Wu & Wu, 2017; Zhao, Goodwin, & Oukaci, 1999). Particles fragmented due to breakage are associated with major differences in the PSD (by size and by volume) of the powders tested before and after the attrition test, as revealed by  $x_{10}$ ,  $x_{50}$  and  $x_{90}$ . On the other hand, the abrasion of particles is associated with few to no changes in  $x_{10}$ ,  $x_{50}$  and  $x_{90}$  as the daughter particles generated are fines which are much smaller than the mother particles. However, the PSD shifts towards a bi-modal size distribution. We analysed the PSD by volume (laser diffraction) as well as the PSD by number (image analysis) for understanding the effects of attrition on the tested samples. The volume analysis is shown in such a way that changes in volume fractions for certain particle sizes can be compared whereas the mean particle sizes for the samples are mentioned in Table 5-5.

For both the VS and F-jet experiments, sample C300 shows an increase in volume fraction by up to 1 to 4% for particle sizes smaller than approximately 240  $\mu\text{m}$  and there



is a similar decrease in volume fraction for particles greater than this threshold size (Figure 5.13a). There is almost no change in the fraction of particles greater than 500  $\mu\text{m}$ , possibly due to the lower presence of such particles during the tests. Also, they may be too heavy to be moved around within both the VS and the F-jet testers. Interestingly, the minimum particle sizes present in the bulk after the testing are seen for the samples tested with the F-jet tester, which although not clearly visible in Figure 5.13a, is confirmed using the results from image analysis of the tested samples.

Figure 5.13b shows multi-faceted changes. In comparison to the pristine, the proportion of fines (up to 20  $\mu\text{m}$ ) is smaller in the samples after the VS and F-jet tests. The percentages of particles having a size between 50  $\mu\text{m}$  and 260  $\mu\text{m}$  are higher for the tested particles. The proportions of particles having sizes between 260  $\mu\text{m}$  and 320  $\mu\text{m}$  are higher for the vortex shaker but lower for the F-jet. The percentages of particles higher than 320  $\mu\text{m}$  is lower for both tested powders, whereby the F-jet tester shows the lowest portions.

The decrease in the fraction of fines is similar for both devices and can be readily attributed to dust leaving the tester. The proportion of particles having intermediary sizes (between 50  $\mu\text{m}$  and 260  $\mu\text{m}$ ) in the pristine is small. Its increase in the tested sample can be interpreted as the result of the breakage of larger particles.

Moreover, the sizes of the powder particles observed after the F-jet test are more evenly distributed than those of the powder particles after the VS test (Figure 5.13b). Stresses applied by the VS and the F-jet are not similar and may affect their size reduction process. The initial breakage of particles may be similar for both testers as it usually occurs with a relatively small amount of forces, and produces only a few daughter particles, which may be due to chipping (also referred to as cleavage in the literature) (Meesters & Hennart, 2014). Later, the newly formed particles (fragments) go through a new active stage of attrition which further reduces their size, based on the stresses applied by the testers. The newer daughter particles with exposed rough surfaces may further attrite either due to abrasion or fragmentation, or a combination of both. This cycle of generation of newer daughter particles will continue until a critical particle size is reached when particle crack density reduces such that its breakage probability reduces (Tavares & King, 1998). Thus the attrition process in C300 is a complex process which includes the chipping, fragmentation and abrasion of particles. Only the smaller-sized

fines generated from abrasion are collected as dust going out of the VS and the F-jet testers. The "flatter" PSD observed with the F-jet tester could be attributed to a greater number of collisions. Those higher cyclic stresses can account for the fact that the proportions of particles having sizes between 260  $\mu\text{m}$  and 320  $\mu\text{m}$  are lower in the case of the F-jet. In the case of the vortex shaker, it is possible that the weaker cyclic stresses only affect particles higher than 320  $\mu\text{m}$ , thereby producing daughter particles between 80  $\mu\text{m}$  and 320  $\mu\text{m}$ .

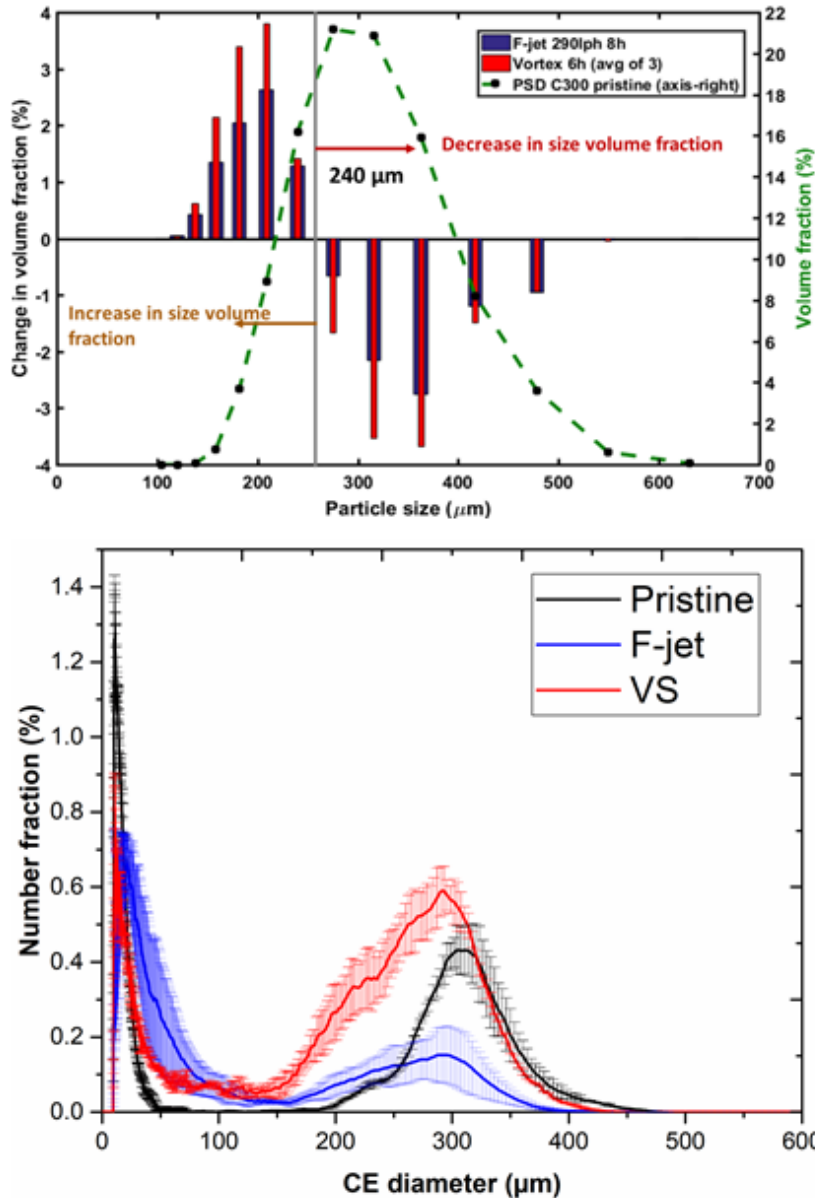


Figure 5.13: C300 - a) Change in volume fraction by size after 8-h of F-jet test (blue, bar graph) and 6-h of vortex shaker test (red, bar graph), with pristine PSD (green, dotted line graph) shown as reference. b) Number size distribution of the pristine and tested samples using the F-jet and the VS testers.

Table 5-5: Particle size and shape properties of C300 particles from image analysis.

<b>Powder samples</b>	<b>Mean CE diameter (SD) in <math>\mu\text{m}</math></b>	<b>Circularity Mean, Max. 1 (SD)</b>	<b>Aspect ratio Mean, Max. 1 (SD)</b>
Pristine powders	55.2 (5.4)	0.87 (0.02)	0.66 (0.01)
VS tested (6h)	94.1 (10)	0.90 (0.01)	0.70 (0.02)
F-jet tested (8h)	44.1 (7.7)	0.89 (0.01)	0.67 (0.00)

In Table 5-5, the mean CE diameter of the VS tested sample increases compared to the pristine sample, whereas for the F-jet tested sample the mean CED undergoes a decrease. This is consistent with the results from Figure 5.13b, where samples from the F-jet and VS tested samples have similar portions of fines, but the VS tested samples shows higher portions of bigger particles.

The particle morphology of the tested samples is characterized by their mean circularity and aspect ratio. The tested samples show a slight increase in circularity and aspect ratio compared to their pristine state, but the VS tested samples show a greater increase when compared to the F-jet. This might be due to the abrasion of particles which is known to reduce the roughness of the surfaces (Laarhoven, Schaafsma, & Meesters, 2012). It may possibly be due to the differences in the type of forces generated by the VS and F-jet testers. The abrasion of particles in the VS tester may be stronger than in the F-jet due to the higher shearing of particles when compared to the non-rotating vertically impinging F-jet tester.

#### 5.2.4.1.2 Dust emission from acetylene coke expressed as mass

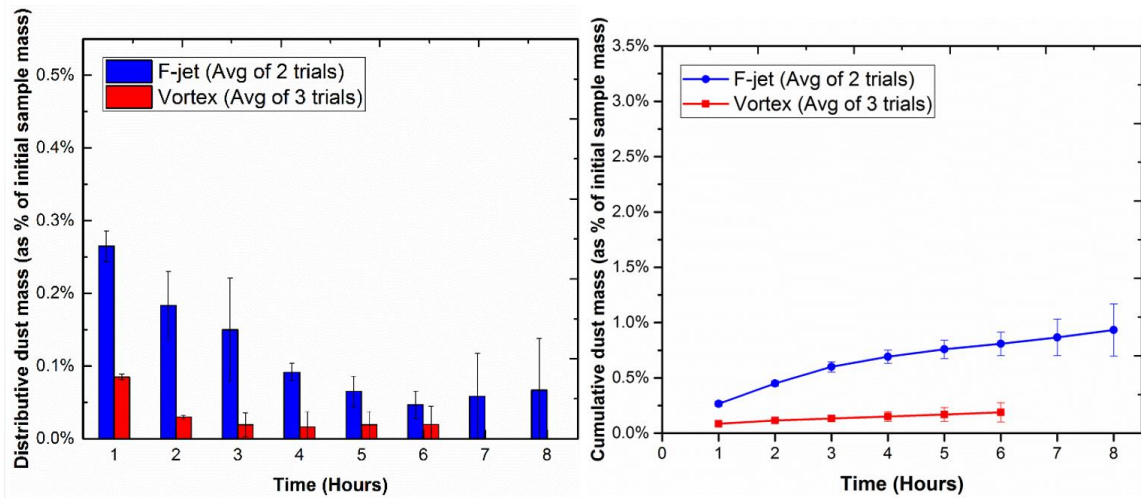


Figure 5.14: C300: Distributive and Cumulative dust mass (as % of the initial powder mass) generated by the F-jet attrition tester (blue) and the vortex shaker tester (red). Error bars show the standard deviations of the repeated trials.

The differences in the emissions from the vortex shaker dustiness tester and the F-jet attrition tester have been studied by measuring the total mass of emitted dust. The 6-hour VS tests were repeated 3 times. For the F-jet tester, the samples were tested for 8 hours and the trial was repeated once. The average values and standard deviations are calculated and shown in Figure 5.14.

For the first six hours of testing, the F-jet releases 4.2 more dust per unit of sample mass than the VS tester.

C300 is characterized by a maximum release of dust per unit of sample mass during the first hour of testing (Figure 5.14). The released mass decreases for both the VS and the F-jet but the values are considerably higher in the latter case. As time goes by, the C300 dust mass emitted by the vortex shaker tends to approach a steady state whereas for the F-jet tester it does not (slight increase for 7th and 8th hour).

Our experimental results shows differences in evolution of dust mass with time for the VS and the F-jet tester, possibly due to differences in their attrition behaviour. The cumulative mass of dust released displays a nonlinear trend and the power law correlation (Gwyn, 1969) shown in (Eq. 5.13) appears to fit our experimental data reasonably well (Figure 5.15). The constant  $K$  indicates the initial attrition rate which is considerably

higher in the case of the F-jet tester (0.315, average of 2) than in the case of the VS (0.083, average of 3), as seen in Table 5-6. Given the very high standard deviations, only limited conclusions about the attrition mechanism can be drawn about the values of the exponent  $n$ . The values for  $n$  were smaller than 1, which suggests that the production of attrited fines decreases with time, so that a steady state is reached.

The fitting of the Gwyn relationship to our experimental data shows no clear indications of a dominant attrition mechanism.

According to the basic assumption of the relationship, only abrasion takes place (Jones et al., 2017; Knight, Ellis, Grace, & Lim, 2014) and this could account for those specific data. However, the results of subsection 3.1 can only be explained if fragmentation of particles also occurs.

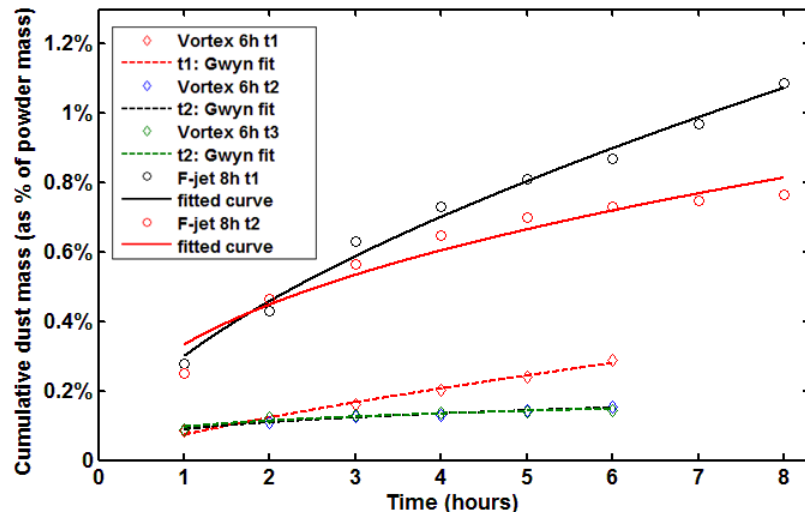


Figure 5.15: Parameters of fitting Eq. (5.13) (Gwyn, 1969) to the attrition data from C300.

Table 5-6: Fitting of Eq. (5.13) to the experimental data for C300 sample using F-jet and VS testers

Tester	Trial	Attrition time, $t$ (hours)	Eq. (5.13): Fitted parameters		
			K	$n$	$R^2$
<b>F-jet</b>	1	6	0.15	1.35	0.99
	2	8	0.25	1.22	0.99
<b>VS</b>	1	6	0.22	0.62	0.96
	2	6	0.32	0.51	0.99
	3	6	0.42	0.59	0.99

### 5.2.4.1.3 Conclusion

Our results indicate that the volume fractions of the particles tested using the VS and the F-jet tester shows changes up to 4% for sizes less than 500  $\mu\text{m}$ . While particles greater than 240  $\mu\text{m}$  show a decrease in volume fraction, a similar increase is observed for particles inferior to 240  $\mu\text{m}$ .

The number size analysis of the powders tested with the F-jet and the VS tester shows a decrease in fines (up to 20  $\mu\text{m}$ ), possibly due to dust emissions when compared to pristine particles. Furthermore, the fractions of bigger particles (greater than 320  $\mu\text{m}$ ) were found to be lower and the portions of intermediary size ranges (50  $\mu\text{m}$  and 260  $\mu\text{m}$ ) shows an increase for the samples tested with both the testers.

While there are some similarities between the F-jet and the VS testers using the acetylene coke C300 sample, but there are also important differences between the testers.

The samples tested with the F-jet tester shows lower proportions of bigger particles and more evenly distributed intermediary size particles when compared to the samples from the VS tester. The released mass decreases for both the VS and the F-jet but the values are considerably higher in the latter case. Furthermore, the tested samples show a slight increase in circularity and aspect ratio compared to their pristine state, but the VS tested samples show a greater increase when compared to the F-jet.

The differences in sample attrition from the F-jet and the VS tester testers may stem from the differences in magnitude and type of stresses applied by the two testers. With higher number of collisions, and stronger normal forces due to the impinging jet, the F-jet tester shows higher prominence in breakage of particles which may relate to testing of powders in a fluidized bed (F. Hamelmann & Schmidt, 2004). On the other hand abrasion of particles in the VS tester may be stronger than in the F-jet due to the higher shearing of particles when compared to the non-rotating F-jet tester, which is representative of processes which require tangential movement of particles.

## 5.2.4.2 Alumina P100

### 5.2.4.2.1 Characterization of particle size distributions of the samples

Figure 5.16 shows the changes in the particle number fraction after the tests. For both the vortex shaker and the attrition bed test, we can see a decrease between 30 and 60  $\mu\text{m}$  (that is more pronounced in the case of the VS) and an increase for the higher diameters (from 80  $\mu\text{m}$  for the VS and 120  $\mu\text{m}$  for the attrition bed). The most likely explanation is that the smaller particles aggregated with bigger ones, thereby increasing their size.

Figure 5.16 shows the change in volume fraction for P100 tested with the vortex shaker and the F-jet tester. In both cases, the changes are very small (not significantly higher than 1%), which mean they might be artefacts rather than genuine trends. This impression is reinforced by the lack of consistency between the results after 6 hours and 8 hours of bed attrition bed. For particle sizes around 100  $\mu\text{m}$ , the change in volume fraction is of 1.5% after 6 hours but of only 0.1% after 8 hours. A measurement uncertainty artefact seems more plausible than the powder completely reverting its trend away from the pristine state. Consequently, unlike C300, the changes in volume fraction are too small to be reliably interpreted.

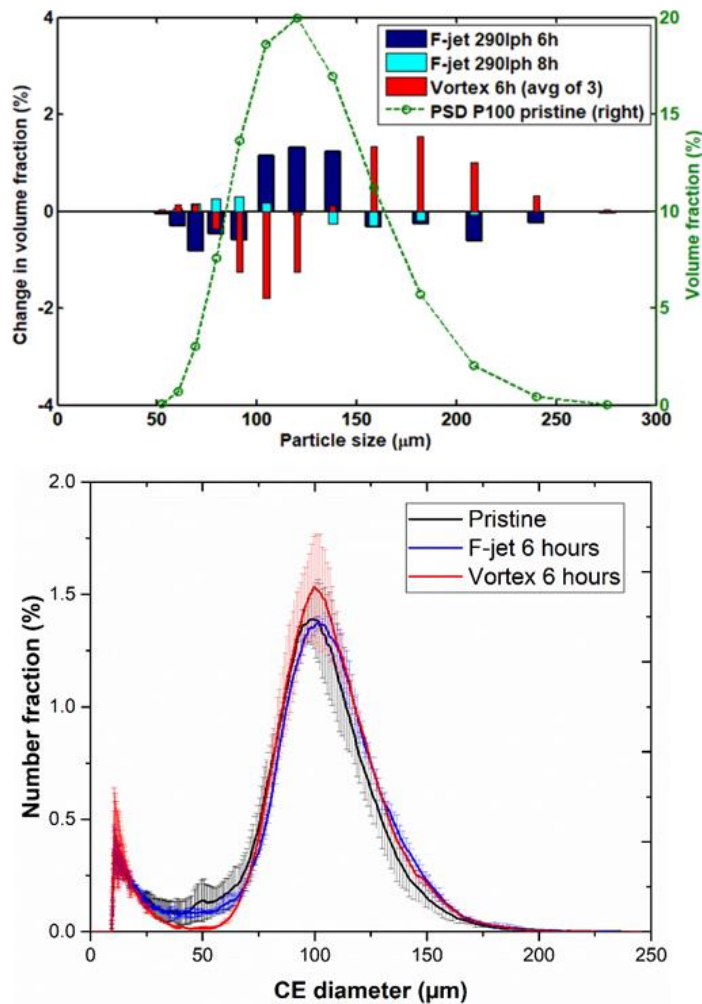


Figure 5.16: P100 – a) Change in volume fraction by particle size for Alumina P100 sample after the 6-h F-jet test (blue, bar graph), 8-h F-jet test (cyan, bar graph) and 6-h vortex shaker (red, bar graph), with pristine PSD (green, dotted line graph) is shown as reference. b) Number size distribution of the pristine (black) and tested samples after 6-h VS (red) and 6-h F-jet (blue) tests.

#### 5.2.4.2.1 Dust emission from alumina expressed as mass

The differences in the emissions from the vortex shaker dustiness tester and the F-jet attrition tester have been studied by measuring the total mass of emitted dust. The 6-hour VS tests were repeated 3 times. For the F-jet tester, while the P100 samples were tested twice with durations of 6 and 8 hours.

Figure 5.17 shows the distributive and cumulative dust mass generated by the VS and the F-jet. P100 is characterized by similar magnitudes of fines released at the first and the second hour and a strong decrease thereafter, so far as the VS is concerned. The



fluidization bed follows a different, much more irregular trend. The emitted dust mass tends to oscillate but it clearly increases on average, with the higher values being found at the 7-th and 8-th hour (repeated once for 8 hours) as shown in Figure 5.18. Dust emissions from the VS gradually decreases to a stable state but on the contrary, the emissions from the F-jet shows an increase after the initial 2 hours of testing and reach their highest value towards the seventh and eighth hour.

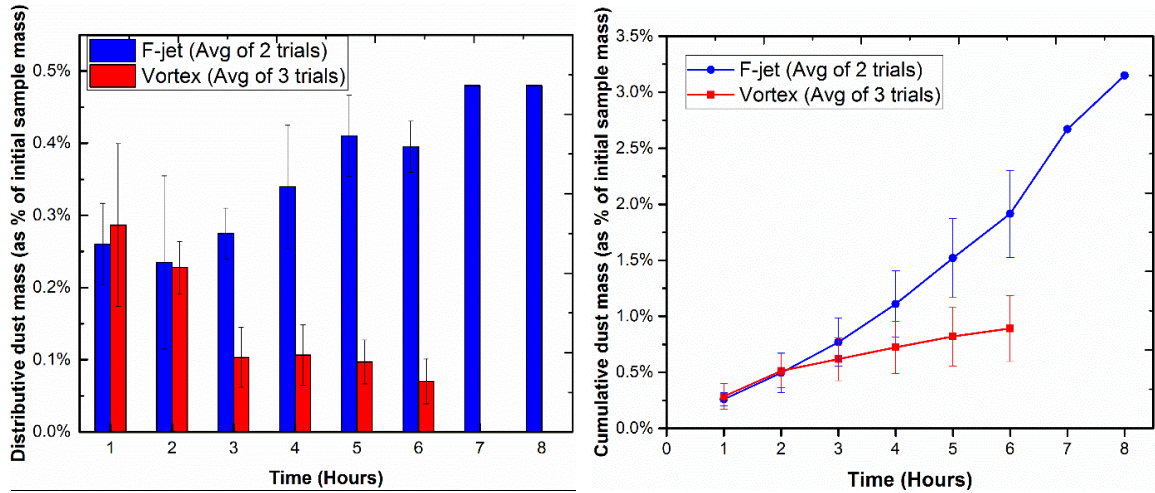


Figure 5.17: P100: Distributive and Cumulative dust mass (as % of the initial powder mass) generated by the F-jet attrition tester (blue) and the vortex shaker tester (red). Error bars show standard deviations of the repeated trials.

Table 5-7 shows the coefficients of the power law correlation (Gwyn, 1969)

$$\frac{m_{fines,cumulative}}{m_{0,powder}} = K \cdot t^n$$

Eq. (5.13) fitted to the evolution

of cumulative dust mass over the test duration (Figure 5.18). The power coefficient  $n$  is higher than 1 in the case of the F-jet, thus reflecting an increase in the generation rate.

Table 5-7: Fitting of Eq. (5.13) to the experimental data for P100 sample using F-jet and VS testers.

Tester	Trial	Attrition time, t (hours)	Eq. (5.13): Fitted parameters		
			K	n	R <sup>2</sup>
F-jet	1	6	0.15	1.35	0.99
	2	8	0.25	1.22	0.99
VS	1	6	0.22	0.62	0.96
	2	6	0.32	0.51	0.99
	3	6	0.42	0.59	0.99

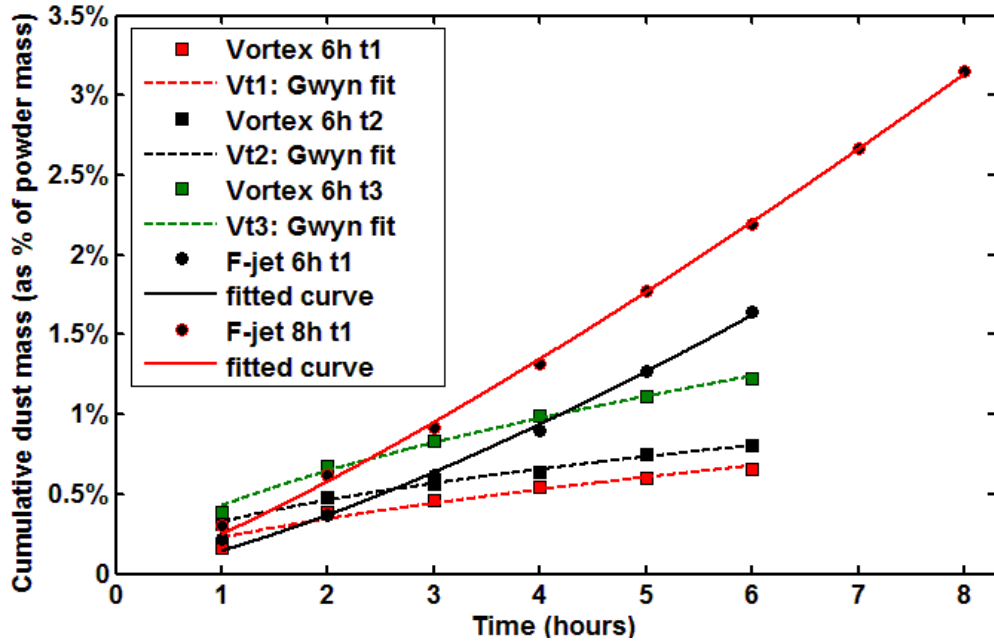


Figure 5.18: Parameters of fitting Eq. (5.13) (Gwyn, 1969) to the attrition data from P100.

#### 5.2.4.2.3 Conclusion

So far as the evolution of the powder properties are concerned, the use of P100 does not lead to significant differences between the vortex shaker and the F-jet attrition tester so far as the evolution is concerned. For both testers, the change in the number fractions consists of a shift to the right which probably reflects the agglomeration of smaller particles to bigger ones. The results of the volume fraction analysis are within the measurement uncertainties so that they cannot be reliably exploited.

However, both testers lead to different dust release trends as a function of time. While dust emission quickly decrease in the case of the VS, they increase in the case of the F-jet. This might be due to differences in powder mass (available particle surface area for abrasion) and the differences in the mechanical stressing of the powder.

### 5.2.4 Summary and outlook

In this study, we focused on comparing the vortex shaker dustiness shaker and the fluid jet attrition tester and only considered two types of powder, namely acetylene coke

referred to as C300 and alumina referred to as P100. In Section 2, we presented the dustiness testers along with the powder properties. In Section 3, we compared the VS and the F-jet with respect to the differences between the pristine and the tested powder and dust emission expressed as mass. We wanted to determine if the vortex shaker which requires lower quantities of powder can possibly replace the fluid jet attrition tester despite the fact that they correspond to two different types of process conditions.

In the case of C300, both testers lead to a decrease in the proportion of particles larger than 240  $\mu\text{m}$  reflecting an increase in the proportion of particles smaller than 240  $\mu\text{m}$  and to a decrease in the percentage of fines that are probably emitted out of the respective testers. The testers differ in that the F-jet tester displays smaller percentages of larger particles and more evenly distributed intermediary size particles in comparison to the samples from the VS tester. The VS tests also lead to a greater increase in circularity and aspect ratio. The released dust mass is considerably higher in the case of the F-jet.

In the case of P100, both tests lead to a higher proportion of larger particles (from 80  $\mu\text{m}$  for the VS and 120  $\mu\text{m}$  for the attrition bed) at the expense of smaller particles (between 30 and 60  $\mu\text{m}$ ). However, the evolution of the dust release rate is different. While it shows similar values for the initial 2 hours, the dust emissions quickly decreases in the case of the VS, whereas it increases in the case of the F-jet. Such a difference can have important industrial consequences.

While the vortex shaker and the attrition bed lead to some similar trends, our study indicate that the results are not interchangeable. As a consequence, it does not appear to be possible to predict the results of using one system from the results of using the other. As (Frank Hamelmann & Schmidt, 2003) pointed out, the physical features of the tester are an intrinsic part of dustiness. The VS and the F-jet represent two different kinds of dust generation tools. The appropriate tester needs to be chosen as a function of the industrial situation one is facing.

Therefore, this shows that the results of the vortex shaker dustiness tester and the fluidized jet attrition tester are not equivalent and thus the two testers correspond to different applications in industry.

## 5.2.5 References

ASTM. (2011). ASTM D5757-11: Standard Test Method for Determination of Attrition of FCC Catalysts

- by Air Jets. Philadelphia, United States.
- Bemrose, C. R., & Bridgwater, J. (1987). A review of attrition and attrition test methods. *Powder Technology*. [http://doi.org/10.1016/0032-5910\(87\)80054-2](http://doi.org/10.1016/0032-5910(87)80054-2)
- Boundy, M., Leith, D., & Polton, T. (2006). Method to Evaluate the Dustiness of Pharmaceutical Powders, *50*(5), 453–458. <http://doi.org/10.1093/annhyg/mel004>
- Breum, N. O. (1999). The Rotating Drum Dustiness Tester : Variability in Dustiness in Relation to Sample Mass , Testing Time , and Surface Adhesion, *43*(8), 557–566. [http://doi.org/http://dx.doi.org/10.1016/S0003-4878\(99\)00049-6](http://doi.org/http://dx.doi.org/10.1016/S0003-4878(99)00049-6)
- Brouwer, D. H., Links, I. H. M., Vreede, S. A. F. D. E., & Christopher, Y. (2006). Size Selective Dustiness and Exposure ; Simulated Workplace Comparisons. *Annals of Occupational Hygiene*, *50*(5), 445–452. <http://doi.org/10.1093/annhyg/mel015>
- BS 2955:1993. (1993). *Glossary of terms relating to particle technology*. London, England.
- Cashdollar, K. L. (2000). Overview of dust explosibility characteristics. *Journal of Loss Prevention in the Process Industries*, *13*(3–5), 183–199. [http://doi.org/10.1016/S0950-4230\(99\)00039-X](http://doi.org/10.1016/S0950-4230(99)00039-X)
- Chakravarty, S., Fischer, M., García-Triñanes, P., García-Triñanes, P., Parker, D., Le Bihan, O., ... Morgeneyer, M. (2017). Study of the particle motion induced by a vortex shaker. *Powder Technology*, *322*, 54–64. <http://doi.org/10.1016/j.powtec.2017.08.026>
- Chakravarty, S., Le Bihan, O., Fischer, M., & Morgeneyer, M. (2017). Dust generation in powders: Effect of particle size distribution. In *EPJ Web of Conferences* (Vol. 140, p. 13018). EDP Sciences. <http://doi.org/10.1051/epjconf/201714013018>
- Chung, K., & Burdett, G. (1994). Dustiness testing and moving towards a biologically relevant dustiness index. *Annals of Occupational Hygiene*. Retrieved from <http://annhyg.oxfordjournals.org/content/38/6/945.short>
- Cowherd, C., Grelinger, M. A., Englehart, P. J., Kent, R. F., & Wong, K. F. (1989). An apparatus and methodology for predicting the dustiness of materials. *American Industrial Hygiene Association Journal*, *50*(3), 123–130. Retrieved from <http://www.tandfonline.com/doi/abs/10.1080/15298668991374408>
- Dahmann, D., & Monz, C. (2011). Determination of dustiness of nanostructured materials. *Gefahrstoffe - Reinhaltung Der Luft*, *71*(11–12), 481–487. Retrieved from [http://www.bgrci.de/fileadmin/BGRCI/Microsites/IGF/Publ\\_1\\_Determ\\_dust\\_nanostruct\\_mat.pdf](http://www.bgrci.de/fileadmin/BGRCI/Microsites/IGF/Publ_1_Determ_dust_nanostruct_mat.pdf)
- Donaldson, K., Stone, V., Clouter, a, Renwick, L., & MacNee, W. (2001). Ultrafine particles. *Occupational and Environmental Medicine*, *58*(3), 211–216, 199. <http://doi.org/10.1136/oem.58.3.211>
- Dubey, P., Ghia, U., & Turkevich, L. A. (2017). Computational fluid dynamics analysis of the Venturi Dustiness Tester. <http://doi.org/10.1016/j.powtec.2017.02.030>
- Eckhoff, R. (2005). Current status and expected future trends in dust explosion research. *Journal of Loss Prevention in the Process Industries*. Retrieved from <http://www.sciencedirect.com/science/article/pii/S0950423005000756>
- EN, C. (2006). EN 15051 Workplace atmospheres—measurement of the dustiness of bulk materials—requirements and test methods. *Brussels, Belgium: European Committee for Standardization*. Retrieved from <http://shop.bsigroup.com/ProductDetail/?pid=000000000030123370>
- Gandy, D. (2007). Carbon Steel Handbook. *Carbon*, *3*(3), 172. <http://doi.org/1014670>
- García-Triñanes, P., Seville, J., & Boissière, B. (2016). Hydrodynamics and particle motion in upward flowing dense particle suspensions: Application in solar receivers. *Chemical Engineering*. Retrieved from <http://www.sciencedirect.com/science/article/pii/S0009250916301105>
- Ghadiri, M., Ning, Z., Kenter, S. J., & Puik, E. (2000). Attrition of granular solids in a shear cell. *Chemical Engineering Science*, *55*(22), 5445–5456. [http://doi.org/10.1016/S0009-2509\(00\)00168-8](http://doi.org/10.1016/S0009-2509(00)00168-8)
- Gwyn, J. E. (1969). On the particle size distribution function and the attrition of cracking catalysts. *AIChE*

- Journal*, 15(1), 35–39. <http://doi.org/10.1002/aic.690150112>
- Hamelmann, F., & Schmidt, E. (2003). Methods of Estimating the Dustiness of Industrial Powders – A Review. *KONA Powder and Particle Journal*, 21(21), 7–18. <http://doi.org/10.14356/kona.2003006>
- Hamelmann, F., & Schmidt, E. (2004). Methods for characterizing the dustiness estimation of powders. *Chemical Engineering and Technology*, 27(8), 844–847. <http://doi.org/http://dx.doi.org/10.1002/ceat.200403210>
- HSE UK. Health and Safety Laboratory, Methods for the determination of hazardous substances 81 (MDHS)—dustiness of powders and materials (1996). UK.
- ISO 9276-6:1998(E). (1998). Representation of results of particle size analysis – Part 6: Descriptive and quantitative representation of particle shape and morphology. Geneva: International Organization for Standardization.
- Jensen, K. A. (2012). *Towards a method for detecting the potential genotoxicity of nanomaterials. D4.6: Dustiness of NANOGENOTOX nanomaterials using the NRCWE small rotating drum and the INRS Vortex shaker*. Copenhagen, DENMARK. Retrieved from [www.nanogenotox.eu](http://www.nanogenotox.eu)
- Jones, T. J., Russell, J. K., Lim, C. J., Ellis, N., & Grace, J. R. (2017). Pumice attrition in an air-jet. *Powder Technology*, 308, 298–305. <http://doi.org/10.1016/j.powtec.2016.11.051>
- Kalman, H. (2000). Particle breakage and attrition. *KONA Powder and Particle Journal*, 18(May), 108–120. <http://doi.org/10.14356/kona.2000017>
- Klippel, A., Scheid, M., & Krause, U. (2013). Investigations into the influence of dustiness on dust explosions. *Journal of Loss Prevention in the Process*. Retrieved from <http://www.sciencedirect.com/science/article/pii/S095042301300154X>
- Knight, A., Ellis, N., Grace, J. R., & Lim, C. J. (2014). CO2 sorbent attrition testing for fluidized bed systems. *Powder Technology*, 266, 412–423. <http://doi.org/10.1016/j.powtec.2014.06.013>
- Laarhoven, B. van, Schaafsma, S., & Meesters, G. M. H. (2012). Toward a desktop attrition tester; validation with dilute phase pneumatic conveying. *Chemical Engineering Science*, 73, 321–328. Retrieved from <http://www.sciencedirect.com/science/article/pii/S0009250911006075>
- Le Bihan, O. L. C., Ustache, A., Bernard, D., Aguerre-Chariol, O., & Morgeneyer, M. (2014). Experimental Study of the Aerosolization from a Carbon Nanotube Bulk by a Vortex Shaker. *Journal of Nanomaterials*, 2014, 1–11. <http://doi.org/10.1155/2014/193154>
- Liu, Z., Wypych, P., & Cooper, P. (1999). Dust generation and air entrainment in bulk materials handling - a review. *Powder Handling and Processing*, 11(4).
- Meesters, G. M. H., & Hennart, S. L. A. (2014). Increased Antimicrobial Activity of Cheese Coatings Through Particle Size Reduction. In H. Merkus & G. Meesters (Eds.), *Particulate Products. Particle Technology Series* (pp. 429–463). Springer, Cham. [http://doi.org/10.1007/978-3-319-00714-4\\_15](http://doi.org/10.1007/978-3-319-00714-4_15)
- Morgeneyer, M., Le Bihan, O., Ustache, A., & Aguerre-Chariol, O. (2013). Experimental study of the aerosolization of fine alumina particles from bulk by a vortex shaker. *Powder Technology*, 246, 583–589. <http://doi.org/10.1016/j.powtec.2013.05.040>
- Morphologi G3 User Manual*. (2008) (MAN0410 Is). Malvern Instruments Ltd. United Kingdom.
- Neil, A. U., & Bridgwater, J. (1999). Towards a parameter characterising attrition. *Powder Technology*, 106(1–2), 37–44. [http://doi.org/10.1016/S0032-5910\(99\)00064-9](http://doi.org/10.1016/S0032-5910(99)00064-9)
- O’Shaughnessy, P. T., Kang, M., & Ellickson, D. (2012). A Novel Device for Measuring Respirable Dustiness Using Low-Mass Powder Samples. *Journal of Occupational and Environmental Hygiene*. <http://doi.org/10.1080/15459624.2011.652061>
- Oberdörster, G. (1995). Lung particle overload: implications for occupational exposures to particles. *Regulatory Toxicology and Pharmacology: RTP*, 21(1), 123–135. <http://doi.org/10.1006/rtph.1995.1017>
- Oberlander, R. K. (1984). Applied Industrial Catalysis. *Academic Press*, 3, 63–113. <http://doi.org/10.1016/B978-0-12-440201-0.50015-1>

- Ogura, I., Kotake, M., Sakurai, H., & Gamo, M. (2012). Emission and exposure assessment of manufactured nanomaterials. English Version.(26 October 2012). NEDO project (P06041)“Research and. Retrieved from <https://en.aist-riss.jp/assessment/2721/>
- Organization, W. H. (1999). Hazard prevention and control in the work environment:: airborne dust. Retrieved from <http://apps.who.int/iris/handle/10665/66147>
- Pensis, I., Mareels, J., Dahmann, D., & Mark, D. (2010). Comparative evaluation of the dustiness of industrial minerals according to European standard en 15051, 2006. *Annals of Occupational Hygiene*, 54(2), 204–216. <http://doi.org/10.1093/annhyg/mep077>
- Peters, A., Wichmann, H. E., Tuch, T., Heinrich, J., & Heyder, J. (1997). Respiratory effects are associated with the number of ultrafine particles. *American Journal of Respiratory and Critical Care Medicine*, 155(September 1990), 1376–1383. <http://doi.org/10.1164/ajrccm.155.4.9105082>
- Ray, Y. C., Jiang, T. S., & Wen, C. Y. (1987). Particle attrition phenomena in a fluidized bed. *Powder Technology*, 49(3), 193–206. [http://doi.org/10.1016/0032-5910\(87\)80128-6](http://doi.org/10.1016/0032-5910(87)80128-6)
- Saleh, K., Moufarej Abou Jaoude, M. T., Morgeneyer, M., Lefrancois, E., Le Bihan, O., & Bouillard, J. (2014). Dust generation from powders: A characterization test based on stirred fluidization. *Powder Technology*, 255, 141–148. <http://doi.org/10.1016/j.powtec.2013.10.051>
- Schneider, T., & Jensen, K. A. (2008). Combined Single-Drop and Rotating Drum Dustiness Test of Fine to Nanosize Powders Using a Small Drum. *Annals of Occupational Hygiene*, 52(1), 23–34. <http://doi.org/10.1093/annhyg/mem059>
- Schubert, O., Sesing, M., Seidemann, L., Karches, M., Grassler, T., & Sohn, M. (2012, April 24). Mechanically stable catalyst based on alpha-alumina. Google Patents.
- Schulze, D. (2008). *Powders and Bulk solids. Behavior, Characterization Storage and Flow*. Springer.
- Sethi, S. A., & Schneider, T. (1996). A gas fluidization dustiness tester. *Journal of Aerosol Science*, 27, S305–S306. [http://doi.org/10.1016/0021-8502\(96\)00225-X](http://doi.org/10.1016/0021-8502(96)00225-X)
- Sperazza, M., Moore, J. N., & Hendrix, M. S. (2004). High-Resolution Particle Size Analysis of Naturally Occurring Very Fine-Grained Sediment Through Laser Diffractometry. *Journal of Sedimentary Research*, 74(5), 736–743. <http://doi.org/10.1306/031104740736>
- Svarovsky, L. (1987). *Powder testing guide. Methods of Measuring the physical properties of bulk powders*.
- Tavares, L. M., & King, R. P. (1998). Simple-particle fracture under impact loading. *International Journal of Mineral Processing*, 54(1), 1–28.
- Thakur, S. C., Ahmadian, H., Sun, J., & Ooi, J. Y. (2014). An experimental and numerical study of packing, compression, and caking behaviour of detergent powders. *Particuology*, 12, 2–12. <http://doi.org/10.1016/j.partic.2013.06.009>
- Turkevich, L. A., Dastidar, A. G., Hachmeister, Z., & Lim, M. (2015). Potential explosion hazard of carbonaceous nanoparticles: Explosion parameters of selected materials. *Journal of Hazardous Materials*, 295, 97–103. <http://doi.org/10.1016/j.jhazmat.2015.03.069>
- Ulusoy, U., & Kursun, I. (2011). Comparison of different 2D image analysis measurement techniques for the shape of talc particles produced by different media milling. *Minerals Engineering*, 24(2), 91–97. <http://doi.org/10.1016/j.mineng.2010.05.011>
- Wu, F., & Wu, D. (2017). Attrition resistances and mechanisms of three types of FCC catalysts. *Powder Technology*, 305, 289–296. <http://doi.org/10.1016/j.powtec.2016.09.077>
- Zhao, R., Goodwin, J. G., & Oukaci, R. (1999). Attrition assessment for slurry bubble column reactor catalysts. *Applied Catalysis A: General*, 189(1), 99–116. [http://doi.org/10.1016/S0926-860X\(99\)00261-6](http://doi.org/10.1016/S0926-860X(99)00261-6)

## 6 Conclusion

Dust particles from industrial operations presents serious health hazards in an occupational setting. The risks of dust exposure to a worker depends on several factors including the physico-chemical properties of the dust particles and the bulk from which the dust is released, the process conditions and the ambient conditions of the workplace. Due to the complex interaction of multiple parameters, theoretical understanding of dustiness is not trivial and currently relies on experimental measurement using dustiness testers.

This thesis presents an overview of the progress made in domain of dust generation from powder handling in industries using experimental and numerical methods. Based on a series of experimental tests related to characterization of powders and their dust generation behaviour, the thesis analyses the role of inter-particle forces and material properties on the dust generation behaviour and proposes possible dust generation mechanisms for different time-scales.

Chapter 2 highlights the key mechanisms involved with dust generation from bulk materials and the influence of several powder parameters affecting dust generation. Chapter 3 delves into the characterization of powder bulk properties such as cohesion and flowability of powders based on the inter-particle forces for particle sizes ranging over two orders of magnitude. The dustiness tests of the powders show that the dust generation behaviour is influenced by the particle size distribution, and the measured bulk cohesion and flowability. Chapter 4 shows the development and application of a methodology to study the generation mechanisms of dust particles on a particle level using the PEPT particle tracking method. It also investigates the role of powder and tester parameters on the solid motion inside a dustiness tester which eventually leads to dust generation and emission. Chapter 5 sheds light on the importance of long-term dustiness tests for assessing the dust generation pattern and mechanisms involved for powder applications which prolong over weeks or months. Furthermore, attrition mechanism of a lab-scale vortex tester is compared with a pilot-scale attrition tester to evaluate the suitability of the vortex shaker as an attrition tester in addition to a dustiness tester.

Section 6.1 summarizes the conclusions drawn from the previous sections and sub-sections pertaining to the objectives of thesis defined in Section 1.2.

### **6.3 Key parameters influencing dust generation from bulk: identification and characterization**

On a fundamental level, dust is generated when the separation forces from powder handling and processing overcomes the binding forces between the particles in bulk. These forces are influenced by several parameters and an extensive literature review enabled to identify key powder parameters and understand how they influence the binding forces, thus influencing dust generation in powders. We identified 10 key parameters including sample mass, particle size and size distribution of the sample, moisture content, bulk density, particle shape, flowability, cohesion, attrition strength, and the application time-scale. The relationship between each one of the parameters and dustiness is not trivial as each parameter shows a different degree of correlation with dustiness, but also among each other.

The effect of particle size and size distribution influences the bulk cohesion, or the inter-particle binding forces due to the van der Waal forces which are the dominant force acting on dry fine powders. Increase in median particle size  $d_{50}$  (Figure B.5) shows an inverse relation with measured bulk cohesion values while the powder flowability increases linearly with increasing  $d_{50}$  (Figure B.6) for the powders studied in Section 3.2. Dustiness, on the other hand, increases with increasing  $d_{50}$  but for powders with  $d_{50} > 10 \mu\text{m}$ , an increasing fraction of fine particles (measured as  $d_{10}$ ) shows a tendency to emit such fine particles as dust.

As reported in literature, bulk density of the powder leads to unsystematic effects, it can either leads to an increase or decrease of dust emissions. In our studies using dry calcium carbonate powders (Chapter 3), bulk density shows an increase with particle size. Increasing particle size reduces the cohesive forces (van der Waals) between the primarily particles which leads to the breakage of particle clusters and reduction in voids in the bulk, thus increasing bulk density. Since bulk density changes during a dustiness test, a real-time analysis of change in bulk density with time can shed further light on its influence on dustiness.



Particle shape was shown to influence dust generation process, especially for the long-duration tests (for the silicon carbide particles, Section 5.1). Higher values of the sphericity or circularity of the powder particles tend to reduce its dustiness. The irregularly-shaped particles are possibly more fragile due to the increase in stress concentrations at the sharp edges during the inter-particle and particle-wall interactions during powder applications. The breakage process is more evident for larger particles as they tend to contain higher number of faults (micro-cracks and other imperfections) in their surface and a higher surface area for the particle interactions compared to the smaller sized particles. For long-term duration, abrasion of particles, removal of shape edges from the particle surfaces tends to increase the sphericity of the particles.

#### **6.4 Selection of experimental setup: vortex shaker dustiness tester**

The vortex shaker tester has been used as the dustiness test for this thesis study due to its prudent use of test material reducing the cost and risks of dustiness testing. The lower requirement for test powder makes it is a promising tester suitable for fine powders, especially nanopowders. The ability of the experimental setup to retain the tested powder after the dustiness test allows the user to evaluate changes in the physical properties of the sample material after testing.

The experimental methodology developed during this study is capable of testing almost all fine powders with a wide range of test parameters including the air/fluid flow rates, rotational speed (stresses) and time duration which can be tuned to be representative of the actual conditions of an industrial operation.

While the respirable fraction of the dust particle emissions were sampled for this study, the vortex tester setup allows easy integration with interchangeable cyclones to sample inhalable and thoracic fractions of dust. The combination of APS and CPC were found to be suitable for determining the respirable dustiness by number and mass for all the powders tested during the thesis with particle median sizes ranging from 2  $\mu\text{m}$  to 275  $\mu\text{m}$ . The powder mass of 2 g and a vortex speed of 1500 rpm were enough to measure the respirable aerosols within the lower and upper bounds of the APS and the CPC.

The number and mass dustiness indices of powders have been interchangeably used for different studies to compare dustiness from different powder samples. While number dustiness index might be more useful to determine the risks from very fine powders, such as nanopowder, a combination of the two indices is recommended for further studies.

The mini-particle-sampler (MPS®) used to capture aerosol dust particles for off-site transmission electron microscope (TEM) analysis can provide physical and chemical characteristics of the emitted dust particles which can aid their emission risk analysis. Furthermore, shape analysis of the emitted dust particles can also provide evidence of the generation mechanism, for example, attrition in the generation of respirable aerosols from silicon carbide particles (as seen in Section 5.1).

### **6.3 Physical mechanisms of dust generation process: role of inter-particle and particle-wall interactions**

Since dust generation from bulk is due to complex set of inter-particle, particle-wall and particle–fluid interactions, the PEPT (Positron Emission Particle Tracking) method was used to understand the nature and magnitude of such influences at the particle-scale. Results from the PEPT analysis (Chapter 4) are necessary to comprehend and to be able to predict the movements of the powder primary particles agitated due to the stresses exerted by the vortex shaker. Section 4.1 introduces a statistical methodology developed to study the particle motion filtering out the experimental noise and validates the methodology using standard conditions (vortex speed 1500 rpm, sample mass 2 g) for the vortex shaker test. Section 4.2 uses the methodology to study the influence of powder mass, the size of the tracer particle, the air flow and the rotation speed on the particle's movements.

The motion of the tracer particle has a cyclical shape with a period close to 1 s. The particles reach their steady-state levels within the initial few seconds of starting the vortex shaker. In the steady-state, valuable data including the population densities, frequency of abrupt changes in direction and distribution of particle velocities and kinetic energy of the particles were obtained from the analysis.

The particle motion shows symmetric normal distributions for position and velocity in the radial direction (horizontal coordinates  $x$  and  $z$  in Chapter 4) due to the centrifugal forces from the periodic rotation of the vortex shaker. The distribution for the vertical velocity  $V_y$ , on the other hand, is not symmetric and skewed towards the negative ( $y$ ) values due to the gravitational forces. The greatest particle velocities are found near the inner wall of the test tube and at the highest heights where the stresses exerted by the walls onto the particles are maximum and the population densities are the lowest, respectively. The particles tend to rise at the middle of the test tube at low speeds while descending near the walls much more rapidly. Besides the gravity, the higher values of the velocity might stem from a decrease in the number of shocks due to lower population densities.

Increasing the powder mass (and thereby the powder bed height) tends to increase the heights reached by the particle and to decrease its velocity  $V$ . At 1000 rpm and 1500 rpm, the  $V$  values are more than two times higher for 2 g than for 4 g but it has an insignificant effect at 2000 rpm. Increase in sample mass is also associated with a higher proportion of sharp angles, which may stem from the greater particle concentration and thus an increased number of particle collisions in the gas phase.

Increasing the size of the tracer particle raises the velocity and the population density in the horizontal axis (towards the wall) while it leads to lower upward and downward velocity (axial direction). Increasing the size leads to a relatively higher velocity  $V$ , much stronger kinetic energy  $E$  and a larger number of sharp angles.

Higher rotation speeds leads to transfer of more energy to the smaller tracer particle (in 2 g) used for the study which allows it to reach greater heights with larger velocities in the vertical axis (axial direction). In the horizontal (radial) direction, the population densities slightly narrows down towards the centre and the horizontal velocities  $|V_x|$  and  $|V_y|$  increase till 1500 rpm before decreasing. The fraction of sharp angles slowly increases till 2000 rpm followed by a rapid increase for 2500 rpm, as can be expected with highly agitated system of powders at 2500 rpm.

The air flow rate considered for the experiments were found to be too low to have any observable effect on the particle's motion but it can be expected to affect the motion with increasing flow rate, which needs to be studied.

Although the results have been obtained for a finite set of experimental conditions as described in Chapter 4, they are perfectly capable of subsequent use for the calibration and validation of numerical models (CFD and DEM) models.

## **6.4 Time-evolution of dust generation processes: mechanisms and applications**

Results from Section 3.2, 5.1 and 5.2 show that the mechanisms not only depends on powder and tester parameters but also the overall time-scale of the test event. For short-time durations, particle size distribution plays an important role determining the dust release mechanism as the dust is formed due to the direct release of particles separated from the bulk. Dustiness of fine cohesive powders show a correlation with median particle size ( $x_{50}$ ) of the powder. The smaller the primary particles, the more cohesive the powder and lower the dust emissions from the bulk. Bi-modal powders with similar flowability but different  $x_{50}$  show similar dustiness behaviour with the powder consisting of largest fraction of particles (by volume) in the 1<sup>st</sup> mode (particularly in the respirable fraction) releases the maximum dust particles. Powders made of larger primary particles may emit dust due to the attrition of large primary particles which depends both on time and the presence of impurities in the sample.

Regarding powder tests prolonging over long durations, two dust generation mechanisms were identified explaining the dust generation behaviour for the silicon carbide, alumina and acetylene coke powder samples tested over 6-hours (Section 5). While at the start of the test the particle size distribution, especially the presence of aerosolizable fine-scale particles in the bulk determines the initial dustiness but with time, the resistance of a bulk material to attrition (fragmentation and abrasion) determines the pattern and level of its dust generation along with the changes in physical characteristics of the powder over time.

For long duration, dustiness of hard particles such as silicon carbide and alumina particles are influenced by surface abrasion which is associated with production and emission of fine-scale daughter particles due to low energy shearing of larger primary particles. The median particle size and shape of the particles influences the abrasion

behaviour of powders as relatively larger and sharply shaped fresh particles show higher levels of dust emissions and an inclination towards becoming rounder (increasing in circularity and aspect ratio) by shedding angular corners through inter-particle and particle-wall collisions. On the contrary, the less dusty particles are smaller in size and retains its circularity and aspect ratio through the test duration. Thus, powders with smaller particle sizes and more circular shapes generate less fines than powders with larger irregular-shaped primary particles.

Relatively larger and fragile acetylene coke powders show signs dust emission through particle fragmentation in addition to abrasion as the resultant daughter particles have sizes of similar order as those of the primary mother particles. Fragmentation of particles is associated with high energy impaction owing to inter-particle and particle-wall collisions.

While the mass of the dust emissions from the vortex shaker dustiness and the attrition test using a fluid-jet bed lead to some similar trends for the alumina and acetylene coke samples, our study indicate that the results are not interchangeable. The differences in sample attrition from the fluid-jet and the vortex tester testers may stem from the differences in magnitude and type of stresses applied by the two testers. With higher number of collisions, and stronger normal forces due to the impinging jet, the fluid-jet tester shows higher prominence in breakage of particles which may relate to testing of powders in a fluidized bed. On the other hand abrasion of particles in the vortex tester may be stronger than in the F-jet due to the higher shearing of particles when compared to the non-rotating fluid-jet tester, which is representative of processes which require tangential movement of particles. Thus the vortex shaker and the fluid-jet testers represents two different applications in industry and the appropriate tester needs to be chosen as a function of the industrial situation one is facing.

## 7 Perspectives

### 7.1 Other parameters which influence dust generation from bulk

This thesis evaluated the most relevant bulk and particle properties which influences the dust generation process in dry powders. There are relatively few studies related to the interactions of dust generation with the different powder properties (such as the PSD, shape, cohesion/flowability etc.) and with a significant number of dustiness testers currently available, it is often difficult to isolate the effects of the tester/process properties on dust generation, and focus on powder parameters.

While van der Waals forces dominate the inter-particle binding forces in dry powders, capillary forces cannot be disregarded for hydrophilic powders. Moisture in powders increases capillary forces between the particles which also increases the binding forces and formation of solid and liquid bridges can further increase the binding forces and thus strongly reduce dustiness.

The effect of electrostatic forces on dust generation is not well understood and they can be important in dust generation from non-conductive materials such as polymers where the static build-up can affect the particle interactions and thus dustiness. The effect is even more pronounced for powder handling in dry ambient conditions. While many dustiness test methods use measures to minimize electrostatic charging, such as removing excess charge build-up in tester by grounding or using conductive tubes for dust particle transportation, but the severity of the electrostatic effects on dustiness and the effectiveness of such measures to reduce electrostatic effects are not known.

With the exception of increasing moisture content in the bulk material, dust remediation strategies are often overlooked in the literature as the conventional dustiness studies focus on estimation of powder dustiness to design and implement containment strategies. But increasing moisture content may not be suitable for materials which react with water or in the case of dry material processes in industry. Modification on the particle surface can be a useful dust remediation technique which can potentially reduce dustiness of powders. For example, a thin (in nm) core-shell coating of relatively softer

and elastic material like aluminium oxide on hard and brittle materials such as silicon carbide particles can change the nature of the collisions between particles while keeping the particle size, shape and density of the material close to its original state. The change in nature of the particle collisions can help reduce the dust generation. Further works are planned to analyse the effect of thin coating on particle surfaces on the physical properties of the material and its effect on dustiness due to changes in inter-particle, particle-wall and particle fluid interactions.

## **7.2 Dustiness tests and testers**

Dustiness tests of powders has traditionally been related to quantifying the mass or mass concentration of the emitted aerosol particles from a specified amount of bulk stressed using a specific amount of mechanical force. The test results barely reflect the intricate physical processes involved from stressing of bulk to separation and generation of dust at the particle-level.

Dustiness index of a powder has conventionally been reported as mass of the dust particles emitted per unit sample mass, however this methodology might not be sufficient in assessing the exposure risks from very fine dust particles such as nano-scale particles (below 100 nm) as their toxicological effect based on physico-chemical characteristics is not fully understood. Thus, emission of such fine-scale dust particles warrants evaluation of their dustiness by number, in addition to mass dustiness.

The dust generation patterns and dustiness levels are both important descriptors of dust generation mechanisms, but while dustiness levels are usually reported in literature the generation patterns are often overlooked. The patterns can potentially be used for more accurate dustiness exposure assessments for specific processes depending on whether the dust is generated during the initial few moments of operation or whether it is continuously released over a prolong duration.

Process parameters from the industrial operations and their effect on powders are often difficult to match with the parameters in the lab. Thus, there is a need for case studies which deals with comparing and eventually optimising lab-scale test conditions to representative of the actual process conditions.

There is a lack of studies related to relatively new dustiness testers (such as the vortex shaker) which can potentially reduce the cost and risks involved with powder testing. With increasing use of nano-scale powders, the powder quantity available for testing can be expensive and its toxicity can be unknown. As a consequence, it can be expected that such testers will be increasingly used over the years to come.

The materials used for this thesis study, while extensive for a study of this size may not be representative of all granular material. Furthermore, quality and reproducibility of results are key aspects for proper material dustiness. Significant scatter in measurements is still common when testing powder dustiness using different testers in different labs/environments. While European research projects like T-MAPPP enabled focusing on this problem by enabling creation of a database consisting of powders and their properties, a larger sample size should hypothetically lead to more accurate or representative results. Similar to the experimental studies performed on the existing powder characterization (shear) testers (in Section 3.1), a round-robin tests of the dustiness testers can greatly benefit determining the quality and reproducibility of the test results.

### **7.3 Characterization of powder**

Many dustiness studies suffer from a lack of independent characterisation tests for the test powders, instead rely on the data provided by the manufacturer which may not be accurate due to changes in material quality during batch production or during transportation. Dust generation analysis based on incorrect material properties can severely undermine their theoretical value and may lead to inefficient dust containment strategies.

Measurement of yield loci, flowability and cohesion for zero or very low normal stresses is not possible using most of the existing shear testers including the Jenike and Schulze ring shear testers. Thus their values for little or no normal stress conditions, often true for non-consolidated bulk samples in a dustiness tester cannot be accurately measured.



While it is assumed that dustiness affects the material quality, there are very few studies which characterizes the powder samples after the dust release from powders. While this thesis study highlights the changes in particle size distribution and shape of particles due to dustiness testing, further studies are required to assess other physico-chemical properties of the tested material to fully understand the changes associated with dustiness and their impact on processes.

The size and shape of particles plays a great role in powder flow and dustiness. While the volumetric size analysis using laser diffraction offers quick and repeatable measurement of the particle size distribution, it may not be suitable for bi-modal powders with the presence of fine particles which may be overlooked or in the case where particle shapes significantly differ from perfect spheres. Number distributions based on static image analysis provides far more measurement options including shape properties suitable for measuring particle with different shapes and the ability to measure fines in bi-modal powders compared to volumetric size analysis. However, the small sample size and long test duration limit its ability to be used independently for all applications. Dynamic image analysis may offer fast determination of particle size and shape for a far larger sample size than static image analysis, however, the measurements from the dynamic analysis may not be reliable using cohesive materials which tend form agglomerates of random size and shape due to interparticle forces between the primary particles.

## **7.4 Approaches towards development of predictive models for material dustiness**

Understanding the physical factors responsible for dustiness and development of predictive models permitting numerical predictions is extremely important as this could greatly diminish the cost of powder testing, and may offer the ability to engineer particles with low dustiness at the design stage.

Section 2.4 illustrates the approaches towards development of predictive modelling of the dust generation process based on the forces subjected to the test material at the particle-level. They include cohesive forces (e.g. Van der Waals forces, capillary

forces etc.) and the mechanical forces (due to the inter-particle and particle-wall) as well hydrodynamic forces due to the particle- fluid interactions.

The simplicity and computationally frugal nature of the empirical models may be of interest but they are only valid for the relatively narrow domain in which the coefficients have been fitted to measurements. Thus they may not be suitable for a wide range of powders or test methods or conditions thus limiting their predictive ability.

Numerical methods such as computational fluid dynamics (CFD) and discrete element method (DEM) are promising methods which can enable reliable predictions for a much wider range of conditions because they are grounded on the real laws underlying powder and fluid dynamics. CFD is widely used in solving fluid mechanical problems over a wide range of applications even for scale large industrial operations. The main disadvantage of CFD models is that they do not address surface forces such as cohesion forces in particles including the van der Waals forces, electrostatics and the capillary forces, which play a crucial role in the dust generation process.

DEM models treat the bulk solid as a system of distinct interacting bodies. It simulates interaction of particles under stresses and can provide an insight into overall bulk response. The details of contact and adhesion forces for each interparticular contact can be considered since contact forces are particularly important for cohesive powders, thus resolving the issue faced by the CFD modelling. However, DEM fails to take into account the particle-fluid interactions which can play an important role in the behaviour of smaller primary particles and aerosols released as dust.

A possible solution could be the combining the CFD description of the fluid flow with the DEM modelling of particles obeying Newton's laws including the cohesion and the separation forces acting upon the powder's particles. Such a combination is referred to as DEM-CFD simulations. Both CFD and CFD-DEM are extremely expensive in terms of computational power.

Future works are planned to use the CFD-DEM method to evaluate and compare the features of the particle movement inside the vortex shaker using previous PEPT results (Chapter 4).

## 8 Appendices

### 8.1 Appendix A: Supplementary data for section 3.1

#### 8.1.1 Test details on yield locus and steady state locus

**Table A-1:** Summary of pre-shear/shear normal stress values used in each shear device to measure yield locus.

Device	Samples	Normal stress applied (kPa)
RST-01	Eskal 300, 500, 15, 30, 80, 150, K0.1–0.5	Pre-shear at 5 Shear at 0.5, 1, 1.5, 2, 3
	Eskal 300, 500, 15, 30, 80, 150, K0.1–0.5, K0.5–0.8	Pre-shear at 20 Shear at 2, 5, 8, 12, 16
	Eskal 300, 500, 15, 30, 80, 150, K0.1–0.5	Pre-shear at 35 Shear at 2, 5, 10, 15, 20
RST-XS	Eskal 300, 500, 15, 150	Pre-shear at 4.3 Shear at 0.35, 0.85, 1.4, 2.1, 3.6
DST	Eskal 300, 500, 15, 150	Pre-shear at 36.1 Shear at 1.4, 13.9, 19.4, 25, 30.5
FT4	Eskal 300, 500, 15, 150	Pre-shear at 20 Shear at 0.1, 0.5, 1, 2, 5, 8, 16
Jenike	Eskal 300, 150	Pre-shear at 5 Shear at 0.5, 1.5, 3

**Table A-2:** Summary of normal stress values applied using direct shear tester (DST) to measure steady state locus.

Samples	Normal stress applied (kPa)
Eskal 300, 500, 15, 150	1.4, 2.8, 4.2, 5.5, 6.9, 8.2, 9.6, 11, 12.3, 13.9, 19.4, 25, 30.5, 36.1
Eskal K0.1–0.5	13.9, 36.1
Eskal K0.5–0.8	13.9, 19.4, 25, 30.5, 36.1

## 8.1.2 Test results of all the powders and devices shown in this paper

**Table A-3:** Data measured from RST-01 for several Eskal powders and different pre-shear stresses.

Device	Sample	$d_{50}$	$\sigma_{pre}$	$c$ (kPa)	$\sigma_1$ (kPa)	$\sigma_c$ (kPa)	$\rho_b$	$\phi_e$ (°)	$\phi$ (°)	$\phi_{ss}$ (°)
RST-01	K0.5–0.8	938	5	0.08	11.49	0.33	1288.00	41.37	40.5	38.97
			20	0.23	45.77	0.51	1275.67	42.53	42.3	40.30
			35	0.06	88.49	0.27	1299.67	42.30	42.2	41.20
	K0.1–0.5	223	5	0.33	9.47	1.33	1463.33	40.37	37.0	35.87
			20	0.45	39.23	1.82	1506.00	38.67	37.6	35.90
			35	0.58	70.17	2.33	1531.67	38.60	37.8	36.27
	Eskal150	138	5	0.01	8.53	0.06	1386.00	32.93	32.2	31.00
			20	0.10	35.34	0.31	1392.33	33.33	33.17	31.37
			35	0.21	66.07	0.19	1400.33	33.93	33.8	31.67
	Eskal80	71	5	0.08	8.88	0.31	1319.33	34.43	32.8	31.87
			20	0.07	35.02	0.25	1341.67	33.10	32.9	31.10
			35	0.19	63.9	0.68	1356.33	32.77	32.5	31.53
	Eskal30	30	5	0.09	8.83	0.31	1309.67	33.03	32.17	31.37
			20	0.14	34.84	0.49	1331.00	33.07	32.7	31.00
			35	0.20	62.20	0.74	1342.00	32.67	32.4	31.07
	Eskal15	19	5	0.21	9.44	0.82	1247.00	36.73	34.6	34.13
			20	0.34	37.08	1.23	1257.67	35.77	34.9	33.77
			35	0.42	64.34	1.31	1262.00	35.13	34.6	33.00
	Eskal500	4.42	5	0.86	10.47	3.25	1011.33	44.43	36.3	39.53
			20	1.76	39.45	5.44	1157.67	39.87	35.70	36.60
			35	1.97	67.79	6.17	1190.00	39.33	37.2	36.03
Eskal300	2.22	5	1.52	11.33	6.21	760.67	51.20	36.9	43.53	
		20	3.59	43.06	12.97	861.00	43.87	36.3	39.93	
		35	4.57	72.81	17.82	932.33	43.47	38.4	39.17	

**Table A-4:** Data measured from RST-XS, FT4 and DST for several Eskal powders and different pre-shear stresses.

Device	Sample	$d_{50}$ ( $\mu\text{m}$ )	$\sigma_{\text{pre}}$ (kPa)	$c$ (kPa)	$\sigma_1$ (kPa)	$\sigma_c$ (kPa)	$\rho_b$ ( $\text{kg/m}^3$ )	$\phi_c$ ( $^\circ$ )	$\phi$ ( $^\circ$ )	$\phi_{\text{ss}}$ ( $^\circ$ )
RST-XS	Eskal150	138	4.3	0.01	7.67	0.13	1447.67	34.13	32.00	29.93
	Eskal15	19		0.07	7.91	0.26	1416.67	34.57	33.80	32.53
	Eskal500	4.42		0.41	8.70	0.93	1015.00	40.83	38.33	37.50
	Eskal300	2.22		1.09	9.39	4.16	767.67	50.90	39.03	42.97
FT4	Eskal150	138	20	0.12	30.88	0.43	1441.45	33.75	33.41	24.91
	Eskal15	19		0.20	32.57	0.75	1297.10	33.51	32.95	29.82
	Eskal500	4.42		0.75	36.68	2.94	1081.57	37.59	35.68	34.16
	Eskal300	2.22		1.92	41.06	7.75	782.16	41.82	37.20	38.21
DST	Eskal150	138	36.08	0.86	59.83	1.95	1429.09	32.61	31.00	31.22
	Eskal15	19		1.30	60.83	3.10	1281.59	35.83	34.08	34.91
	Eskal500	4.42		2.13	61.33	7.40	1204.08	37.60	34.61	35.24
	Eskal300	2.22		3.67	64.47	10.07	952.30	42.01	37.21	38.27
Jenike	Eskal150	138	5	0.22	18.17	0.35	1445.63	35.31	34.13	32.09
	Eskal300	2.22		1.71	11.30	7.17	788.91	47.95	33.83	37.95

## 8.2 Appendix B: Supplementary data for section 3.2

The following figures and table are part of the poster presentation at the Powders and Grains 2017, Montpellier (France) and may not reflect on the published scientific communication on the EPJ Web of Conferences, EDP Sciences, 2017.

**Table B-1:** Sample dustiness and flow properties

Samples	$X_{50}$ , $\mu\text{m}^*$ (COV, %)	Total aerosol conc. ( $\#/\text{cm}^3$ )	Flowability, FFc <sup>^</sup> (COV, %)	Cohesion <sup>^</sup> , Pa (COV, %)
Eskal 300 (A1)	2.2 (3.1)	2.1e+02	2.3 (11)	1.1e+3 (8)
Eskal 500 (A2)	4.1 (0.1)	6.7e+03	9.6 (20)	412 (10)
Eskal 1000 (A3)	4.6 (1.4)	4.6e+03	8.4 (3)	390 (10)
Eskal 10 (B1)	10 (1.1)	5.6e+03	19 (19)	130 (20)
Eskal 14 (B2)	14 (0.3)	5.3e+03	26 (16)	104 (11)
Eskal 15 (B3)	16 (0.1)	9.5e+03	31 (16)	74 (5)
Eskal 20 (B4)	20 (0.2)	9.7e+03	23 (12)	81 (13)
Eskal 150 (C1)	136 (0.1)	2.9e+02	180 (18)	11 (56)

\* Powder PSD by volume measured using laser diffraction (3 repeats).

<sup>^</sup> Powder flowability and cohesion measured using Schulze ring shear tester at 4.3kPa (3 repeats).

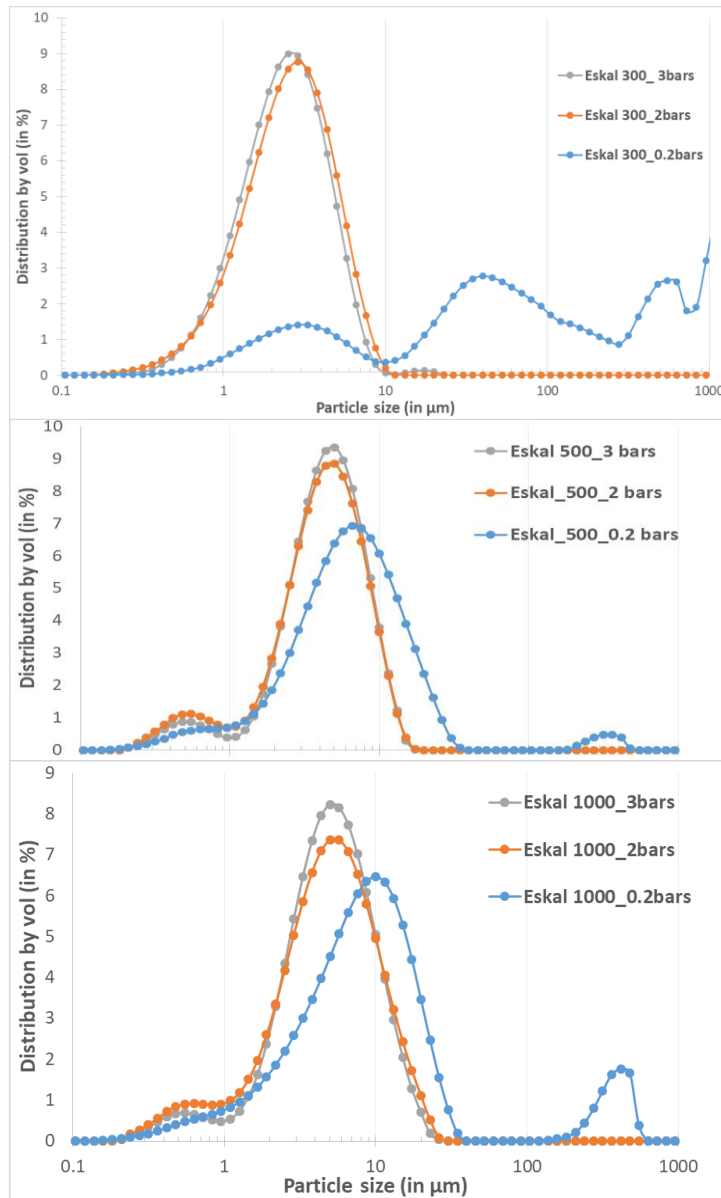


Figure B 1: Powder size distribution by volume using different operating pressure values (in bar) using laser diffraction size analysis in dry form for Group A powders.

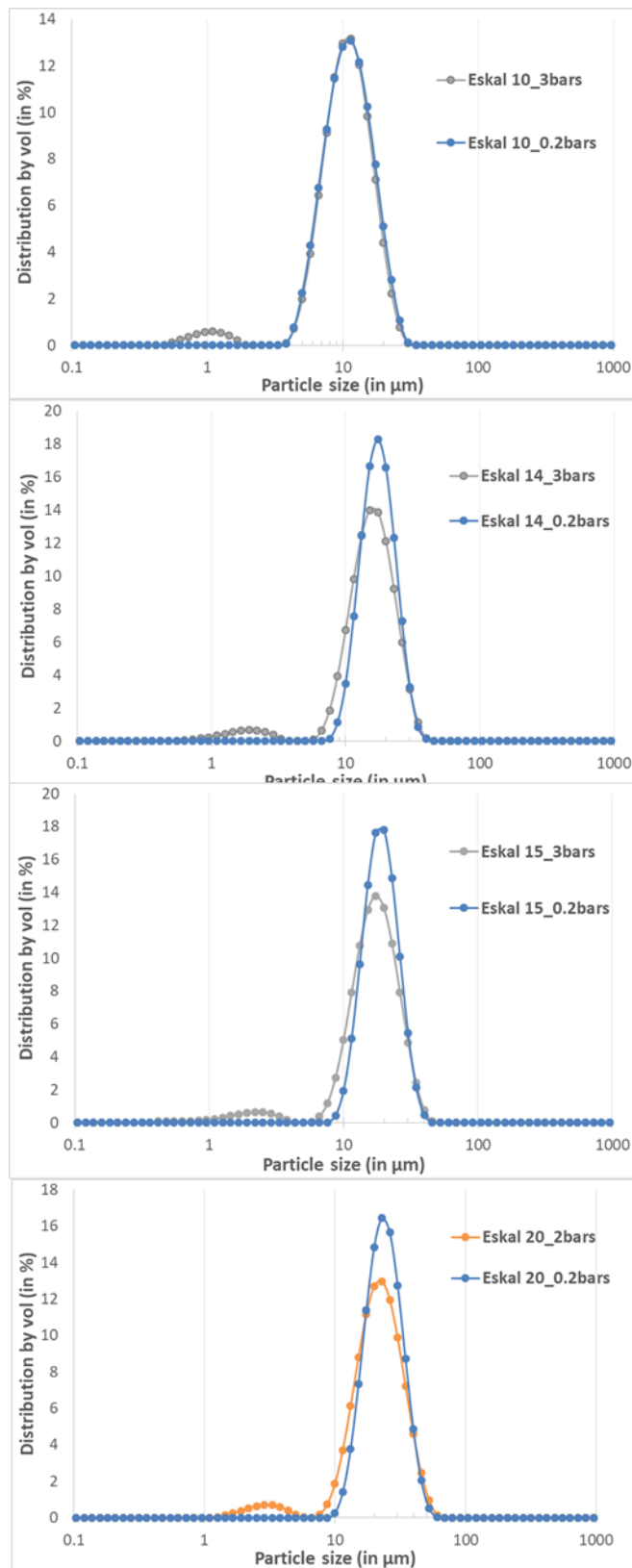
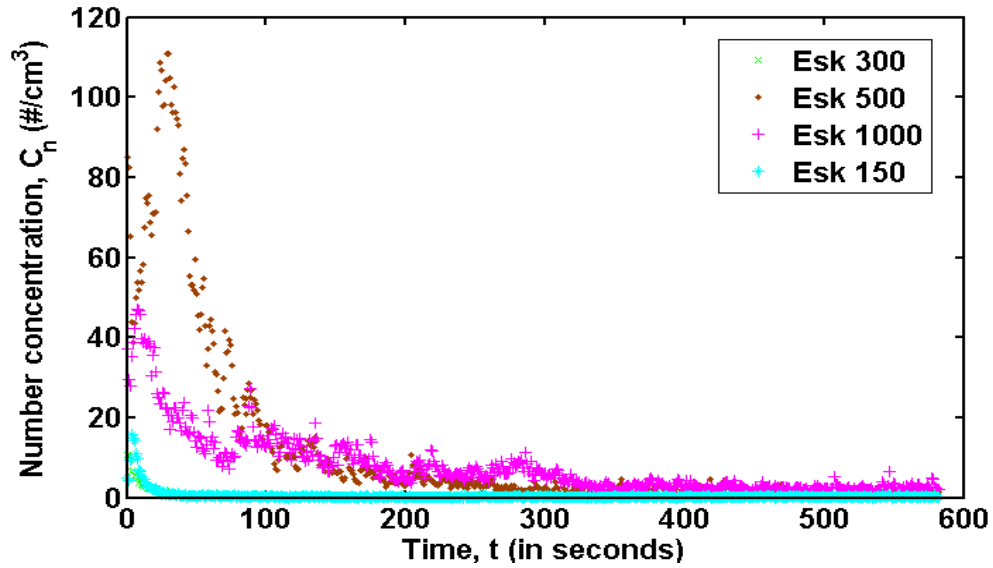
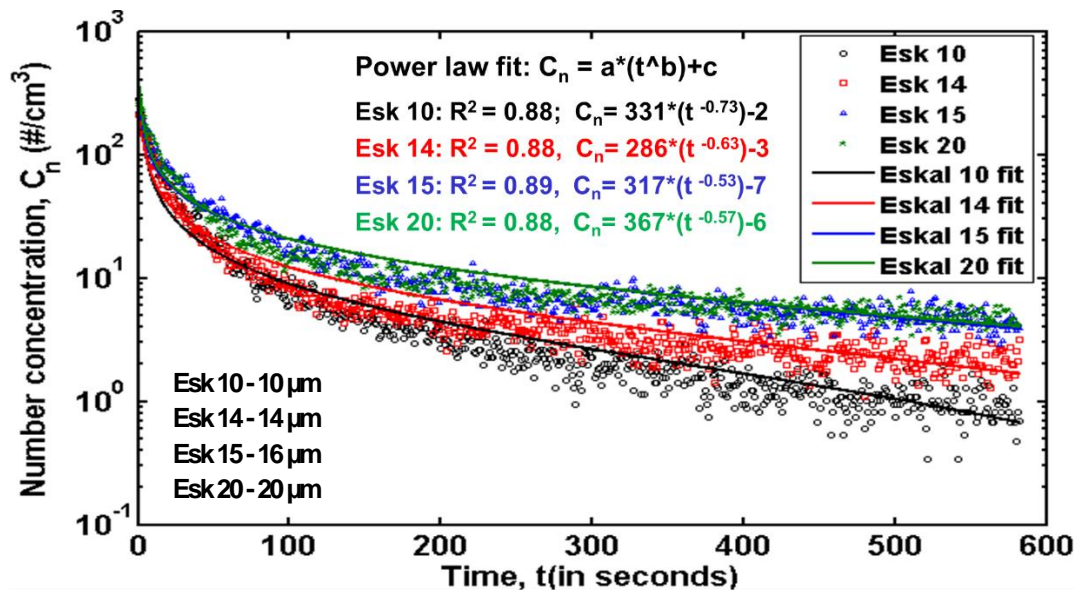


Figure B 2: Powder size distribution by volume using different operating pressure values (in bar) using laser diffraction size analysis in dry form for Group B powders.



**Figure B.3:** Dustiness pattern for cohesive (Esk 300, 500, 1000) and non-cohesive (Esk 150) powders



**Figure B.4:** a) Dustiness pattern for bi-modal powders (Esk 10, 14, 15, 20)



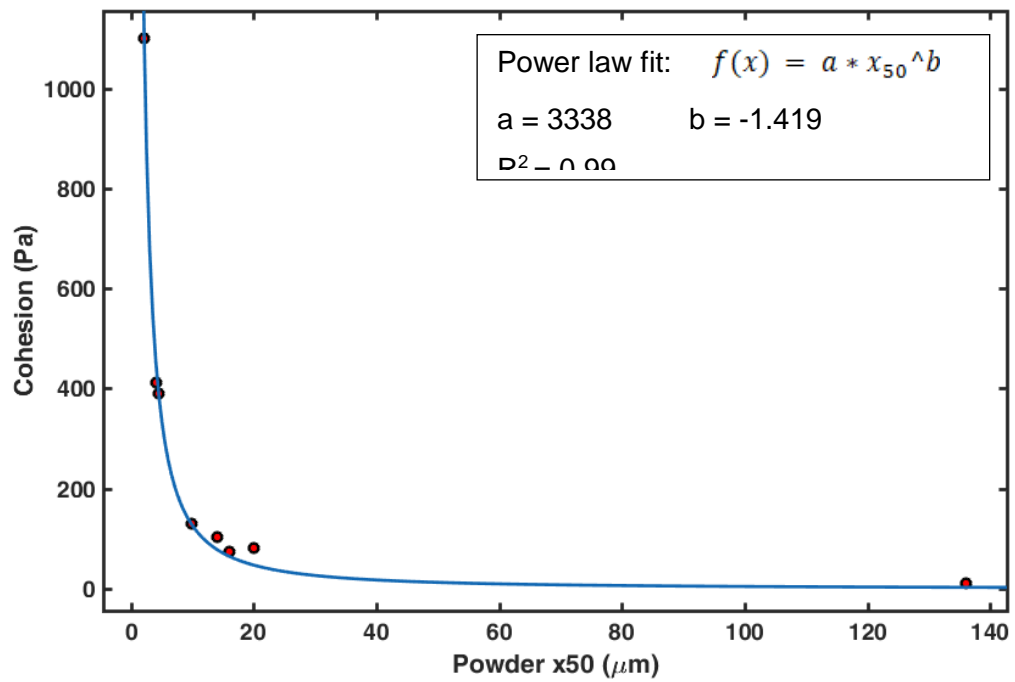


**Figure B.5:** Change in powder cohesion with median particle size. Power law fit (in blue)

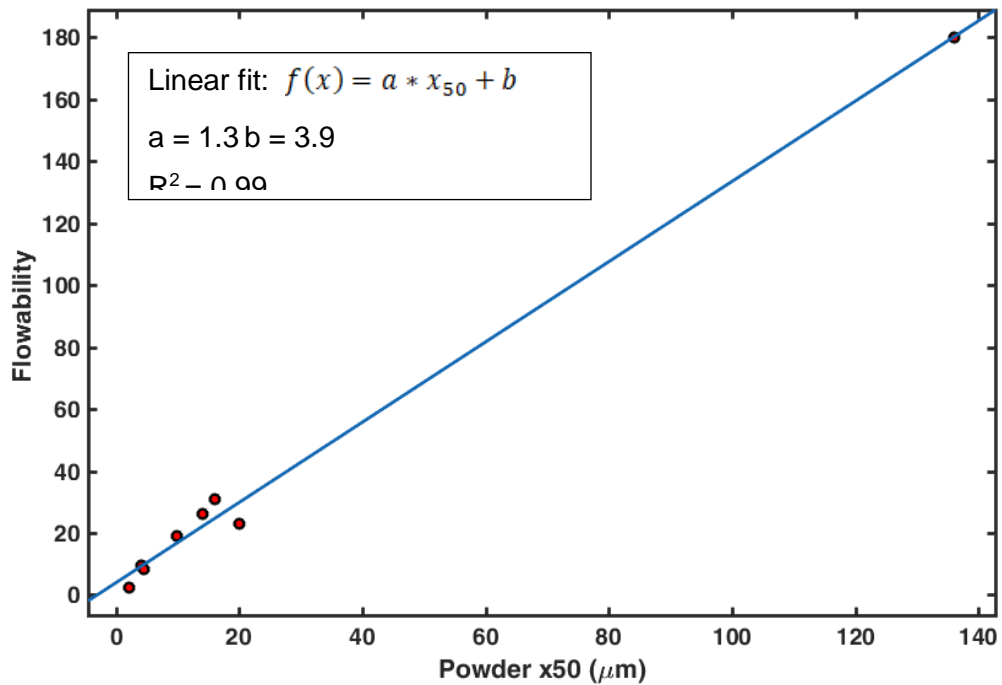


**Figure B.6:** Change in powder flowability with median particle size. Linear fit (in blue)

### 8.3 Appendix C: Supplementary data for section 4.1

Figure A.1 shows a bulk sample and a powder sample after a vortex shaker experiment. In Figure A.2, the locally averaged values of the particle's position in the stationary case are shown. Since the particle should be immobile, those random “movements” are completely spurious. Even a large amount of time points is not sufficient for evening out the measurement errors.

We further computed the frequency of the particle's coordinates in the stationary case, that is to say the frequency distribution of the experimental noise. In Figure A.3, the probability densities  $f(x)$ ,  $f(y)$  and  $f(z)$  are represented.

It can be seen that the probability distributions obtained from the frequencies of the measured positions can be well fitted to Gaussian curves.



**Figure C.1:** Test tube after a vortex shaker experiment.

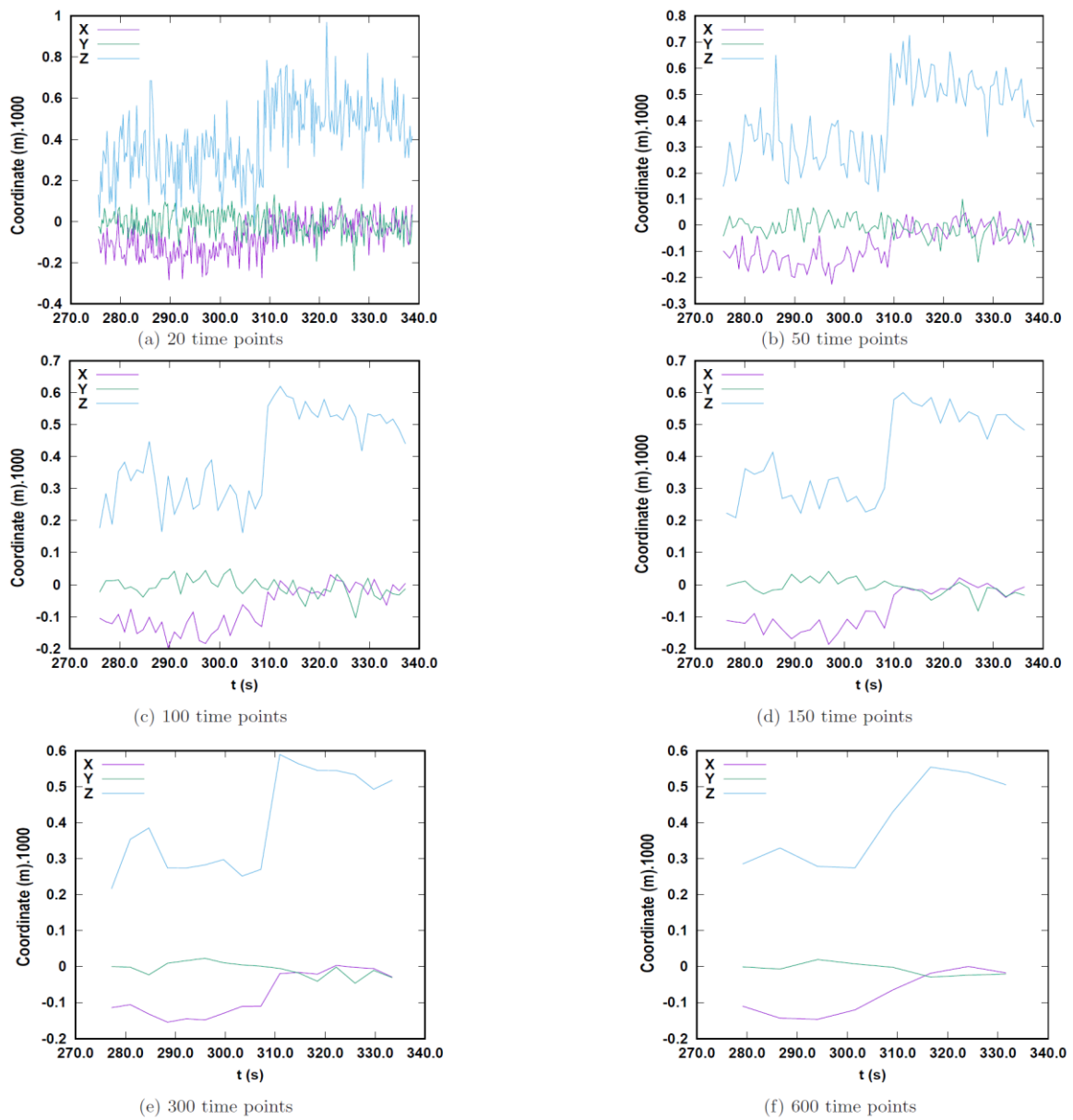


**Figure C.2:** Locally averaged coordinates.

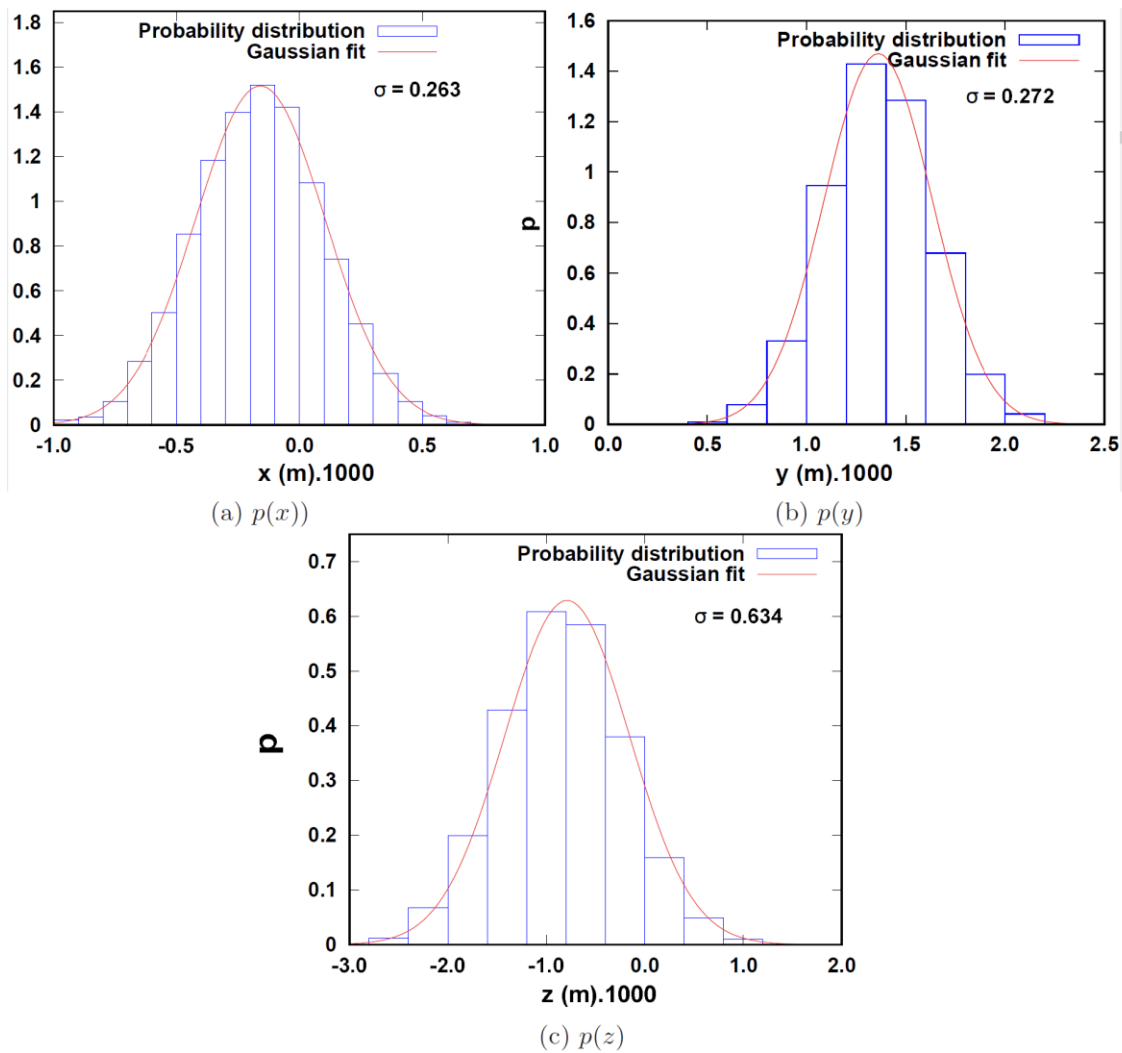


**Figure C.3:** Frequency distribution of  $X$ .

In what follows, for each considered variable ( $x$ ,  $y$ ,  $z$ ,  $V_x$ ,  $V_y$ ,  $V_z$ ,  $V$  and  $E$ , respectively), we show both repeated trials for the standard conditions (open test tube,  $\omega = 1500 \text{ rpm}$  and 2 g of powder). In Figures A.7 and A.8, we show the average velocity ( $\bar{V}$ ,  $\bar{V}_x$  and  $\bar{V}_y$  as a function of the horizontal coordinate  $x$  and the vertical coordinate  $y$ .

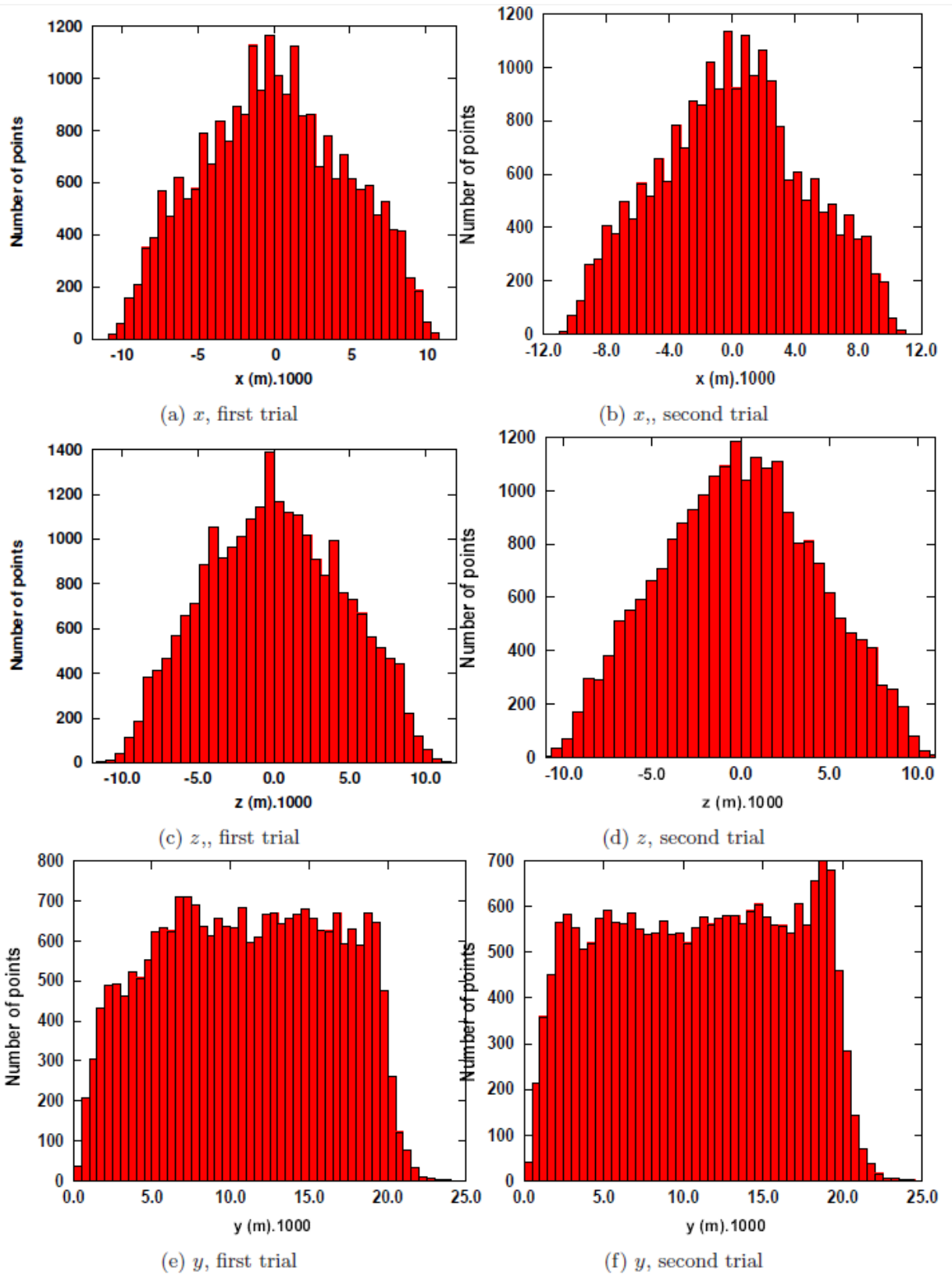


**Figure C.4:** Frequency distribution of the coordinates.

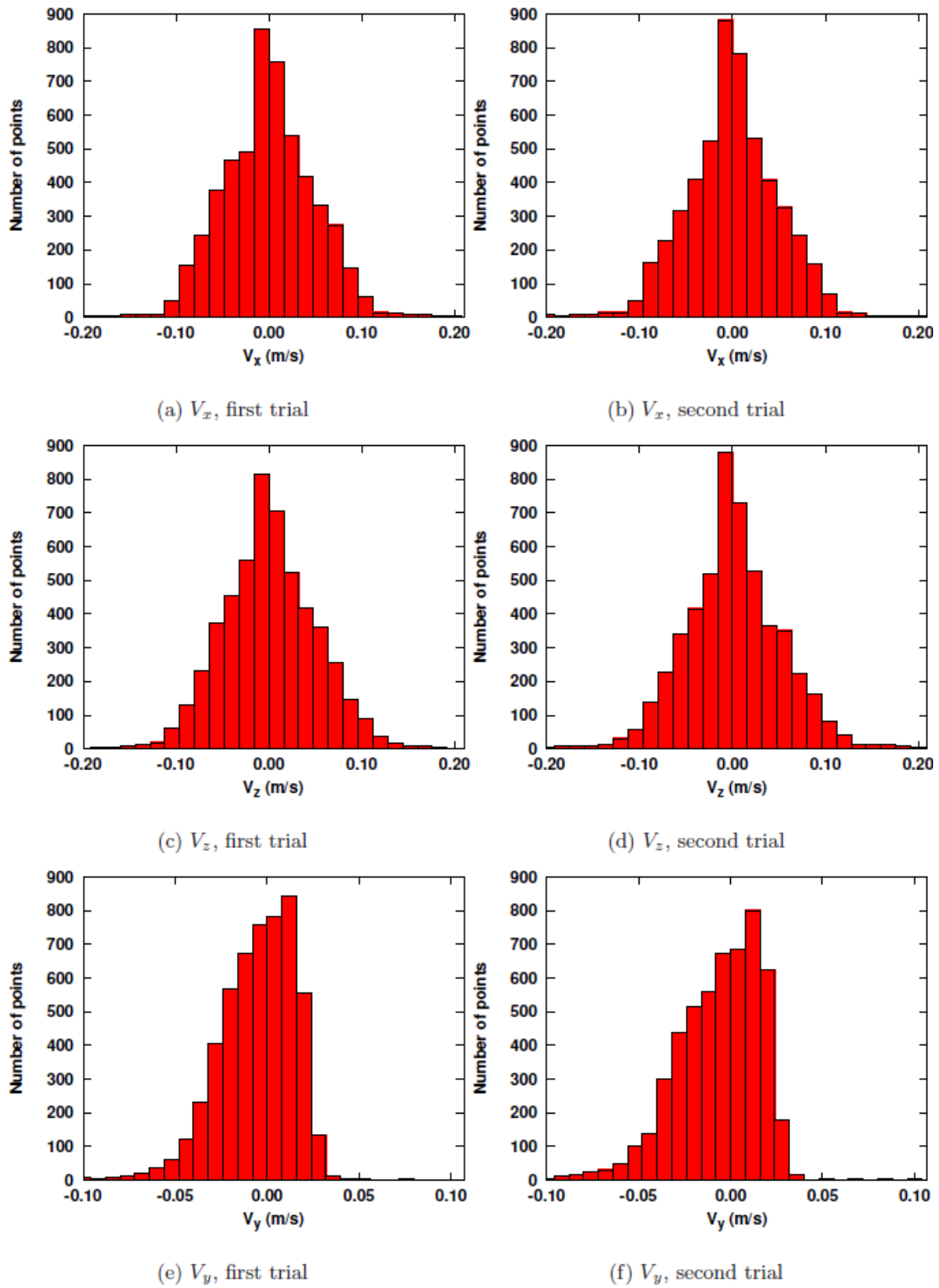
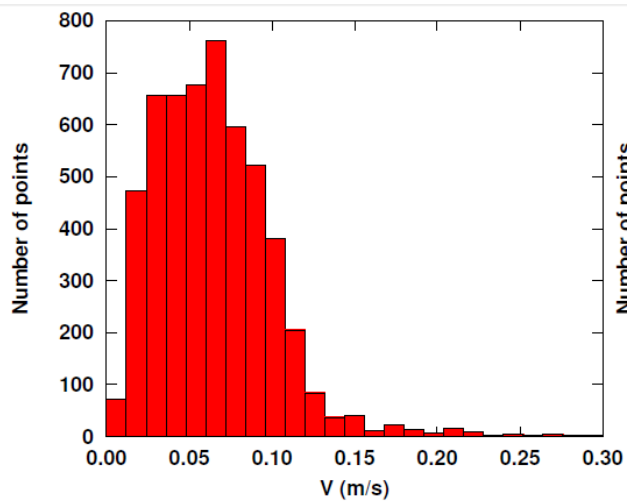
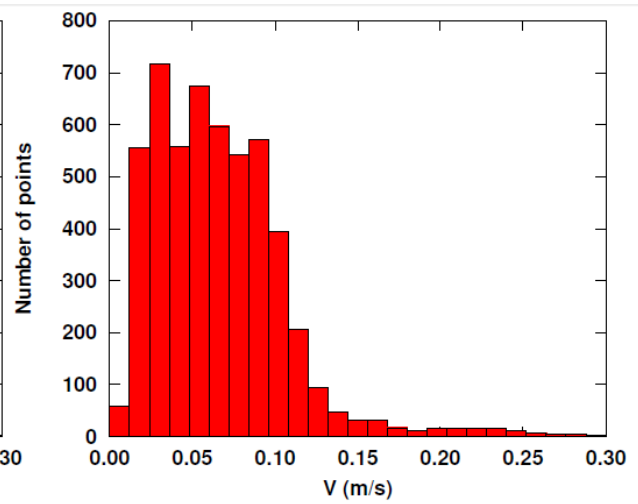


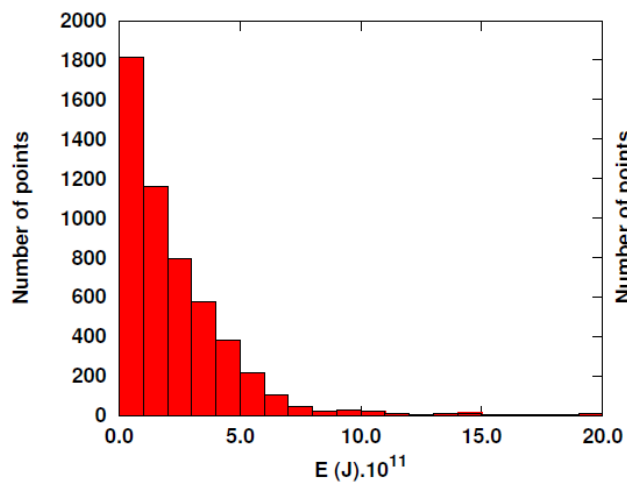
**Figure C.5:** Frequency distribution of the velocity components.



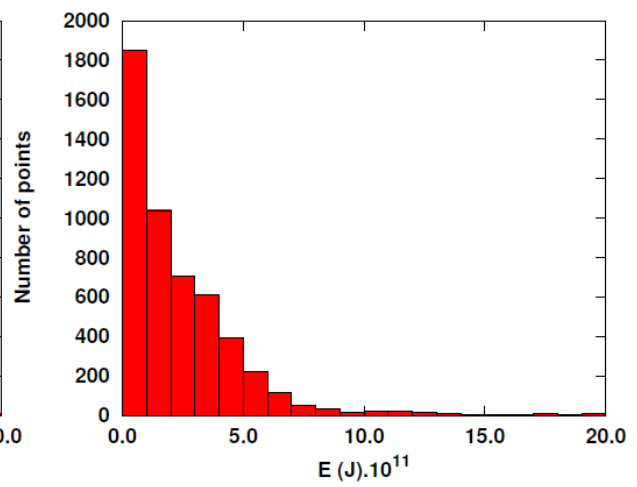
(a)  $V$ , first trial



(b)  $V$ , second trial



(c)  $E$ , first trial



(d)  $E$ , second trial

**Figure C.6:** Frequency distribution of the velocity.

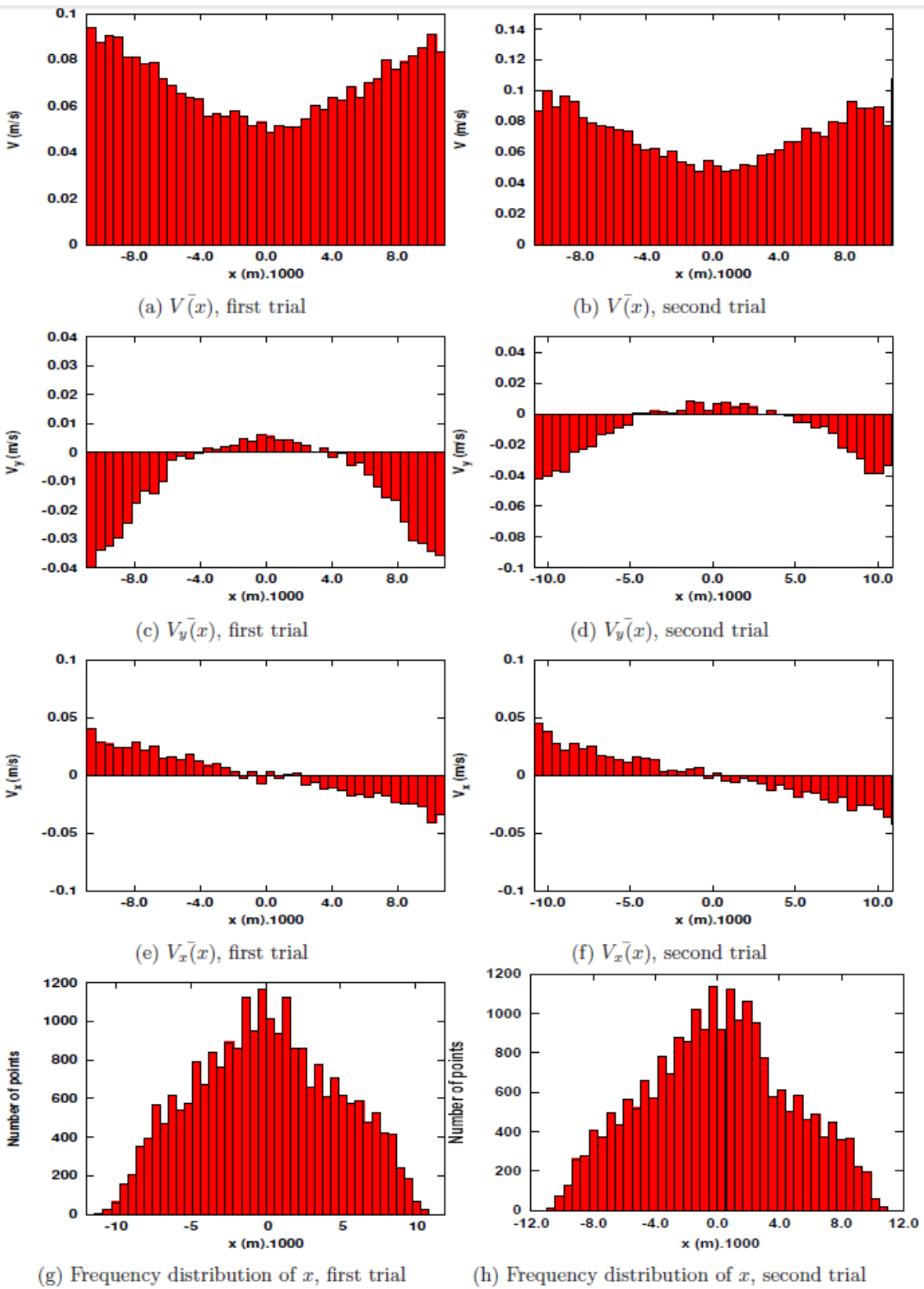


**Figure C.7:** Velocity as a function of  $x$ .



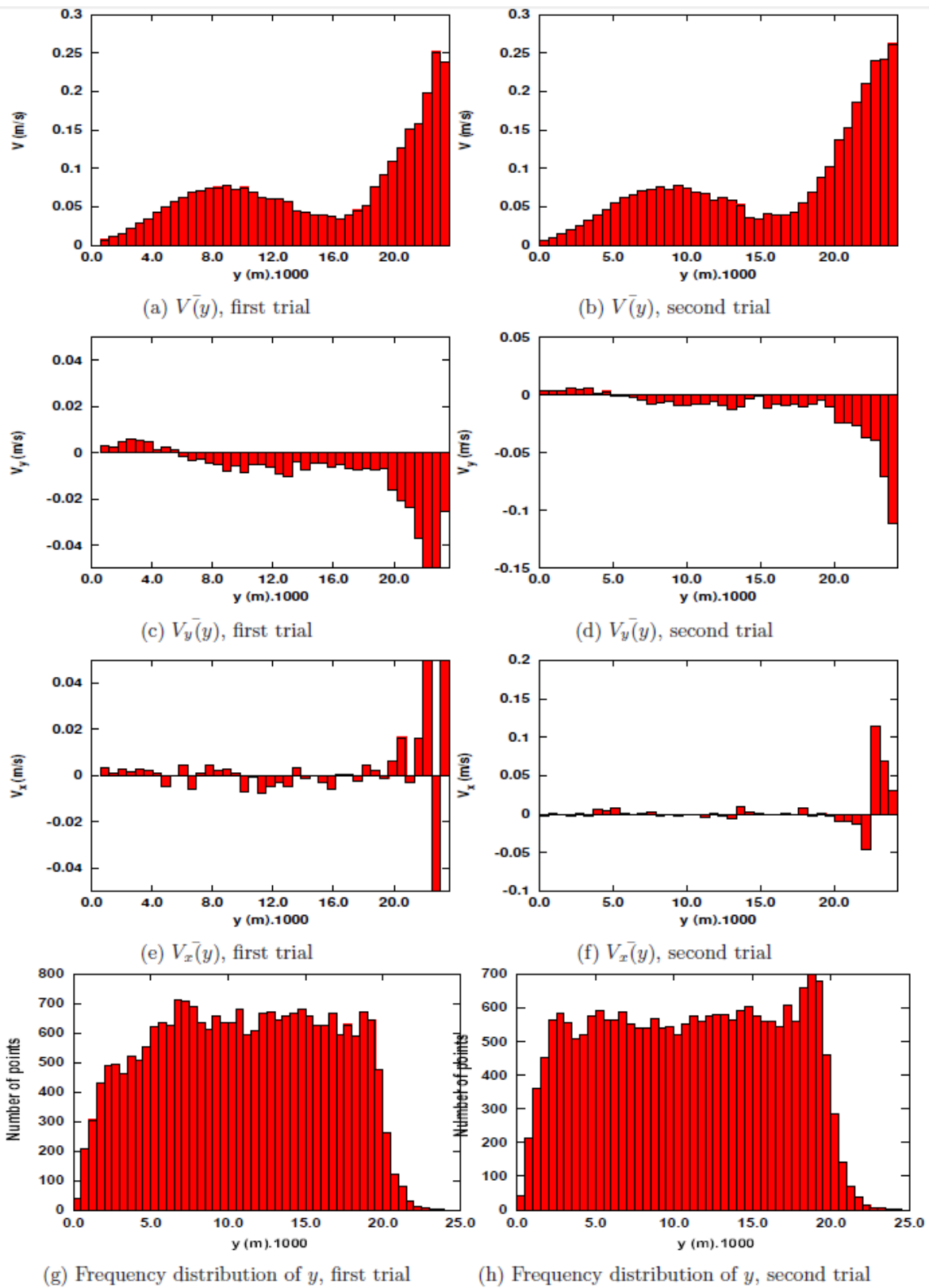


**Figure C.8:** Velocity as a function of  $y$ .